DEVELOPMENT OF NANOCATALYSTS VIA CO-PRECIPITATION CUM MODIFIED STÖBER METHOD AND APPLICATION TO METHANE DECOMPOSITION

MUHAMMED ASHIK.U.P

THESIS SUBMITTED IN FULFILMENT OF THE REQUIREMENTS FOR THE DEGREE OF DOCTOR OF PHILOSOPHY

FACULTY OF ENGINEERING
UNIVERSITY OF MALAYA
KUALA LUMPUR

2016

UNIVERSITI MALAYA

ORIGINAL LITERARY WORK DECLARATION

Name of Candidate: **Muhammed Ashik.U.P** (Passport No.:)

Registration/Matric No.: **KHA120027**

Name of Degree: **Doctor of Philosophy**

Title of Project paper/Research Report/ Dissertation/ Thesis ("this work"):

Development of Nanocatalysts via Co-Precipitation cum Modified Stöber Method and Application to Methane Decomposition

Field of Study: **Reaction Engineering**

I do solemnly and sincerely declare that:

1. I am the sole author/writer of this work;
2. This work is original
3. Any use of any work in which copyright exists was done by way of fair dealing and for permitted purposes and any excerpt or extract form, or reference to or reproduction of any copyright work has been disclosed expressly and sufficiently and the title of the work and its authorship have been acknowledged in this work;
4. I do not have any actual knowledge nor do I ought reasonably to know that the making of this work constitutes an infringement of any copyright work;
5. I hereby assign all and every rights in the copyright to this work to the University of Malaya ("UM"), who henceforth shall be owner of the copyright in this work and that any reproduction or use in any form or by any means whatsoever is prohibited without the written consent of UM having been first had and obtained;
6. I am fully aware that if in the course of making this work I have infringed any copyright whether intentionally or otherwise, I may be subject to legal action or any other action as may be determined by UM.

Candidate's Signature Date

Subscribed and solemnly declared before,

Witness's Signature Date

Name:

Designation:

ABSTRACT

Nanoparticle formation from their respective precursors through bottom-up method is a very fascinating practice in nanotechnology. This research contribution discusses two promising bottom-up methods: i) controlled precipitation of Ni, Fe, and Co nanoparticles and reinforcement with silicate through modified Stöber method, and ii) chemical vapor deposition of nanocarbon from methane. Thermocatalytic decomposition of methane is a fully green single step technology for producing hydrogen and nanocarbon. In spite of having great success in the laboratory scale production, industrial thermocatalytic decomposition of methane for greenhouse gas free hydrogen production is still in its infancy. However, deactivation of catalyst is the prime drawback found in thermocatalytic decomposition of methane. In this research contribution, *n*-NiO/SiO_2, *n*-FeO/SiO_2, and *n*-CoO/SiO_2 nano-structured catalysts were prepared by co-precipitation cum modified Stöber method and used for thermocatalytic decomposition of methane to produce hydrogen and carbon nanotubes. Our experimental results reveal that the metal oxide particles were formed as single crystal nanoparticles upon the addition of silicate and exhibited catalytic activity promoting features, such as lower particle size and higher surface area and porosity. Temperature programmed methane decomposition from 200 to 900 °C were conducted in a fixed bed pilot plant as preliminary catalytic examination and further isothermal analysis were performed in between 475 and 700 °C. Production of hydrogen at each experimented temperature and corresponding carbon yield were measured. Among the three catalysts inspected, *n*-NiO/SiO_2 found as the most efficient one for thermocatalytic methane decomposition and exhibited methane transformation activity more than 300 min, without a significant deactivation at temperature range from 475 to 600 °C, designating the resistance capability of analyzed nano-structured catalyst irrespective of many reported catalysts. *n*-NiO/SiO_2 produced an enormous carbon yield of ~5000% at 600 °C within 5 h of experiment. While, the rapid deactivation of the *n*-

FeO/SiO_2 and *n*-CoO/SiO_2 catalysts were attributed to the particle agglomeration and irregular formation of nanocarbon due to the metal fragmentation. Most efficient *n*-NiO/SiO_2 catalyst was selected for further studies. Methane decomposition kinetics over *n*-NiO/SiO_2 catalyst were studied by considering thermodynamic deposition of carbon at a temperature range of 550 to 650 °C and methane partial pressure from 0.2 atm to 0.8 atm. The findings concluded that the enhancement occurred with carbon formation rate when increasing the methane partial pressure, which is very much evident at higher temperature such as 650 °C. The effects of methane partial pressure and reaction temperature on the specific molar carbon formation rate were examined. The calculated reaction order and activation energy were found to be 1.40 and 60.9 kJ mol^{-1}, respectively. The governance of porosity and methane decomposition activity sustainability of *n*-NiO/SiO_2 catalyst by changing synthesis parameters such as nickel/silicate ratio, C18TMS/TEOS ratio and different solvents were also conducted. Physical and chemical characteristics of produced nano-catalysts were performed by N_2 adsorption-desorption measurement (BET), X-ray diffraction (XRD), transmission electron microscopy (TEM), field-emission scanning electron microscopy - Energy-dispersive X-ray spectroscopy (FESEM-EDX), and hydrogen-temperature programmed reduction (H_2-TPR). Produced nanocarbons were inspected with TEM, FESEM, and XRD.

ABSTRAK

Pembentukan nanopartikel daripada rumusan asalnya kaedah bottom-up adalah amalan yang sangat menarik dalam teknologi nano. Dua kaedah bottom-up telah digunakan dalam penyelidikan ini iaitu; i) mendakan terkawal nano-partikel Ni, Fe dan Co dan pengukuhannya dengan silikat dengan kaedah Stöber yang telah diubahsuai dan ii) pemendapan wap kimia nano karbon daripada metana. Penguraian pemangkin haba metana adalah satu langkah teknologi hijau untuk menghasilkan hidrogen dan nano karbon. Walaupun mempunyai kejayaan besar dalam pengeluaran skala makmal, penguraian pemangkin haba metana bagi pengeluaran gas rumah hijau tanpa hydrogen dalam industri masih di peringkat awal. Walau bagaimanapun, penyahaktifan mangkin adalah kelemahan utama yang ditemui dalam penguraian pemangkin haba metana. Sumbangan kajian ini, *n*-NiO/SiO_2, *n*-FeO/SiO_2 dan *n*-CoO/SiO_2 pemangkin berstruktur nano menyediakan pemangkin melalui mendakan yang diubahsuai menggunakan kaedah Stöber untuk penguraian pemangkin haba metana bagi menghasilkan hidrogen dan karbon nanotube dalam membangunkan pemangkin yang sangat stabil. Hasil eksperimen menunjukkan bahawa zarah logam oksida terbentuk sebagai zarah nano kristal tunggal melalui penambahan silikat dan mempamerkan aktiviti pemangkin yang mempunyai ciri-ciri seperti saiz zarah yang lebih rendah dan luas permukaan yang lebih tinggi dan keliangan. Penguraian metana yang di programkan suhu dibuat di sebuah kilang perintis katil tetap sebagai pemeriksaan awal pemangkin dan analisis sesuhu lanjut telah dilakukan di antara 475 dan 700 °C. Jumlah pengeluaran hidrogen pada setiap suhu eksperimen dan hasil karbon dicatatkan. Antara tiga pemangkin yang dikaji, *n*-NiO/SiO_2 merupakan pemangkin yang paling berkesan untuk penguraian pemangkin haba metana dan telah mempamerkan aktiviti transformasi metana lebih daripada 300 minit tanpa banyak penyahaktifan pada julat suhu 475 – 600 °C, tidak seperti kebanyakan kajian yang mengkaji kebolehan pemangkin berstruktur nano terhadap keupayaan kalangan.

Sementara itu, penyahaktifan pesat pemangkin *n*-FeO/SiO_2 dan *n*-CoO/SiO_2 menyumbang kepada aglomerasi zarah dan pembentukan nano karbon yang tidak sekata disebabkan oleh pemecahan logam. Pemangkin *n*-NiO/SiO_2 yang merupakan pemangkin yang paling efisien telah dipilih bagi kajian lanjut. Kinetik penguraian metana ke atas pemangkin *n*-NiO/SiO_2 telah dikaji dengan mempertimbangkan pemendapan termodinamik karbon dalam pelbagai suhu di antara 550 °C sehingga 650 °C dan tekanan separa metana dari 0.2 atm sehingga 0.8 atm. Hasil kajian mendapati bahawa peningkatan itu berlaku dengan kadar pembentukan karbon apabila maningkatkan tekanan separa metana pada suhu yang labih tinggi seperti 650 °C. kesan tekanan separa metana dan tindak balas suhu pada molar spesifik bagi kadar pembentukan karbon telah dikaji. Orde reaksi dan tenaga pengaktifan yang telah dikira masing-masing sebanyak 1.40 dan 60.9 kj mol^{-1}. Kajian terhadap keliangan dan aktiviti penguraian metana bagi memastikan kemampanan pemangkin *n*-NiO/SiO_2 dengan menukarkan parameter sintesis seperti nisbah nikel/silikat, nisbah C18TMS/TEOS dan pelurat yang berbeza turut dijalankan. Cir-ciri fizikal dan kimia yang dihasilkan pemangkin nano telah dijalankan melalui pengukuran penjerapan-penyaherapan N_2 (BET), pembelauan sinar-X (XRD), transmisi mikroskop electron (TEM), imbasan mikroskop electron – Tenaga sebaran sinar-X (FESEM-EDX) dan pengurangan suhu hidrogen diprogramkan (H_2-TPR). Nano karbon yang dihasikan telah diperiksa dengan TEM, FESEM dan XRD.

ACKNOWLEDGEMENTS

In the name of God, Most Gracious, Most Merciful
Read! In the name of your Lord who created - Created the human from something which clings - Read! And your Lord is Most Bountiful - He who taught (the use of) the Pen - Taught the human that which he knew not.
(Holy Quran 96:1-5)

My deepest gratitude is to my supervisor, Prof. Dr. Wan Mohd Ashri Wan Daud. I have been amazingly fortunate to have an advisor who gave me the freedom to explore on my own, and at the same time the guidance to recover when my steps faltered.

Special thanks to Dr. Hazzim Fadhil Abbas, Department of Chemical Engineering, University of Nizwa, Oman, for his inspiration and support. Sincere thanks go to all those who have helped me in the various stages of this work, even with a mere word of encouragement. Thanks are also due to my fellow researchers, senior researchers in our group, all technicians, and staff in the Department of Chemical Engineering. It is their support that helped me to complete my project work successfully.

Most importantly, none of this would have been possible without the love and patience of my family. Both *Urampully* and *Thanappadath* families to whom this thesis is dedicated to, have been consistent sources of love, concern, support, and strength all these years. My profound thanks and gratitude are extended with full respect, honor, and love to my beloved parents, who were my first teachers. I am really short of suitable words to express my gratitude and appreciation to my better half Shanu, who supported and tolerated me throughout this work.

Finally, I appreciate the financial support from University of Malaya through High Impact Research Grant (UM.C/HIR/MOHE/ENG/11).

Above all I prostrate myself in front of God almighty, the most merciful.

"*O my Sustainer! Increase my knowledge"* (Holy Qur'an 20:114).

Muhammed Ashik.U.P
March 2016

TABLE OF CONTENTS

LIST OF FIGURES

LIST OF TABLES

LIST OF SYMBOLS AND ABBREVIATIONS

LIST OF SYMBOLS

ΔH^0	-	Change of enthalpy (kJ mol^{-1})
ΔG_r^0	-	Gibbs free energy (kJ mol^{-1})
vol%	-	Volume percentage
W	-	Catalyst weight (g)
T	-	Temperature in (°C)
P_{CH_4}	-	Methane partial pressure (atm)
F	-	Flow rate (L/min)
Rt	-	Residence time (min)
H_2 (%)	-	Hydrogen volume percentage
iH_2	-	Initial hydrogen (%)
CH_4 (%)	-	Methane volume percentage
iCH_4	-	Initial methane (%)
$i\chi_{CH_4}$	-	Initial methane fractional conversion
R^2	-	Correlation coefficient
$R_{CH_4,0}$	-	Initial rate of methane decomposition (mmol($g_{cat.}$min)$^{-1}$))
F	-	Flow rate of total gas stream
F_{CH_4}	-	Molar flow rate of methane (mmol/min)
$\dot{F}_{H_2}$	-	Molar flow rate of hydrogen (mmol/min)

R_{max}	-	Maximal specific molar carbon formation rate (mol/g_{cat}.min)
A	-	Pre-exponential factor in equation 4.10
Ea	-	Activation energy (kJ mol^{-1})
R	-	Gas constant (8.31 JK^{-1} mol^{-1})
Kp	-	Rate constant
C_{dep}	-	Carbon deposit (g_c/g_{cat})
r_C	-	Rate of carbon deposit (g_c/g_{cat}.h)
t_{max}	-	Time at which maximum methane conversion occur (h)
t	-	Time (h)

LIST OF ABBREVIATIONS

TCD	-	Thermocatalytic Decomposition of Methane
TPMD	-	Temperature Programmed Methane Decomposition
SRM	-	Steam Reforming of Methane
POX	-	Partial Oxidation
DRM	-	Dry Reforming of Methane
GHG	-	Green-House Gas
NG	-	Natural Gas
CNF	-	Carbon Nanofibers
MSI	-	Metal–Support Interaction
GHSV	-	Gas Hourly Space Velocity

VHSV	-	Volume Hourly Space Velocity
TLC	-	Thin Layer Catalysts
AC	-	Activated Carbon
CB	-	Carbon Black
ACPS	-	Activated Carbon from Palm Shell
CNT	-	Carbon Nanotube
NCB	-	Nano-sized Carbon Black
MWNT	-	Multi Walled Nanotube
CLR	-	Coal Liquefaction Residue
HES	-	High-Energy Sites
HPC	-	Hierarchical Porous Carbon
OSG	-	Oxygen Surface Group
OCM	-	Oxidative Coupling of Methane
DFT	-	Density Functional Theory
n	-	Nano
BET	-	Brunaur–Emmett–Teller
H_2-TPR	-	Hydrogen Temperature-Programmed Reduction
XRD	-	X-Ray Diffraction
TEM	-	Transmission Electron Microscopy
FESEM	-	Field Emission Scanning Electron Microscopy
EDX	-	Energy-Dispersive X-Ray Spectroscopy

XPS	-	X-Ray Photoelectron Spectroscopy
IR	-	Infra Red
FBR	-	Fixed bed reactor
FlBR	-	Fluidized bed reactor
CFR	-	Continuous flow reactor
RBR	-	Rotary bed reactor
MLR	-	Multilayer reactor

LIST OF APPENDICES

CHAPTER 1: INTRODUCTION

1.1 GENERAL

Hydrogen, the simplest, the lightest and the most abundant element in the known universe appears to be one of the auspicious energy carriers, however, the greenest one if produced from renewable resources. This alternative green fuel is indispensable in the contemporary scenario of huge greenhouse gas (GHG) emission from the combustion of fossil fuel. Since, fossil fuels dominate energy consumption with a market share of 87%, all the while, renewable energy accounts 2% only (*Statistical Review of World Energy*, 2012). According to the International Energy Agency's World Energy Outlook (2012), the global energy requirement expected to grow by more than one-third over the period 2035. The rise in energy consumption causes the elevation in the emission of GHGs like CO_x, C_xH_y, NO_x, SO_x, etc. (Jos G.J. Olivier, 2012). Consequently, atmospheric CO_2 level hits awful record highs (Fourth Assessment Report: Climate Change, 2007). This increasing CO_2 emissions will lead to anthropogenic global warming, climate change, and ocean acidification, which would have severe consequences for ecosystem and for sustainability of human society. Moreover, fossil fuel is about to run out of availability soon as its limited reserve in earth. Hence, it is essential to place the worldwide energy system onto a more sustainable, secure, and environmentally benign path. Unfortunately, energy sources such as, wind, solar, bio, and nuclear are not desirable for economic energy production, because of their undeveloped technology, establishment cost, and safety concerns. Hence, hydrogen being considered as a clean fuel as it produces water only on its combustion (Serrano et al., 2010; Stephens-Romero et al., 2009). Furthermore, H_2–O_2 fuel cells are environmentally benign and highly efficient devices which convert chemical energy of hydrogen directly into electricity. Moreover, H_2-O_2 fuel cells overcome the limitations imposed by the Carnot efficiency.

Hydrogen produces three times higher quantity of energy (39.4 $kWh.kg^{-1}$) during its combustion than that produced by any other fuel on a mass basis, e.g. liquid hydrocarbons (13.1 $kWh.kg^{-1}$) (Züttel, 2004). Hence, one gallon of gasoline has about the same energy as one kilogram of hydrogen gas and it is expected that the hydrogen can replace all forms of fossil fuels in recent future. Approximately 100 times of the present hydrogen production (more than 3×10^{12} kg) would have to be produced per year to fulfill world's demand for fossil fuel. There is no natural resource of hydrogen and therefore it is not a primary fuel. Hence, hydrogen must be extracted at low cost from other abundant primary energy sources like coal, natural gas, naphtha, heavy oil, biomass, wastes, solar, wind, or nuclear power, without harming the environment (Nasir Uddin et al., 2013; Navarro et al., 2009; Ueno et al., 2007).

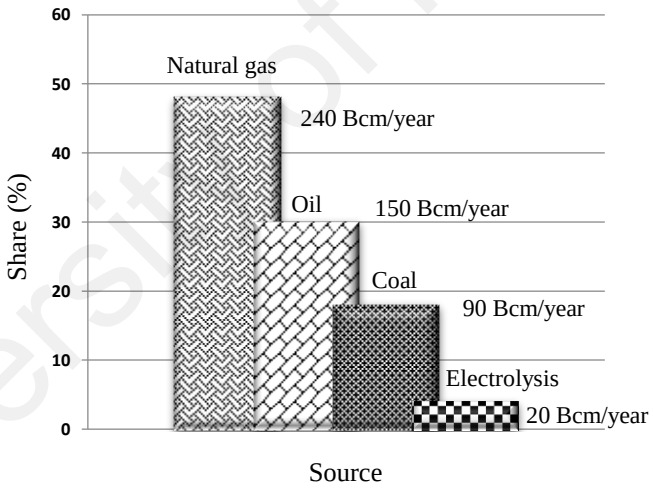

Figure 1.1 Worldwide hydrogen production by sources.

Global statistics illustrate that 48% (240 Billion cubic meters (Bcm)/year) of hydrogen is produced from natural gas (NG), 30% (150 Bcm/year) from petroleum, and 18% (90 Bcm/year) from coal, while only 4% (20 Bcm/year) is obtained through water electrolysis (Balat & Balat, 2009). The worldwide contribution of different sources to overall hydrogen production are shown in Figure 1.1. The major contribution of NG for

hydrogen production owe to the availability of huge methane reserves in deep ocean bed as well as in industrialized countries like United States (Konieczny et al., 2008).

Various hydrogen production method were developed, such as bio-hydrogen production, reviewed elsewhere (Brentner et al., 2010), steam reforming of methane (SRM), partial oxidation (POX), coal gasification, water splitting, biomass gasification and thermochemical processes (Abbas & Daud, 2010b; S. Wang, 2008). Water splitting process, consuming renewable solar and wind energy is very fascinating, but not economical because of its poor efficiency and higher processing cost. Water can be directly converted to H_2 and O_2 with zero CO_2 emission by using photoelectrodes with sunlight illumination in aqueous electrolytes. The integration of solar energy concentration systems with systems capable to split water is of immense value and impact on the energetics and economics worldwide. For this application, the photoelectrode materials must have an appropriate band gap and special catalytic properties and needs to be stable in the aqueous environment under illumination (Khaselev & Turner, 1998). Unfortunately, nearly all known materials today fail to fulfil these conditions (Nowotny et al., 2005). The highest reported solar to hydrogen conversion efficiency till 1998 was 12.4% (Khaselev & Turner, 1998) for an illuminated area of 0.2 cm^2, referring to the lower heat value of hydrogen. Peharz et al. (2007), achieved an efficiency of 18% in 2007 for the solar to hydrogen production under outdoor conditions. The hydrogen production rate obtained with water splitting process is too low due to quick charge recombination of photo-generated electron/hole pairs, quick backward reaction and inability to utilize visible light efficiently (Ni et al., 2007). Furthermore, the dissociation of water is a reaction not favored thermodynamically; one has to go up to extremely high temperatures (>2200 °C) for obtaining some significant dissociation degree (Kodama, 2003). Moreover, direct one-step water splitting requires the energy intensive process of high temperature oxygen‑hydrogen separation coupled with expensive membrane technology

and therefore is considered of little chance for technical and economic viability in the near future.

The gasification and reforming of biomass are extensively explored for producing hydrogen from several biomass resources such as forest residues, wood wastes, crop residues, waste water treatment, biogas, etc. (Westermann et al., 2007). Nevertheless, the major limitations of these technologies are the necessity of coupling of further stages like gas separation/purification treatments and the occurrence of further sophisticated reactions which reduces hydrogen selectivity (P. Jana et al., 2012). Figure 1.2 depicts different sources, preparation methods, intensity of GHG emission of each process and utilization of hydrogen.

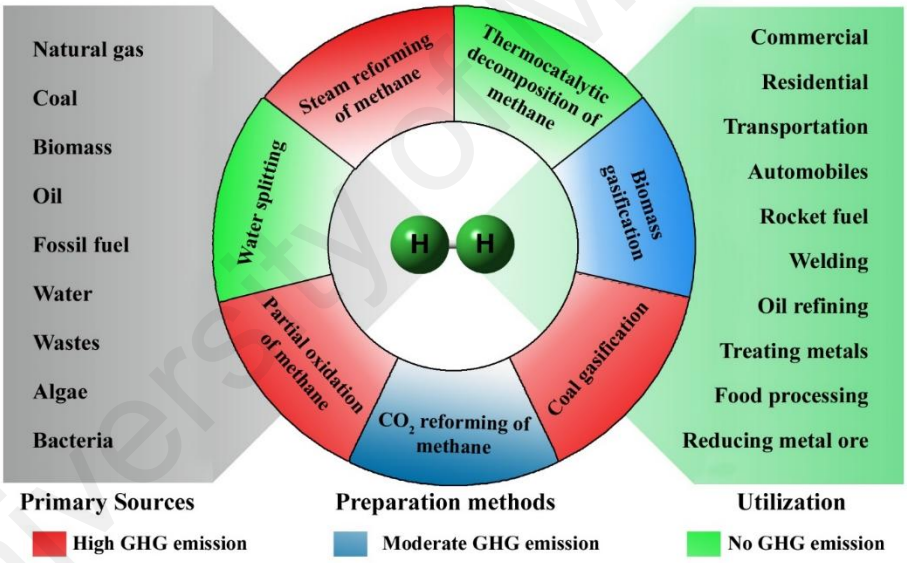

Figure 1.2 Schematic representation of the sources, preparation methods, and utilization of hydrogen.

SRM and POX are the current thermochemical processes for hydrogen production from methane, the main constituent of NG having highest C - H ratio. SRM has been considered as the one of the most common and regularly adopted technique for many years. In spite of its high process efficiency (50%) and comparatively low cost, SRM causes high emissions of CO_x (at least 1 mol of CO_2 per mol of converted methane) and requires more

process energy (T. Zhang & Amiridis, 1998). Moreover, fuel reforming process is multifaceted containing CO elimination by water gas shift reaction together with selective CO oxidation. Hence, the post-reaction mixture contains huge quantities of CO even after the purification. Similarly, the POX process also causes GHG emission. Consequently, thermocatalytic decomposition of methane (TCD) or so-called methane cracking seems to be attractive as a novel technique for eco-friendly hydrogen production. In this moderately endothermic process, methane is thermally decomposed to solid carbon and gaseous hydrogen in a technically simple one step process as shown in equation (1.1).

$$CH_4 \rightarrow C + 2H_2 \qquad \Delta H_{298K} = 74.52 \text{ kJ/mol} \qquad (1.1)$$

Catalysts are crucial in TCD process for hydrogen generation and, accordingly, improvement in the catalyst properties should have a significant impact on the efficiency of the production. Thermal decomposition of methane requires elevated temperatures (in excess of 1200 °C), therefore, much research on the development of efficient catalysts for the process has been conducted since early 1960s (Jang & Cha, 2007; Y. Li et al., 2000; J. L. Pinilla et al., 2010; Saraswat & Pant, 2011; Shah et al., 2001). Most of the efforts in this area were focused on methane decomposition over transition metal catalysts (Ni, Fe, Co) (Derbyshire & Trimm, 1975; Robertson, 1972). Metallic catalysts are distinguished from carbon-based catalysts in their ability to sustain the cracking reaction for a longer period of time after carbon deposition begins due to the diffusion of deposited carbon through the active metal site, which then precipitates on the other side of the metal particle to form a carbon filament. The efficiency of catalysts refer not only to the reaction rate and operating temperatures achieved, but also to the chemical and thermal stability of the catalyst against the feedstock impurities, as well as the ability to accumulate as large amounts of carbon deposits as possible, while preserving the activity.

1.2 SCOPE OF WORK

Establishment of low cost methodology for the production of highly stable catalyst to convert methane to hydrogen at lowest possible temperature is the major challenge in TCD process. In this study, *n*-NiO/SiO_2, *n*-FeO/SiO_2, and *n*-CoO/SiO_2 nanocatalysts were synthesized through co-precipitation cum modified Stöber method. Ni-, Fe-, and Co-based catalysts have gained major attention in research on methane decomposition because of their advantages, such as wide availability, low cost, and improved activity and stability (Awadallah et al., 2014; Cunha et al., 2009b; Dou et al., 2014; Venugopal et al., 2007a; G. Wang et al., 2013). Stöber method was presented in order to safeguard nano metal active phase with SiO_2 like inert materials. There was no surfactants used in this method and the SiO_2 formation reaction was conducted in alcoholic medium, avoiding water content. The detailed physicochemical characteristics of prepared catalysts are presented. Temperature programmed methane decomposition (TPMD) was carried out from 200 to 900 °C as preliminary experiments in order to determine the temperature ranges where the as-synthesized catalysts were active for TCD. The evaluation of long term stability of catalyst (TCD) was conducted in a fixed-bed pilot plant in a temperature range from 475 to 700 °C. The virgin and used catalyst were characterized using various characterization methods. Additionally, the influence of methane flow rate, decomposition temperature, and methane partial pressure on the methane conversion, initial decomposition rate, and yield of as-produced nanocarbon were determined. The experimental data was also used to study the kinetic of methane decomposition over *n*-NiO/SiO_2 catalyst and reported in this work.

1.3 AIM OF STUDY

Establishment of consistent co-production of hydrogen and nanocarbon from methane at lowest possible temperature with rational yield over the suitably stable catalyst prepared without using any expensive reagents.

1.4 OBJECTIVES OF STUDY

The objectives of the study were:

- To synthesize SiO_2 supported nanocatalysts such as NiO, FeO, and CoO through co-precipitation cum modified Stöber method.
- To conduct a comparative assessment on the physicochemical properties and catalytic performance of prepared catalysts.
- To examine the change of activity of prepared catalysts using a temperature range of 475 – 700 °C and flow rate of 0.64, 1.07, and 1.43 L/min.
- To study the influence of methane flow rate, temperature, and methane partial pressure on TCD in a fixed bed pilot plant.
- To find out methane decomposition kinetic and reaction rate over *n*-NiO/SiO_2 catalyst.
- To study the influence of nickel/silicate ratio, C18TMS/TEOS ratio, and different solvents on the catalytic activity and stability of *n*-NiO/SiO_2 catalyst.

1.5 THESIS STRUCTURE

This thesis is consisted of five chapters:

Chapter 1: Introduction

General information on the impact of fossil fuel combustion and the importance of hydrogen energy in the current scenario of heavy GHG emission is indicated in Introduction. Furthermore, a basic note on different sources of hydrogen and various hydrogen production methods developed were given. The scope of this research work, objective of study and thesis structure are also presented in Introduction.

Chapter 2: Literature Review

This chapter reviews and summarizes the developments in TCD in the last few decades. The progresses in the synthesis of various kinds of catalysts, influences of operating conditions and catalyst deactivation were discussed.

Chapter 3: Materials and Methods

The materials used in this research were reported in this chapter. In addition to that, the detailed note on the co-precipitation cum modified Stöber method for catalyst synthesis, the experimental setup for TCD analysis, experimental parameters, and characterization techniques adopted to study physicochemical properties of virgin and used catalysts are also given in Chapter 3.

Chapter 4: Results and Discussions

The chapter presents the results on comparative study on the physicochemical properties and catalytic performance of *n*-NiO/SiO_2, *n*-FeO/SiO_2, and *n*-CoO/SiO_2 nanocatalysts synthesized through co-precipitation cum modified Stöber method. Additionally, influence of preparation parameter on the activity of *n*-NiO/SiO_2 and the kinetics of methane decomposition also have been discussed.

Chapter 5: Conclusion and Recommendation for Future Studies

This chapter concludes the findings of this study and gives recommendations for future studies.

CHAPTER 2: LITERATURE REVIEW

2.1 HYDROGEN ENERGY

Searching for new energy sources is highly desirable for the next generations when rapidly changing factors are considered such as population, increasing pollution and exhaustion of fossil fuels. Hence, there is a need for clean, safe, and efficient energy carriers or forms of energy that can be transported to the end user. Hydrogen with its unique properties such as abundance, light weight, low mass density, high energy density, and nonpolluting nature attract many researchers' attention as an ideal carrier and minimize the use of fossil fuels, which are responsible for global warming due to carbon dioxide emissions to the atmosphere. Hence, hydrogen and nanocarbon are the two most emerging research topics in the field of environmentally benign energy and material science, respectively. These two treasured products can be simultaneously produced by methane transformation in a single step chemical approach as shown in equation 1.1. There has been an intense research effort on this topic in recent years.

It is believed that hydrogen will play a pertinent role as an energy vector in the near future mainly because of two reasons (Demirci & Miele, 2013). Firstly, it can be produced from renewable raw materials such as water, biomass or biogas. Secondly, it generates water as the only by-product during its combustion and oxidation as shown in equation (2.1) (Serrano et al., 2010; Stephens-Romero et al., 2009). With these advantages in mind, auto industries, science laboratories, and governments have turned greater attention toward hydrogen as a possible alternative fuel to succeed both in widespread production and distribution.

$$H_2 + \tfrac{1}{2}O_2 \rightarrow H_2O \qquad \Delta H^0 = -285.83 \text{ kJ/mol} \qquad (2.1)$$

However, hydrogen does not occur in significant amounts as a free hydrogen molecule, but it is found combined with other elements such as oxygen and carbon, i.e. water (either

as liquid, ice or in hydrated minerals), hydrocarbons or biomass. This fact reflects the reactivity of the hydrogen molecule under atmospheric conditions. Thus, the formation of water by hydrogen oxidation is an exothermic reaction, which occurs as shown in equation (2.1) (Dell, 2008). This high enthalpy, along with the low density of hydrogen, results in the best energy-to-weight ratio of any fuel. Although, in contrast, its energy-to-volume ratio is poor. Interestingly, hydrogen can be efficiently transformed into electricity using fuel cells, producing water vapor as the only residue. This possibility of easily interconverting chemical into electrical energy turns hydrogen into an ideal energy vector (Serrano et al., 2013).

The annual global hydrogen consumption in 2006 was about 50 million tons, including industrial applications and merchant use (Abbas & Daud, 2010a; Abbas & Daud, 2010; Amin et al., 2011; Italiano et al., 2010). The sector wise usage of hydrogen is exhibited in Figure 2.1. The average annual increase in hydrogen demand was 4% from 1997 to 2006, and 9.5-10% for carbon monoxide free hydrogen from 1997 to 2006 (Amin et al., 2012). Approximately 100 times of the present hydrogen production (more than 3×10^{12} kg) would have to be produced per year to fulfill world's demand for fossil fuel, as mentioned in section 1.1.

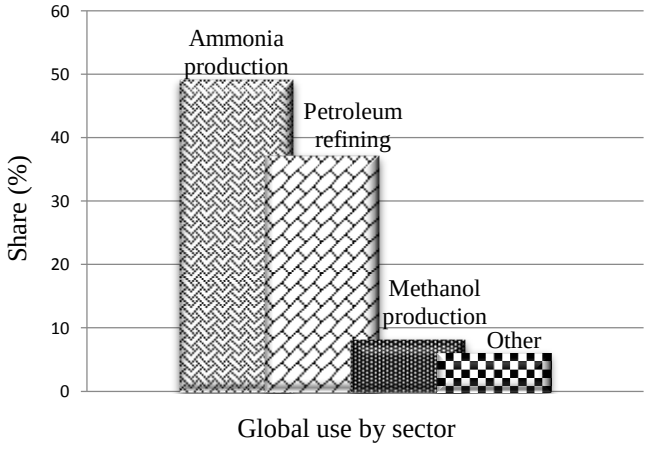

Figure 2.1 Sector-wise usage of hydrogen.

With regard to resources of hydrogen, methane has the highest H/C ratio (=4) among all the hydrocarbons and which is the main constituent of natural gas. Methane conversion to hydrogen and nanocarbon is of interest because of the existence of large reserves of natural gas (>80% CH_4 by volume), petroleum-associated gas, and methane hydrate (Y. Zhang & Smith, 2004). The chemical and physical properties of hydrogen and methane are furnished in Table 2.1.

Table 2.1. Physical and chemical properties of hydrogen and methane (Uddin & Daud, 2014).

Properties	H_2	CH_4
Molecular weight (g/mol)	2.016	16.04
Mass density (kg/NA m^3)[a]	0.09	0.72
Mass density of liquid H_2 (kg/$N_A m^3$)[b]	70.9	N/A
Boiling point (K)	20.2	111.6
HHV (MJ/kg)[c]	142.0	55.5
LHV (MJ/kg)[d]	120.0	50.0
Flammability limits (vol %)	4.0−75.0	5.3−15.0
Detonability limits (vol %)	18.3−59.0	6.3−13.5
Diffusion velocity in air (cm/s)	200.0	51.0
Ignition energy (mJ)[e]	0.02	0.29
Ignition energy (mJ)[f]	10	20
Flame velocity in air (cm/s)	265−325	37−45
Toxicity	Nontoxic	Nontoxic

[a] Mass density measured at a pressure of 1 atm and temperature of 0 °C. [b] Mass density of liquid H_2 measured at temperature of 20 K. [c and d] Includes water and steam production in higher heating value (HHV) and lower heating value (LHV), respectively. [e and f] Ignition energy measured at stoichiometric mixture and lower flammability limit, respectively.

Amongst the methods introduced to produce hydrogen from methane, which are briefly described in section 1.1, TCD or so-called methane cracking has attracted widespread attention. The major driving force of research interest on TCD is because of production of highly desirable products like carbon nanotube (CNT) or carbon nanofiber (CNF) instead of gaseous CO_x, in addition to nonpolluting hydrogen fuel. This reaction eliminates the need for CO_x separation and sequestration processes altogether. Hence, storage and consumption of solid carbon is easier and safer compared with gaseous CO_x.

2.2 THERMOCATALYTIC DECOMPOSITION OF METHANE

Production of pure hydrogen by TCD process can be considered as a milestone towards the development of hydrogen economy. However, due to the very strong C–H bond (440 kJ/mol) and high symmetry of the molecular structure, methane is the one of the most inactive hydrocarbons, and its decomposition can only take place efficiently at a temperature higher than 1200 °C in the absence of a catalyst. Various metal and carbonaceous catalysts have been introduced in the interest of reducing decomposition temperature. In pursuance of producing CO_2 free hydrogen, methane decomposition mechanism mainly involves five steps (Suelves et al., 2009) as follows. (i) The chemisorption of methane on the leading face of a catalyst particle, (ii) detachment of a chemisorbed methane molecule through progressive breaking of four C-H bonds as follows,

$$(CH_4)_g \rightarrow (CH_3)_a + (H)_a \qquad (2.2)$$

This step is followed by a series of surface stepwise dissociation reactions leading to elemental carbon and hydrogen (Nazim Muradov et al., 2005):

$$(CH_{3-x})_a \rightarrow (CH_{2-x})_a + (H)_a \qquad (2.3)$$

where $0 < x < 2$; subscripts (a), (c), and (g) denote adsorbed, crystalline and gaseous species, respectively. (iii) aggregation of adsorbed atomic hydrogen into molecules, followed by gas phase emission,

$$2(H)_a \rightarrow (H_2)_g \qquad (2.4)$$

(iv) atomic carbon aggregation into encapsulated carbon, leading to progressive catalyst deactivation, or atomic carbon diffusion through the bulk catalyst from the leading face to the trailing face, driven by the existing pronounced concentration gradient, and (v) carbon nucleation followed by the formation and growth of carbon nano-fibers (CNFs) in the trailing face of the catalyst particle.

$$(C)_a \rightarrow 1/n\ (C_n)_c \quad \text{(Carbon crystalline growth)} \qquad (2.5)$$

The kinetic laws (pre-exponential factor, activation energy, and reaction order) of each intermediate elementary reaction step are still unknown (Dufour et al., 2009). TCD process has less environmental impact compared to commercial hydrogen production method like SRM. However, catalyst deactivation and their regeneration are the major challenges TCD process facing nowadays.

In TCD process, the activity and stability of the catalyst and the carbon species formed during methane transformation are very important, since both influence the life of the catalyst and the selectivity and yield to the desired products (Y. Zhang & Smith, 2004). Establishment of cost effective production of hydrogen and nanocarbon deliberately depends on the development of highly active and stable catalyst, optimized experimental parameters and development of proper reactors. The following literature review would provide a panoramic view on the various catalysts developed for TCD and the influence of experimental parameters on the yield of hydrogen and nanocarbon during TCD process.

2.2.1 Metal Catalysts for TCD

Over the past few decades, many efforts have been devoted for developing simple and efficient synthesis protocols for the preparation of suitable catalyst in order to realize the TCD process with a moderate condition. Various metal catalysts (Bartholomew, 1982; Rostrup-Nielsen, 1974; Takenaka et al., 2004; Trimm, 1977), different supports and numerous carbonaceous catalysts have been studied extensively (J. Ashok et al., 2008; J. Ashok et al., 2007; Takenaka et al., 2001). In addition to hydrogen, ordered nanocarbons are forming with metal catalyst, while carbonaceous catalysts produce amorphous carbon having a variety of morphology (Guil-Lopez et al., 2011; Suelves et al., 2008). The general reaction mechanism on different metal catalysts has been supposed to be similar. However, the chemical composition and preparation method, the catalyst support and promoter influence the activity and stability of catalyst and determine the structure and morphology of the carbon formed. Catalytic activity and stability of various kind of catalysts are compared in Table 2.2, which comprises the conserved stability, activity and maximum methane conversion or hydrogen production of various metal catalysts had already been studied.

Table 2.2 Catalytic activity and stability of various metal-based catalysts recently studied.

Catalyst	W	Stability & Activity maintained		Max. CH_4 conversion	Max. H_2 produced	t/T/F	Ref.
		T	t	at t, T & F			
Ni	0.04	650	130	35	--	0/650/45000[a]	W. Zhang et al., 2011
Ni	0.04	500	37	9	--	0/500/60[b]	W. Zhang et al., 2009
Fe	2	900	>75	98	--	14/800/20[b]	Konieczny et al., 2008
Ni-Cu	1	900	5	96	--	0.5/900/110[c]	Cunha et al., 2009b
Fe-Cu	0.75	600	5	51	--	1.6/600/110[c]	Cunha et al., 2009a
Ni-Cu-Al	0.05	800	2.75	--	75	0.5/700/120000[a]	Suelves et al., 2009
Ni/Ce-MCM-41	0.05	580	>23	75	--	18/580/75[b]	Guevara et al., 2010
Ni-Cu-Zn/MCM-22	1	800	>50	85	--	0/750/10[b]	Saraswat & Pant, 2011
Ni/SiO_2	0.15	600	>10	22	--	0/600/--	Venugopal et al., 2007b
Ni/SiO_2	0.03	650	4	42	--	0/650/15[b]	W. Wang et al., 2012
Ni/TiO_2	0.3	700	8	--	73	0.1/700/20[b]	Lázaro et al., 2008
Ni/Al_2O_3	--	700	3	--	73	0/700/12[a]	J. L. Pinilla et al., 2011

Table 2.2 Continued

Ni/La_2O_3	0.53	600	5	75	--	1/600/110[c]	Figueiredo et al., 2010
Fe/Al_2O_3	--	800	3	--	91	0.4/800/1.5[a]	J. L. Pinilla et al., 2011
Fe/Al_2O_3	0.02	900	6	68	--	0/900/6000[a]	Torres et al., 2012
Fe/MgO	0.15	800	3	--	55	0/800/12000[a]	J. L. Pinilla et al., 2011
$NiCu/Al_2O_3$	10	750	>7	--	80	0/750/12000[a]	J. L. Pinilla et al., 2010
$Ni–Ca/SiO_2$	0.05	580	3	39	--	0/580/100[b]	Zapata et al., 2010
$Ni–K/SiO_2$	0.05	580	3	40	--	0/580/100[b]	Zapata et al., 2010
$Ni–Ce/SiO_2$	0.05	580	3	90	--	0/580/100[b]	Zapata et al., 2010
$Ni-Fe/SiO_2$	0.03	650	>4	46	--	0/650/15[b]	W. Wang et al., 2012
$Ni-Cu/SiO_2$	1	750	45	88	86	5/750/1800[a]	Saraswat & Pant, 2013
$Ni–Cu–TiO_2$	0.3	700	8	--	80	0/700/20[b]	Lázaro et al., 2008
Ni-Cu/MgO	--	700	3	--	79	0.75/700/12[a]	J. L. Pinilla et al., 2011
$Ni/MgAl_2O_4$	0.1	700	5	37	--	1/550/80[b]	Giselle D. B. Nuernberg et al., 2012
$Ni-Cu/La_2O_3$	0.53	900	>26	97	--	0/900/110[c]	Figueiredo et al., 2010

Table 2.2 Continued

$Ni/Ce–SiO_2$	0.2	600	2	50	--	0.3/600/100[b]	Tapia-Parada et al., 2013
Fe-Mo/MgO	--	800	3	--	92	0/700/1.5[a]	J. L. Pinilla et al., 2011
FeMo/MgO	0.15	950	3	--	96	0.3/950/1000[a]	J. L. Pinilla et al., 2011
$FeMo/Al_2O_3$	0.15	800	3	--	88	0/800/12000[a]	J. L. Pinilla et al., 2011
$Co/Ce–TiO_2$	0.2	500	2	5	--	1.9/500/100[b]	Tapia-Parada et al., 2013
$Co/Al_2O_3/SiO_2$	--	700	30	90	--	$0/700/1900h^{-1}$	Italiano et al., 2010
$CoO\text{-}MoO/Al_2O_3$	0.4	700	2	78.9	--	0/700/250[b]	Lee et al., 2012
MgO/SiO_2	--	900	200	--	45	0/750/60–65[b]	Hussain & Iqbal, 2011
$Ni/K/MgO/SiO_2$	--	900	200	--	61	0/700/60–65[b]	Hussain & Iqbal, 2011
$LaNiO_3$ perovskite	0.05	700	4	81	--	1.2/700/15[b]	Sierra Gallego et al., 2010
$LaNiO_3$ perovskite	--	800	5	91	--	0.5/800/20[b]	Maneerung et al., 2011
NiO/La_2O_3	--	800	5	93	--	0/800/20[b]	Maneerung et al., 2011

(W= weight (g), T= temperature (°C); t=time (h); F = flow rate ([a]$mL/(g_{cat.}h)$ [b]mL/min [c]NmL/min, unless other units are stated); conversion (%); --, not mentioned in the original paper)

2.2.1.1 Non-supported catalysts

It has been reported that the rate of methane decomposition of non-supported metal catalysts are in the order of Ni, Co, Ru, Rh >Pt, Re, Ir>Pd, Cu, W, Fe, Mo (J. Zhang et al., 2013). Among them, Ni, Co, and Fe catalyst gained major attention because of their advantages like availability, low cost, better activity, and stability (Cunha et al., 2009b; Venugopal et al., 2007b). Ni crystal size has immense influence on the methane decomposition and carbon formation. Its direct relationship with coking threshold (thermodynamic equilibrium constant) was revealed in 1975 (Rostrup-Nielsen, 1975). Rapid aggregation and carbon encapsulation deactivate non-supported Ni-catalyst rapidly, especially at a temperature higher than 600 °C (Zapata et al., 2010). However, theoretical thermodynamic equilibrium study was evaluated by using a commercial Outokumpu HSC Chemistry 5.11 chemical equilibrium calculation software illustrated that methane conversion is thermodynamically inadequate at this temperature (Prabhas Jana et al., 2010; Roine, 2002), resulting to a low hydrogen yield (Venugopal et al., 2007b). On the other hand, despite showing hasty deactivation on continuous cycles directing short life time, Fe catalysts have more stability at higher temperature range of 700-1000 °C (Takenaka, Serizawa, et al., 2004). Moreover, Fe-based catalysts produce thin wall carbon nanotubes as byproduct, which are invaluable among nanocarbons (M. A. Ermakova & Ermakov, 2002). Hence, most of the work with Fe-based catalysts have devoted for the production of nanocarbon other than hydrogen production. While, cobalt catalyst didn't get as much attention as Ni and Fe catalysts. Partially filled 3d orbitals of Fe, Co, and Ni facilitate the dissociation of the hydrocarbon molecules through partially accepting electrons. This interaction along with "back-donation" from the metal into the unoccupied orbital in the hydrocarbon molecule changes the electronic structure of the adsorbed molecule so that the dissociation of the molecule occurs (Dupuis, 2005). While, copper, a non-transition metal with its 3d shell completely filled, was observed to

yield very less hydrogen and amorphous carbon. Likewise, noble metals (Rh, Ru, and Pt) do not provide heartening results in terms of methane conversion in TCD (Prabhas Jana et al., 2010). The main advantage of non-supported catalyst is the magnetic properties associated with those materials which facilitate the recovery of the catalyst after the reaction, once the latter is mixed with the produced carbon (Prabhas Jana et al., 2010; Otsuka et al., 2003).

2.2.1.2 Metal supported catalysts

The metal-supported catalyst belongs to the heterogeneous catalysis. The metal would be polarized by the influence of charge enclosed in the support (Chambers et al., 1998), which make changes in their properties. Strong Metal–Support Interaction (MSI) increases the dispersion of metal by decreasing its mobility. MSI can make changes on the crystallography and the electronic state of the metal particles depending on the intensity of the interaction (Y. Li et al., 2011). The factors influencing the catalytic activity are the electronic state of the metal particles, crystalline size, dispersion of metal particles, textural properties, pore geometry of the support (Salmones et al., 2009), catalyst composition (J. L. Pinilla et al., 2010), catalyst preparation method (D. Chen et al., 2005), and catalyst rinsing solvent (W. Zhang et al., 2009). Numbers of efforts have been devoted in favor of improving catalytic activity and stability by bringing changes in the above mentioned factors.

Various types of metal supported catalysts like Ni-Cu (Hornés et al., 2012; Saraswat & Pant, 2011), Ni-Zn (Lua & Wang, 2013), Fe-Pd, Fe-Mo, Fe-Ni (Shah et al., 2001) and Ni/Cu/Al (Suelves et al., 2006) had been introduced in order to improve the activity. Addition of Cu in to Ni and Fe by in situ thermal treatment has immense enhancement on their catalytic activity and stability. Ni-Cu catalyst shows catalytic stability up to 700-750 °C with a 70-85% methane conversion (Cunha et al., 2009b; Lua & Wang, 2013). There is no significant catalytic deactivation occurred for 300 min. Cu

doped Ni produces octopus and porous CNF with high surface area. Similarly, Cu addition in to Fe improves with 51% methane conversion with better life span than monometallic Fe catalyst (Cunha et al., 2009a). This higher stability and activity of supported catalysts explained in terms of ensemble effect, which decreases the rate of formation of encapsulating carbon. Furthermore, Density Functional Theory (DFT) calculations show that Cu-W and Cu-Mo composite particles have binding energies in the same range as Fe, Co, and Ni. The addition of a dopant to Cu in an appropriate ratio modifies the binding energy into a certain range suitable for C-H bond cleavage formation (Z. Li et al., 2008; O'Byrne et al., 2010). Moreover, Fe gives better results while coupling with Mg, Co, Pd, Ni, and Mo than monometallic Fe at 700-800 °C (Punnoose et al., 2003; Shah et al., 2001; Shah et al., 2003).

2.2.1.3 Metal oxide supported catalysts

Metal supported on metal oxide catalysts (Co/Mo/Al_2O_3 (Lee et al., 2012; Qian et al., 2004), Ni-Cu/SiO_2 (Saraswat & Pant, 2013), Ni-Cu/Al_2O_3 (J. L. Pinilla et al., 2010), Mo-Fe/Al_2O_3 (Shah et al., 2004)) have gained tremendous attention as they exhibit high catalytic activity and stability for TCD process. However, the methodology for selecting the third component is not systematically illustrated until now. It is reported that oxide support can alter the surface chemistry of metal catalyst particles through epitaxial, spillover, and migration effects (Chambers et al., 1998). Lee et al. (2012) conducted TCD over CoO-MoO/Al_2O_3 and found the initial methane conversions are 50.8, 65.5, 71.6, and 78.9% over the catalyst with 10, 20, 30, and 40 wt% CoO-MoO loading, respectively. It showed a gradual increase in initial methane conversion with metal loading. In a broad-spectrum, the examined operating temperatures for Ni-based catalysts are ranged from 500 to 900 °C with the highest methane conversion of 85% at 750 °C, while that for Fe-based catalysts are 200-1200 °C with >90% methane conversion at 800 °C (Konieczny et al., 2008; Lua & Wang, 2013; J. L. Pinilla et al., 2011). In 1998, N. Z. Muradov (1998)

generated CO_2 free hydrogen yield very close to the equilibrium value with Fe_2O_3 catalysts at 850 °C. Fe-Mo/MgO (J. L. Pinilla et al., 2011) withstands temperature up to 950 °C with methane conversion of higher than 90% for 3 h continuously. Fe/Al_2O_3 (Torres et al., 2012) also showed better performance at higher temperature. In spite of having better stability at higher temperature range, the overall performance of the Fe-based catalysts are not as good as that of Ni-based catalysts. It paved the way to introduce Fe incorporated Ni-based catalysts. The addition of Fe in to Ni/SiO_2 catalysts boost up its activity by about 3 times without much deactivation (W. Wang et al., 2012). The addition of Cu and Zn in to Ni-based catalysts enhance the catalytic stability up to 800 °C with 72% methane conversion (Saraswat & Pant, 2011). Ni-Cu-SiO_2 (50:10:40) showed higher activity with a maximum methane conversion of 88% corresponding to a hydrogen yield of 86% at a temperature 750 °C and GHSV 1800 mL/h.g_{cat} (Saraswat & Pant, 2013). 10% Cu loading shows maximum activity, but further addition of Cu lower the activity and stability, especially at high temperature, as the higher amount of Cu make the catalyst particles easily in quasi-liquid state. The addition of Ce enhanced the stability of both Ni and Fe-based catalyst by more than 10 times of that of Ni/SiO_2 catalyst (Guevara et al., 2010; Tang et al., 2010; Tapia-Parada et al., 2013). It is attributed to the conversion of formed carbon to CO_x because of Ce^{4+}/Ce^{3+} mechanism (Guevara et al., 2010). Hence, a small amount of CO_x has been detected throughout the experiments.

2.2.1.4 Ceramic and red-mud based catalyst

Ceramic materials have high melting point, high resistant to chemical attack, good mechanical strength, low acidity, good interaction with metallic phase (Giselle D. B. Nuernberg et al., 2012), and do not form metal carbide (Hussain & Iqbal, 2011). All these properties are desirable for a catalyst support. Furthermore, unlike metal catalyst, ceramic catalyst can govern the reaction for producing specific product, which is one of its additional advantages (Hussain & Iqbal, 2011). As expected, $Ni/MgAl_2O_4$ illustrated

better activity with 37% methane conversion for 1 h without much deactivation (Giselle D. B. Nuernberg et al., 2012). The contact time of reactant molecules was extremely important for methane decomposition and MgO have the affinity for sustaining hydrogen which was bonded to methane, in this way it increased the sustain time of methane on the ceramic surface, which was responsible for decomposition of methane. However, addition of Pt to the above mentioned ceramic support didn't favor catalytic result (Giselle De B. Nuernberg et al., 2011). Addition of K in to MgO/SiO_2 ceramic catalyst increased its activity to produce 77% maximum hydrogen yield and stability up to 900 °C even after 200 h (Hussain & Iqbal, 2011). Doping of K provides greater active sites and surface area to the catalyst for better decomposition and higher stability. However, K addition inhibited coke formation and carbon deposition during the decomposition reaction and hence did not suffer fast deactivation. Silica reacted with potassium oxide to form stable silicates which was actually responsible for the stability of ceramic materials for better active life (S. Tajammul Hussain et al., 2008; Syed T. Hussain et al., 2008). Ceramic catalysts produces multiwalled carbon nanotubes which approximately same at optimized temperatures of Ni catalyst. No impurities were detected in nanotubes produced from cracking of methane from ceramics (Hussain & Iqbal, 2011).

Red mud is a waste product of the aluminium industry. It is composed of iron oxides/oxyhydroxides/hydroxide, aluminium oxide/oxyhydroxide/hydroxide, silica, titania and a range of alkali and alkaline earth metal compounds such as sodium oxide and calcium oxide (Balakrishnan et al., 2009). Of these, the iron compounds are generally the major phase constituents. Balakrishnan et al**.** (2009) considered methane itself as a reductand and conduct methane decomposition over red-mud without any prior reduction step. Red-mud containing relatively high content of titanium seems to have reduced activity for methane conversion compared to a sample containing a comparable proportion of iron. The maximum hydrogen formation rate observed, 3.80×10^{-5} mol_{H2}/g.s,

was associated with a sample containing the highest proportion of iron and a lower concentration of alkali metal (Balakrishnan et al., 2009). Elsewhere, alkali metals have been reported to be very effective poisons for the methane decomposition reaction (Marina A. Ermakova et al., 2001). The efficacy of the red mud samples is variable, which is related to differences in their composition which in turn reflects the purity of the bauxite ores from which they are produced. Advanced studies on red mud catalyst has yet to be conducted.

2.2.1.5 Thin layer catalysts

Thin Layer Catalysts (TLCs) are recently attracted the attention of investigators (Frusteri et al., 2011; Italiano et al., 2010). Frusteri et al. (2011) found that the Ni and Co TLC supported on Al_2O_3 samples are suitable for a cyclic dual-step process, which is comprised of TCD and catalyst regeneration by oxygen without damaging the catalyst. Furthermore, both Ni and Co exhibit a strong interaction with Al_2O_3 support surface and it is noticed that the formation of encapsulating carbon is depressed and only filamentous carbon forms. Despite of this advantage, Ni and Co silica supported catalyst were not found apt for long time catalysis as their deactivation by time. In fact, Co/Al_2O_3/Silica TLC is stable up to 700 °C for 32 h and convert more than 80% methane to hydrogen (Italiano et al., 2010). Cobalt particles strongly adsorb on Al_2O_3 support giving rise to the formation of $CoAl_2O_4$-type structures, which ensure an elevated metal dispersion inhibiting also the occurrence of sintering phenomena (Chai et al., 2006, 2007). Irrespective of Co loading, initial hydrogen production increases with reaction temperature, while the relation between lifetime and activity of TLC with other operating parameters or catalyst characteristics have yet to be optimized. It is found that, 20% Co ensures both long lifetime and high hydrogen productivity.

2.2.1.6 Experimental parameters influencing activity of metal catalyst

Catalyst stability and activity depends on the experimental parameters such as reaction temperature, partial pressure, space velocity, etc. (Nasir Uddin et al., 2014). In general, the hydrogen content in the initial output of TCD process with metal catalysts is incredibly high, but their activity decreases very fast with time. It is clear from exploited metal catalysts that the activity increase as increasing the temperature up to a particular level then deactivation of catalyst starts (Guevara et al., 2010; J. L. Pinilla et al., 2010; Saraswat & Pant, 2011; W. Zhang et al., 2011).

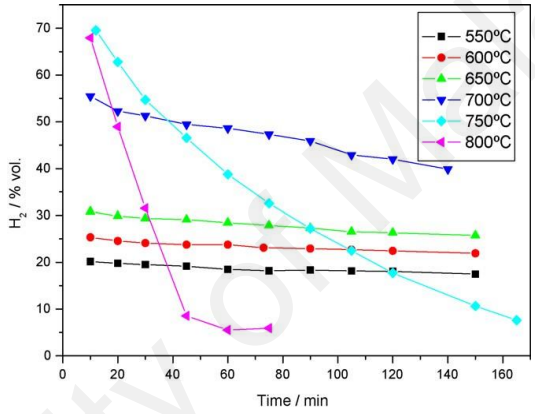

Figure 2.2 Influence of reaction temperature on the evolution of hydrogen concentration at space velocity 120 $lg_{cat}^{-1}h^{-1}$ (Suelves et al., 2009).

Ni-Cu-Al catalyst has maintained its initial activity at low reaction temperatures, that is, 550, 600, and 650 °C, with low hydrogen production of 20, 26, and 31 vol%, respectively, were measured in the outlet gas (Suelves et al., 2009). On the other hand, the initial hydrogen concentrations were much higher, 55, 67, and 70 vol% at 700, 750, and 800 °C, respectively (Figure 2.2). However, the evolving hydrogen concentrations dropped quickly, indicating rapid catalyst deactivation. This effect was more evident as reaction temperature increased. This rapid deactivation of catalyst at higher temperature is attributed to the metal particle sintering and the formation of more ordered carbon. In a kinetic point of view, temperature and pressure are the main parameters influencing

hydrogen formation rate over time. Kinetic studies are chemical stages conducted for developing a suitable model which describes the rate of reaction and defines the chemical process (H. Y. Wang & Lua, 2014). Recent studies (Abbott & Harrison, 2008) have shown that the initial C–H bond breaking of CH_4 is the rate determining step over the metal catalyst at high temperatures, although the activation energy for CH_4-bond dissociation decreased from 440 kJ/mol in the gas phase to 65 kJ/mol on a Ni (100) surface. Wang & Lua (2014) were carried out kinetic studies on methane decomposition over Ni catalyst and found that the average reaction order and activation energy for the methane decomposition over the unsupported nickel was 0.63 and 65.4 kJ/mol, close to those previously published values furnished in Table 2.3. The wide range of reported activation energies may be due to many factors, including the difficulty of collecting true kinetic data and the highly dynamic characteristics of the process (Kvande et al., 2008). Wang & Lua (2014) found that, when P_{CH_4} was increased from 0.2 atm to 1 atm, the hydrogen formation rate significantly increased but the catalyst activity decreased. The faster deactivation of the catalyst was subjected to a higher reaction temperature, which accelerated methane dissociation and increased the diffusion rate. Generally, increasing reaction temperature increases methane dissociation due to the endothermic nature of the reaction while at the same time the diffusion rate also increases accordingly. In the case of 2Ni–1Co–1Cu, a faster carbon diffusion rate at a higher temperature would probably speed up the fragmentation of the catalyst (H. Y. Wang & Lua, 2014) and leads to deactivation. Nasir Uddin et al. (2014) reported that Ni/Zeolite Y showed reaction order and activation energy were 2.65 and 61.77 kJ/mol, respectively for methane decomposition in a fixed bed reactor. The kinetic experiment indicates that the optimum temperature range should be maintained to achieve the highest performance from 30% Ni/Y zeolite in terms of hydrogen formation rate, average hydrogen formation rate, total

hydrogen formation, average carbon formation, total carbon formation, and carbon formation rate.

Table 2.3 The activation energy of the TCD process reported in literature over different catalysts.

Catalyst	Ea (kJ/mol)	Ref.
Ni	65.4	Wang & Lua, 2014
Ni	59	Snoeck et al., 1997b
Ni	59	Li et al., 2000
Ni	53.9	Zavarukhin & Kuvshinov, 2004
Ni-Al	64.6	Kvande et al., 2008
Ni/SiO_2	29.5	Fukada et al., 2004
Ni–Co–Cu	67.5	Wang & Lua, 2014
Ni/SiO_2	90	Chesnokov & Chichkan, 2009
Ni/TiO_2	60	Sharif Zein et al., 2004
Ni/Zeolite Y	61.77	Nasir Uddin et al., 2014
Ni-Cu/MgO	50.4	Borghei et al., 2010
Ni/Al_2O_3-CaO	88	Zongqing Bai et al., 2007
HT-Ni	64.6	Kvande et al., 2008

Furthermore, the catalyst deactivation significantly increases as space velocity goes up (Giselle D. B. Nuernberg et al., 2012; Suelves et al., 2009; W. Wang et al., 2012). NiCuAl exhibit high stability from 20 to 60 $lg_{cat}^{-1}h^{-1}$ with 75 vol% of hydrogen in the outlet stream (Figure 2.3) (Suelves et al., 2009). While, at the higher space velocity over 120-1200 $lg_{cat}^{-1}h^{-1}$, hydrogen concentration severely decreased to 5vol% within 60 min due to decrease in contact time between methane molecules and the catalyst surface (Figure 2.3).

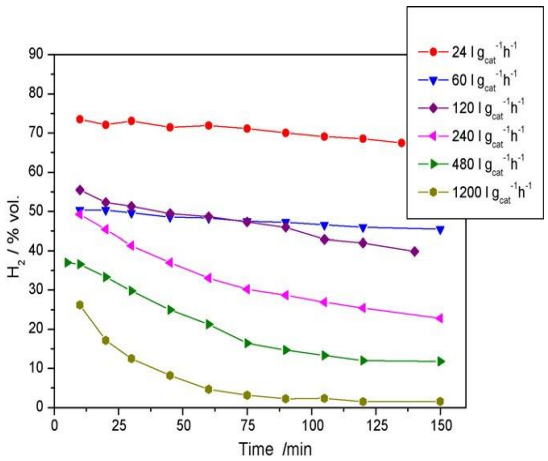

Figure 2.3 Influence of space velocity on the evolution of hydrogen concentration at temperature 700 °C (Suelves et al., 2009).

Increasing the space velocity has two clear effects: the hydrogen concentration in the outlet gases diminishes, and the catalyst deactivation substantially increases. Furthermore, Xiong et al. (2012) stated that the activity of supported catalyst strongly depend on the amount of loaded metal by studying various amount of Ni supported on SiO_2. It is due to increasing availability of active sites for reaction. Nasir Uddin et al. (2014) stated that the carbon deposition is directly related to the metal content of the catalyst. The high distribution of nickel species into the zeolite Y cages and, possibly more significantly, the synergistic influence between the microporous surfaces of zeolite Y and metallic nickel resulted in the higher catalytic performance of 30% Ni/Y zeolite (de Lucas et al., 2005). A greater electron density on the surface of metallic nickel and an increase in the retention capacity of hydrogen in the Ni/Y zeolite catalysts were caused by the synergistic effects, which may include the interactions between the higher ionic microporous surface of zeolite Y and the nickel particles.

2.2.1.7 Deactivation of Metal Catalysts

The common challenge of TCD process is the catalytic deactivation. In general catalytic reaction, the catalyst does not maintain permanent activity and selectivity. Some catalysts deactivate very rapidly, within seconds, on the other hand some other catalysts

maintain its activity for long time of the order of months. Poisoning, coking (carbon deposition), mechanical degradation and sintering are the main reasons behind the deactivation of the catalysts (Abbas & Daud, 2009b). There are number of studies titled on catalytic deactivation in order to lengthen the catalyst life. Most of the studies focused on parameters affecting deactivation, the period of stable catalytic performance and the complete deactivation time. Table 2.7 (Metal catalyst) explicitly shows the loss of catalytic activity of various metal catalysts with time during TCD of methane. Table 2.7 contains initial methane conversion or hydrogen production and those at time t and deactivation time, if any, at particular experimental parameters with which the examination had conducted. Those previously conducted experimental results give a clear indication about the catalytic activity loss with time of each catalyst.

Polyaromatic structure with high carbon-to-hydrogen ratio, filamentous, amorphous, and graphitic carbon are the different carbon forms with various chemical structures produced during methane cracking (Y. Li et al., 2011). Most of the researchers agreed that the carbon formation is the main reason of catalyst deactivation. Methane decomposition mechanism involves the dissociative adsorption of the methane on the metal surface, the dissolution and subsequent diffusion of the adsorbed carbon atoms through the metal, and the precipitation of carbon at the backside of the metal particles originating carbon filaments. Nevertheless, once metal crystallites are detached, carbon filaments grow for extended periods of time, until the metal crystallites become deactivated by encapsulating carbon. The reaction steps involved are summarized in Figure 2.4 (Figueiredo, 1982).

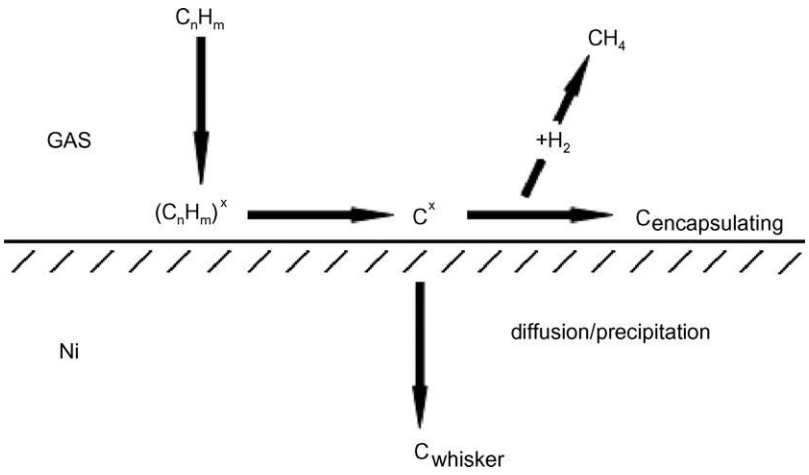

Figure 2.4 Mechanism proposed for hydrocarbon decomposition on Ni catalysts (Figueiredo, 1982).

Many other mechanisms also have been put forwarded by researchers in last decades to explain carbon filament growth. Basically it is considered as a four step process of carbon formation (Baker et al., 1972). (i) methane chemisorption on the leading face of a catalyst particle through progressive breaking of the four C-H bonds, (ii) aggregation of chemisorbed atomic hydrogen into molecules and further emission into gas phase, (iii) diffusion of atomic carbon through catalyst bulk from the leading face to the trailing face, and finally (iv) carbon nucleation in the catalyst trailing face to the formation of CNFs. According to Baker et al. (1972), carbon formation takes place in three steps. Hydrocarbons got adsorbed and decomposed on active sites of the catalysts as first stage which is followed by dissolution of some of the carbon species into the bulk and diffusion through the metal particle from the hotter leading face (exposed to the gas) to the cooler rear face (facing the support), where carbon is precipitated from the solution to form carbon filaments. Finally, decreasing the growth rate as the catalyst encapsulated by carbon formed. Hence, the deactivation rates have good correlation with carbon diffusion rate. Catalyst can maintain its activity if the carbon diffusion rate is greater than the carbon formation rate. Otherwise carbon can encapsulate catalyst and leads to catalyst deactivation. The studies reveal that the carbon deposition is inversely proportional to

methane partial pressure and directly proportional to the temperature (Villacampa et al., 2003). Higher carbon accumulation may leads to the disintegration of the catalyst. Moreover, carbon formation may affect activity in the following ways either individually or in combination (Amin et al., 2011). The carbon can: i) be adsorbed strongly on the active phase surrounding and blocking access to the active phase surface; ii) encapsulate the active metal particle; iii) plug the micro and mesopores, denying access to the active phase inside the pores; iv) accumulate as strong carbon filaments leading to catalyst pellet disintegration; and v) in extreme cases, physically block the reactor.

Table 2.4 Summary of the main parameter obtained in the experiments at different temperatures over NiCuAl catalyst (WHSV = 120 $lg_{cat}^{-1}h^{-1}$) (Suelves et al., 2009).

T (°C)	$R_{CH4,0}$ (mmol/min.g_{cat})	CH_4 (%)	C_{dep} (g/g_{cat})	r_C (g_C/g_{cat}.h)
550	10.02	10.20	16.4	6.56
600	12.96	13.19	21.3	8.51
650	16.25	16.17	26	10.40
700	34.27	31.20	46.8	20.03
750	47.60	22.06	39	14.18
800	45.95	19.41	15.6	16.22

The operating conditions like flow rate (GHSV), reaction temperature (M. A. Ermakova et al., 2000), methane partial pressure, and hydrogen partial pressure (Villacampa et al., 2003) also strongly influence the catalytic deactivation. The impact of reaction temperature and flow rate on methane cracking rate as well as catalytic deactivation are widely studied and both of them are considered as having such a high influence. The methane decomposition rate and carbon formed during the reaction over NiCuAl catalyst done by Suelves et al. (2009) in a fixed bed reactor at different

temperatures are furnished in Table 2.4 and 2.5. The maximum carbon deposit was observed at 700 °C, but at higher temperatures like 750 and 800 °C, catalyst were completely deactivated by producing 39 and 15.6 g_C/g_{cat}. In the opinion of W. Zhang et al., (2011), at higher temperature the methane decomposition rate is too high and hence nucleation rate of carbon too. Hence, the diffusion of carbon could not catch up with the increased nucleation rate; thereby the surfaces of active Ni particle were covered by the deposited carbon and the catalyst deactivated rapidly. Table 2.5 shows that 141 g of carbon are deposited per g_{cat} in 60 min at a space velocity of 1200 $lg_{cat}^{-1}h^{-1}$. It is observed that catalyst become completely deactivated at 480 and 1200 $lg_{cat}^{-1}h^{-1}$ space velocity quickly, comparing with those at lower space velocities.

Table 2.5 Summary of the main parameter obtained in the experiments at different space velocity over NiCuAl catalyst (T = 700 °C) (Suelves et al., 2009).

WHSV ($lg_{cat}^{-1}h^{-1}$)	$R_{CH4,0}$ (mmol/min.g_{cat})	CH_4 (%)	C_{dep} (g/g_{cat})	r_C (g_C/g_{cat}.h)
24	10.38	54.61	45.8	7.02
60	15.01	31.36	39	15.60
120	34.27	31.2	46.8	20.06
240	58.31	20.09	64.6	25.84
480	79.95	11.63	84[a]	33.60
1200	134.74	8.77	141[a]	56.40

[a] catalyst deactivated

Moreover, the rate of carbon nucleation would become quicker at higher space velocities which breaks the competitive balance exists between the carbon diffusion and nucleation. Hence, more active site would be covered with the excess nucleated carbon and the catalyst would deactivate more rapidly. Thus, lower space velocity produce higher

hydrogen and carbon than at higher space velocities. These results clearly reveal the influence of space velocity and reaction temperature on catalytic deactivation. Higher temperature deactivates catalyst rapidly and increase hydrogen content in the post-reaction stream. On the other hand, higher space velocity diminishes hydrogen content in the outlet gas stream and deactivates catalyst quickly.

According to Suelves et al., (2009), thermal sintering of Ni particles does not have any influence on catalytic deactivation. A comparison study on the sizes of used catalysts using powder XRD patterns exhibit comparable sizes at both temperatures of 550 and 800 °C (José Luis Pinilla et al., 2008). Hence, catalyst deactivation is not the result of Ni sintering during the decomposition conducted in the fixed bed reactor indicating the possibility of prevention of Ni sintering by produced hydrogen. The formation of more ordered carbon is only responsible for deactivation of catalyst at higher temperature (Suelves et al., 2009). While**,** Ishihara et al. (1995) says that the large amount of deposited carbon is not responsible to catalyst deactivation as their 10% Ni/SiO_2 catalyst actively crack methane even after depositing up to a 200-carbon atom per nickel atom ratio. NiCuAl also showed lengthen activity for several more hours even after depositing 46.8 g/g_{cat} at 150 min. This extended activity may be attributed to the catalytic activity of formed carbon. Those observation supports the space limitation in the reactor while running reaction results in deactivation (Aiello et al., 2000; T. Zhang & Amiridis, 1998).

2.2.2 Carbonaceous Catalyst for TCD

The hydrogen content in the initial output of TCD process with metal catalysts is incredibly high, but their activity decreases very fast with time. It is clear that decrease in activity results from the blocking of catalyst's active site by the carbonaceous deposit produced according to equation (1.1). Formation of metal carbide is the other main challenge of using metal catalysts. These problems have partly overcome by using

carbonaceous catalysts. Carbonaceous catalysts are highly stable, relatively cheap, and resistant to poisoning by Sulphur compounds and other elements, and undergo deactivation to a much lower degree than metallic catalysts (Malaika & Kozłowski, 2009). Carbon has been using as a catalyst (Dufour et al., 2008) as well as a catalyst support (Jüntgen, 1986). The main advantages of carbon over metal catalysts are: 1) low cost; 2) high temperature resistance; 3) tolerance to sulfur and other potentially harmful impurities in feedstock like amino and tarry compounds; 4) production of marketable by-product carbon (which could be substantially reduce the net cost of hydrogen production); 5) mitigation of overall CO_2 emissions from the process; 6) higher fuel flexibility; and 7) no metal carbides formation, hence metal carbide formation can make the metal catalyst regeneration more complicated (N. Muradov et al., 2005; Serrano et al., 2013). In TCD, carbon bears more advantages as follows: 1) produced carbon can catalyze further process, hence external catalyst required only for the start-up of the action, avoiding the supply of external and usually expensive catalyst produced by sophisticated production techniques; and 2) it is not essential to separate produced carbon from the catalyst.

Activated carbon (AC) (Moliner et al., 2005), carbon black (CB) (E. K. Lee et al., 2004), coal chars (Dufour et al., 2008), glassy carbon (N. Muradov, 2001), MWNT (Guil-Lopez et al., 2011) acetylene black (N. Muradov, 2001), soot (N. Muradov, 2001), graphite (Guil-Lopez et al., 2011), diamond powder (N. Muradov, 2001), CNT (Guil-Lopez et al., 2011), fullerenes (N. Muradov, 2001) and carbon materials with monolithic honeycomb design (Gatica et al., 2013) are the different carbon materials used as catalyst for TCD process. Most of the researches have been done on AC (contrived from lignocellulosic precursors like coconut, almond, peach, plum, olive, palm and cherry), and CB because of their noble activity and better stability (Lázaro et al., 2010; N. Muradov, 2001; Nazim Muradov et al., 2005). TCD on carbon catalysts, such as CB, AC, ordered mesoporous carbon, CNF, and graphite, needs a high activation energy (143–236

kJ/mol) and has to be operated at higher temperatures (800‑1100 °C) than on metal catalysts (Dufour et al., 2009; M. H. Kim et al., 2004; E. K. Lee et al., 2004; K. K. Lee et al., 2004; Nazim Muradov et al., 2005; Serrano et al., 2009; Serrano et al., 2008). Different factors are associated with activity of carbonaceous catalyst: pore-size distribution (Abbas & Daud, 2010a; Botas et al., 2010; Krzyżyński & Kozłowski, 2008; Serrano et al., 2008; J. Zhang et al., 2012), surface area (Lázaro et al., 2008; Suelves et al., 2007), polar surface groups (Z. Bai et al., 2012; Moliner et al., 2005; Suelves et al., 2008; Zhuang et al., 1994), structural disorders, crystallinity (J. Zhang et al., 2011; J. Zhang et al., 2012), flow rate (Lázaro et al., 2008), reaction temperature (Abbas & Baker, 2011), composition of reaction gas, pressure (Abbas & Daud, 2009a), etc. While, the genuine reason behind its activity and reaction mechanism are not completely elucidated yet. Ordered mesoporous material found exhibiting higher activity because of its reduced diffusion restriction, studies were reviewed elsewhere (Serrano et al., 2013). In general, high temperature and low methane space velocity favor hydrogen production (Table 2.6), in a similar manner as metal catalysts done.

It is believed that the methane decomposition mechanism over carbonaceous catalyst initiates with dissociative adsorption of methane followed by a sequence of stepwise surface dissociation reactions leading to the formation of elemental carbon and hydrogen, as mentioned for metal catalyst (Nazim Muradov et al., 2005). The comprehensive mechanism of methane decomposition is yet to be fully elucidated. Initially methane molecules interact with chemically reactive carbon crystallites (or other energetic abnormalities and/or active surface radicals) to break C-H bond in order to form new C–C bonds in a hexagon layer of carbon form. This carbon crystallite growth is likely to occur at the periphery of existing crystallites (Nazim Muradov et al., 2005). This new carbon phase formation is constituted by two processes named carbon nuclei formation and carbon crystallites growth. The rate of carbon nuclei formation is proportional to High

Energy Site (HES) density or substrate surface area. The research results among the AC and CB reveals that, CB has highest stability because of ease of accessibility for methane molecules, but its catalytic activity is comparatively low (Suelves et al., 2007; Suelves et al., 2008). While, AC shows very high initial catalytic activity, its stability is pitiable because of the presence of micropores as well as the prevention of methane diffusion to AC pore by huge carbon deposit formed (Serrano et al., 2010). The activation energies for the activated carbons are in a range from 160 to 201 kJ/mol and the reaction orders in a range from 0.5 to 0.6 (Ryu et al., 2007). While, the reported activation energies for the carbon blacks varied in a wide range from 148 to 236 kJ/mol and the reaction orders were from 0.5 to 1.0. However, these differences among various carbon materials have not well been elucidated and moreover no definite conclusion has been made on the mechanism. Serrano et al. (2009) suggested CB for short and long term reaction as it provide moderately high rate of hydrogen. On the other hand, AC is fare for short term reaction. The kinetic and deactivation studies reveal that AC undergoes fast deactivation, even having high initial rate. AC produced from coconut shells displayed the highest initial activity producing hydrogen up to 70-75 vol %. Unfortunately, it is followed by dramatic drop in catalytic activity to attain a steady state of very low hydrogen output within 3 h (N. Z. Muradov, 1998). Very recently, Gatica et al. (2013) applied monolithic honeycomb design to carbon material (Figure 2.5) for TCD in a mass spectrometer. Similar to other catalysts, monoliths also undergo activity loss of 35-50%, 50-67% and 50-55% at 750, 800, and 900 °C during 1 h reaction duration, respectively. Eventually, this deactivation is similar or smaller compared to other carbon catalysts. Mass spectrometer signal analysis reveals that TCD is highly selective towards pure hydrogen and elemental carbon with similar amount of methane disappearance and hydrogen production. Furthermore, monoliths shows satisfactory mechanical resistance with no characteristic changes even after TCD process and possess efficient hydrogen production starting at relatively low

temperature of 600 °C. The influence of crystallinity and defect concentration of monoliths on its activity and nature of carbon produced from methane are under investigation.

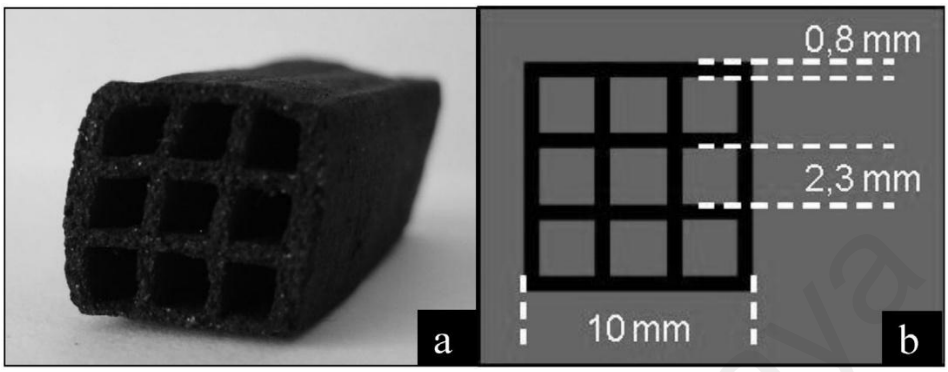

Figure 2.5 a) Image of the carbon based honeycomb monoliths; b) drawing with the geometric parameters of the monolithic structure (Gatica et al., 2013).

N. Muradov (2001) studied around 30 different carbonaceous catalysts including samples of elemental carbon, AC, CB, nanostructured carbons, glassy carbons, graphite, etc. and concluded that the disordered forms of carbon (e.g., AC and CB) are catalytically more active than the ordered ones (e.g., graphite and diamond). The order of activity of carbon catalysts for TCD according to its structure obeys the following order: amorphous > turbostratic > graphite (Nazim Muradov et al., 2005). Dislocations, low-coordination sites, vacancies, atoms with free valences, discontinuities, and other energetic abnormalities on the surface of amorphous carbons because of irregular array of carbon bonds have imperative impacts on the activity of carbon catalysts. Remarkably, the entire surfaces of the catalyst do not participate in gas-solid interface methane decomposition, but it occurs through a dissociative adsorption of methane molecules on surface active sites of the catalyst (M. H. Kim et al., 2004). This portion is termed as high-energy sites (HES) (Krzyżyński & Kozłowski, 2008), can be different in each AC. Furthermore, the edges or defects on the surface of carbon materials are generally accepted as the active sites for decomposition (S. Y. Lee et al., 2008; Suelves et al., 2007).

2.2.2.1 Experimental parameters influencing activity of carbonaceous catalyst

GHSV and temperature are the main parameters influencing hydrogen production rate over carbonaceous catalyst, similar to the behavior of metal catalyst. GHSV is the volume of gas feed per hour per volume of catalyst. Table 2.6 covers maximum and final CH_4 conversion/H_2 production over various carbon catalysts, those are previously studied. Hence, it simplifies the understanding of different parameter effect on conversion rate. Generally it is observed that the hydrogen production rate increase as decreasing the GHSV (Lázaro et al., 2008) as well as increasing the temperature (Abbas & Baker, 2011). Low GHSV allows methane molecule to interact with catalysts as well as to enhance the decomposition rate. The experiments conducted on CB at the temperature 850 °C gave an initial conversion of 17%, whereas the conversion at 950 °C was 77% (Lázaro et al., 2008). Such type of conversion rates are expected because of the endothermic nature of methane decomposition reaction. Influence of partial pressures of methane, P_{CH_4} on methane decomposition is also studied recently. At higher P_{CH_4}, the rate of mass gain also increases. Abbas & Baker (2011) carried out an attempt to study the effect of P_{CH_4} on the initial specific rate of carbon formation for first time. They found that at higher P_{CH_4}, the catalyst produces maximum quantity of carbonaceous deposit in a shorter period, which was supported by further study results (Abbas & Daud, 2009a). It is due to the increase in the rate of diffusion of methane into the interior part of the particle. The optimal conditions for the catalyst depend on the final use of the hydrogen produced. For instance, high temperature and low methane space velocity favor production of high purity hydrogen suitable for fuel cells application. Moreover, low methane/nitrogen ratio also preferred.

Table 2.6 Comparative study of influence of experimental parameters on the activity of carbonaceous catalysts

Catalyst	Operating conditions			Maximum		t_{max}	CH_4	H_2	t	Ref.
	T	F	W	CH_4	H_2		At time 't'			
				at t_{max}						
DCC-N103(P)	850			2	--	0.1	1	--	2	Ryu et al., 2007
(CB)	870			4	--	0.1	2	--	2	
	900	15,000[a]	0.1	5	--	0.25	3	--	2	
	925			5	--	0.1	5	--	2	
	950			13	--	0.1	7	--	2	
CG Norit (CB)		20[b]	--	--	72	0.1	--	30	4	Suelves et al., 2007
	850	50[b]	--	--	62	0.1	--	17	4	
		100[b]	--	--	48	0.1	--	8	4	
Fluka 05120	850	20[b]	--	--	60	0.1	--	38	4	
		50[b]	--	--	51	0.1	--	28	4	

Table 2.6 Continued

NORIT CG (commercial AC)	950	600[a]	2	--	94	1.1	--	38	4	Moliner et al., 2005
	900			--	85	0.6	--	30	4	
	850			--	68	0.5	--	30	4	
Xiaolongtan char	1000	200[b]	10	96	90	0	19	18	2	Wei et al., 2011
	850			69	48	0	20	10	2	
	700			29	20	0.1	9	8	2	
	600			10	9	0.1	5	5	2	
ACPS	850	1764h^{-1}	20	49.8	47.9	0	--	--	--	Abbas & Daud, 2010a
	850	882 h^{-1}	40	34.9	62.5	0	--	--	--	
	850	441 h^{-1}	80	21.2	77	0	--	--	--	
	850	294 h^{-1}	120	16.7	81.6	0	--	--	--	
	850	294 h^{-1}	40	13.2	83.1	0	--	--	--	
	850	441 h^{-1}	40	22	78.3	0	--	--	--	
	850	882 h^{-1}	40	34.9	62.5	0	--	--	--	

Table 2.6 Continued

	850	1764h^{-1}	40	41.5	57.9	0	--	--	--	
	850	882 h^{-1}	40	34.9	62.5	0	--	--	--	
	825	882 h^{-1}	40	37.6	60.9	0	--	--	--	
	800	882 h^{-1}	40	48.7	50.9	0	--	--	--	
	775	882 h^{-1}	40	59.5	39.1	0	--	--	--	
Ni-AC	550			4	--	0	0	--	1	Zongqing Bai et al., 2007
	650			6	--	0	1	--	2	
		50[b]	0.20							
	750			13	--	0	2.5	--	2	
	850			27	--	0	2.5	--	1	
BP1300 (CB)		36 h^{-1}	--	--	92	0	--	46	6.5	Lázaro et al., 2008
	850	72 h^{-1}	--	--	70	0	--	26	6.5	
		144 h^{-1}	--	--	41	0	--	15	6.5	
BP2000 (CB)		36 h^{-1}	--	--	59	0	--	28	6.5	
	850	72 h^{-1}	--	--	35	0	--	20	6.5	
		144 h^{-1}	--	--	18	0	--	11	6.5	

Table 2.6 Continued

BP2000 (CB)	950		--	--	78	0	--	62	6.5
	900	144 h^{-1}	--	--	59	0	--	38	6.5
	850		--	--	18	0	--	11	6.5

(T, temperature (°C); F, flow rate ([a]mL/($g_{cat.}$h) [b]mL/min, unless other units are stated); W, catalyst mass (g); Conversion (%); t_{max}, time at which maximum methane conversion or hydrogen production occur (h); t, time (h); --, not mentioned in the original paper)

2.2.2.2 Deactivation of carbonaceous catalysts

Similar to the metal catalyst deactivation, shielding of the active sites is the major reason of carbon catalyst deactivation too. The carbon produced as the by-product of TCD process has a structural order in between that of amorphous and graphite and has lower surface area. As mentioned before, while amorphous carbon shows better activity, well-structured graphitic carbon bear poor activity only (Abbas & Wan Daud, 2010). Deactivation of the carbonaceous catalyst is a type of transformation of catalyst surface from an active state in the fresh sample to an inactive state in the used sample. In another words, disordered carbon to more ordered carbon. The activation energy of the carbon nuclei formation during methane thermal decomposition (316.8 kJ/mol) is much higher than the activation energy of the carbon crystallites growth (227.1 kJ/mol) (Nazim Muradov et al., 2005). This implies that, in general, the rate of carbon crystallites growth tends to be higher than the rate of carbon nuclei generation. The rapid crystallite growth may lead to the formation of a pseudo-ordered (turbostratic) carbon (accompanied with the loss in surface area and the concentration of HES) and, as result, loss in catalytic activity.

Oxygen surface groups (OSGs) have the ability to make changes on the catalyst surface as it desorbed as CO and CO_2 from the surface and pores in the early phase of the reaction. Hence, the long-term deactivation is not associated to the OSG concentration. While, the characteristic of carbon deposit have heavy impact on carbon catalyst deactivation. XRD, XPS, and Raman spectroscopy studies on fresh and deactivated catalysts do not give any characteristic structural difference in fresh and used catalysts (Moliner et al., 2005). Hence, loss of effective surface area of catalyst particles because of deposition of inactive carbon plays a major role in deactivation. The experimental results show that, 50–100 mg_C/g_{cat} is enough to deactivate coal-derived AC, but commercial ACs like SUPRA and CG need 350 and 450 mg carbons per gram catalyst,

respectively. Deposition of 450 mg of carbon reduces the surface area from 1300 to 46 m^2/g. Lázaro et al. (2008) confirm the rapid diminish in surface area upon carbon formation. They observed a decrease in surface area from 1300 m^2/g to 300 m^2/g in 120 min and fell gradually to negligible values by 900 min. It proposes that the non-porous carbon deposit grows on the pore mouth and hence the entire porous fresh sample is gradually transformed into non-porous. Moreover, a linear relationship is found in between the quantity of carbon deposited and total pore volume (Suelves et al., 2008). Thus, the pore volume establishes the maximum amount of carbon that the catalyst can accommodate before deactivation, i.e., the maximum hydrogen production per mass of catalyst.

Moliner et al. (2005) concluded with the results that the catalyst deactivation is not only controlled by the amount of carbon deposited, and it becomes apparent that the capability of the catalyst to accommodate carbon depends on the experimental conditions. Two effects can be recognized: i) molecular sieve effect and ii) activated diffusion effect. Molecular sieve effect has a strong association with pore mouth blocking. The pore mouth decreases with carbon deposition progresses and inner pore surface becomes inaccessible for methane adsorption. Activated diffusion effect is defined with molecular diffusion of methane to the inside of minute sized pores. The rate of diffusion increases with temperature which increases the deposition inside the pores. Hence, TCD at high temperatures take place mostly inside the pores, where majority of the high energy AC surfaces located.

The mesoporous carbons were directly prepared from CLR by KOH activation termed as RC showed extremely different behavior from other catalysts with a three-step linear variation in deactivation of catalyst with reaction time (N. Muradov, 2001; Nazim Muradov et al., 2005). Methane conversion of RC touched 25% from 41% within first 2 h, and then it went up slightly to 27% in another 3 h and decreased gradually to 13% at

40 h (J. Zhang et al., 2012). This behavior indicates the autocatalytic ability of the system. Catalytic activity decline sharply as the porosity is blocked by the carbon produced in the earlier stages. Hence, the pores of the carbon catalyst were completely blocked and the surface was thickly covered. Eventually, the produced carbons create new active sites for TCD by growing to the outside of the catalyst pores and undergo further carbonization with time under the reaction conditions, results in a promoted methane conversion to some more extent. With the sequence going, the carbon catalyst shows a better activity and improved stability for TCD. Moreover, the catalyst will be getting deactivated when the deactivation rate of the earlier active sites is higher than the production rate of new ones.

2.2.3 Carbon Catalytic Activity Boost by Metal Doping

Very recently, few researchers explored the possibility to amplify the activity of carbonaceous catalyst by doping with small amount of metals; a comprehensive utilization of advantages of both metal and carbon (H. Li et al., 2010; Morales-Torres et al., 2011; J. Zhang et al., 2013). In addition, the high temperature reducibility of carbon is helpful for in-situ reduction of metal oxides supported on carbon carrier to metal catalyst during pre-treatment (J. Zhang et al., 2013). This in-situ metal oxide reduction helps to avoid additional hydrogen reduction step, which simplifies the conventional preparation processes. According to Nazim Muradov et al. (2005) small amount of metal impurities in the carbon catalysts, whether it is doped or genuinely present in carbon, govern its activity for methane decomposition. By the addition of metal, carbon turns to amorphous which results in the development of active HESs. Hence, activity enhancement of catalyst may be proportional to the concentration of the active sites on its surface. The trials conducted on nano-sized carbon black (NCB) and AC discloses that the loading of metals like Co and Ni efficiently increases the initial activity of carbonaceous catalysts (Zongqing Bai et al., 2007; J. Chen et al., 2009). J. Chen et al.

(2009) explained the higher methane conversion of Co/NCB and Ni/NCB in two ways; i) Ni and Co metal particles can take an important role in activating methane molecules in the induction period of methane decomposition to generate the intermediates on the surface of Ni or Co, and then the active intermediates immigrate to the surface of NCB and decompose to carbon and hydrogen; ii) the activity of Ni and Co metals are much higher than that of NCB in methane decomposition. Hence, methane can be directly decomposed on the surface of metal particles.

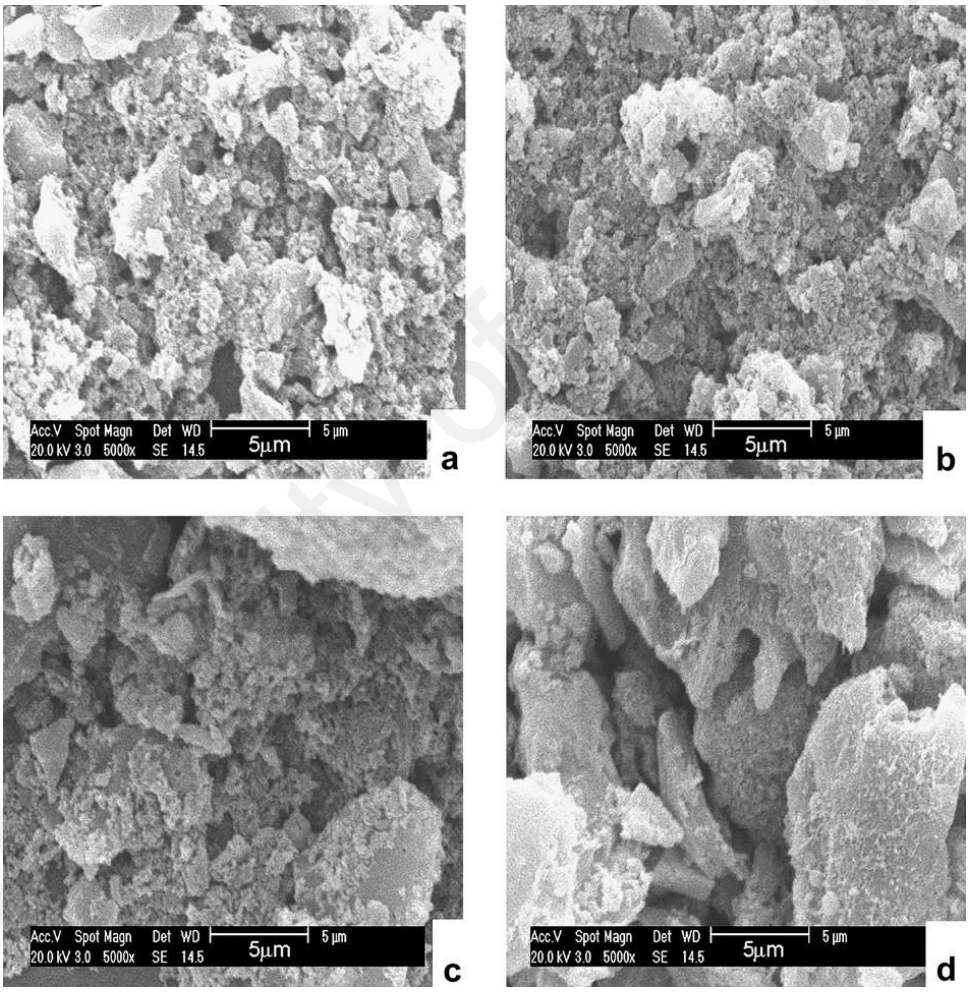

Figure 2.6 SEM images of carbon produced from methane decomposition on different NCB at 850 °C: (a) untreated NCB; (b) Ni/NCB; (c) Co/NCB; (d) Pd-Ni/NCB (J. Chen et al., 2009).

The second reason strictly supports the rapid decrease in activity of Ni/NCB and Co/NCB after 4 and 6 min of reaction. Carbons produced by decomposition of methane

over doped and non-doped carbon catalyst are shown in Figure 2.6. Pd–Ni/NCB produced carbon flakes of comparatively larger size [Figure 2.6 (c)] than those produced over NCB, Ni/NCB and Co/NCB, indicating extended growth time and improved stability of Pd–Ni/NCB. The authors (J. Chen et al., 2009) also speculate that carbon flake might be originated from a new carbon crystallite on unsaturated carbon atoms. Hence, large size carbon flake cannot be produced, because initially formed carbon atoms can quickly satisfy the valance constraints and energetic stabilization of unsaturated carbon atoms in the defects. Eventually, doping of Pd-Ni and Pd-Co with NCB gave poor results than that doped with Ni or Co alone, but still it is higher than that of untreated NCB and it improves the stability of NCB slightly. Furthermore, the addition of SiO_2 or SBA-15 to AC, which increases its pore volume and surface area, gives better overall activity than that of un-doped AC with initial activity of 30 and 27% at 850 °C, respectively (J. Zhang et al., 2011). Meanwhile, AC and CB have larger surface area and pore volume than that of AC/SiO_2, but exhibit lower activity because of their very poor micropore contribution to the total porosity. J. Zhang et al. (2013) found that Ni doped carbon exhibit more stable and consistent activity than the metal catalysts, coal, and CLR-based carbons at 850 °C. CLR based carbons, Ni/SiO_2, and Ni/Al_2O_3 shows 20, 50, and 40% initial methane conversion, respectively, and the activity declined to 10% by the first 3 h of examination at 850 °C. Contrary to the above results, Ni doped carbon showed an increase in its activity with time from a 30% initial methane conversion to 80% by 6 h run. Among the three Ni-doped carbon, Ni/RC showed lower activity because of higher sulfur content of CLR than those in SH-Coal and SL-Coal, might easily poison the Ni active site. Furthermore, J. Zhang et al. (2013) examined TCD in a fixed bed reactor over commercial AC from coconut shell supported Fe-Al_2O_3 catalysts prepared by impregnation method. Despite of the metal loading quantity, Fe-Al_2O_3/AC convert slight volume of methane (5.7%) only at 750 °C as the active site of Fe need high temperature to catalyze the

decomposition of methane. It is noticed that loading of Fe and Al_2O_3 decrease the surface area and pore volume of carbon catalyst. 40% Fe/Al_2O_3 loading with ratio of 16/24 to 24/16 produces catalysts with narrow mesopore distribution which displayed relatively high methane conversion. Although, loading of Al_2O_3 in to AC (0Fe-40Al/AC) showed poorer activity and stability with an initial methane conversion of 28.6% and negligible final conversion of 2.2% after 100 min. However, as increasing the Fe content, the TCD followed a decrease-increase-decrease trend with reaction time. Especially, on the 40Fe-0Al/AC catalyst, the conversion decreased quickly from 21.3% to 12.7% at first 60 min, and then increased gradually to 26.7% in another 140 min, followed by a steady decrease to 13.1% at 360 min, which suggests that the three-step variation is mainly related with the catalytic behaviors of Fe catalyst. The authors found that the initial catalytic activity is mainly from the AC itself as xFe-yAl/AC with different Fe content shows almost similar initial methane conversion. The weakening of AC with reaction time decreases the methane conversion. After a particular period of time, methane conversion starts to increase with a transitional period before Fe particles reach its full capacities. This phenomena resulted a decrease-increase-decrease trend in this TCD which is also found in TCD over Ni-doped carbons (J. Zhang et al., 2013).

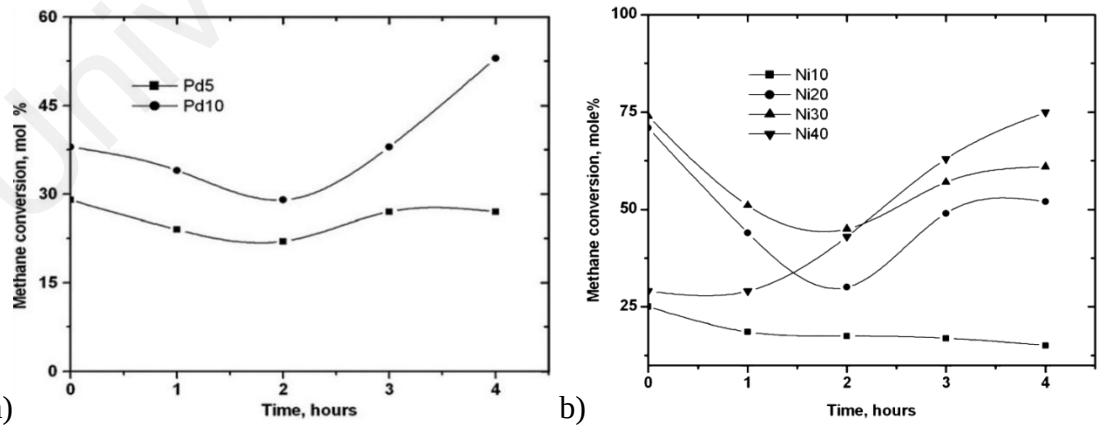

Figure 2.7 Methane conversion (mol%) over AC supported a) Pd and b) Ni catalysts (T: 850 °C, VHSV: 1.62 l/hg_{cat}) (Prasad et al., 2010; Sarada Prasad et al., 2011).

Prasad et al. (2010) studied the influence of metal quantity on activity of AC. They found that the initial methane conversion rate for AC/Pd-10 is more than that of AC/Pd-5 [Figure 2.7 (a)]. Higher activity of AC/Pd-10 is ascribed to its higher surface area (245.17 m^2/g) than that of AC/Pd-5 (44.21 m^2/g), even after methane cracking. Correspondingly, all AC/Ni catalysts (Ni-10, Ni-20, Ni-30 and Ni-40) also exhibited improved activity than AC (Sarada Prasad et al., 2011) [Figure 2.7 (b)]. It is clear from Figure 2.7 (b) that Ni-30 provide maximum initial methane conversion of 74 mol% (Sarada Prasad et al., 2011). At the same time, Ni-40 gives lower initial methane conversion of 29 mol%, but 75 mol% conversion after a reaction span of 4 h. The decrease in the activity for the first 2 h in the case of Ni-20 and Ni-30 is attributed to BET surface area and crystal size of Ni. Furthermore, the lower particle size of Ni (14-46 nm) may be the reason of the enhancement in methane conversion rate after 2 h. Hence, all the AC supported Ni catalysts (Ni-10, Ni-20, Ni-30 and Ni-40) exhibited sophisticated activity in TCD. However, Ni crystal size increasing and the new crystallite Ni_3C formation during the process lead to the deactivation of the catalysts (Zongqing Bai et al., 2007).

Addition of silica or silicate increases the microporosity of CLR derived carbon by 28%, along with the ratio of mesoporosity (2-50 nm) to microporosity (<2 nm) being close to 1:1, results in the formation of hierarchical porous carbon (HPC) (J. Zhang et al., 2013). Among the prepared catalysts, 1SiRC (1 g of SiO_2 as additive) have the optimum composition towards methane decomposition with a methane conversion about 5% higher than that of RC. Whereas, HPC with Al_2O_3 as additive (AlRC) exhibit outstanding methane conversion from 27 to 61% together with fibrous carbon production (36 g/g_{AlRC}) after 10 h of experiment in a fixed bed reactor at 850 °C with a total flow rate of 50 mL/min. For the best of authors' knowledge, production of fibrous carbon reported for the first time from TCD using carbon-based catalyst.

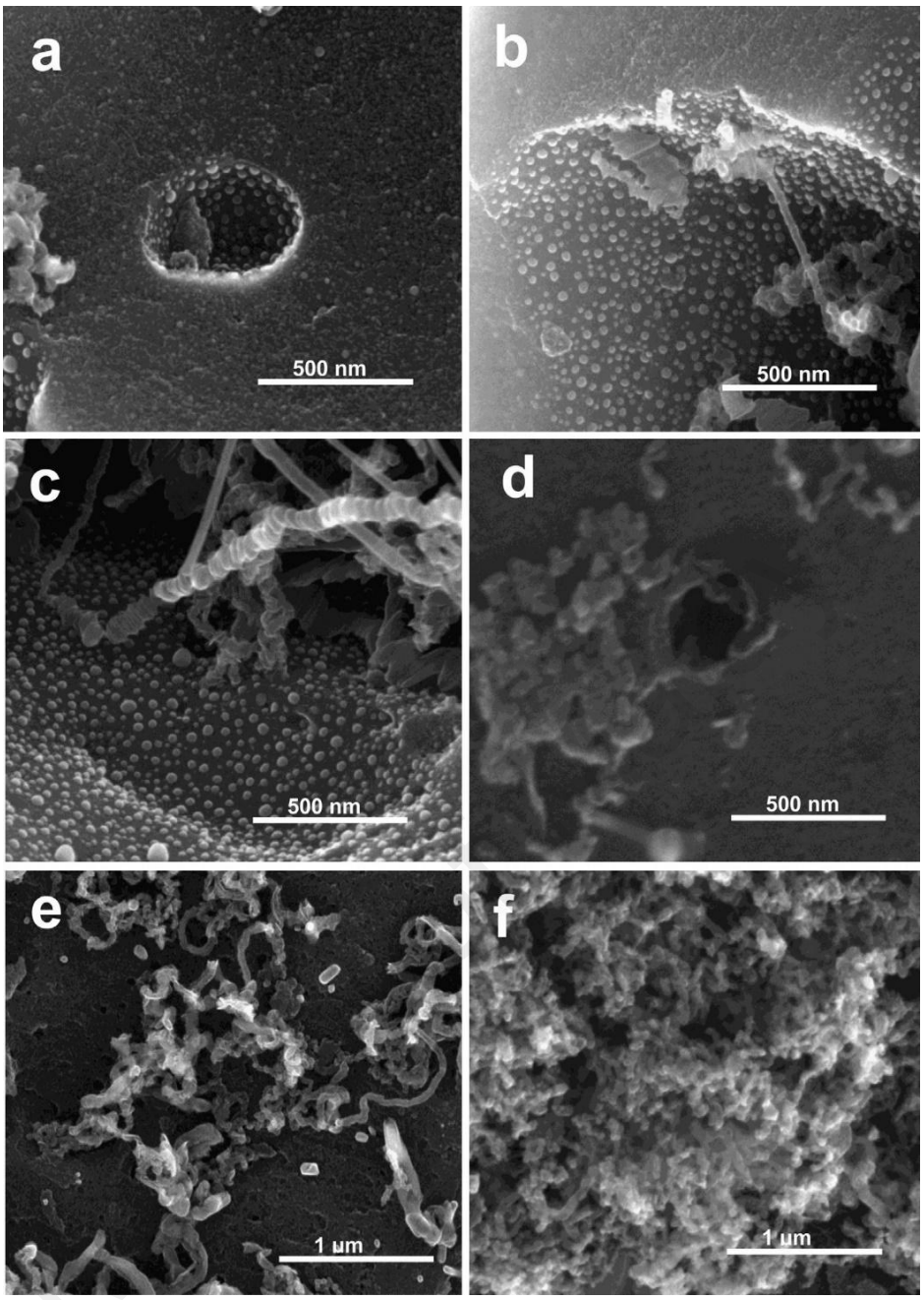

Figure 2.8 The nucleation and growth process of the fibrous carbon deposits described by SEM images: (a) 15 min, (b) 30 min, (c) 45 min, (d) 60 min, (e) 90 min, and (f) 10 h in the TCD of methane over AlRC sample (J. Zhang et al., 2013).

The enhanced catalytic activity of HPC for TCD is attributed to the synergistic effect between the micropores and mesopores in it. Hence, the effective collision of methane molecule on the discontinuous surface of the HPC surface offer stronger scattering in a limited space and results in high methane conversion. Fibrous carbon formation mechanism is displayed in Figure 2.8. Fibrous carbon nucleation and growth

starts either inside the pores or at the edges of the catalyst particles [Figure 2.8 (a-d)]. Further methane decomposition for several hours leads to block the pore [Figure 2.8 (d-f)] by carbon deposit. IR spectroscopy and EDX studies reveal that the intensity of OSGs on HPC reduced sharply after 10 h of experiment. Meanwhile, formed fibrous carbon contains typical quantity of OSG with the O/C ratio of about 0.03, which is lower than that of fresh AlRC. Hence, oxygen atoms transferred from the carbon catalyst to the produced fibrous carbons, which also facilitate further catalytic activity. Though, the carbon deposits produced on the other samples (CC, RC, and SiRC) are amorphous particles, with a negligible contribution to the catalytic activity for methane decomposition and hindering the activation of methane on the active sites. Evidently, the formation of active fibrous carbons is the key to the excellent catalytic performance on AlRC.

2.2.4 Comparison between Metal and Carbonaceous Catalysts

Comparisons between metal and carbonaceous catalysts are complicated because of the differences in its active center concentration as well as the nature of these active sites. A comparison of initial and final activity of metal and carbonaceous catalysts have done in Table 2.7. It is reported that mild reaction condition is used to produce better CNFs, but drastic condition is required to get higher hydrogen output (Abbas & Wan Daud, 2010). While using metal catalyst, removal of produced CNFs without harming deactivated metal catalyst for reactivation and re-usage of metal catalyst is necessary requirement for economic hydrogen production. In fact, regeneration of catalyst is not required in TCD using carbonaceous catalyst. In the best of authors' knowledge, only one article is available on the comparative study of metal and carbonaceous catalysts. Guil-Lopez et al. (2011) have experimented with a series of metal and carbonaceous catalysts for comparison. The different metal catalysts are as follows, six Ni-based catalysts: commercial bulk nickel oxide (NiO-com), NiO supported on SiO_2, and on Al_2O_3 (Ni/SiO_2

and Ni/Al_2O_3, respectively), Ni–Al spinel (Ni-spinel) and two NiMgAl-mixed oxides from hydrotalcite-like materials (Ni-ex LDHs) with different metal loading. Furthermore, two commercial bulk iron oxides, hematite (Fe_2O_3-hem), and magnetite (Fe_3O_4-mag), were used as metal-catalysts too. Six commercial carbons, belong to four diverse classes having different properties and morphologies, were used as carbon catalysts for methane decomposition: CB, AC, CNTs, and graphite. Four groups of catalysts were as follows: CBs of having different textural properties (Vulcan XC72, CB-v; and black pearls 2000, CB-bp), microporous AC (AC-micro), mesoporous AC (AC-meso), multi-wall nanotubes (MWNT), and graphite (graph) as a highly crystalline carbon catalyst. Considering BET area, they have classified these six carbon catalysts in to three groups as follows: low specific surface area (graph), high specific surface area (AC-meso, AC-micro, and CB-bp, which present high microporous areas), and intermediate specific surface area (MWNT and CB-v).

The intrinsic catalytic activity of both metal and carbonaceous catalysts are completely different. Moreover, the surface reduced metal, Ni particle size, and Ni-environment (mixed oxide matrix, spinel or simple oxide) can be the root of the activity of metal catalyst. In the case of carbon catalysts, it is connected to the quantity of structural imperfections present in the graphene layers. Initial activities and catalyst deactivation of the two catalysts types have been studied with the purpose of comparing the catalytic performance of metal and carbon catalyst. From the experimental results of Guil-Lopez et al. (2011), the initial activity (T_{th}) follows the order: Ni-ex LDH-II≈Ni-ex LDH-I >NiO-com > Ni-spinel > AC-meso>CB-bp≈AC-micro> CB-v > Ni/Al_2O_3>MWNT> Ni/SiO_2> graph > Fe_2O_3-hem > Fe_3O_4-mag. Moreover, pre-reduced Ni-ex LDH-II with hydrogen begins decomposition of methane at lower temperature than the most active non-reduced Ni-ex LDH-II, because a high temperature is mandatory to reduce Ni^{2+} phase. Though, metal catalysts deactivated very rapidly.

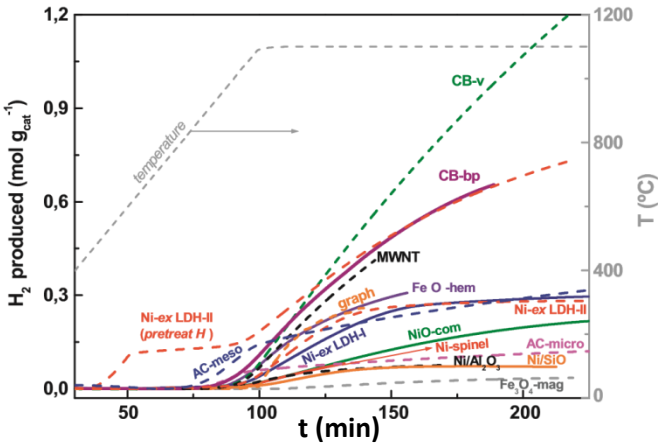

Figure 2.9 Thermo gravimetric decomposition of methane over metal and carbon catalyst (Guil-Lopez et al., 2011).

All examined metal and carbon catalysts underwent deactivation at different degrees which depends on their nature and methane decomposition pathways. Among the studied group, CB-v showed better resistance to deactivation and its ability was attributed to the well-defined concentric graphene layers, which generate large inter-particle spaces (Serrano et al., 2009). It is clear from the Figure 2.9; carbon catalysts are more resistant against deactivation than metal catalysts. The resistance against deactivation is calculated by measuring hydrogen produced after 30 min at 1100 °C, which implies that a high hydrogen production after 30 min at 1100 °C is associated to a low deactivation degree, and the order as follows: CB-v>CB-bp>MWNT>>graph≈Fe_2O_3-hem>Ni-ex LDH-II>AC-meso> Ni-ex LDH-I>> NiO-com> AC-micro> Ni-spinel> Ni/Al_2O_3≈Ni/SiO_2>> Fe_3O_4-mag (Guil-Lopez et al., 2011).

Table 2.7 Comparison of catalytic activity of metal and carbonaceous catalyst; initial activity and final activity of recently studied catalysts are listed.

Catalyst	Reactor	Reaction parameters			Initial		CH_4	H_2	t-time	d	Ref.
		T	CH_4 Flow	Total flow	CH_4	H_2	at time t				
Metal catalysts											
Ni	FBR	550	--	45000[a]	<20	--	8	--	100	130	W. Zhang et al., 2011
Ni	FBR	500	60[b]	90000[a]	9	--	6	--	50	52	W. Zhang et al., 2009
Fe	FBR	800	--	20[b]	33	--	98	--	14	--	Konieczny et al., 2008
Ni-Cu	CFR	600	--	110[c]	80	--	84	--	5	--	Cunha et al., 2009b
Ni-Cu	CFR	900	--	110[c]	97	--	40	--	5	--	
Fe-Cu	CFR	600	--	110[c]	22	--	32	--	5	--	Cunha et al., 2009a
Ni-Cu-Al	FBR	700	--	120000[a]	--	75	--	70	2.5	--	Suelves et al., 2009
Ni/Ce-MCM-41	FBR	580	--	75[b]	70	--	72	--	23	--	Guevara et al., 2010
Ni/SiO_2	FBR	600	--	--	22	--	7	--	10	11	Venugopal et al., 2007b
Ni/SiO_2	FBR	650	15[b]	--	42	--	5	--	4	--	W. Wang et al., 2012
Ni/TiO_2	FBR	700	--	20[b]	--	70	--	60	8	--	Lázaro et al., 2008

Table 2.7 Continued

Ni/Al_2O_3	RBR	700	--	--	--	73	--	68	3	--	J. L. Pinilla et al., 2011
Ni/La_2O_3	--	600	--	110[c]	75	--	73	--	5	--	Figueiredo et al., 2010
Fe/Al_2O_3	RBR	800	--	--	--	90	--	81	3	--	J. L. Pinilla et al., 2011
Fe/Al_2O_3	FlBR	800	--	3000[a]	62	--	32	--	6	--	Torres et al., 2012
Fe/MgO	FBR	800	--	12000[a]	--	55	--	15	3	--	J. L. Pinilla et al., 2011
$NiCu/Al_2O_3$	FlBR	700	--	12000[a]	--	69	--	42	7	--	J. L. Pinilla et al., 2010
$Ni–Ca/SiO_2$	FBR	580	--	100[b]	39	--	12	--	3	--	Zapata et al., 2010
$Ni–K/SiO_2$	FBR	580	--	100[b]	40	--	5	--	2.5	3	
$Ni–Ce/SiO_2$	FBR	580	--	100[b]	90	--	69	--	3	--	
$Ni-Fe/SiO_2$	FBR	650	15[b]	--	46	--	27	--	4	--	W. Wang et al., 2012
$Ni–Cu–TiO_2$	FBR	700	--	20[b]	80	--	69	--	8	--	Lázaro et al., 2008
Ni-Cu/MgO	RBR	700	--	--	--	76	--	75	3	--	J. L. Pinilla et al., 2011
$Ni/MgAl_2O_4$	FBR	550	--	80[b]	34	--	23	--	3	4	Giselle D. B. Nuernberg et al., 2012

Table 2.7 Continued

Ni-Cu/La_2O_3	CFR	600	--	110[c]	35	--	60	--	10	--	Figueiredo et al., 2010
Ni-Cu/La_2O_3	CFR	700	--	110[c]	90	--	11	--	10	--	
Ni/Ce–SiO_2	FBR	600	--	100[b]	40	--	27	--	1	1.3	Tapia-Parada et al., 2013
Fe-Mo/MgO	RBR	700	--	--	--	92	--	58	3	--	J. L. Pinilla et al., 2011
FeMo/MgO	FBR	800	--	1000[a]	--	95	--	85	3	--	J. L. Pinilla et al., 2011
FeMo/MgO	FBR	800	--	12000[a]	--	81	--	19	3	--	
FeMo/Al_2O_3	FBR	800	--	12000[a]	--	88	--	15	2.5	--	
Co/Ce–TiO_2	FBR	500	--	100[b]	0	--	5	--	2	--	Tapia-Parada et al., 2013
Pt-Ni/$MgAl_2O_4$	FBR	700	--	80[b]	45	--	3	--	1.6	4	Giselle De B. Nuernberg et al., 2011
Co/Al_2O_3/Silica	MLR	650	--	1900h^{-1}	80	--	10	--	30	--	Italiano et al., 2010
MgO/SiO_2	FBR	750	60–65[b]	--	--	45	--	10	200	--	Hussain & Iqbal, 2011
K/MgO/SiO_2	FBR	800	60–65[b]	--	--	77	--	60	200	--	
Ni/K/MgO/SiO_2	FBR	700	60–65[b]	--	--	61	--	0	1	1	

Table 2.7 Continued

$LaNiO_3$ perovskite	--	700	15[b]	--	5	--	58	--	4	--	Sierra Gallego et al., 2010
$LaNiO_3$ perovskite	FBR	800	20[b]	--	75	--	74	--	5	--	Maneerung et al., 2011
NiO/La_2O_3	FBR	650	20[b]	--	62	--	44	--	5	--	
Metal doped carbonaceous catalysts											
AC/Pd-5	FBR	850	54[b]	16200[a]	30	--	28		4	--	Prasad et al., 2010
AC/Pd-10	FBR	850	54[b]	16200[a]	38	--	52	--	4	--	
AC/Ni-10	FBR	850	54[b]	16200[a]	25	--	15.1	--	4	--	Sarada Prasad et al., 2011
AC/Ni-20	FBR	850	54[b]	16200[a]	71	--	52	--	4	--	
AC/Ni-30	FBR	850	54[b]	16200[a]	74	--	61	--	4	--	
AC/Ni-40	FBR	850	54[b]	16200[a]	29	--	75	--	4	--	
Ni/SHCC	FBR	850	--	50[b]	30	--	80	--	5.5	--	J. Zhang et al., 2013
Ni/SLCC	FBR	850	--	50[b]	30	--	76	--	5.1	--	

Table 2.7 Continued

Ni/RC	FBR	850	--	50[b]	14	--	59	--	9	--	
Al/RC	FBR	850	--	50[b]	29	--	60	--	5	--	J. Zhang et al., 2013
Si/RC	FBR	850	--	50[b]	23	--	11	--	5	--	
Carbonaceous catalysts											
AC from coconut	FBR	850	--	--	--	79	--	13	1.5	3.5	N. Z. Muradov, 1998
AC (AX-21)	FBR	850	--	--	--	50	--	21	4	--	
CB (Vulcan XC-72)	FBR	850	--	--	--	20	--	5	4	--	
Graphite	FBR	850	--	--	--	4	--	2	4	3.2	
CB	FBR	850	10[b]	15000[a]	22	--	12	--	2	--	J. Zhang et al., 2011
RC (AC)	FBR	850	3000[a]	15000[a]	31	--	22	--	10	--	J. Zhang, et al., 2012
AC-0 (AC)	FBR	850	3000[a]	15000[a]	29	--	3	--	2	--	
BP2000 (CB)	FBR	850	3000[a]	15000[a]	21	--	3	--	4	--	

Table 2.7 Continued

DCC-N103(p) (CB)	FBR	950	25[b]	15000[a]	13	--	7	--	2	--	Ryu et al., 2007
DCC-N220(p) (CB)	FBR	950	25[b]	15000[a]	7	--	6	--	2	--	
DCC-N550(p) (CB)	FBR	950	25[b]	15000[a]	8	--	5	--	2	--	
Carbopack B (CB)	FBR	850	20[b]	38 h^{-1}	--	12	--	12	4	--	Suelves et al., 2007
Carbopack C (CB)	FBR	850	20[b]	38 h^{-1}	--	8	--	8	8	--	
Fluka 03866 (CB)	FBR	850	20[b]	38 h^{-1}	--	68	--	12	4	--	
Fluka 05120 (CB)	FBR	850	20[b]	38 h^{-1}	--	60	--	34	8	--	
BP2000 (CB)	FBR	850	20[b]	38 h^{-1}	--	59	--	28	8	--	
HS-50	FBR	850	20[b]	38 h^{-1}	--	29	--	17	8	--	
CG Norit	FBR	850	20[b]	38 h^{-1}	--	72	--	8	7.5	--	

Table 2.7 Continued

CG (commercial AC)	FBR	850	20[b]	600[a]	51	67	18	30	4	--	Moliner et al., 2005
SUPRA (commercial AC)	FBR	850	20[b]	600[a]	32	49	12	21	4	--	
GAC (commercial AC)	FBR	850	20[b]	600[a]	25	38	16	27	4	--	
SCA750 (coal-derived AC)	FBR	850	20[b]	600[a]	19	31	3	5	4	--	
SCA600 (coal-derived AC)	FBR	850	20[b]	600[a]	20	32	2	4	4	--	
SC800 (coal-derived AC)	FBR	850	20[b]	600[a]	26	41	2	4	4	--	
Shengli lignite char	FBR	850	--	200[b]	87	90	29	38	2	--	Wei et al., 2011

Table 2.7 Continued

Xiaolongtan lignite char	FBR	850	--	200[b]	81	82	17	20	2	--	
Binxian bituminous char	FBR	850	--	200[b]	70	68	10	13	1	2	
Jincheng anthracite char	FBR	850	--	200[b]	36	27	3	4	1	2	
BP1300 (CB)	FBR	850	20[b]	144 h^{-1}	--	42	--	15	6.5	--	Lázaro, et al., 2008
BP2000(CB)	FBR	850	20[b]	144 h^{-1}	--	17	--	12	6.5	--	

(FBR, fixed bed reactor; FlBR, fluidized bed reactor; CFR, continuous flow reactor; RBR, rotary bed reactor; MLR, multilayer reactor; T, temperature (°C); F, flow rate ([a]mL/($g_{cat.}$h), [b]mL/min, [c]NmL/min, unless other units are stated); Conversion (%); t, time (h); d, complete deactivation (h); --, not mentioned in the original paper)

Table 2.7 comprises initial and final activity as well as the stability of various metal, metal doped carbon, and carbonaceous catalysts under diverse experimental parameters and reactors. Those prior study results are also revealing that metal catalyst maintain high activity and conversion rate, but undergo drastic deactivation with time, which is clear from the experimental data furnished in Table 2.7. However, carbonaceous catalysts and metal doped carbon catalysts hold better stability and lower deactivation rate compared to metal catalysts. Despite of better stability of carbonaceous catalysts, unfortunately give poorer methane conversion than metal catalysts. In addition, metal catalysts offers very reactive CNTs (Nazim Muradov et al., 2006), carbon filaments (K. K. Lee et al., 2004) or nanocarbons showing properties of molecular sieves (de la Casa-Lillo et al., 2002), while, carbonaceous catalysts produce amorphous carbon having a variety of morphology.

CHAPTER 3: MATERIALS AND METHODS

3.1 INTRODUCTION

Experimental section is comprised of four parts with each part incorporating a specific subject of study:-

- Part 1 :

  Stabilization of Ni, Fe, and Co nanoparticles through modified Stöber method to obtain excellent catalytic performance: Preparation, characterization, and catalytic activity for methane decomposition.

- Part 2 :

  Probing the differential methane decomposition behaviors of *n*-NiO/SiO_2, *n*-FeO/SiO_2, and *n*-CoO/SiO_2 catalysts prepared through co-precipitation cum modified Stöber method.

- Part 3 :

  Methane decomposition kinetics and reaction rate over *n*-NiO/SiO_2 catalyst.

- Part 4 :

  Governance of porosity and methane decomposition activity sustainability of *n*-NiO/SiO_2 catalyst by changing synthesis parameters.

3.2 PART 1: STABILIZATION OF Ni, Fe, AND Co NANOPARTICLES THROUGH MODIFIED STÖBER METHOD TO OBTAIN EXCELLENT CATALYTIC PERFORMANCE: PREPARATION, CHARACTERIZATION, AND CATALYTIC ACTIVITY FOR METHANE DECOMPOSITION.

Nanoparticle formation from their respective precursors through bottom-up method is a very fascinating practice in nanotechnology. The research contribution in Part 1 discusses two promising bottom-up methods: i) controlled precipitation of Ni, Fe, and Co nanoparticles and reinforcement with silicate through modified Stöber method and ii) the preliminary methane decomposition activity of produced catalysts for the production of nanocarbon and hydrogen.

3.2.1 Materials

Nickel (II) Nitrate Hexahydrate ($Ni(NO_3)_2.6H_2O$), Cobalt (II) Nitrate Hexahydrate ($Co(NO_3)_2.6H_2O$), and Octadecyl trimethoxy silane (C18TMS) were purchased from Acros Organics. Iron (III) nitrate nonahydrate ($Fe(NO_3)_3.9H_2O$) and Tetraethyl orthosilicate (TEOS) were purchased from Aldrich and used as such. NH_3 solution and ethanol bought from R&M solutions. 99.999% hydrogen, 99.995% methane, and 99.99% nitrogen were purchased from Linde Malaysia Sdn. Bhd.

3.2.2 Experimental Section

Co-precipitation method was adopted for preparing fine nano-sized metal hydroxide precipitate and those hydroxides were effectively supported with silicate. Initially, nano-sized M-OH containing suspension was prepared by treating metal nitrate with ammonia solution at room temperature. Hence, agglomeration of metal oxides at comparatively higher temperature was effectively eluded. The SiO_2 support was fabricated through modified Stöber method. It involves the hydrolysis of a mixture of tetraethylorthosilicate (TEOS) and Octadecyl trimethoxy silane (C18TMS) with aqueous solution of ammonia in the suspension of nano-M-OH.

3.2.2.1 Preparation of *n*-NiO, *n*-FeO, and *n*-CoO nano-particles through co-precipitation

Nanosized metal hydroxide suspension was prepared through co-precipitation by treating the respective metal nitrate solution with ammonia. Nickel (II) nitrate hexahydrate, iron (III) nitrate nonahydrate, and cobalt (II) nitrate hexahydrate were used as precursors for *n*-NiO, *n*-FeO, and *n*-CoO, respectively. First, 0.02 mole metal nitrate was homogeneously dissolved in 200 mL of water through sonication using Sonics Vibra Cell (model CV33). Metal hydroxide was precipitated by drop-wise addition of 6 mL of 30% NH_3 solution under sonication for 1 h. The resulting suspension was stirred for another 1 h with a magnetic stirrer at room temperature. The precipitated metal hydroxide was acquired by centrifugation at 4000 rpm for 30 min. Sigma Laborzentrifugen 2-15 was used for centrifugation. The precipitate was thoroughly washed with distilled water and ethanol and then dispersed in 100 mL of ethanol and continuously stirred for 15 h with magnet. The metal hydroxide precipitate was collected through centrifugation and dried at 100 °C for 15 h under air circulation. The dried sample was calcined at 350 °C for 3 h to convert metal hydroxides into metal oxides. The produced samples were named accordingly as *n*-NiO, *n*-FeO, and *n*-CoO.

3.2.2.2 Stabilization of nanometal oxides using silicate through the modified Stöber method

Nanometal oxide particles were stabilized using the modified Stöber method (Stöber et al., 1968), which involves hydrolysis of a mixture of tetraethylorthosilicate (TEOS) and octadecyl trimethoxy silane (C18TMS) with aqueous solution of ammonia in nano M-OH suspension. The M-OH dispersion in ethanol was prepared as described above in the co-precipitation of metal hydroxides. A total of 4 mL of 8M NH_3 solution was added to the M-OH dispersion in ethanol and sonicated for 10 min. Afterward, 0.4 mL of TEOS and 0.4 mL of C18TMS were simultaneously added to the dispersion while

sonicating. The use of alcoholic medium can reduce the agglomeration of particles and formation of free silicates (Stjerndahl et al., 2008; Zou et al., 2014). No surfactant was added during the preparation. C18TMS was added to the reaction mixture to increase the porosity of SiO_2 support. Sonication was further continued for 1 h, and the reaction mixture was stirred with magnet for another 5 h. The precipitate was separated through centrifugation and dried in an oven at 100 °C for 15 h under air circulation. The dried product was calcined at 450 °C for 3 h to produce metal oxide/silica nanostructures by removing all organic moieties. The added C18TMS helped to sparse silica polymerization and produced numerous pores inside the silica network after calcination. The produced samples were named as *n*-NiO/SiO_2, *n*-FeO/SiO_2, and *n*-CoO/SiO_2. Catalyst preparation is schematically shown in Figure 3.1.

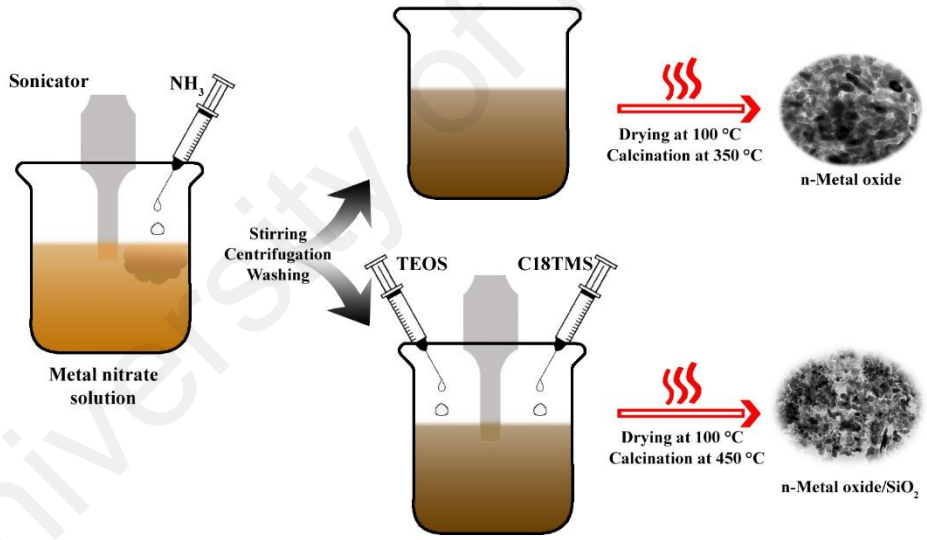

Figure 3.1 Schematic representation of the synthesis of nano-metal oxides and nano-metal oxide/silicates.

3.2.2.3 Characterization techniques

Investigation of physicochemical properties of the catalyst done by means of different characterization methods such as N_2 adsorption-desorption measurement, X-ray diffraction (XRD), transmission electron microscopy (TEM), field emission scanning

electron microscopy (FESEM), Energy-dispersive X-ray spectroscopy (EDX), and hydrogen temperature programmed reduction (H_2-TPR).

a) Nitrogen adsorption–desorption analysis

Nitrogen adsorption‑desorption measurements (BET method) were carried out in Micromeritics ASAP 2020 BET apparatus at -196 °C. Surface area, pore size distribution and structure, pore volume, and the mean particle size were measured. Samples were previously degased using N_2 at 180 °C for 4 h. The surface area was determined according to the standard Brunaur–Emmett–Teller (BET) method in a relative pressure range of 0.04–0.2 and the total volume was evaluated from the amount of adsorbed N_2 at a relative pressure (P/P_0) of about 0.98. The pore diameter distributions were calculated based on desorption isotherms by the Barrett–Joyner–Halenda (BJH) method.

b) X-ray diffraction

X-ray diffraction (XRD) patterns of the fresh and spent catalysts were collected at room temperature in PANalytical diffractometer to determine the crystal phase and structure of the metal oxides. The evaluation of the diffractograms was made by X'pert HighScore software. The intensity was measured by step scanning in the 2θ range of 8‑80° with a step of 0.026° and a scan rate of 0.0445°/s. The average crystallite size was obtained using the global Scherrer equation as follows:

$$D_{avg} = \frac{0.9\lambda}{\beta cos\theta}\left(\frac{180}{\pi}\right) \qquad (3.1)$$

In equation, the average crystallite size, peak length, line broadening full width at half-maxima after subtracting the instrumental line broadening (in radians), and the Bragg's angle are expressed as D_{avg} (nm), λ (1.54056 Å), β, and 2θ, respectively. 0.9 is the Scherrer constant.

c) Transmission electron microscopy, Field emission scanning electron microscopicy and Energy-dispersive X-ray spectroscopy

Transmission electron microscopy (TEM) images of fresh catalyst and produced nanocarbon were acquired by using FEI Tecnai™ controlled at an accelerating voltage of 200 keV. The samples were first dispersed in ethanol with ultrasonic treatment. A drop of the prepared suspension was vaporized onto an electron carbon supported 300 mesh copper grid for TEM image capturing.

Field emission scanning electron microscopic (FESEM) images of produced nanocarbon and elemental composition of the catalysts were obtained with FEG Quanta 450, EDX-OXFORD.

d) Temperature-programmed reduction

Temperature-programmed reduction (H_2-TPR) measurements were carried out using a Micromeritics TPR 2720 analyzer. Typically, 0.03 g of catalyst sample was placed in a U-tube holder and the sample was first cleaned at 130 °C for 60 min by flushing with helium gas. Upon degassing, the reductive gas mixture consisting of 5% hydrogen balanced with nitrogen at a flow rate of 20 mL/min streamed through the sample. The sample was heated from 200 to 700 °C to obtain the TPR profiles of the sample.

3.2.2.4 Preliminary catalytic activity analysis

A fixed catalyst bed pilot plant constructed with stainless steel was used for conducting temperature-programmed methane decomposition (TPMD). A quartz frit with 150–200 µm porosity was used as catalyst bed. About 1 g of the catalyst was homogeneously distributed over the catalyst bed, and nitrogen was purged with a flow rate of 1 L/min for 30 min at room temperature to clean the furnace and the catalyst. The bed temperature was increased to 550 °C with a ramp of 20 °C/min, and 30% H_2 balanced with N_2 was passed for 2.5 h to reduce the metal oxide catalyst to its metallic form. After

completing the reduction stage, the furnace temperature was decreased to 200 °C by using an air cooler under N_2 flow. Subsequently, 99.995% methane was passed with a flow rate of 0.64 L/min for temperature-programmed decomposition from 200 to 900 °C with a ramp of 5 °C/min. The out stream gases were allowed to pass through the filters (38 M membrane, Avenger, USA) to separate solid particles. The mole percentage of gas component in the outstream gas was calculated using the online analyzer Rosemount Analytical X-STREAM (UK).

3.3 PART 2: PROBING THE DIFFERENTIAL METHANE DECOMPOSITION BEHAVIORS OF *n*-NiO/SiO_2, *n*-FeO/SiO_2, AND *n*-CoO/SiO_2 CATALYSTS PREPARED THROUGH CO-PRECIPITATION CUM MODIFIED STÖBER METHOD

In part 2, the as-prepared *n*-NiO/SiO_2, *n*-FeO/SiO_2, and *n*-CoO/SiO_2 nano-catalysts were applied for thermocataltytic decomposition of methane in order to investigate their thermal stability and activity to produce greenhouse gas free hydrogen and nanocarbon. The materials mentioned in 3.2.1 and the catalyst preparation methodology and characterization techniques described in 3.2.2 were the same as those used for the experiments carried out in this part.

3.3.1 Experimental Setup for TCD

Schematic representation of catalytic methane decomposition unit is shown in Figure 3.2. The fixed catalyst bed reactor constructed with stainless steel (SS310S) has the following dimension: outer diameter = 6.03 cm, wall thickness = 0.87 cm, and height = 120 cm. A quartz tube (3.56 cm internal diameter, 4 cm outer diameter, and 120 cm height), obtained from Technical Glass Products (Painesville, USA), was placed inside the reactor in order to avoid interaction of feed gas with stainless steel. A quartz frit with 150 µm to 200 µm porosity was used as the catalyst bed. The upward movement of the bed was constrained with silica ball of height ~6 cm inserted above it. Temperature was

supplied with a vertically mounted, three-zone tube furnace (model TVS 12/600, Carbolite, UK).

Temperature measurements were recorded by using two K-type thermocouples (1/16 in diameter, Omega, USA). The first thermocouple was fixed on the exterior surface of the stainless steel tube. The second thermocouple was inserted into the quartz tube momentarily for calibration and removed afterward from the quartz tube prior to testing because its internal copper material could affect the TCD of methane (Al-Hassani et al., 2014). In addition, pressure and temperature indicators were placed at different locations to control the operating conditions.

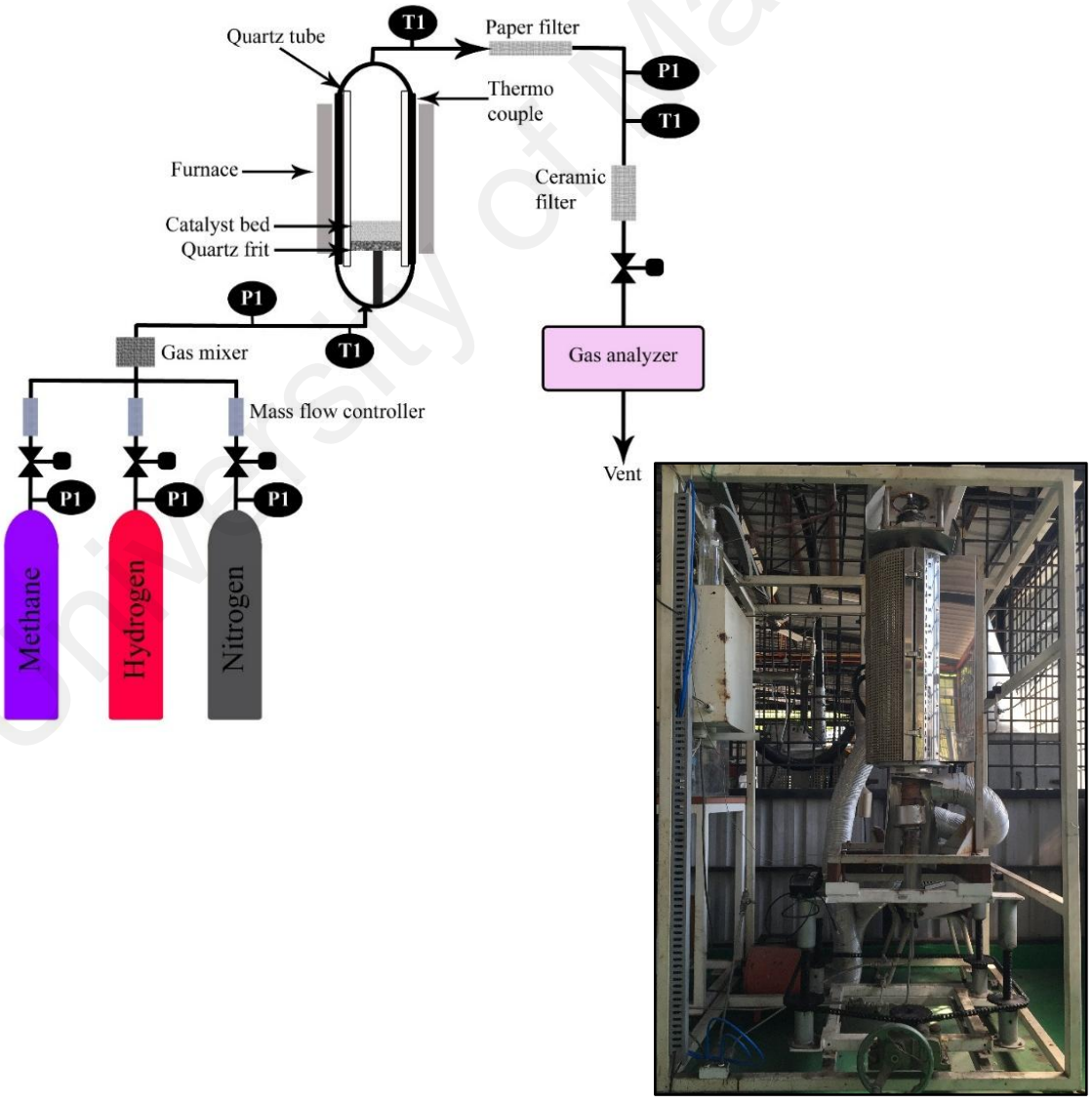

Figure 3.2. Simplified schematic visualization and photograph of methane decomposition unit.

A two-differential pressure transducer (0" H_2O to 4" H_2O) was supplied by Sensocon to measure the pressure drop across the reactor. Mass flow controllers (Dwyer, USA) in the range of 0‑2 L/min were used to control the gas flow rates. The outflow gas was then cooled down to room temperature by means of an air cooler. Solid particles that had sizes greater than 2 nm and high molecular weight components were separated using two filters (38 M membrane, Avenger, USA). A calibrated Rosemount Analytical X-STREAM (UK) was used as an online analyzer to compute the mole percentage of methane and hydrogen in the effluent gas stream. The gas analyzer was calibrated using certified gases of nitrogen, methane, and hydrogen, and the accuracy of these measurements was tested using blended gas mixtures. The lowest methane and hydrogen measuring range that can detected by the gas analyzer is 0 – 1000 ppm and 0–2%, respectively, while the highest measuring value is 100% for both gases.

3.3.2 Thermocatalytic Decomposition of Methane

Catalyst bed was uniformly covered with 0.5 g of catalyst. Pure nitrogen was passed for 30 min in order to clean the furnace and catalyst at flow rate of 1 L/min. Then, the system temperature was increased to 550 °C with a ramp of 20 °C/min. Reduction of catalyst was conducted at 550 °C by passing 30% H_2 in N_2 feed for 2.5 h. Then, increase/decrease the temperature to reaction temperature under N_2 flow, accordingly. Based on the results of TPMD, TCD experiments were conducted for detailed catalysis evaluation at temperatures like 500, 600, and 700 °C. Once destination temperature reached, N_2 flow was replaced with 99.995% methane with a flow rate of 0.64 L/min for evaluating methane conversion. The effect of methane feed flow rate on hydrogen production in percentage with time on stream was also studied. Flow rates like 0.64, 1.07, and 1.43 L/min were analyzed at 550 °C over 0.5 g of catalyst.

3.4 PART 3: METHANE DECOMPOSITION KINETICS AND REACTION RATE OVER *n*-NiO/SiO_2 CATALYST

Kinetic analysis is an important aspect in any catalysis process. Kinetic studies are chemical steps performed in order to find a model that describes the rate of reaction and defines the chemical process. In part 3, experimentation was conducted to assess the catalytic activity of *n*-NiO/SiO_2 catalyst with methane partial pressure for the purpose of studying the methane decomposition kinetics and reaction rate at a temperature range of 550 to 650 °C.

3.4.1 Materials

Precursors for the preparation of catalyst are the same as mentioned in 3.2.1. Methane cylinders with partial pressure of 0.2, 0.4, 0.6, and 0.8 atm was purchased from Linde Malaysia Sdn. Bhd. 99.99% nitrogen was used for flushing the reactor and the catalyst reduction was done using 99.999% hydrogen.

3.4.2 Experimental Setup

The TCD experiment was conducted in a fixed catalyst bed reactor built with stainless steel material. The experimental setup described in 3.3.1 was used for TCD analysis. The required amount of catalyst, as shown in Table 3.1, was uniformly distributed over catalyst bed. Nitrogen was purged with a flow rate of 1 L/min for 30 min at room temperature to clean the furnace and the catalyst. The bed temperature was increased to 550 °C with a ramp of 20 °C/min, and 30% H_2 balanced with N_2 was passed for 2.5 h to reduce the metal oxide catalyst to its metallic form. The reactor temperature was increased to the TCD temperature, accordingly, under N_2 flow. Subsequently, the reaction commenced with the flow of 0.64 L/min of the CH_4/N_2 mixture over the catalyst bed with varying amounts of methane (20%, 40%, 60%, and 80%) at a set temperature. Experiments was conducted at 550, 600, and 650 °C. The mole percentage of methane

and hydrogen in the out stream was recorded in a calibrated Rosemount Analytical X-STREAM (UK) online analyzer. As-produced nanocarbons were studied with TEM and XRD.

Table 3.1 The experimental conditions for kinetic study.

No.	Weight (g)	Temperature (°C)	P_{CH4} (atm)
1	0.6	650	0.2
2	0.6	650	0.4
3	0.6	650	0.6
4	0.6	650	0.8
5	0.6	600	0.2
6	0.6	600	0.4
7	0.6	600	0.6
8	0.6	600	0.8
9	0.6	550	0.2
10	0.6	550	0.4
11	0.6	550	0.6
12	0.6	550	0.8

3.5 PART 4: GOVERNANCE OF POROSITY AND METHANE DECOMPOSITION ACTIVITY SUSTAINABILITY OF *n*-NiO/SiO_2 CATALYST BY CHANGING SYNTHESIS PARAMETERS

In this part, an in-depth study on the variance of physicochemical characteristics and methane decomposition activity and sustainability of *n*-NiO/SiO_2 catalysts with different preparation parameters are discussed. Influence of nickel/silicate ratio, C18TMS/TEOS ratio and different solvents were investigated. The materials mentioned in 3.2.1 were the same as those used for the experiments carried out in this part.

3.5.1 Synthesis of *n*-NiO/SiO_2 catalysts through co-precipitation cum modified Stöber method

Co-precipitation cum modified Stöber method was adopted for preparing fine nano-powder of nickel supported with silicate (Stöber et al., 1968). It is a compiling of M-OH precipitation and SiO_2 support formation over precipitated M-OH consecutively. Appropriate amount of $Ni(NO_3)_2.6H_2O$ was accurately weighed and dissolved in 200 mL of deionized water under sonication. The quantity of each substrate for the production of nano-catalysts and corresponding naming are furnished in Table 3.2. Dissolved metal nitrate was allowed to precipitate corresponding hydroxide by the drop-wise addition of 20 mL of 30% NH_3 solution under sonication for 1 h. The temperature rise during sonication was controlled with an ice bath. Consequently, resulting $Ni(OH)_2$ suspension was stirred for another 1 h with magnet at room temperature. Subsequently, nano-sized $Ni(OH)_2$ was separated by centrifugation at 4000 RPM for 30 min and washed twice with water and once with corresponding solvent, as indicated in Table 3.2.

The separated product was, then, dispersed in 100 mL of corresponding solvent and stirred constantly for 15 h with magnet. Successively, 4 mL of 8M NH_3 solution was added to the dispersion under sonication. Proper quantity of TEOS and C18TMS

simultaneously added to the basic dispersion under sonication in order to form silicate support to guard active metal phase, named modified Stöber method. Sonication was further continued for 1 h, and the reaction mixture was stirred with magnet for another 5 h. Subsequently, $Ni(OH)_2/SiO_2$ precipitate was separated by centrifugation and dried in an oven at 100 °C for 15 h. Dried $Ni(OH)_2/SiO_2$ precipitate was calcined at 450 °C in a programmable furnace at the rate of 10 °C/min and allowed to stay for 3 h. The calcination converted hydroxide to *n*-NiO/SiO_2. Finally, *n*-NiO/SiO_2 nano-catalysts were reduced to *n*-Ni/SiO_2 by treating with 30% H_2 for 2.5 h, just before the activity examination in methane decomposition unit.

Table 3.2 The quantity of each substrates and the solvents used for the production of *n*-NiO/SiO_2.

No.	Catalyst	$Ni(NO_3)_2.6H_2O$ (g)	TEOS (mL)	C18TMS (mL)	Solvent
1	*n*-NiO/SiO_2_(1)	5.81	0.3	0.3	Ethanol
2	*n*-NiO/SiO_2_(2)	11.63	0.6	0.6	Ethanol
3	*n*-NiO/SiO_2_(3)	17.45	1.2	1.2	Ethanol
4	*n*-NiO/SiO_2_(4)	17.45	0.6	0.6	Ethanol
5	*n*-NiO/SiO_2_(5)	17.45	0.3	0.3	Ethanol
6	*n*-NiO/SiO_2_(6)	17.45	1.2	0	Ethanol
7	*n*-NiO/SiO_2_(7)	17.45	0	1.2	Ethanol
8	*n*-NiO/SiO_2_(8)	17.45	0.9	0.3	Ethanol
9	*n*-NiO/SiO_2_(9)	17.45	0.3	0.9	Ethanol
10	*n*-NiO/SiO_2_(10)	17.45	0.6	0.6	Methanol
11	*n*-NiO/SiO_2_(11)	17.45	0.6	0.6	2-Propanol
12	*n*-NiO/SiO_2_(12)	17.45	0.6	0.6	n-Butanol

The characterization techniques described in 3.2.2 were the same as those used for the experiments carried out in this part.

3.5.2 Thermocatalytic decomposition of methane

The experimental setup described in 3.3.1 was used for TCD analysis in this part. TPMD was conducted using 0.5 g of catalyst to identify the catalytically active temperature zone of each catalysts. After identifying the active temperature zone, TCD was conducted at 625 °C over each catalysts with a methane feed flow of 0.64 L/min. The experimental methodology is the same as described in 3.3.2.

CHAPTER 4: RESULTS AND DISCUSSION

4.1 PART 1: STABILIZATION OF Ni, Fe, AND Co NANOPARTICLES THROUGH MODIFIED STÖBER METHOD TO OBTAIN EXCELLENT CATALYTIC PERFORMANCE: PREPARATION, CHARACTERIZATION, AND CATALYTIC ACTIVITY FOR METHANE DECOMPOSITION.

4.1.1 X-Ray Diffraction Analysis

Figure 4.1 shows the XRD patterns of the calcined *n*-NiO, *n*-NiO/SiO_2, *n*-FeO, *n*-FeO/SiO_2, *n*-CoO, and *n*-CoO/SiO_2 nanostructures. The crystalline size and plane that correspond to each peak according to the Scherrer equation are provided in Table 4.1. The crystallite size calculated from XRD approve the mean particle size obtained from N_2 adsorption–desorption analysis (furnished in Table 4.2). The crystalline structure and phase purity were analyzed using XRD patterns. The catalyst performance and its longevity are strongly influenced by the degree of structural order.

The XRD patterns for *n*-NiO and *n*-NiO/SiO_2 [Figure 4.1 (a)] exhibit three major diffraction peaks, which correspond to (111), (200), and (220) solid reflections. The patterns also include (311) and (222) reflections. The diffraction peaks for *n*-NiO centered at 2θ = 37.20°, 43.47°, 62.75°, 75.43°, and 79.39° with corresponding *d*-spacing values of 2.414, 2.079, 1.479, 1.259, and 1.205 Å, respectively. The positions of diffraction peaks in the *n*-NiO catalyst are in good agreement with those given in JCPDS No. 00-047-1049 for cubic NiO phase. On the contrary, the diffraction peaks of *n*-NiO slightly varied after the addition of silicate, and the revised peaks are in good agreement with cubic NiO (JCPDS No. 01-073-1523). The diffraction peaks are centered at 2θ = 37.22°, 43.27°, 62.84°, 75.36°, and 79.36°, with *d*-spacing values of 2.415, 2.090, 1.477, 1.260, and 1.206 Å, respectively. It is obvious from the XRD patterns that the peaks for silicate-

supported NiO are broader than that of pure *n*-NiO peaks, indicating its smaller crystalline size after being supported with SiO_2.

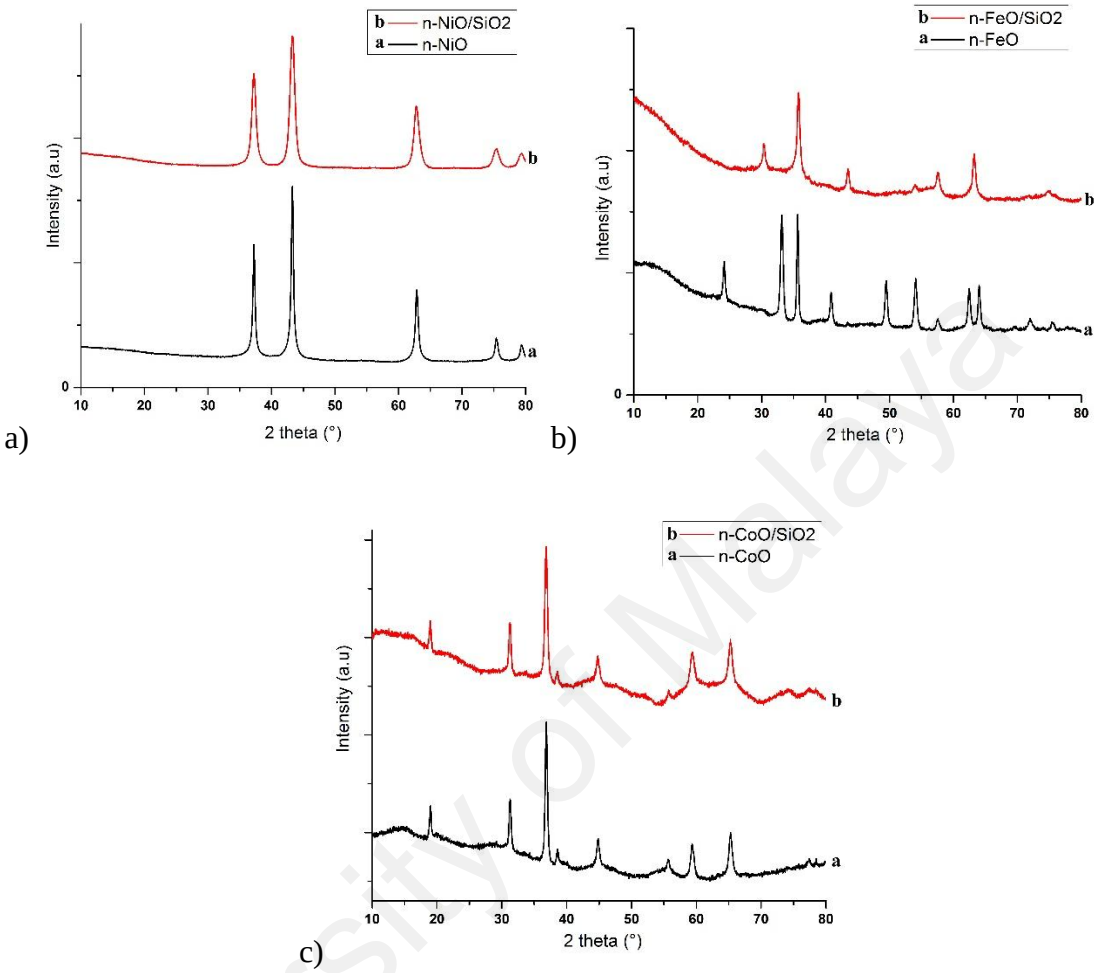

Figure 4.1 XRD patterns of a) *n*-NiO and *n*-NiO/SiO_2, b) *n*-FeO and *n*-FeO/SiO_2, and c) *n*-CoO and *n*-CoO/SiO_2.

These results are clearly supported by the BET mean particle sizes shown in Table 4.2, whereas variations in the XRD and BET values of naked metal oxides are explained in Figure 4.3. Furthermore, silicate addition slightly reduced the intensity of NiO peaks. *n*-FeO exhibited various crystal planes, as shown in Figure 4.1 (b). The major planes are as follows: (012), (104), (110), (024), (116), (214), and (030), with XRD peaks centered at $2\theta = 24.10°$, 33.16°, 35.61°, 49.47°, 54.08°, 62.43°, and 64.01°, respectively, and the corresponding *d*-spacing values for the *n*-FeO peaks are 3.692, 2.701, 2.521, 1.842, 1.695, 1.487, and 1.454 Å, respectively. The planes and peak positions for *n*-FeO

are in good agreement with hematite Fe_2O_3 (JCPDS No. 98-015-4190), which is converted into Fe_3O_4 magnetite after being supported with silicate under high-temperature calcination. *n*-FeO/SiO_2 exhibits peaks at 2θ = 30.35°, 35.78°, 43.52°, 53.97°, 57.56°, 63.32°, and 74.76°, with *d*-spacing values of 2.994, 2.509, 2.079, 1.698, 1.601, 1.470, and 1.269 Å, respectively. These diffraction peaks are similar to that of JCPDS No. 01-075-0449. The 2θ position of *n*-CoO nanoparticles are located at 18.97°, 31.36°, 36.88°, 38.59°, 44.85°, 55.72°, 59.37°, and 65.31°, with *d*-spacing values of 4.676, 2.850, 2.437, 2.333, 2.020, 1.649, 1.556, and 1.428 Å, respectively.

Table 4.1 Major crystal planes and their corresponding crystallite sizes of naked and silicate supported Ni, Fe, and Co nanoparticles from XRD analysis.

Sample	Plane/(nm)	Plane/(nm)	Plane/(nm)	Avg. (nm)
n-NiO	(111)/30.91	(200)/32.89	(220)/39.46	34.42
n-NiO/SiO_2	(111)/33.25	(200)/31.74	(220)/31.19	32.06
n-FeO	(104)/24.18	(110)/42.6	(116)/26.02	30.93
n-FeO/SiO_2	(220)/36.04	(311)/32.19	(440)/20.01	29.41
n-CoO	(022)/37.45	(113)/26.31	(044)/24.09	29.28
n-CoO/SiO_2	(220)/30.65	(311)/26.31	(440)/24.08	27.01

The XRD patterns of *n*-CoO [Figure 4.1 (c)] are similar to that of cubic $Co_{2.84}O_4$ (JCPDS No. 98-017-3820). The XRD peaks of *n*-CoO also exhibit minor variation upon silicate addition. XRD peaks of silicate supported *n*-CoO centered at 2θ = 18.98°, 31.34°, 36.81°, 38.64°, 44.81°, 55.71°, 59.37°, 65.20°, 74.22°, and 77.28° [Figure 4.1 (c)]. These peaks are similar to those of cubic Co_3O_4 (JCPDS No. 01-074-1657). The XRD peaks of *n*-FeO and *n*-CoO are slightly broader and less intense after being supported with silica. However, the impact is less severe compared with that in *n*-NiO/SiO_2, indicating the

lower interaction of silicate with *n*-FeO and *n*-CoO. The metal oxide phases are generally supposed to establish a sophisticated catalytic condition through their interaction with silicate, which results in active catalytic performance. The absence of specific peaks for silicate may be attributed to its amorphous characteristics.

4.1.2 Porosity Analysis

Porosity analysis on the exposed surfaces of the prepared nanoparticles was conducted using N_2 adsorption–desorption measurements. The corresponding N_2 adsorption–desorption isotherms of *n*-NiO, *n*-NiO/SiO_2, *n*-FeO, *n*-FeO/SiO_2, *n*-CoO, and *n*-CoO/SiO_2 are shown in Figures 4.2 (a–f). The Type IV N_2 adsorption–desorption isotherms of the nanoparticles revealed their mesoporous characteristics. However, the beginning portion of the isotherms analogous to Type I isotherm can be attributed to the presence of low amounts of micropores in the materials. Isotherms of *n*-FeO and *n*-CoO resembles Type II, which can also be reflected in their low surface area. The pore diameter distributions of the samples were obtained from the desorption division of the isotherm and calculated using the BJH method; the results are shown in the Appendix A. The single-point surface area, BET surface area, pore volume, average pore size, and average particle size of the produced nanocatalysts are also presented in Table 4.2.

The single-point surface area, BET surface area, and mesoporous area marginally increased after silicate addition. The single-point surface area of *n*-NiO increased from 62.22 m^2/g to 91.50 m^2/g after being supported with silicate. Similarly, the surface area of *n*-FeO and *n*-CoO increased from 35.13 and 14.29 m^2/g to 97.31 and 48.96 m^2/g, respectively. The enhanced surface area can be attributed to the formed porous protection by TEOS and C18TMS. Furthermore, the BET particle size of the unsupported metal oxides (*n*-NiO = 48.02 nm, *n*-FeO = 85.09 nm, and *n*-CoO = 207.99 nm) marginally decreased after the incorporation of the silicate support. The BET particle

sizes of *n*-NiO/SiO_2, *n*-FeO/SiO_2, and *n*-CoO/SiO_2 are 32.19, 30.26, and 49.92 nm, respectively. This shrinkage of particle size is attributed to the protection of metal oxide particles from agglomeration during high-temperature calcination.

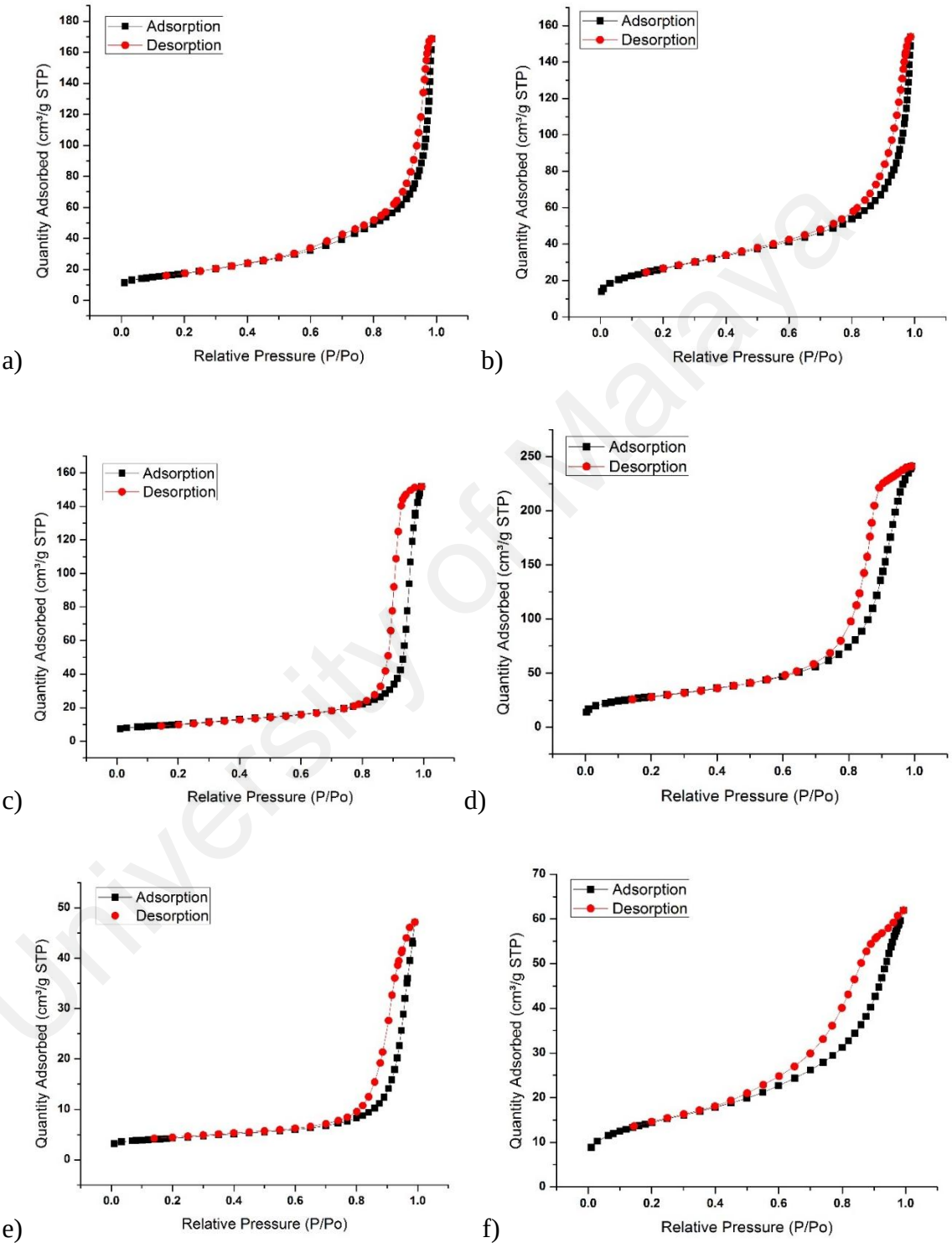

Figure 4.2 N_2-adsorption–desorption isotherms of a) *n*-NiO, b) *n*-NiO/SiO_2, c) *n*-FeO, d) *n*-FeO/SiO_2, e) *n*-CoO, and f) *n*-CoO/SiO_2.

The BET particle size was calculated from the specific surface area by using the equation 4.1 (B. Akbari et al., 2011; Bowen, 2002), assuming that the particles are in a spherical form.

$$\text{BET particle size} = \frac{6000}{(\text{BET surface area}) \times (\text{density})} \qquad (4.1)$$

The BET mean particle size of naked nanometal oxide (Table 4.2) significantly differed from the crystallite size measured from the XRD patterns using the Scherrer equation 3.1 (Table 4.1). However, the BET particle size and XRD crystallite sizes were comparable among silicate-supported metal oxides, which can be explained by the representation of particle size measurement pattern in Figure 4.3.

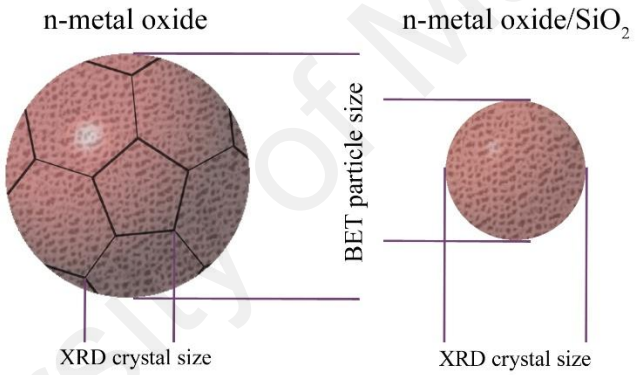

Figure 4.3 Schematic representation of the method for evaluation of XRD crystal size and BET particle size for nano metal oxide before and after silicate support.

Silicate support prevents the agglomeration of individual metal oxide particles and allows the gas to access most surface areas, thus providing actual particle size similar to XRD crystal size (Tables 4.1 and 4.2). These findings reveal that the silicate-supported *n*-NiO and *n*-FeO were formed as single-crystal nanoparticles. However, the particle size of *n*-CoO/SiO_2 is twice higher than its crystal size, which may be attributed to the existence of two crystals in the same particles. The naked *n*-NiO, *n*-FeO, and *n*-CoO exhibited small XRD crystal size and large BET particle size (Tables 4.1 and 4.2). This difference is mainly due to the loss of the surface after agglomeration of primary particles,

as visualized in Figure 4.3. Therefore, these XRD and BET results clearly illustrate the importance of unceasing co-precipitation cum modified Stöber method for preparing silicate supported metal oxide nano particles, which effectively improve the surface area and particle size.

The synthesized silicate-supported metal oxides, regardless of the naked metals used, exhibited catalytic activity enhancing features, such as lower particle size and higher surface area and porosity. The BJH pore-width distributions covered a range of 0–150 nm with Ni- and Co-based nanoparticles (Appendix A) and were extended to 200 nm with Fe-based nanoparticles. This result may be attributed to the presence of unsupported *n*-FeO particles, which underwent agglomeration during calcination under air. However, void formation caused by the contact of inter-nanoparticles also leads to the formation of larger pores. Furthermore, it is worth to note that the BET pore size of *n*-NiO centered at 16.27 nm was reduced to 9.98 nm after being supported with silicate. Similar trends were observed on *n*-FeO and *n*-CoO.

Table 4.2 Physical characteristics of *n*-NiO, *n*-NiO/SiO_2, *n*-FeO, *n*-FeO/SiO_2, *n*-CoO, and *n*-CoO/SiO_2 from N_2 adsorption-desorption analysis.

Catalyst	Single point SA[a] (m^2/g)	BET SA (m^2/g)	Micropore area[b] (m^2/g)	Mesopore + external area[c] (m^2/g)	Micropore volume[d] (cm^3/g)	Mesoporous volume (cm^3/g)	Total pore volume[e] (cm^3/g)	BET pore size (nm)	Mean particle size (nm)
n-NiO	62.22	62.46	5.17	57.28	0.0020	0.2479	0.2499	16.274	48.02
n-NiO/SiO_2	91.50	93.18	5.17	88.01	0.0024	0.2277	0.2301	9.987	32.19
n-FeO	35.13	35.25	7.67	27.57	0.0035	0.2311	0.2346	26.581	85.09
n-FeO/SiO_2	97.31	99.11	7.02	92.08	0.0033	0.3678	0.3712	14.977	30.26
n-CoO	14.29	14.42	5.81	8.61	0.0028	0.0693	0.0721	20.001	207.99
n-CoO/SiO_2	48.96	50.06	7.25	42.80	0.0035	0.0922	0.0957	7.579	49.92

[a] Represents the values calculated at a relative pressure (P/P_o) of N_2 equal to 0.301.
[b-d] Represents the values calculated from *t*-plot method.
[e] Represents the total pore volume evaluated from nitrogen uptake at a relative pressure (P/P_o) of N_2 equal to 0.98

4.1.3 Morphology and Composition Analysis

TEM images of the produced *n*-NiO, *n*-NiO/SiO_2, *n*-FeO, *n*-FeO/SiO_2, *n*-CoO, and *n*-CoO/SiO_2 are shown in Figures 4.4 (a–f), respectively. The morphological illustration of the prepared nanoparticles revealed their uniform distribution, and the particles presented different shapes.

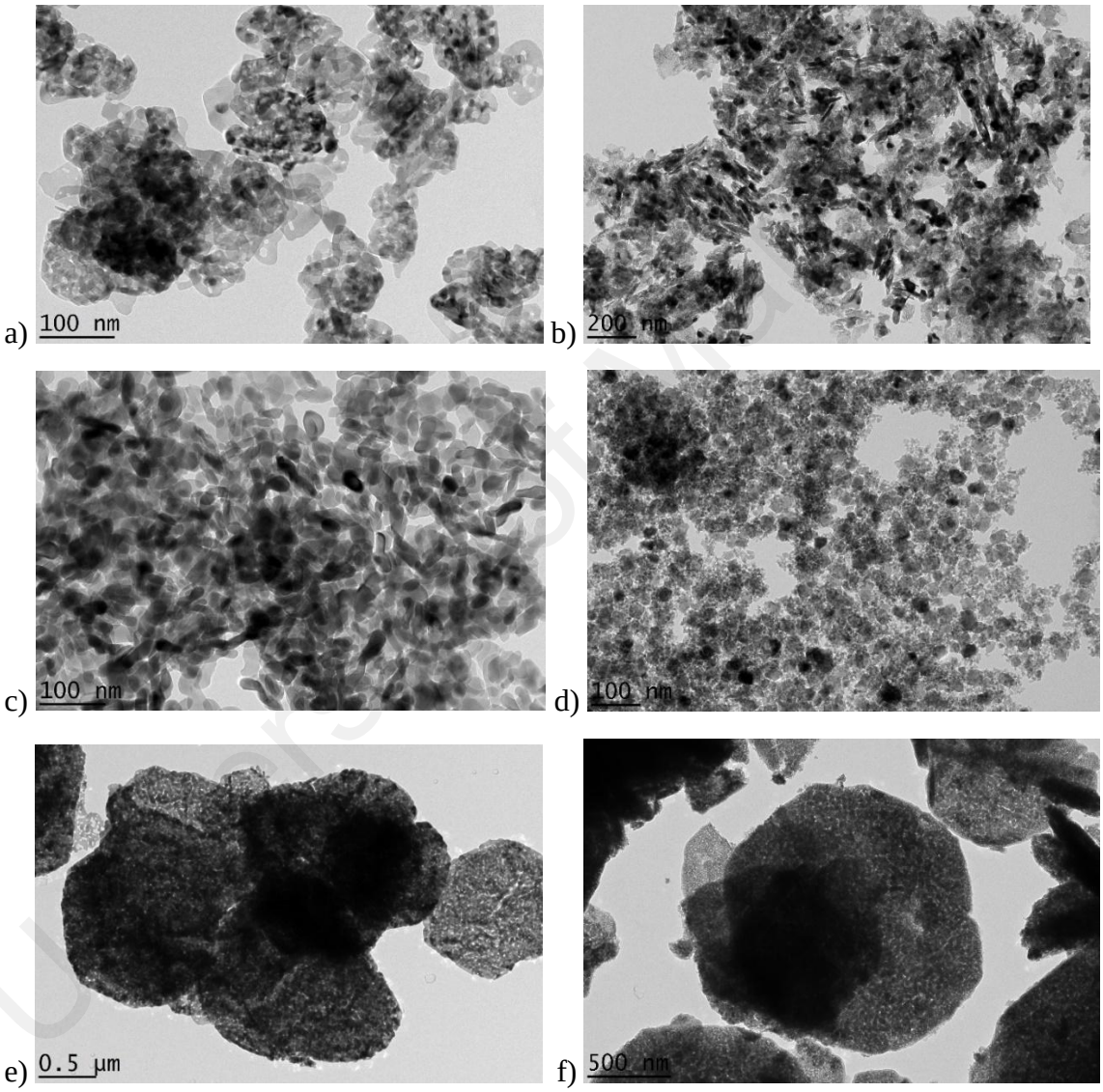

Figure 4.4 TEM images of a) *n*-NiO, b) *n*-NiO/SiO_2, c) *n*-FeO, d) *n*-FeO/SiO_2, e) *n*-CoO, and f) *n*-CoO/SiO_2.

Electron transmission investigation showed large particles with smooth external surfaces and edges for *n*-NiO and *n*-FeO before being supported with SiO_2 [Figures 4.4 (a and c)]. After supporting with silicate, the *n*-NiO and *n*-FeO particles exhibited

relatively rough morphology with smaller size [Figures 4.4 (b and d)]. However, sharpness variation is not dominant in Co nanoparticles after silicate incorporation [Figures 4.4 (e and f)]. Decrease in size observed with particles is in good agreement with the BET (Table 4.2) and XRD (Figure 4.1 and Table 4.1) results. The elemental composition and mapping of the external surface of the naked and silicate-supported nanoparticles are shown in Figures 4.5 (a-f). The peaks for Ni, Fe, Co, Si, and O elements were observed. Weight and atomic percentage of each element were visible in the table near the mapping [Figures 4.5 (a-f)]. The quantities of Ni, Fe, and Co decreased after adding TEOS and C18TMS, whereas Si and O percentage increased accordingly.

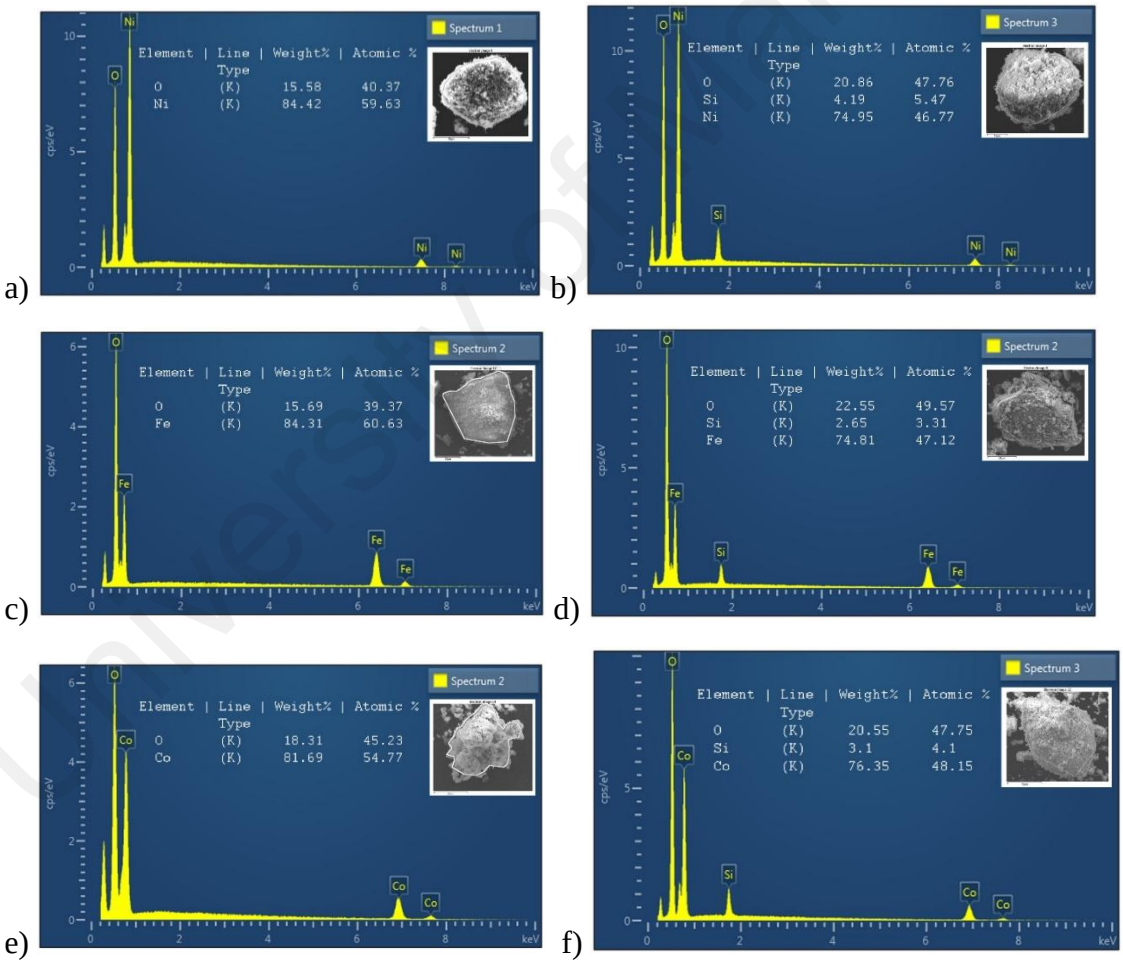

Figure 4.5 EDX mapping and elemental composition of a) *n*-NiO, b) *n*-NiO/SiO_2, c) *n*-FeO, d) *n*-FeO/SiO_2, e) *n*-CoO, and f) *n*-CoO/SiO_2.

4.1.4 Reduction Behavior

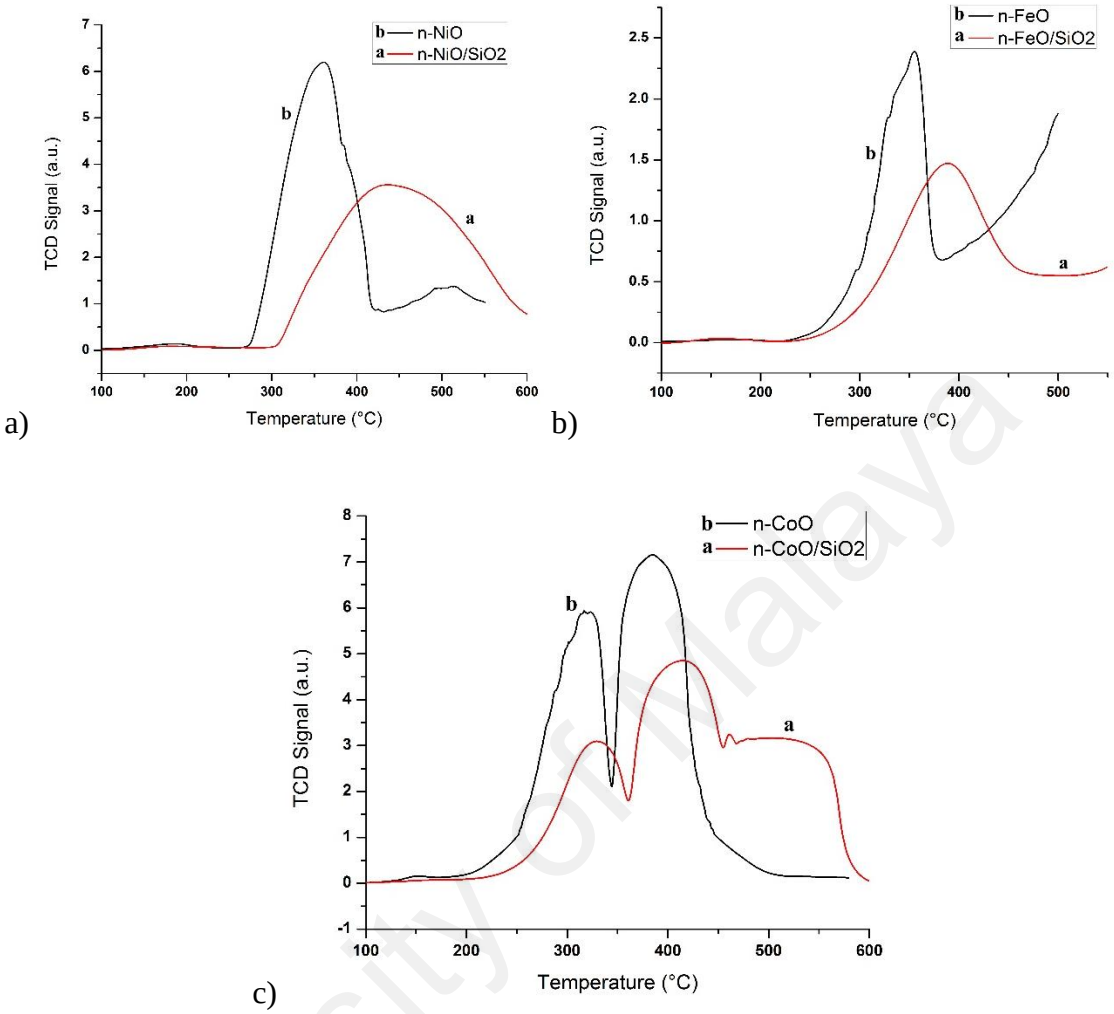

Figure 4.6 H_2-TPR profile of a) *n*-NiO and *n*-NiO/SiO_2, b) *n*-FeO and *n*-FeO/SiO_2, and c) *n*-CoO and *n*-CoO/SiO_2.

The H_2-TPR profiles of *n*-NiO, *n*-NiO/SiO_2, *n*-FeO, *n*-FeO/SiO_2, *n*-CoO, and *n*-CoO/SiO_2 are displayed in Figures 4.6 (a–c). The H_2-TPR profile of *n*-NiO displayed a single peak similar to the *n*-NiO/SiO_2 peak, thereby implying the complete transformation of NiO into metallic Ni. NiO reduction became more complicated after supporting with silicate because of the interaction between metal phase and silicate support. Therefore, the reduction peak shifted toward high temperatures. According to the literature, NiO reduction occurred between 300 and 600 °C (X. Chen et al., 2013; X.-K. Li et al., 2005). As shown in Figure 4.6 (a), the peak corresponding to *n*-NiO reduction was found

between 276 and 422 °C with the maximum peak at 361 °C. However, the single peak exhibited by *n*-NiO/SiO_2 was detected between 297 and 670 °C with the maximum peak at 420 °C; this finding indicates the homogeneous metal support interaction, as supported by previous records (L. Li et al., 2012; L. Li et al., 2012(b)). The main peak can be attributed to the $Ni^{2+} \rightarrow Ni^0$ transition. The difference between the beginning of the reduction peak for naked (276 °C) and supported (297 °C) *n*-NiO reveals the uniform distribution of silicate and the absence of unsupported NiO after silicate formation. Furthermore, analysis with ChemiSoft TPx V1.02 software showed that hydrogen conception values of 282.82 and 330.3 mL/g_{cat} for *n*-NiO and *n*-NiO/SiO_2, respectively. In addition, the reduction peak of *n*-NiO/SiO_2 is broader than that of the reported Ni/SiO_2 catalyst prepared using conventional methods, specifying the strong interaction between the metal and the support (L. Li, He, et al., 2012; Xie et al., 2011). Similarly, *n*-FeO and *n*-FeO/SiO_2 also exhibited a single peak below 450 °C [Figure 4.6 (b)]. The reduction peak for *n*-FeO started at 257 °C and end at 378 °C with the maximum hydrogen conception at 355 °C, whereas the peak for *n*-FeO/SiO_2 ranged from 264 to 448 °C. Peaks below 450 °C may be attributed to the conversion of hematite (Fe_2O_3) → (magnetite) Fe_3O_4 (X. Chen et al., 2013; Jung & Thomson, 1991), supporting the XRD results [Figure 4.1 (b)]. Furthermore, the formation of a second peak starting at 380 and 525 °C for *n*-FeO and *n*-FeO/SiO_2, respectively, may be attributed to the complete reduction of Fe_2O_3 to metallic Fe. Generally, the formation of metallic Fe from Fe_3O_4 through FeO formation occurred between 520 and 680 °C (X. Chen et al., 2013; Yang et al., 2006; C.-H. Zhang et al., 2006). The reduction profile of *n*-FeO showed two minor shoulders before the highest reduction peak at 300 and 342 °C, irrespective of the smooth profile of *n*-FeO/SiO_2. However, only one peak was seen in their reduction. This was attributed to the temperatures at which changes between oxidation states ($Fe_2O_3 \rightarrow Fe_3O_4 \rightarrow FeO \rightarrow Fe$) occurred were very close to each other. *n*-CoO exhibited a reduction peak from 215 to

443 °C with two peaks, whereas *n*-CoO/SiO_2 exhibited peaks between 223 and 587 °C. The reduction of Co_3O_4 to metallic Co transformed through CoO formation (P. Jana et al., 2012). The distinct peak observed with *n*-CoO and *n*-CoO/SiO_2 may be because of the distinguishable temperatures at which oxidation state changes ($Co_3O_4 \rightarrow CoO \rightarrow Co$) occurred. The reduction peak for *n*-FeO/SiO_2 and *n*-CoO/SiO_2 are broader than that for *n*-CoO and *n*-FeO, indicating the difficulty in reduction after silicate formation. However, *n*-FeO/SiO_2 and *n*-CoO/SiO_2 did not show any peaks above 600 °C because of the weaker metal support interaction than that of *n*-NiO/SiO_2 (Lund & Dumesic, 1981). Furthermore, the reduction peak of *n*-CoO, *n*-FeO, and their silicate-supported samples started almost at the same temperature, which may be attributed to the presence of free metal oxide particles even after silicate support. On the contrary, the silicate-supported *n*-NiO started to reduce at high temperature compared with naked *n*-NiO, validating the complete silicate protection over *n*-NiO nanoparticles after applying the modified Stöber method.

4.1.5 Temperature Programmed Methane Decomposition

The catalytically active temperature zones of the prepared catalysts were estimated by temperature-programmed methane decomposition, and the results are displayed in Figure 4.7. 99.995% methane was purged with a flow rate of 0.64 L/min over 1 g of the reduced catalyst to conduct TPMD from 200 to 900 °C with a temperature ramp of 5 °C/min. Only hydrogen and methane were detected as gaseous products by using Rosemount Analytical X-STREAM, as indicated in the balanced methane decomposition equation 1.1 ($CH_4 \rightarrow 2H_2 + C$).

Figure 4.7 clearly shows that the methane decomposition starts above 880 °C in the absence of any catalyst. However, *n*-NiO and *n*-CoO reduced the decomposition temperature to 700 °C, and the conversion percentage increased with increasing temperature, supporting the endothermic behavior of methane decomposition.

Furthermore, the silicate support on *n*-NiO and *n*-CoO created huge changes on the catalyst activity.

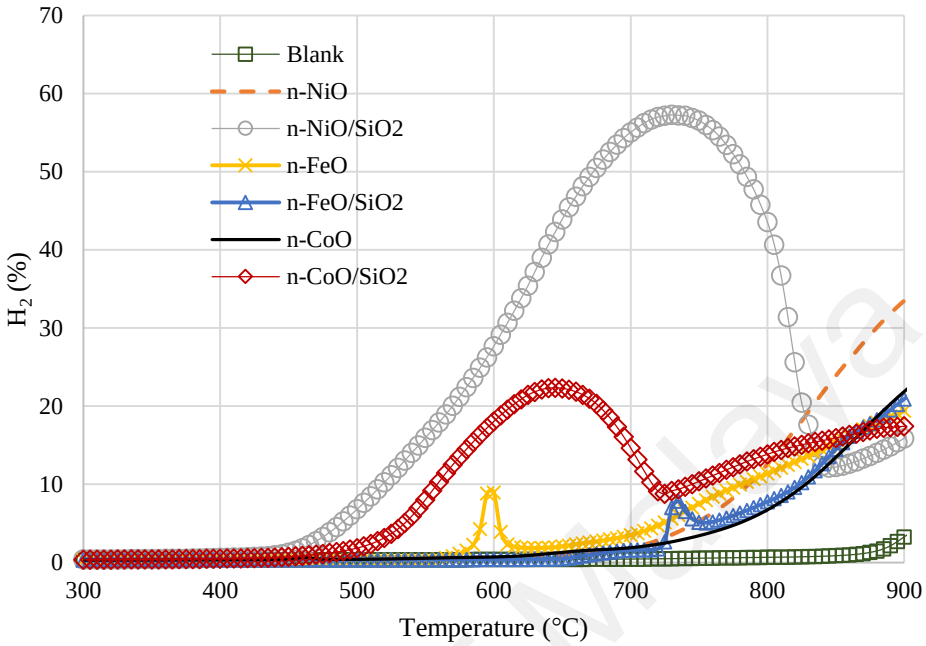

Figure 4.7 Production of hydrogen (in percentage) during TPMD over 1g of *n*-NiO, *n*-NiO/SiO_2, *n*-FeO, *n*-FeO/SiO_2, *n*-CoO, and *n*-CoO/SiO_2 catalysts. Temperature ranged between 200 to 900 °C with a flow rate of 0.64 L/min.

Irrespective of the activity zone of *n*-NiO, *n*-NiO/SiO_2 nanoparticles exhibited a remarkable catalytically active zone between 450 and 730 °C, with a maximum hydrogen production of 57.28% at 730 °C. *n*-NiO/SiO_2 started to deactivate above 730 °C, and hydrogen production decreased to 12% at 845 °C and then started to gradually increase according to the endothermic nature of methane decomposition. In a similar manner, the *n*-CoO/SiO_2 catalyst was clearly active from 510 to 645 °C, with a maximum hydrogen production of 22.3% at 645 °C. The silicate-supported Co catalyst showed catalytically active temperature zones similar to those of silicate-supported Ni, supporting previous reports (Y. Zhang & Smith, 2002). By contrast, the Co-based catalyst exhibited lower methane conversion than that of Ni-based catalyst (Lee et al., 2012). The deactivation of *n*-NiO/SiO_2 and *n*-CoO/SiO_2 after achieving the maximum hydrogen production

percentage may be attributed to thermal degradation at high temperatures. Despite the performance of Ni- and Co-based catalysts, *n*-FeO and *n*-FeO/SiO_2 exhibited poor performance during TPMD. *n*-FeO was slightly active at 595 °C with a maximum hydrogen production of 9% and sharply diminished to 2% within minutes. Furthermore, *n*-FeO/SiO_2 produced 7.8% hydrogen at its most active temperature, whose range was very narrow. Based on the results of TPMD, the *n*-NiO/SiO_2 and *n*-CoO/SiO_2 catalysts were active between 475 – 730 °C and 500 – 645 °C, respectively. The experimented *n*-NiO/SiO_2 and *n*-CoO/SiO_2 catalysts are superior to the naked and supported Ni- and Co-based catalysts prepared using conventional methods at 500 to 700 °C (Jangam Ashok et al., 2009; Figueiredo et al., 2010; Giselle D. B. Nuernberg et al., 2012). This finding clearly shows the advantages of co-precipitation cum modified Stöber method. However, Fe-based catalyst produced using the modified Stöber method exhibited poor catalytic performance. Fe_3C formation, metal disintegration, and complete encapsulation of catalyst by the as-obtained carbon are the major reasons for the extremely poor performance of Fe-based catalyst, as explained by the XRD [Figures 4.8 (a-c)] and TEM [Figures 4.9 (a-f)] results of the produced nanocarbon in section 4.1.6. However, particle agglomeration was found to be minimal with *n*-NiO/SiO_2 and *n*-CoO/SiO_2 after TPMD, as shown by the TEM images in Figures 4.9 (b and f), thereby resulting in higher activity. The lower activity of naked metal oxides and *n*-FeO/SiO_2 may be accredited to the sintering of metal particles to giant sizes, which exceeds the critical size for carbon nanofilament growth, as observed in Figures 4.9 (a, c, d, and e). Furthermore, metal particles with very large size cannot grow carbon nanofilaments (Jangam Ashok et al., 2009).

4.1.6 Characterization of As-produced Nanocarbon

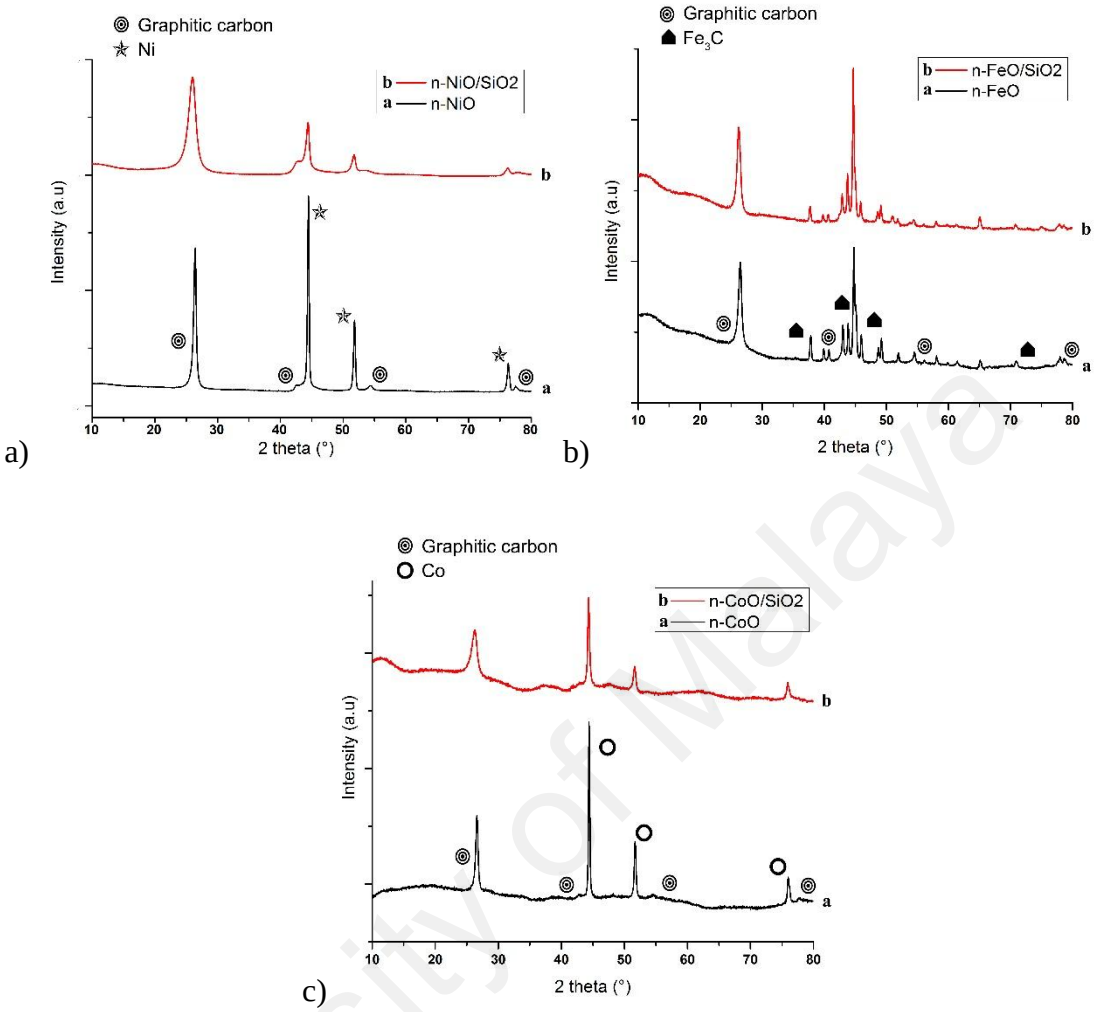

Figure 4.8 XRD patterns of a) *n*-NiO and *n*-NiO/SiO_2, b) *n*-FeO and *n*-FeO/SiO_2, and c) *n*-CoO and *n*-CoO/SiO_2 after TPMD. Peaks corresponds to graphitic carbon, Ni, Fe_3C and Co are indicated.

The presence of graphitic carbon can be easily identified by the XRD patterns of *n*-NiO, *n*-NiO/SiO_2, *n*-FeO, *n*-FeO/SiO_2, *n*-CoO, and *n*-CoO/SiO_2 after temperature-programmed methane decomposition (Figure 4.8). The as-obtained carbon over Ni-based catalysts can be distinguished by diffraction peaks observed at $2\theta = 26.44°$, 42.49°, 44.47°, 54.48°, and 76.34° in Figure 4.8 (a), which are in good agreement with JCPDS No. 00-001-0640 for hexagonal graphitic carbon. Furthermore, the diffraction peaks for completely reduced Ni can be seen at $2\theta = 44.47°$, 51.83°, and 76.34°, indicating the reduction capability of

methane. The diffraction peaks for Ni observed over *n*-NiO and *n*-NiO/SiO_2 after TPMD are similar to the peaks in JCPDS No. 01-070-1849 for cubic metallic Ni. Fe-based catalysts also produced graphitic carbon, which is evident from the peaks observed at 2θ = 26.53°, 42.95°, 44.76°, and 54.48°, as shown in Figure 4.8 (b). Iron carbide (Fe_3C) is also a major component observed in the XRD pattern of Fe-based catalyst after methane decomposition. The peaks observed at 2θ = 37.83°, 39.90°, 43.82°, and 45.93° are in good agreement with the peaks in JCPDS No. 03-065-0393 for orthorhombic Fe_3C. Similar to Ni- and Fe-based catalysts, Co-based catalysts produced graphitic carbon with XRD peaks at 2θ = 26.61°, 42.76°, 44.32°, 54.74°, and 77.73°, as displayed in Figure 4.8 (c). Carbon produced over Co-based catalysts showed excellent resemblance to JCPDS No. 00-026-1080 for hexagonal carbon. Moreover, *n*-CoO and *n*-CoO/SiO_2 exhibited peaks for Co at 2θ = 44.38°, 51.69°, and 76.01°, which are in good agreement with JCPDS No. 98-007-6632 for cubic Co-alpha.

The TEM images of *n*-NiO, *n*-NiO/SiO_2, *n*-FeO, *n*-FeO/SiO_2, *n*-CoO, and *n*-CoO/SiO_2 are shown in Figure 4.9. The unsupported *n*-NiO, *n*-FeO and *n*-CoO particles underwent fast agglomeration resulted in the formation of large particles, and were completely encapsulated by the as-produced nanocarbon [Figures 4.9 (a, c, and e)]. The carbon covered and isolate metal particles from the reaction medium and prevented further methane decomposition. Thus, the formation of carbon filaments was restricted over non-supported metal oxide nanoparticles. Previously reported research contributions also revealed that naked metal oxide nanocatalysts are incapable of producing carbon nanofilaments in hydrocarbon media (M. S. Kim et al., 1991). However, silicate-supported *n*-NiO and *n*-CoO effectively prevented particle agglomeration and allowed advanced methane decomposition, resulting in the production of nanocarbon filaments [Figures 4.9 (b and f)]. By contrast, silicate-supported *n*-FeO cannot produce

nanofilaments as *n*-FeO/SiO_2 underwent fast agglomeration [Figure 4.9 (d)] because of inefficient interaction between Fe and silicate support.

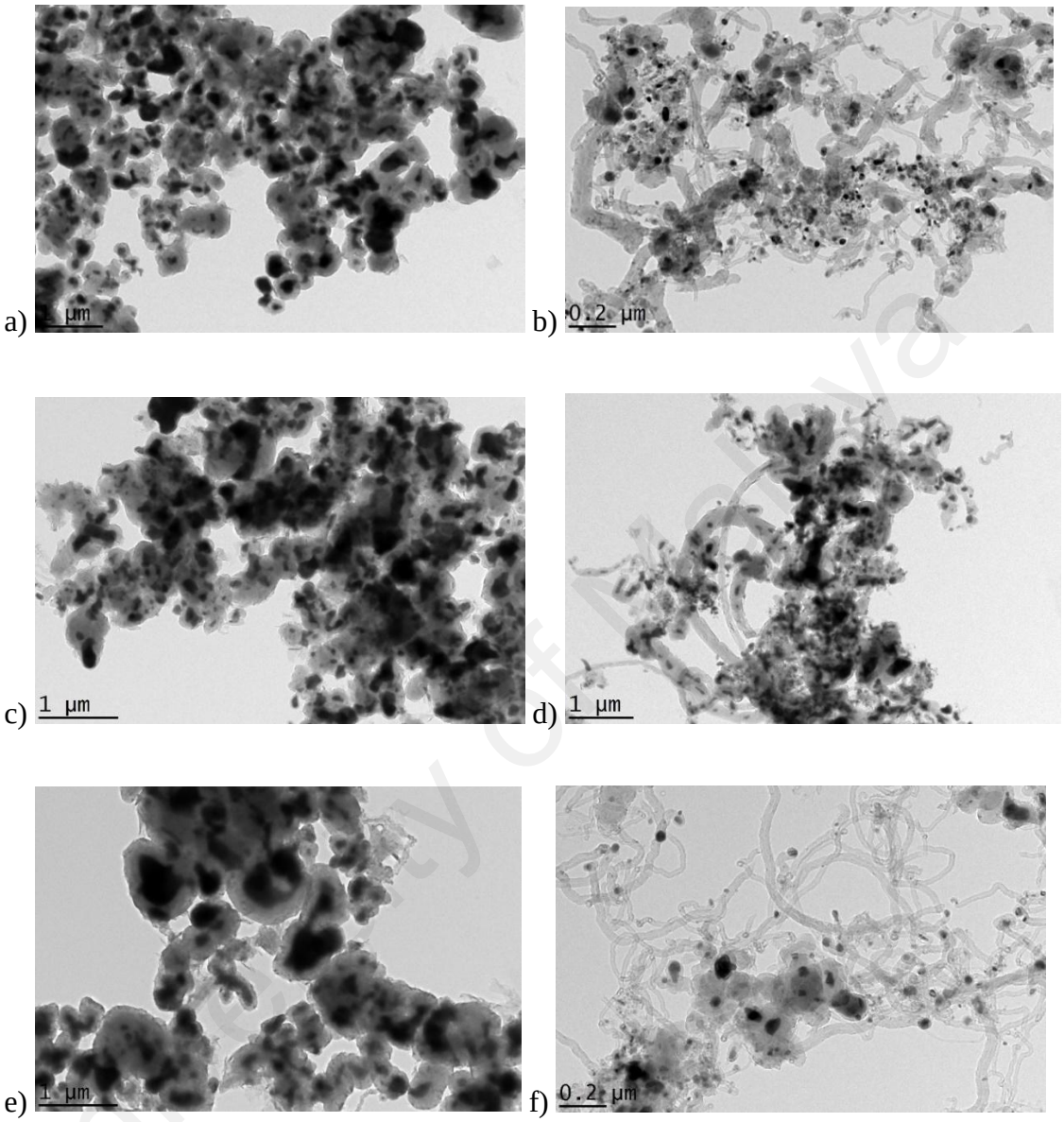

Figure 4.9 TEM images of nano-catalysts after TPMD. a) *n*-NiO, b) *n*-NiO/SiO_2, c) *n*-FeO, d) *n*-FeO/SiO_2, e) *n*-CoO, and f) *n*-CoO/SiO_2.

Nanocarbon filaments were formed from single-carbon atoms produced from methane according to the balanced chemical equation 1.1 [$CH_4 \rightarrow 2H_2 + C$]. Various carbon formation mechanisms are described by many researchers, explained elsewhere (Snoeck et al., 1997a). Carbon deposits in the form of graphite are generally developed at metal–support interface. However, the formed carbon layer induced the detachment of

the metals from the silicate support, as evidenced by the formation of nanocarbon through tip growth mechanism in TPMD over silicate-supported nanoparticles. Furthermore, metal particles at the tip of the as-obtained carbon are supposed to be active until complete encapsulation by carbon. The interaction between the metal and the support plays a vital role during nanofiber growth. Furthermore, the metal–support interaction can also influence the morphology of the as-obtained carbon (Snoeck et al., 1997a). According to the literature, Ni-based catalysts produce Ni_3C metastable compound as an intermediate product in methane transformation and can be decomposed to metallic Ni and graphite at a low temperature of 400 °C (Guevara et al., 2010). The separated Ni remained at the tip of the carbon nanofilament and facilitated further methane decomposition. *n*-CoO/SiO_2 behaved similar to the Ni catalyst. However, the formation of disk-type nanocarbon over the Co catalyst may be the reason for less Co activity over Ni-based catalyst. Irrespective of the carbon formation methodology of Ni and Co catalysts, Fe-based catalysts produce graphitic carbon and Fe_3C, as shown in the XRD pattern [Figure 4.8 (b)]. The appalling activity of Fe-based catalyst can be attributed to its incapability to decompose Fe_3C to Fe and graphite.

4.1.7 Summary of Major Findings

Physicochemical characteristics of metal oxide enhanced upon silicate incorporation. The particle sizes of *n*-NiO, *n*-FeO, and *n*-CoO marginally decreased from 48.02, 85.09, and 207.99 nm to 32.19, 30.26, and 49.92 nm, respectively. *n*-NiO/SiO_2 catalysts exhibited an outstanding performance between 450 and 730 °C with a maximum hydrogen production value of 57.28% at 730 °C.

4.2 PART 2: PROBING THE DIFFERENTIAL METHANE DECOMPOSITION BEHAVIORS OF *n*-NiO/SiO_2, n-FeO/SiO_2, AND *n*-CoO/SiO_2 CATALYSTS PREPARED THROUGH CO-PRECIPITATION CUM MODIFIED STÖBER METHOD

4.2.1 Influence of Temperature on TCD over *n*-NiO/SiO_2, n-FeO/SiO_2, and *n*-CoO/SiO_2 Catalysts

Based on the results of TPMD, TCD experiments were conducted for detailed catalysis evaluation at temperatures like 500, 600, and 700 °C.

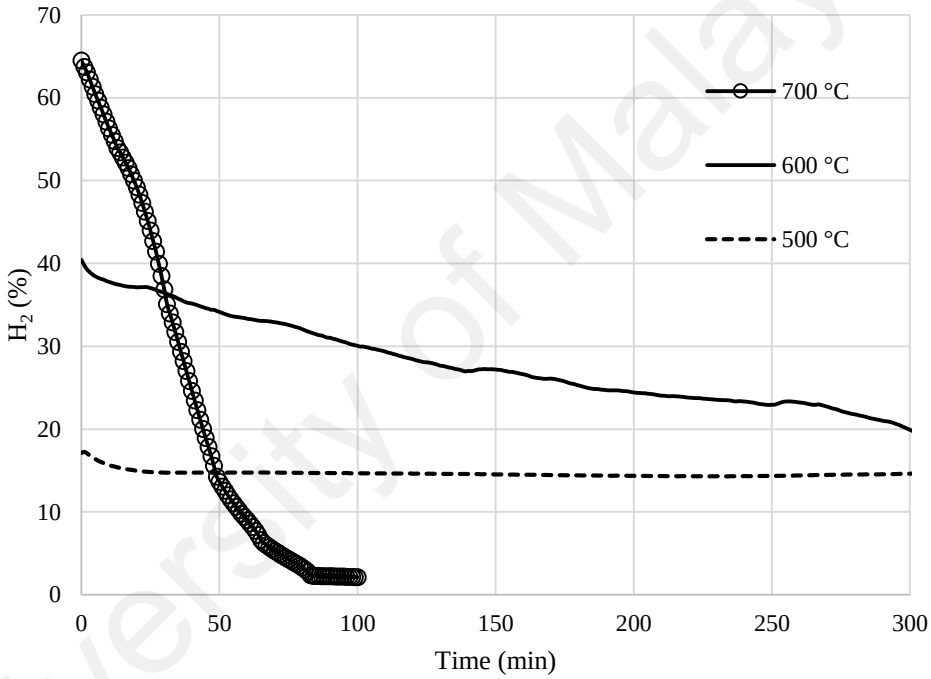

a)

Figure 4.10 (a) Hydrogen formation percentage during TCD over n-NiO/SiO_2.

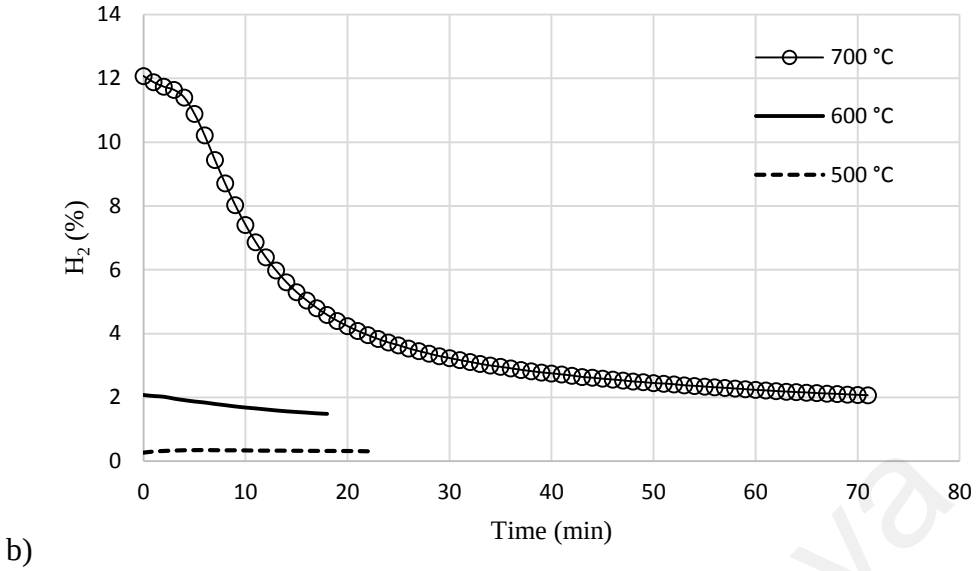

b)

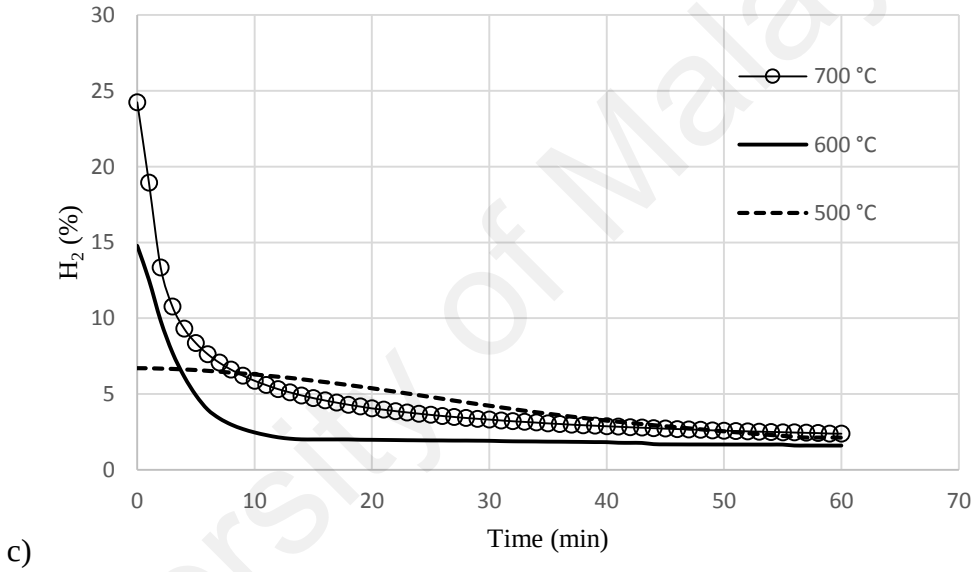

c)

Figure 4.10 Hydrogen formation percentage during TCD over b) n-FeO/SiO_2 and c) n-CoO/SiO_2 catalysts at different temperature. Flow rate = 0.64 L/min and catalyst weight = 0.5 g.

Figure 4.10 shows the changes in hydrogen production percentage with time on stream for the TCD over *n*-NiO/SiO_2, *n*-FeO/SiO_2, and *n*-CoO/SiO_2 catalysts at 500, 600, and 700 °C. Influence of temperature on hydrogen production, activity and temperature sustainability of each catalysts are analyzed. All isothermal examinations were conducted with 99.995% methane. Rosemount Analytical X-STREAM detected only hydrogen and methane as gaseous products as indicated in the balanced methane decomposition

equation 1.1 ($CH_4 \rightarrow 2H_2 + C$). The maximum hydrogen production percentage was observed in the very beginning of methane decomposition experiment, just after the contact of methane with catalyst. Afterwards, the hydrogen production found decreased gradually with time on stream according to the performance of catalyst. Figure 4.10 (a) shows that, *n*-NiO/SiO_2 catalyst exhibits a wide range of activity with hydrogen production from 17% to 65% in the experimented temperatures. The experiments were extended up to 300 min in order to evaluate the stability of *n*-NiO/SiO_2. Maximum hydrogen production was observed at 700 °C with *n*-NiO/SiO_2 catalyst, while catalyst was deactivated rapidly and turn out to be completely inactive within 100 min of experiment. However, it is interesting to notice that, *n*-NiO/SiO_2 maintain its activity even after 300 min of experimental duration with a very low catalytic deactivation at 600 and 500 °C. Nevertheless, minimum deactivation was observed at 500 °C.

Undesirably, *n*-FeO/SiO_2 catalyst was active at 700 °C only. Furthermore, the initial hydrogen production was very less (12.2%) compared to *n*-NiO/SiO_2 catalyst and reached negligible value by 1 h of methane stream. It was completely inactive at experimented temperatures like 600 and 500 °C as observed in TCD [Figure 4.10 (b)], supporting TPMD results (Figure 4.7). However, *n*-CoO/SiO_2 given moderate initial hydrogen production at 700 and 600 °C. While, catalytic stability was pitiable and dip to 5% within 10 min after methane stream reached the catalyst, similar rapid catalytic deactivation were observed by Lee et al. (2012) over Co-based catalysts. It is reported that higher methane decomposition to hydrogen and nanocarbon occurs over coalesced metal particles, while it continues until the crystal size of sintered particle favor the nanocarbon growth (Avdeeva et al., 1996).

It is worth to notice that the Ni-particle agglomeration is very less after methane decomposition as shown in TEM images (Figure 4.14), indicates the lengthier hydrogen production [Figure 4.10 (a)] as well as huge carbon yield (Figure 4.12). However, the

lower activity of *n*-CoO/SiO_2 [Figure 4.10 (c)] and *n*-FeO/SiO_2 [Figure 4.10 (b)] may be attributed to the sintering of metal particle to giant sizes which exceed the critical size for carbon nano-filament growth, as observed in Figure 4.15 and 4.16, respectively. Furthermore, Jangam Ashok et al. (2009) reported that metal particles of very large size were unable to grow carbon nano-filaments. Among the studied catalysts, *n*-NiO/SiO_2 catalyst is superior to Fe and Co based catalyst by all aspects. It is observed that the initial catalytic activity and deactivation rate increases as increasing decomposition temperature, indicates the temperature sensitivity of TCD process. However, it is worth to note that the isothermal methane conversion over all experimented catalysts clearly follows the hydrogen production percentage and active temperature zone revealed by TPMD (Figure 4.7). Hence, temperature programmed methane decomposition can be considered as an efficient step in order to identify catalytically active temperature zone of any catalyst.

4.2.2 Influence of Methane Feed Flow Rate on TCD over *n*-NiO/SiO_2 Catalyst

The effect of methane feed flow rate on hydrogen production in percentage with time on stream is shown in Figure 4.11. Flow rates like 0.64, 1.07, and 1.43 L/min were analyzed at 550 °C over 0.5 g of catalyst. It is observed from Figure 4.11 that the initial hydrogen production decreased from 26.8% to 21.04% when flow rate was increased from 0.64 L/min to 1.43 L/min. It can be speculated that higher methane flow rate results in the lower contact time with catalyst and hence resulted in the lower hydrogen production (Cunha et al., 2008; Y. Li et al., 2000). Furthermore, it is found that the catalytic deactivation rate is decreased as increasing flow rate, because of low residence time at higher flow rate.

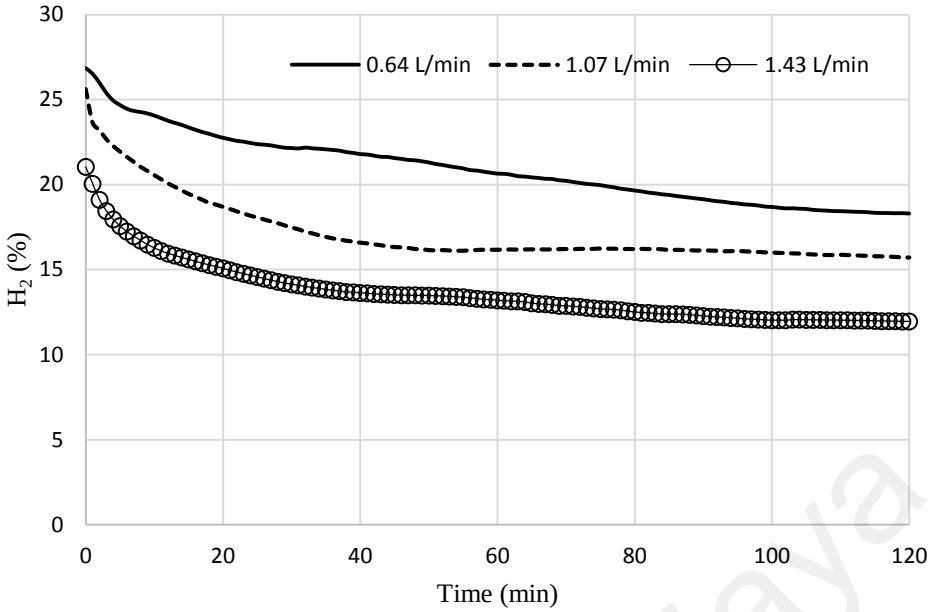

Figure 4.11 Methane decomposition over *n*-NiO/SiO_2 catalyst at different methane feed flow rate. Temperature = 550 °C and catalyst weight = 0.5 g.

Furthermore, it is worth pointing out that the experimented *n*-NiO/SiO_2 catalyst is noticeably superior to the naked and supported Ni-based catalyst prepared by conventional methods at a temperature range of 500 - 700 °C (Figueiredo et al., 2010; Giselle D. B. Nuernberg et al., 2012; Puliyalil et al., 2015; W. Wang et al., 2012; Zapata et al., 2010), clearly demonstrate the advantage of co-precipitation cum modified Stöber method for preparation of *n*-NiO/SiO_2 catalyst (see Table 4.3).

Table 4.3 Comparison of catalytic activity of previously reported metal catalyst with *n*-NiO/SiO_2 catalyst. Initial activity and activity at time 't' and deactivation time are listed. Values are taken from reference as such.

Catalyst (Ref.)	Reaction parameters			Initial		CH_4 H_2 at time t		t-time	d
	T	CH_4 Flow	Total flow	CH_4	H_2				
Ni/SiO_2 (W. Wang et al., 2012)	650	15[b]	--	42	--	5	--	4	--
Ni–Ca/SiO_2 (Zapata et al., 2010)	580	--	100[b]	39	--	12	--	3	--
Ni–K/SiO_2 (Zapata et al., 2010)	580	--	100[b]	40	--	5	--	2.5	3
Ni-Fe/SiO_2 (W. Wang et al., 2012)	650	15[b]	--	46	--	27	--	4	--
Ni/$MgAl_2O_4$ (Giselle D. B. Nuernberg et al., 2012)	550	--	80[b]	34	--	23	--	3	4
Ni-Cu/La_2O_3 (Figueiredo et al., 2010)	600	--	110[c]	35	--	60	--	10	--
n-NiO/SiO_2 (this work)	700	640[b]	640[b]	33.8	64.4	97.4	2.3	1.5	1.6
n-NiO/SiO_2 (this work)	600	640[b]	640[b]	57.2	40.4	79.5	19.9	4	--
n-NiO/SiO_2 (this work)	500	640[b]	640[b]	74.4	17.2	85.3	14.6	4	--
n-NiO/SiO_2 (this work)	550	640[b]	640[b]	68.5	29.4	76.9	22.9	2	--
n-NiO/SiO_2 (this work)	550	1070[b]	1070[b]	72.9	25.6	84.2	15.7	2	--
n-NiO/SiO_2 (this work)	550	1430[b]	1430[b]	78	21	87.3	11.9	2	--

(T, temperature (°C); F, flow rate ([a]mL/($g_{cat.}$h), [b]mL/min, [c]NmL/min, unless other units are stated); Conversion (%); t, time (h); d, complete deactivation (h); --, not mentioned in the original paper)

4.2.3 Characterization of Produced Nanocarbon

Enormous quantity of carbon were formed over *n*-NiO/SiO_2 compared to *n*-CoO/SiO_2 and *n*-FeO/SiO_2. The carbon yield percentage over each catalyst at respective temperatures were calculated with the following equation (4.2) (Chai et al., 2011; Saraswat & Pant, 2011) and the results are depicted in Figure 4.12. The carbon yield of the catalysts was evaluated based on the extent of methane conversion against time on stream at a CH_4 flow rate of 0.64 L/min. Carbon deposition period was 5 h for *n*-NiO/SiO_2 at 500 and 600 °C, while all other percentages are up to the complete deactivation of respective catalyst.

$$\text{Carbon yield (\%)} = \frac{\text{weight of deposited carbon on the catalyst}}{\text{weight of metal portion}} \text{ x } 100 \qquad (4.2)$$

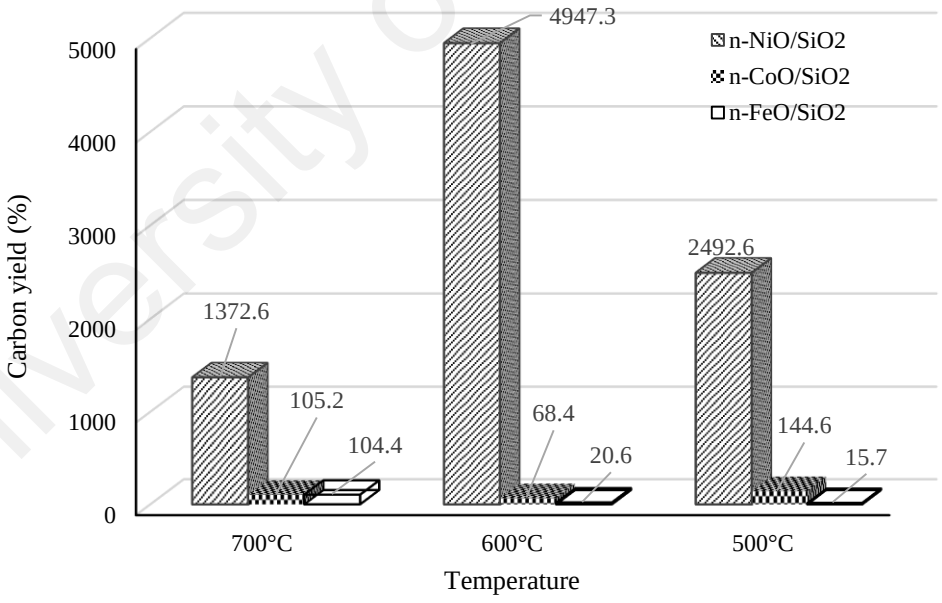

Figure 4.12 Comparison of calculated carbon yield in percentage produced over respective catalyst at 700, 600, and 500 °C.

Figure 4.12 comprises the comparison of produced carbon yield over each experimented catalyst which reveals that *n*-NiO/SiO_2 produced very high quantity of nanocarbon compared to *n*-CoO/SiO_2 and *n*-FeO/SiO_2. *n*-NiO/SiO_2 produced 4947.3% of

carbon at 600 °C during 5 h of experiment. Hence, it was not deactivated during the experimented period at 600 °C. However, *n*-NiO/SiO_2 produced 1372.6% nanocarbon at 700 °C before it deactivated in 100 min. However, 105.2% and 144.6% nanocarbon were formed over *n*-CoO/SiO_2 catalyst before its complete deactivation at 700 and 600 °C, respectively. Whereas, it was very low at 600 °C as *n*-CoO/SiO_2 undergone fast deactivation. Very regrettable performance was shown by *n*-FeO/SiO_2, which produced 104.4% of nanocarbon at 700 °C. Though, *n*-FeO/SiO_2 was almost inactive at 500 and 600 °C as observed in TPMD (Figure 4.7). The observed carbon yield was outstanding compared to many other available results over Ni-based catalyst (Saraswat & Pant, 2011). However, the performance of *n*-CoO/SiO_2 and *n*-FeO/SiO_2 were pitiable. Likewise, such disgraceful results were reported by Zadeh and Smith(Zadeh & Smith, 1998) over Co-based catalysts. This deprived catalyst performance can be attributed to the faster particle agglomerations and complete catalyst encapsulation with produced carbon as shown in TEM images (Figure 4.15 and 4.16).

4.2.3.1 XRD analysis

Figure 4.13 displays the XRD patterns of *n*-NiO/SiO_2, *n*-FeO/SiO_2, and *n*-CoO/SiO_2 catalysts after TCD process at experimented temperatures (500, 600, and 700 °C). XRD peaks for *n*-FeO/SiO_2 after TCD at 500 and 600 °C were omitted as carbon production was negligible at those temperatures. Graphitic carbon produced over *n*-NiO/SiO_2 catalyst can be identified by the diffraction peaks at $2\theta = 26.26°$ and 44.45° as indicated in Figure 4.13 (a). Those peaks are in good agreement with the JCPDS No. 98-005-3781 for graphite. However, reduced Ni-phases can be recognised at peaks $2\theta =$ 44.5°, 51.83°, and 76.28°, confirmed with Ni peaks in JCPDS No. 01-070-1849. *n*-FeO/SiO_2 and *n*-CoO/SiO_2 produced graphitic carbon as the peaks observed at $2\theta =$ 26.38° and 44.39° in Figure 4.13 (b & c), are in good agreement with JCPDS No. 00-041-1487. Furthermore, the presence of iron carbide (Fe_3C) can be identified over *n*-FeO/SiO_2

catalyst after TCD (Figure 4.13 (b)) with the peaks at 2θ = 37.76°, 45.01°, 70.88°, and 78.65°, which correspond to the peaks in JCPS No. 00-034-0001.

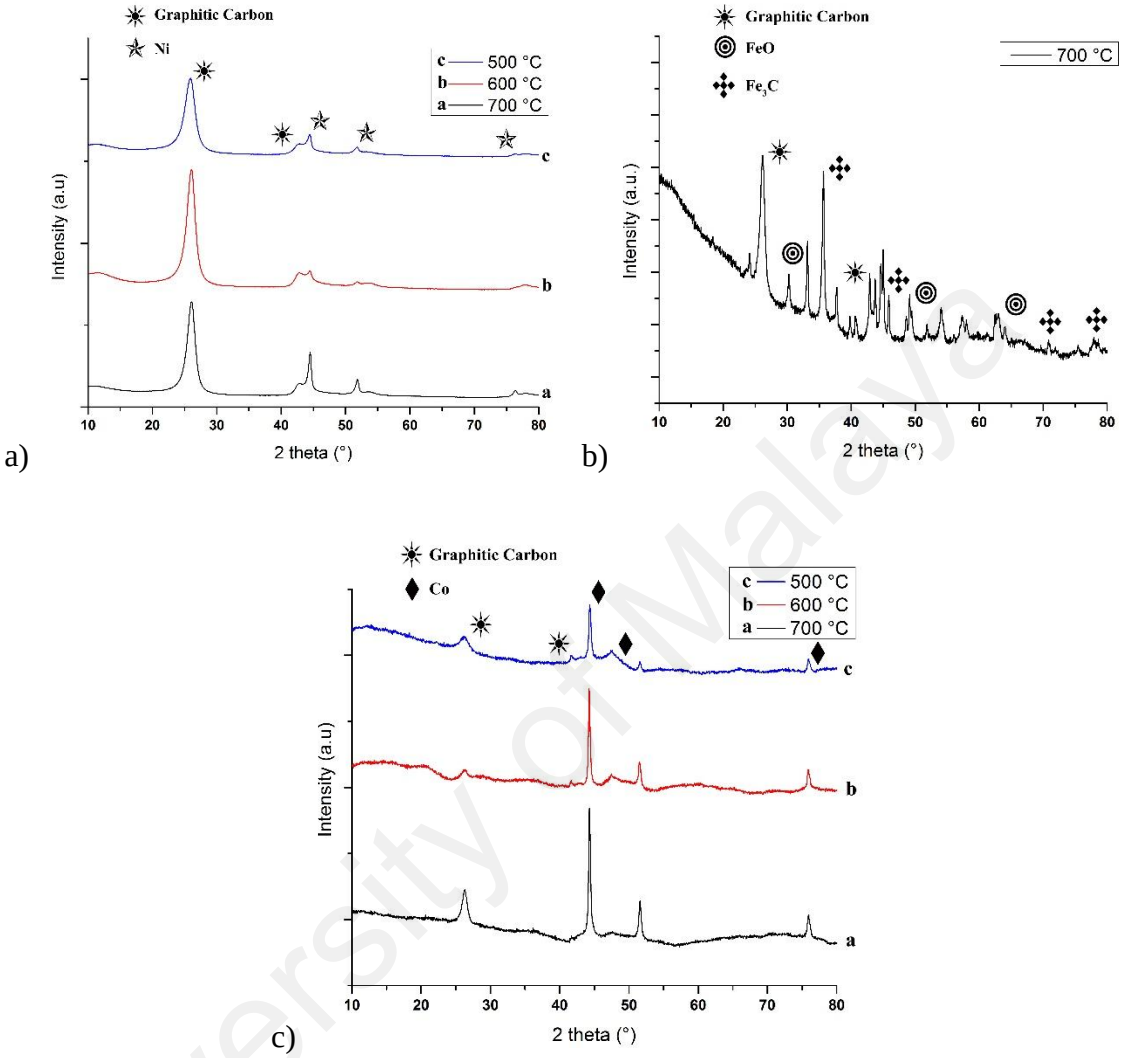

Figure 4.13 XRD patterns of a) *n*-NiO/SiO_2, b) *n*-FeO/SiO_2, and c) *n*-CoO/SiO_2 after isothermal methane decomposition at different temperature. Peaks corresponds to graphitic carbon, Ni, FeO, Fe_3C, and Co are indicated.

The intensity of peaks corresponds to graphite produced over *n*-FeO/SiO_2 and *n*-CoO/SiO_2 are not high as those observed with *n*-NiO/SiO_2. However, it is observed that the graphitization intensity of produced nanocarbon improved as increasing decomposition temperature. It is clear from the amendment of the carbon peaks to higher

values in Figure 4.13 (a & c) in a similar manner to those produced over Ni impregnated zeolite catalyst as observed by Nasir Uddin et al. (2015).

4.2.3.2 TEM analysis

Figures 4.14 (a-c) display TEM images of produced nanocarbon over *n*-NiO/SiO_2 catalyst at 700, 600, and 500 °C, respectively. However, TEM images of produced nanocarbon over *n*-CoO/SiO_2 and *n*-FeO/SiO_2 exhibited in Figure 4.15 and Figure 4.16, respectively.

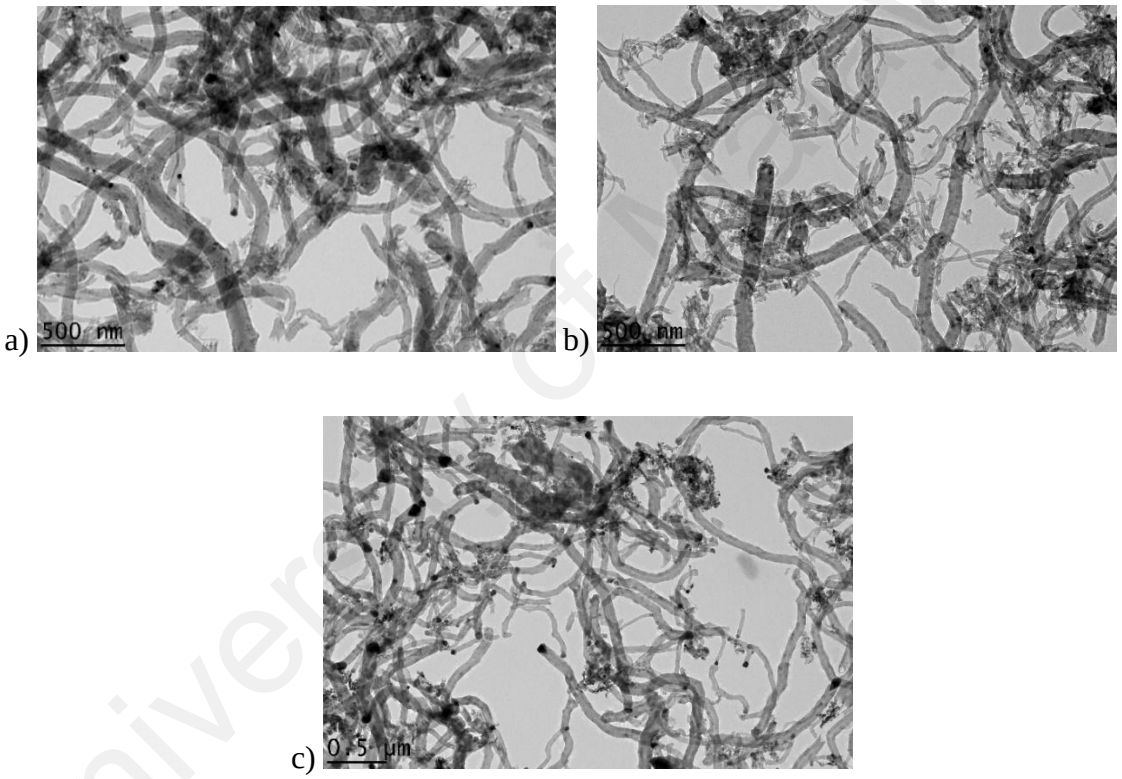

Figure 4.14 TEM images of produced nanocarbon over *n*-NiO/SiO_2 at a) 700, b) 600, and c) 500 °C.

TEM images (Figures 4.14 and 4.15) elucidate that *n*-NiO/SiO_2 and *n*-CoO/SiO_2 mainly produced carbon nano-tubes, while small quantity of nano-fibers were also identified. Hence, nano-tube can be recognized with the presence of a hallow cavity, though it is absent with nano-fibers (Serp et al., 2003). It is apparent from the Figure 4.14 and 4.15 that the Ni- and Co-catalysts produced carbon nanotubes with thick walls and the internal

cavity posturing a "*fish-bone*" or "*bamboo*" morphology. Furthermore, *n*-NiO/SiO_2 catalyst also produced different types of nanocarbons as follows: carbon nano tubes with open end, carbon nano tubes with closed end and carbon nanotube with Ni particle embedded in it. Ni and Co metals can be seen at the dip of formed nanocarbon. Very low carbon yield observed over *n*-CoO/SiO_2 at 600 °C can be attributed to the complete encapsulation of catalyst with produced nanocarbon and heavy agglomeration of catalyst as shown in Figure 4.15 (b). However, pear or diamond shaped metals with its sharp tail inserted to the produced nano-tubes can be seen in Figures 4.14 (a-c), following tip-growth carbon formation mechanism (Sinha et al., 2000), which is reinforcing many previous works (Baird et al., 1974; Baker et al., 1972; Tesner et al., 1970).

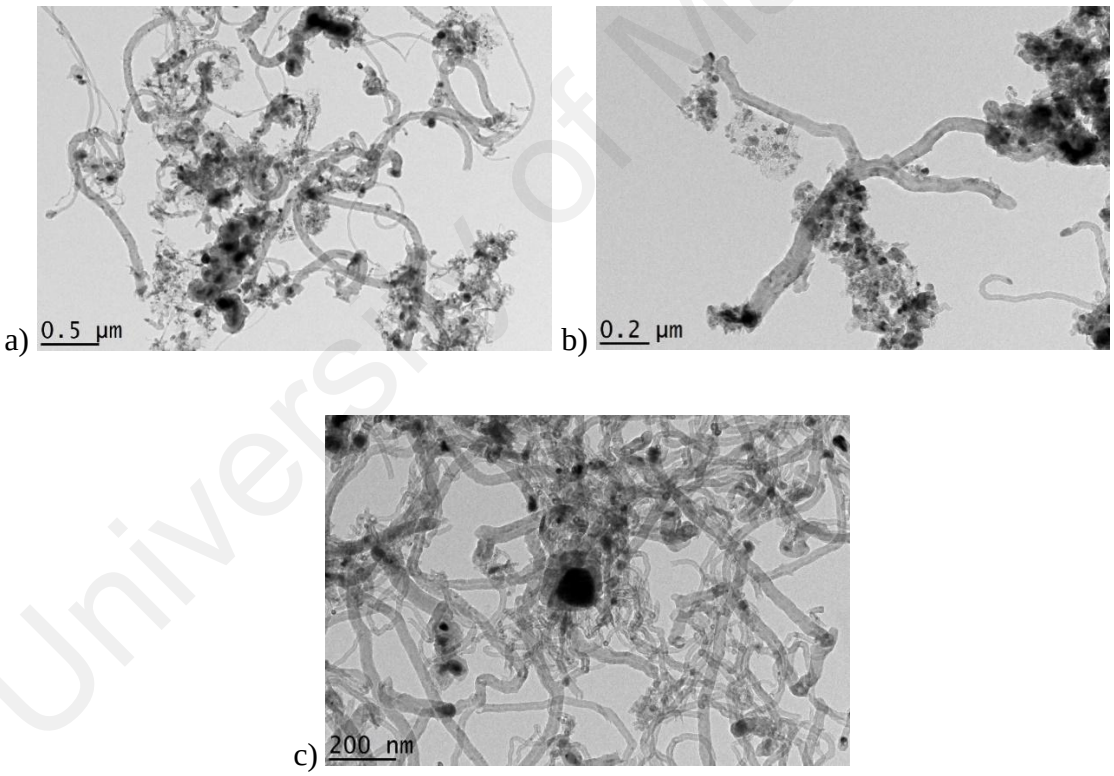

Figure 4.15 TEM images of produced nanocarbon over *n*-CoO/SiO_2 at a) 700, b) 600, and c) 500 °C.

The Ni particle were spherical or sphere shaped embedded in SiO_2 before decomposition process [Figure 4.4 (b)]. The structural changes in to pear or diamond shape after TCD stipulates the possibility of the existence of Ni particle in the quasi liquid

state during the process, even at lower experimental temperature than its melting point (1452 °C) and Tamman temperature (726 °C). The occurrence of lower temperature quasi liquid is because of formation of highly unstable, compared to Ni and graphite, Ni_3C metastable compound as an intermediate product in the methane transformation process which can be decomposed to metallic Ni and graphite at lower temperature of 400 °C. Furthermore, the higher gradient of Ni_3C concentration over Ni particle during the process because of the uninterrupted graphite formation sets up a pressure at the graphitic envelope (Guevara et al., 2010). Hence, mass transfer of carbon occurred by diffusion through the bulk particle as the consequence of built up of pressure tries to squeeze out the Ni particle in the quasi liquid state. However, the lower temperature Ni_3C to metallic Ni and graphite and internal pressure build up explain the change in the shape of Ni particle after TCD process as well as the manifestation of Ni particle inside the carbon nanotubes. However, it is very significant to notice that such structural alteration is very less with *n*-CoO/SiO_2 catalyst after TCD.

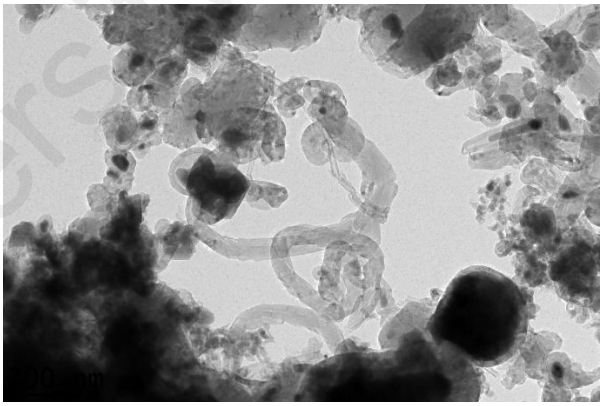

Figure 4.16 TEM images of produced nanocarbon over *n*-FeO/SiO_2 at 700 °C.

n-FeO/SiO_2 did not produce different types of nanocarbons as Ni-catalyst did. In addition to carbon nano-tubes, irregular carbon formulation was observed over *n*-CoO/SiO_2 and *n*-FeO/SiO_2 [Figure 4.15 (a and b) and Figure 4.16, respectively], could be attributed to the occurrence metal particle fragmentation which maintains the availability of more active metal phases (Bartholomew, 2001). The availability of such higher active

metal phases because of the diffusion of supersaturated nanocarbon results in the formation of more nanocarbon around the catalyst particles by methane decomposition which leads to its complete encapsulation. Furthermore, the carbon diffusion occurred may be attributed to the less effective interaction between Co and Fe metals with the silicate supports or their incomplete shielding which results in the domination of Co and Fe metal phases at their surface. It is obvious from the displayed TEM images (Figure 4.15 and 4.16) that *n*-CoO/SiO_2 and *n*-FeO/SiO_2 catalysts were rapidly agglomerated and encapsulated with produced carbon after methane came in contact with it and hence loose its activity completely. However, such metal particle fragmentation is absent with *n*-NiO/SiO_2 because of the efficient interaction between Ni metal phase and silicate support results in the enhanced activity and stability. It is worth to note that nanocarbon with larger diameter were formed over *n*-CoO/SiO_2 at 600 °C [Figure 4.15 (b)] and over n-FeO/SiO_2 at 700 °C (Figure 4.16) may be attributed to the formation of carbon over agglomerated larger catalysts particles, and hence encapsulated by carbon leads to their faster deactivation. Similar result was already reported by P. Jana et al. (2012) over the spinel catalysts. It was reported that the outer diameter of the carbon nanotubes greatly depend on the size of catalyst particles. Hence, larger particles produce carbon nanotubes with larger diameter (Guevara et al., 2010). Furthermore, M. A. Ermakova & Ermakov (2002) reported similar speedy catalyst encapsulation with carbon over Fe-based catalyst. However, there is no such agglomeration or encapsulation can be seen with *n*-NiO/SiO_2 (Figure 4.14) which endured a longer activity and produced a huge carbon deposition at all their experimented temperatures (Figure 4.12). The formation of nanocarbon over *n*-NiO/SiO_2 occurred at the interface between the Ni particle and silicate support and hence metal is detached from support (Y. Zhang & Smith, 2004). However, Ni-particle maintained its activity at the surface of growing carbon filaments which results in the longer activity of *n*-NiO/SiO_2. Furthermore, almost similar graphite formation was

observed with *n*-CoO/SiO_2, while the carbon deposited on it encapsulates active metal face and hence results in its rapid deactivation (Kuvshinov et al., 1998). In accordance to previous reports (Y. Zhang & Smith, 2002), our results also reveals that stable catalytic performance and catalytic decomposition depend on the catalysts, catalytic characteristics and operating parameters.

4.2.3.3 FESEM analysis

FESEM images of produced carbon nanocarbon over *n*-NiO/SiO_2 at respective temperature are displayed in Figures 4.17 (a-c) and the diameter distribution histogram in Figure 4.18.

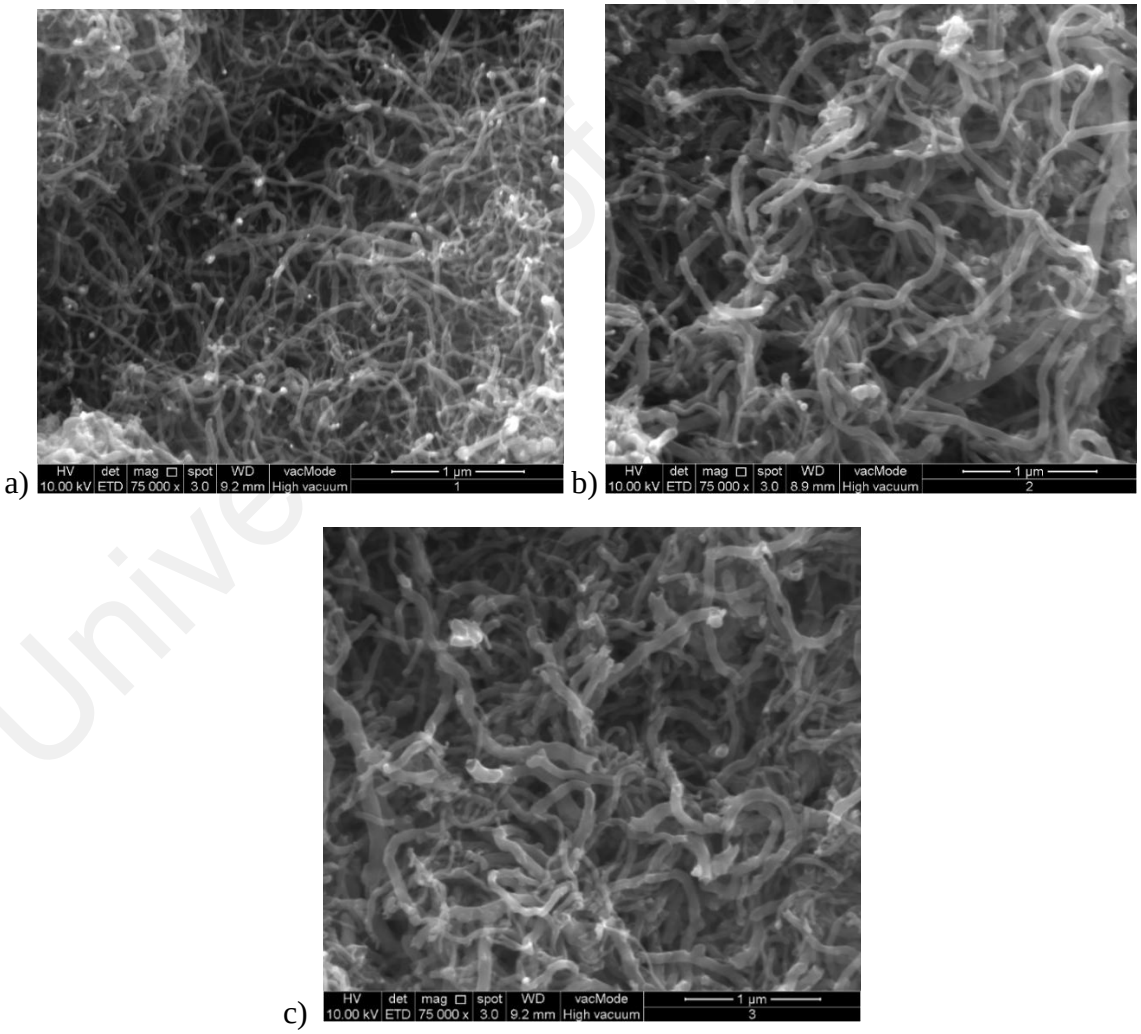

Figure 4.17 FESEM images of produced nanocarbon over *n*-NiO/SiO_2 catalyst at a) 700, b) 600, and c) 500 °C.

FESEM images disclose that the produced nanocarbons have smooth elliptical shape with diameter covering a range of 5 nm to 145 nm. It is very difficult to compute the actual length of the carbon nanocarbon as they exist in an interweaving manner. However, it can speculate that the length exceeds some micrometers. The brighter spot observed in Figure 4.17 (a-c) at the tips of carbon nano-tubes are Ni-metal particle and it is worth to note that the diameter of nanocarbon are similar to that of Ni-particles. The diameter of nanocarbons were measured with ImageJ software. The average diameter calculated from 50 nanocarbons were 35.75 ± 7.8 nm, 52.64 ± 11.5 nm and 56.34 ± 15.2 nm at 700, 600, and 500 °C, respectively. These results are in well consistent with the Ni-crystallite size calculated from XRD patterns using Scherrer equation. Hence, calculated crystallite sizes are 34.2, 47.03, and 50.22 nm at 700, 600, and 500 °C. This strong consistency between carbon diameter and Ni-crystallite size are clearly reveal the dependability between them, supporting previous reports (V. R. Choudhary et al., 2001; de Lucas et al., 2005).

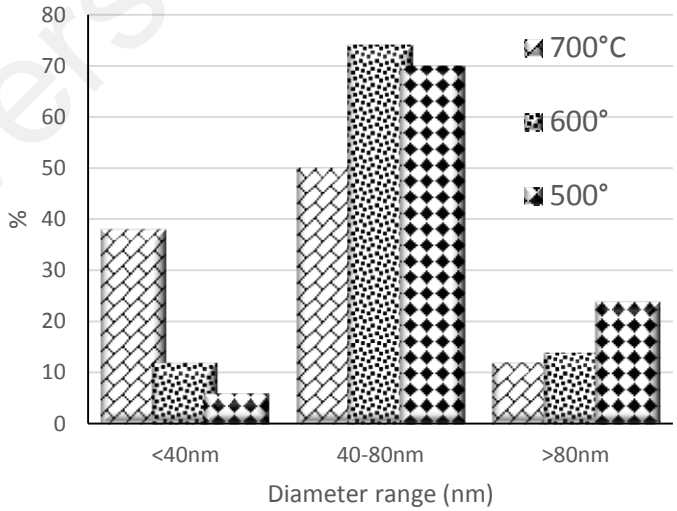

Figure 4.18 The diameter distribution histogram of nanocarbon produced over *n*-NiO/SiO_2. Diameter of 50 nanocarbons were measured with ImageJ software.

Furthermore, the diameter distribution histogram (Figure 4.18) reveals that the diameters of the most of produced nanocarbons are in between 40 and 80 nm. It is clear from the FESEM images that the morphology and quality of produced nanocarbons are almost similar at all experimented temperature over *n*-NiO/SiO_2 catalyst. However, methane decomposition at 700 °C produced more nanocarbon with very low (<40 nm) diameter compared to 600 and 500 °C. Furthermore, nanocarbon with open end, closed end and with metal particle at the dip also can clearly found in the FESEM images, seconding the TEM images shown in Figure 4.14.

4.2.4 Summary of Major Findings

n-NiO/SiO_2 catalyst exhibited an outstanding performance with a maximum hydrogen production of 64.4% at 700 °C, while minimum deactivation after 240 min of examination was found at 500 °C. A variety of nanocarbons were formed over *n*-NiO/SiO_2 catalyst. According to our experimental results, the performance of analyzed catalysts in terms of their stability and activity follow this order *n*-NiO/SiO_2 > *n*-CoO/SiO_2 > *n*-FeO/SiO_2.

4.3 PART 3: METHANE DECOMPOSITION KINETICS AND REACTION RATE OVER *n*-NiO/SiO_2 CATALYST.

4.3.1 Establishment of Carbon Deposition in Methane Decomposition over *n*-NiO/SiO_2 Catalyst

According to the pre-reported mechanisms in methane decomposition, methane molecules diffuse through pores of catalysts and chemisorbed on the active metals phase, and lastly transform to carbon and hydrogen atoms. The overall methane decomposition reaction is expressed as $CH_4 \rightarrow C + 2H_2$ (equation 1.1). Table 4.4 exhibits the summary of all the experiments and the major findings. Conferring to the stoichiometric equation 1.1, the amount of the carbon molecules accumulated upon TCD process is the half of the quantity of hydrogen molecule formed. iH_2 and iCH_4 was derived from the curve fitting of H_2 (%) and CH_4 (%) vs. time in minute (t) using a polynomial equation of order four with R^2 values higher than 0.99. Value of time was given zero in the right-hand side of the curve fitting equations to get iH_2 (%) and iCH_4 (%). Furthermore, the instantaneous percentage of H_2 measured by Rosemount Analytical X-STREAM analyzer expresses the fraction of decomposed methane (χ_{CH_4}) according to following equation:

$$\chi_{CH_4} = \frac{H_2\ (\%)}{200 - H_2\ (\%)} \qquad (4.3)$$

The H_2 (%) was subtracted from 200 in equation 4.3 is because the volume of methane is half of the hydrogen as per balanced equation 1.1.

The curve fitting of χ_{CH_4} vs. t using a 4^{th} order polynomial equation was used to calculate the initial fraction of decomposed methane. The final values after substituting time = 0 in the right hand side of curve fitting equation provide the initial fraction of decomposed methane. The regression coefficient was > 0.99. The methane decomposition rate (R_{CH_4}) in (mmol/($g_{cat.}$min)) was calculated using the following equation:

$$R_{CH_4} = (\dot{F}_{CH_4} . \chi_{CH_4}) / W_{cat} \qquad (4.4)$$

where $\dot{F}_{CH_4}$ is the molar flow rate of feeding methane in mmol min^{-1}. $R_{CH_4,0}$ was calculated from the curve fitting of R_{CH_4} vs. t and then by substitution of time equal to zero in the right-hand side of the curve fitting equation.

The values of fraction of converted methane was used to compute the molar flow rate of hydrogen (mmol min^{-1}) with following equation:

$$\dot{F}_{H_2} = 2 . \dot{F}_{CH_4} . \chi_{CH_4} \qquad (4.5)$$

where $\dot{F}_{H_2}$ is the molar flow rates of hydrogen in mmol min^{-1}.

The carbon flux [ψ_{carbon} (g/min)] enters to the reactor, which can be calculated using the following equaiton:

$$\psi_{carbon} = \frac{f_{CH_4} . 12}{22.4} \qquad (4.6)$$

where f_{CH_4} is the volumetric flow rate of methane, 12 g/mol is the atomic weight of carbon, and 22.4 L/mol the volume of 1 mol of gas at STP. The reliance of as-produced carbon with time throughout the TCD process can be estimated using equation (4.7):

$$Ct = \psi_{carbon} \int_0^t \chi_{CH_4}(t) . dt \qquad (4.7)$$

Eq. (4.7) was used to predict the thermodynamic deposition of carbon in this TCD process. However, Eq. (4.7) can assess the quantity of accumulated carbon from thermal decomposition of methane. The right-hand side of Eq. (4.7) can be determined using Eq. (4.6) and by integrating the curve fitting against time by using a 4^{th} order polynomial equation having a regression coefficient > 0.99.

Table 4.4 Summary of experimental conditions and the main findings in kinetic analysis.

No.	W	T	P_{CH_4}	VHSV	Rt	iH_2	iCH_4	$i\chi_{CH_4}$	$R_{CH_4,0}$	$\dot{F}_{CH_2}$
1	0.6	650	0.2	2408.3	0.025	12.65	6.932	0.067	3.217	3.863
2	0.6	650	0.4	2408.3	0.025	25.33	13.34	0.145	6.901	8.294
3	0.6	650	0.6	2408.3	0.025	42.05	16.77	0.267	12.69	15.22
4	0.6	650	0.8	2408.3	0.025	56.71	22.75	0.396	18.87	22.63
5	0.6	600	0.2	2408.3	0.025	8.487	10.75	0.045	2.112	2.534
6	0.6	600	0.4	2408.3	0.025	19.15	19.62	0.105	5.042	6.056
7	0.6	600	0.6	2408.3	0.025	32.98	26.42	0.198	9.413	11.29
8	0.6	600	0.8	2408.3	0.025	45.01	33.96	0.290	13.83	16.61
9	0.6	550	0.2	2408.3	0.025	3.713	15.92	0.019	0.902	1.082
10	0.6	550	0.4	2408.3	0.025	11.37	27.75	0.060	2.870	3.447
11	0.6	550	0.6	2408.3	0.025	21.95	37.82	0.123	5.870	7.051
12	0.6	550	0.8	2408.3	0.025	26.91	52.75	0.156	7.412	8.892

[W = catalyst weight (g); T= temperature (°C); P_{CH_4} = methane partial pressure (atm); F = flow rate (L/min); VHSV = Volume hourly space velocity (h^{-1}); Rt = Residence time (min); iH_2 = initial hydrogen (%); iCH_4 = initial methane (%); $i\chi_{CH_4}$ = initial methane fractional conversion; $R_{CH_4,0}$ = initial rate of methane decomposition ($mmol(g_{cat.}min)^{-1}$)); and $\dot{F}_{H_2}$ = molar flow rate of hydrogen (mmol/min)]

4.3.2 Influence of Methane Partial Pressure and Decomposition Temperature

The increase in reaction temperature has positive influence on methane decomposition because of its endothermic nature. However, higher temperature results in the faster deactivation due to the higher carbon buildup, which encapsulate the catalyst active phases (Amin et al., 2012). The reported initial hydrogen in the Table 4.4 is

increased when the temperature and P_{CH_4} was increased. The initial hydrogen production at P_{CH_4} of 0.8 atm was 26.9% at TCD temperature of 550 °C, which was increased to 56.7% at 650 °C. The findings are expected since TCD is an endothermic process. The similar trend was observed at other experimented P_{CH_4} of 0.2, 0.4, and 0.6 atm. However, the variation in H_2 (%) was negligible at P_{CH_4} of 0.2 atm. Hence, the chemical conversion improves when increasing the temperature (Nasir Uddin et al., 2014). Figure 4.19 (a-c) exhibit the methane decomposition rate with reaction time over *n*-NiO/SiO_2 catalyst at various partial pressures (0.2, 0.4, 0.6, and 0.8 atm) at temperature a) 650, b) 600, and c) 550 °C, respectively. The methane decomposition rate was decreased by time at all experimented temperatures as well as at all P_{CH_4}. Rate of methane conversion was highly stable at 550 °C, however the declivity in methane decomposition rate was increased at higher temperatures such as 600 and 650 °C. The rapid methane cracking and higher diffusion rate observed at higher temperature might be the reason of faster deactivation at 650 °C. The highest initial methane conversion rate at 650 °C and P_{CH_4} of 0.8 atm was 18.87 (mmol/g_{cat}.min), which declined to 5.78 (mmol/g_{cat}.min) by end of 90 min of analysis. However, the initial methane conversion rate at P_{CH_4} = 0.8 atm at 600 and 550 °C are 13.83 and 7.40 (mmol/g_{cat}.min), which abridged to 9.53 and 6.31 (mmol/g_{cat}.min) by the end of experimented duration. The results showed that the intensity in methane decomposition downward trend was lessen at lower decomposition temperature, which is endorsed by the activity loss plot in Figure 4.20. Figure 4.20 reveals that the activity loss increase as increasing temperature as well as decreasing the P_{CH_4}. *n*-NiO/SiO_2 catalyst was completely deactivated with in very short time of less than an hour, when methane stream with P_{CH_4}= 0.2 atm was decomposed at 650 and at 600 °C (Figure 4.19 and 4.20). Similar absolute deactivation was observed at 650 °C and P_{CH_4} of 0.4 atm, while the stability was higher than that at P_{CH_4} = 0.4 atm. Furthermore, it is remarkable to notice

that the *n*-NiO/SiO_2 catalyst exhibited lower catalytic activity loss at all studied P_{CH_4} at 550 °C, despite of the lower methane conversion (Figure 4.20).

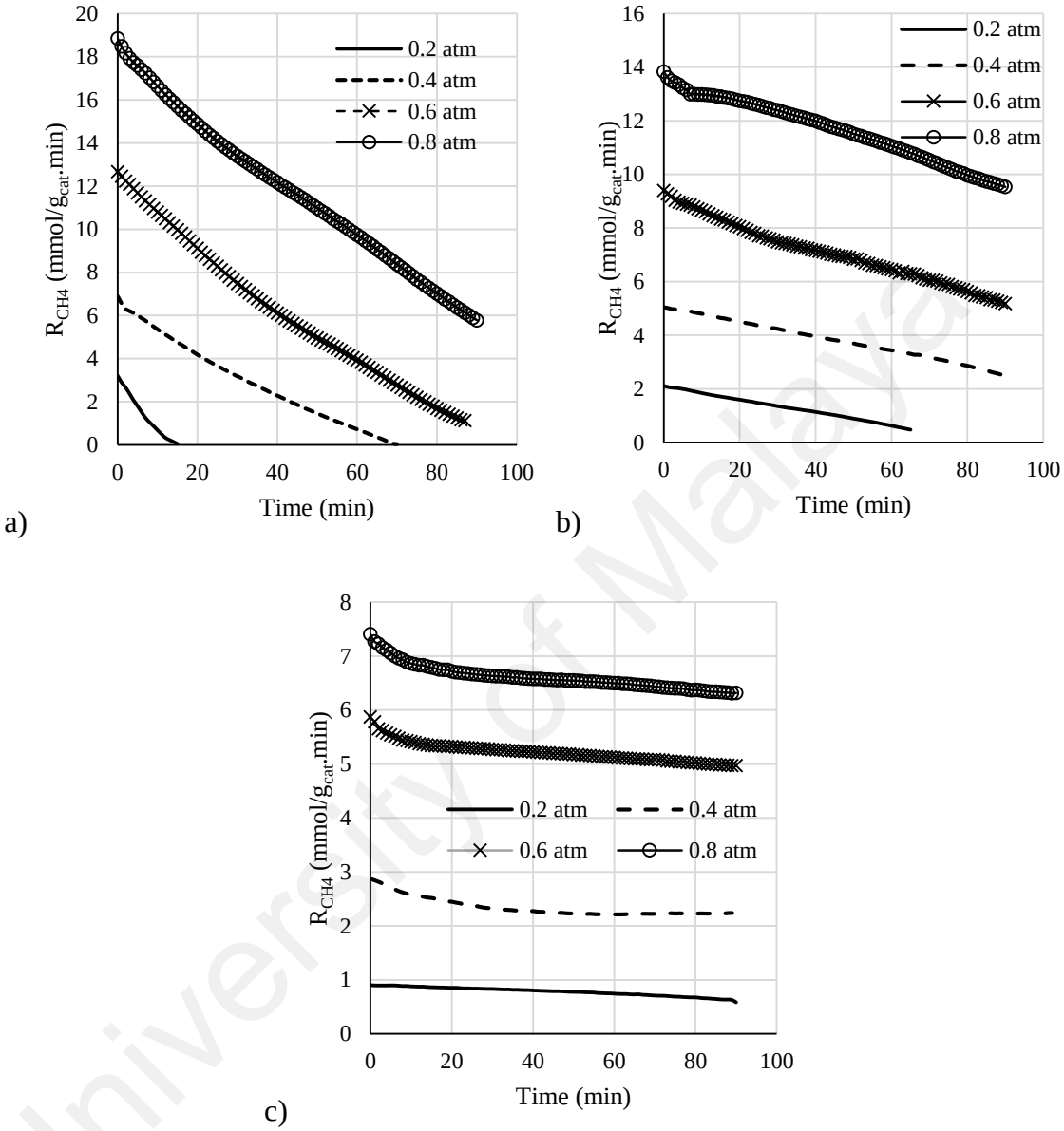

Figure 4.19 Methane decomposition rate (R_{CH_4}) vs. reaction time over *n*-NiO/SiO_2 catalyst at different partial pressure (0.2, 0.4, 0.6, and 0.8 atm) at temperature a) 650, b) 600, and c) 550 °C, respectively.

The catalyst exhibited lengthier activity for the whole studied P_{CH_4} range, except at 0.2 atm. The poor methane conversion at P_{CH_4}= 0.2 atm may be due to the insufficient quantity of reactant molecule in the stream. The highest initial methane decomposition rate at 650 °C, and the lengthier catalytic performance at 550 °C indicate the existence of

an optimum temperature for *n*-NiO/SiO_2 catalyst in between 550 and 650 °C, which is supported by the previous studies. However, a particular maximum value so called induction period through which methane conversion passed was absent with TCD over *n*-NiO/SiO_2 catalyst (T. V. Choudhary et al., 2001). Michalkiewicz & Majewska (2014) reported that the Ni-based catalysts deactivate rapidly below 450 °C and above 750 °C. Similar to the action of temperature, the methane decomposition rate was increased as P_{CH_4} increased. The initial decomposition rate at 600 °C was 2.11 (mmol/g_{cat}.min) at P_{CH_4} of 0.2 atm, which was increased to 13.8 (mmol/g_{cat}.min) at P_{CH_4} of 0.8 atm. Similar trend was exhibited by Ni–Co–Cu alloy catalyst in a kinetic evaluation by Lua & Wang (2013). They observed that the rate of hydrogen production was significantly increased from 0.2 atm to 1 atm, however, the catalytic activity found decreased gradually. Furthermore, the methane decomposition was increased as increasing the reaction temperature, supporting the endothermic nature of TCD and hence the diffusion rate also increases accordingly. Authors assumes that a faster carbon diffusion rate at a higher temperature would probably speed up the fragmentation of the catalyst and lead to deactivation in the case of 2Ni–1Co–1Cu (H. Y. Wang & Lua, 2014).

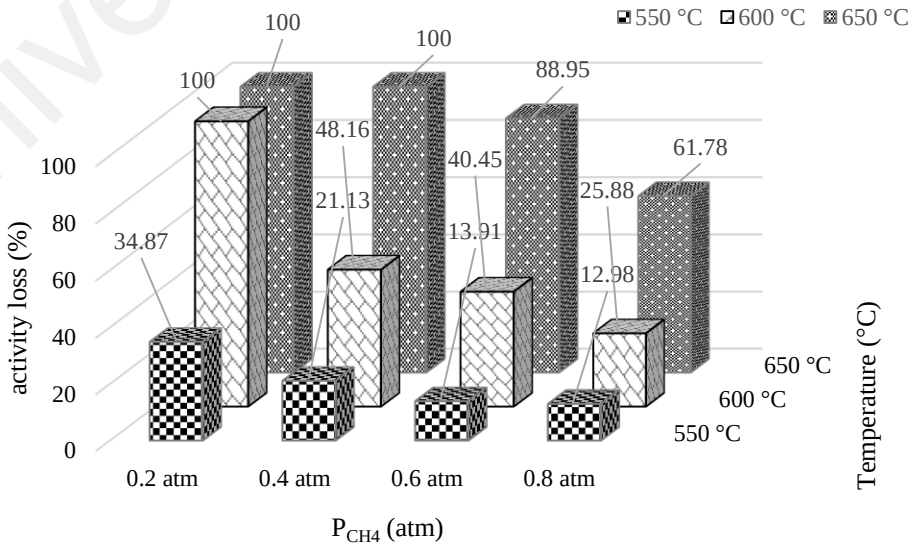

Figure 4.20 Activity loss in percentage at each temperature and methane partial pressure after 1.5 h of activity examination.

Figure 4.21 (a-d) depict the accumulation of as-produced carbon (g_{Dep}/g_{Cat}) with time at different temperatures (650, 600, and 550 °C) with different methane partial pressure (P_{CH_4}) such as 0.2, 0.4, 0.6, and 0.8 atm. At 650 °C, the quantity of carbon accumulation was increased by the time and, obviously, the deactivation of catalyst was observed after achieving a specific maximum carbon deposition at all experimented P_{CH_4}. However, the catalyst accumulation was efficiently maintained at 550 °C without going much deactivation at all the studied partial pressures.

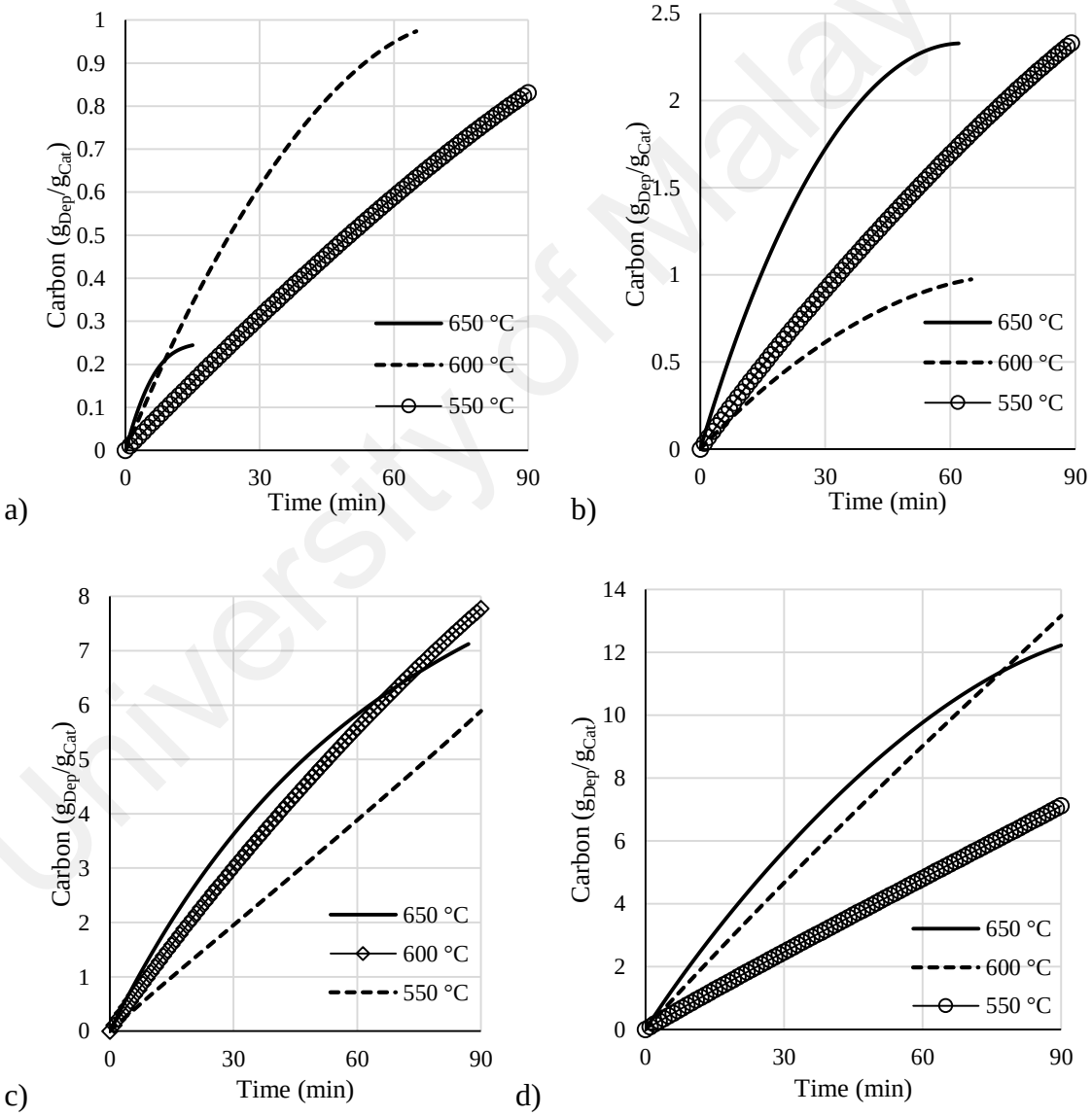

Figure 4.21 Accumulation of carbon with time over *n*-NiO/SiO_2 catalyst at different temperatures (650, 600, and 550 °C) at methane partial pressure (P_{CH_4}) a) 0.2, b) 0.4, c) 0.6, and d) 0.8 atm.

The carbon accumulation was negligible at P_{CH_4} of 0.2 atm at all experimented temperatures. The observed result is supported by the carbon yield plot in Figure 4.22. Similar trend was reported by Amin et al. (2012) over Ni supported on porous and non-porous alumina catalysts. They observed an increase in carbon formation with increasing P_{CH_4} from 0.5 to 0.9 atm. An increment in carbon deposition up to 45% was observed when P_{CH_4} increased from 0.9 to 1.0 atm at all experimented temperatures, except at 550 °C. Because of the endothermic nature of methane decomposition, the rate of carbon formation is mainly reliant on temperature. However, the effect of P_{CH_4} is very much dependent on temperature. The upsurge in carbon formation rate when increasing P_{CH_4} is more and more prominent as the temperature increases. Nevertheless, at 550 °C and below, the carbon formation remains almost unchanged when changing P_{CH_4}.

According to D. Chen et al. (2005), the low partial pressure results in the low driving force of carbon diffusion, which in turn caused in low carbon production over the Ni crystal sites. As such, the catalyst was ominously deactivated at low partial pressure (Michalkiewicz & Majewska, 2014). *n*-NiO/SiO_2 catalyst was completely deactivated at 650 °C at all experimented P_{CH_4} (Figure 4.20). The higher temperature such as 650 °C results in the condensation of free radicles or polyaromatic hydrocarbons which lead to the formation of carbon materials. According to Reilly & Whitten (2006), the condensed hydrocarbon free radicles are liable to hasty rearrangement at 650 °C and hence results in the recombination of radicles to generate hydrogen and diverse species of carbon over the catalyst. So that, the catalyst undergo a structural reorganization as increasing the carbon deposit, which results in the development of growth centers in the carbon fibers (Zavarukhin & Kuvshinov, 2004). Hence, the metallic active phases saturated with as-produced nanocarbon and prevent further methane decomposition results in catalyst deactivation at 650 °C (Figure 4.19). In addition, the observation is supported by the

highest initial methane conversion observed at 650 °C (Table 4.4 and Figure 4.19). Hence, the carbon removal rate from the active catalyst phase was essentially lower than the carbon production rate, which caused in the deposition of nanocarbon on the catalyst surface. The deposited nanocarbon encapsulate the active catalyst surface and prevent further chemisorption of methane molecule, which eventually decreases the catalyst lifetime. Hence, the weakening in the carbon formation rate at 550 and 600 °C with prolonged duration of reaction can be connected with the slow encapsulation of active metal phases with produced carbon (Anderson & Rodríguez, 2000).

It is reported that the factors such as saturation concentration of growth carbon fibers, diffusion flux area, carbon diffusion flux and diffusion path length regulate the catalyst deactivation and rate of carbon accumulation. The studies on TCD over activated carbon by Abbas & Wan Daud (2009) reveal that the increase in the temperature and P_{CH_4} results in the augmentation of methane diffusion rate, which lead to the enhancement in the methane decomposition rate and carbon deposition rate. This higher carbon accumulation results in the rapid filling of catalyst pore mouth which precludes the accessibility of methane molecule into the interiors pores of catalyst, which costs the catalyst deactivation.

The yield of as-produced nanocarbon exhibited in Figure 4.22, which was calculated using the equation 4.2 (Chai et al., 2011; Saraswat & Pant, 2011). The lowest carbon yield of 204.69, 499.13, and 544.52% was observed at 550, 600, and 650 °C, respectively, when the P_{CH_4} was 0.2 atm. It may be attributed to the low solubility of carbon in to metal active sites at low temperature and pressure (Michalkiewicz & Majewska, 2014). In addition to that, the methane molecules in the main stream which initiates the carbon material growth is very limited at 0.2 atm (Shaikjee & Coville, 2012).

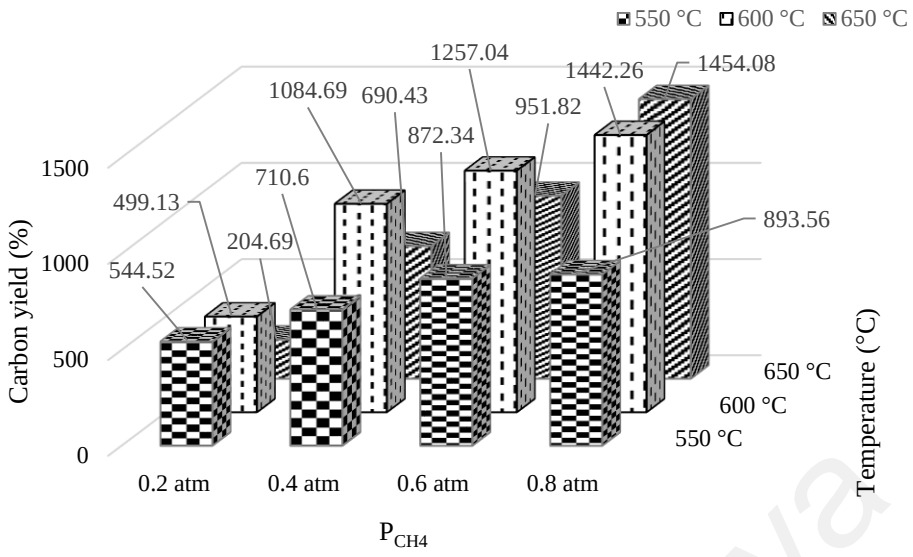

Figure 4.22 Carbon yield over *n*-NiO/SiO_2 catalyst at different reaction temperatures and methane partial pressures.

The carbon yield found to be increased as increasing the P_{CH_4} in the main stream at all experimented temperatures. However, the carbon yield at a specific P_{CH_4} was not followed an upward trend as increasing temperature. The Figure 4.22 evidently demonstrate that the yield at P_{CH_4} = 0.6 atm was 872.34, 1257.04, and 951.82% at 550, 600, and 650 °C respectively. The similar trend was also observed at P_{CH_4} of 0.2 and 0.4 atm. However, the carbon yield was 1442.26% at 600 °C when the P_{CH_4} was 0.8 atm, which is very close to the yield of 1454.08% observed at 650 °C, may be attributed to the availability of higher methane molecule over the active nickel phase to decompose in the very short residence time. Nevertheless, the maximum carbon yield was observed at 650 °C after the reaction was completed at P_{CH_4} of 0.8 atm. The observed results conspicuously accentuate the existence of an optimum temperature in TCD process.

The transmission electron microscopy images of catalyst after TCD experiment at temperature of 550, 600 and 650 °C in Figure 4.23 (a, c and e), respectively, clearly demonstrate that the lowest accumulation of nanocarbon occurred at P_{CH_4} of 0.2 atm, supporting the carbon yield plot in Figure 4.22. Furthermore, the aggregation of

nanocatalysts in the lower carbon growth is also observed at P_{CH_4} of 0.2 atm. Hence, the catalyst was covered by as-produced carbon crust which isolates them from the reaction medium and resist further methane decomposition, which results in the production of nanofilaments with lower length at P_{CH_4} = 0.2 atm.

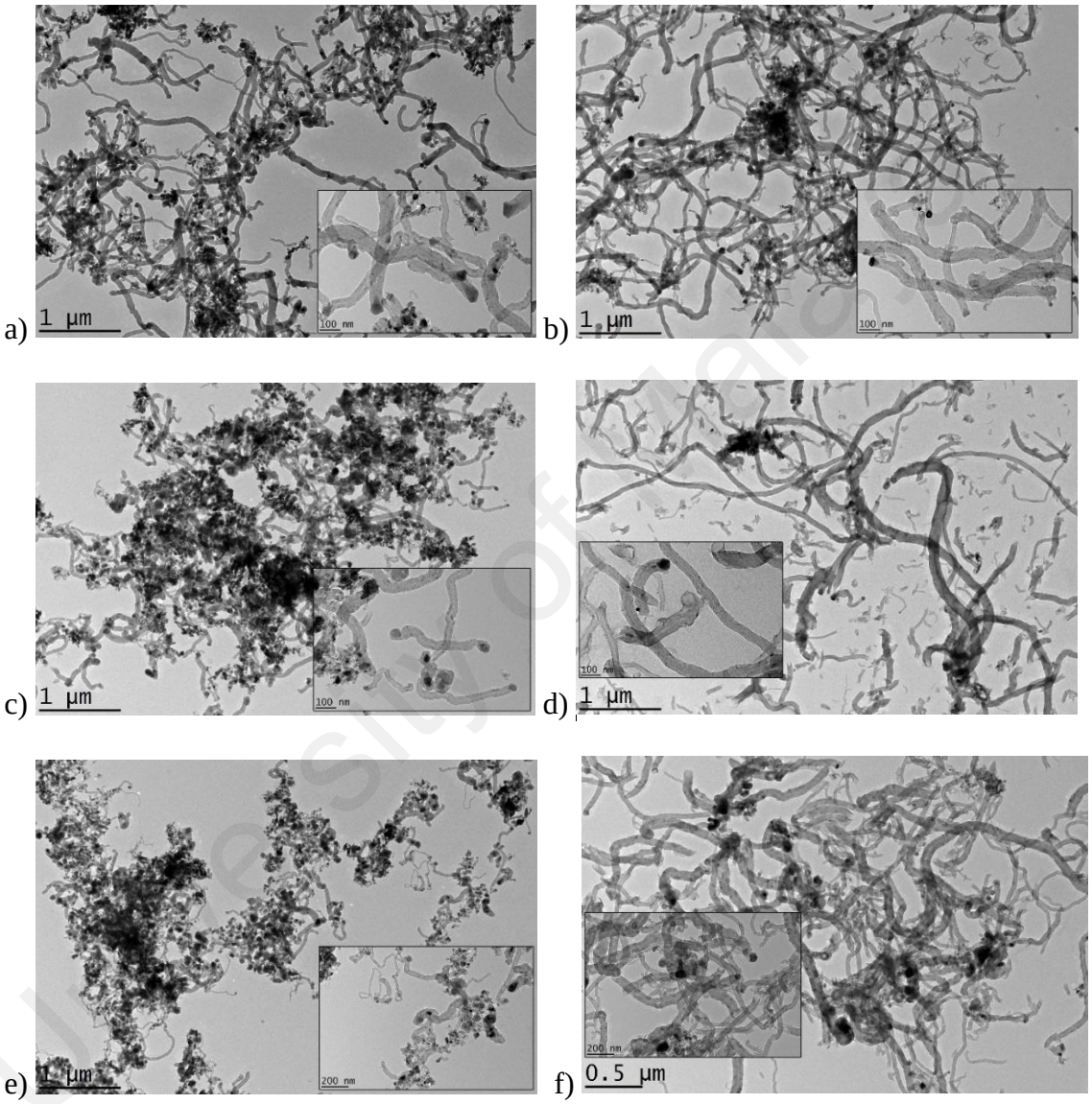

Figure 4.23 TEM images of produced nanocarbon after TCD analysis at a) T = 550 °C and P_{CH_4} = 0.2 atm, b) T = 550 °C and P_{CH_4} = 0.8 atm, c) T = 600 °C and P_{CH_4} = 0.2 atm, d) T = 600 °C and P_{CH_4} = 0.8 atm, e) T = 650 °C and P_{CH_4} = 0.2 atm, and f) T = 650 °C and P_{CH_4} = 0.8 atm. Inset figures exhibit the higher resolution TEM images at respective reaction condition.

The morphological variation of produced nanocarbon with experimental conditions was examined using the TEM images shown in Figure 4.23 (a-f). A large number of nanocarbons were accumulated over the catalyst after TCD, especially at higher temperature and P_{CH_4}. The black spot in the images indicates the Ni-metal particles. Heavy aggregation of Ni-particles was observed at all temperatures when P_{CH_4} = 0.2 atm [Figure 4.23 (a, c, and e)]. However, the efficient tip-growth carbon formation mechanism occurred, especially at higher partial pressure of 0.8 atm resulted in the formation of lengthier nanocarbons [Figure 4.23 (b, d, and f)]. Hence, the Ni-particles can be seen inserted the sharp tail of pear/diamond shape to the nanocarbon at their tip, which reinforces many previous works (Baird et al., 1974; Baker et al., 1972; Tesner et al., 1970). The transformation of spherical like structure to pear/diamond shape after TCD is discussed in section 4.2.3.2. The length and size of the accumulated nanocarbon varied at different experimental conditions. The measurement of length of as-produced nanocarbons was difficult as they existed in an interweaving manner. However, it can speculate that the length exceeded some micrometers. The higher resolution TEM images shown inset to the Figure 4.23 demonstrate the "*fish-bone*" or "*bamboo*" morphology in the internal cavity of as-produced nanocarbon. Furthermore, the nanocarbons with open end, closed end and those embedded Ni-particles are also can be seen in the TEM micrographs, similar to those reported in 4.2.3.2. The diameter of nanocarbons were measured with ImageJ software. 60 nanocarbons were considered to measure the average diameter from TEM images, shown in Table 4.5. The TEM average diameter of nanocarbons are evidently close to the average size of Ni-particles calculated from XRD pattern using Scherrer equation, shown in Table 4.6. At 650 °C, the outer diameter of produced nanocarbon at P_{CH_4} of 0.2 and 0.8 atm are 33.84±4.82 and 46.53±8.94 nm, respectively, which are very close to the calculated XRD crystallite size of 31.52 and 36.42 nm for Ni-particles. Experimental values at 550 and 600 °C are also followed the

same trend. Similarly, the reviews on the pre-experimented studies reveal that the outer diameter of the carbon nanotubes greatly depends on the size of Ni particles: larger Ni particle leads to carbon nanotubes with larger diameter (Guevara et al., 2010).

Table 4.5 The average diameter measured from the TEM images at respective reaction conditions.

Temperature	Methane partial pressure	
	0.2 atm	0.8 atm
550 °C	48.04±9.15 (nm)	44.33±7.61 (nm)
600 °C	44.45±7.36 (nm)	48.67±8.26 (nm)
650 °C	33.84±4.82 (nm)	46.53±8.94 (nm)

Table 4.6 Crystallite sizes of Ni-metal nanostructures after TCD process at respective reaction conditions.

Temperature	Methane partial pressure			
	0.2 atm	0.4 atm	0.6 atm	0.8 atm
550 °C	35.56 nm	36.23 nm	31.57 nm	31.39 nm
600 °C	32.52 nm	24.68 nm	28.18 nm	31.26 nm
650 °C	31.52 nm	28.35 nm	36.61 nm	36.42 nm

XRD patterns of the *n*-NiO/SiO_2 catalyst after TCD analysis at 550, 600, and 650 °C are exhibited in Figure 4.24 (a-c), respectively. The presence of graphitic carbon is characterized by the peaks at $2\theta = 26$ and 42°. The intensity, width at half maxima and 2θ values slightly varied with experimental conditions. The intensity of graphitic carbon peaks when the P_{CH_4} was 0.2 atm at all temperatures were very less compared to other P_{CH_4}, clearly demonstrate the lower carbon accumulation. The observed result supports the carbon yield chart in Figure 4.22. However, the intensity of peaks correspond to graphitic carbon increased with temperature. The positions of the diffraction peaks for

graphitic carbon are in good agreement with those given in JCPDS No.: 98-005-3781 for hexagonal graphitic carbon. The diffraction at 2θ = 44, 51 and 76° categorized for the cubic Ni-phases, which resembles with JCPDS No.: 98-005-3808.

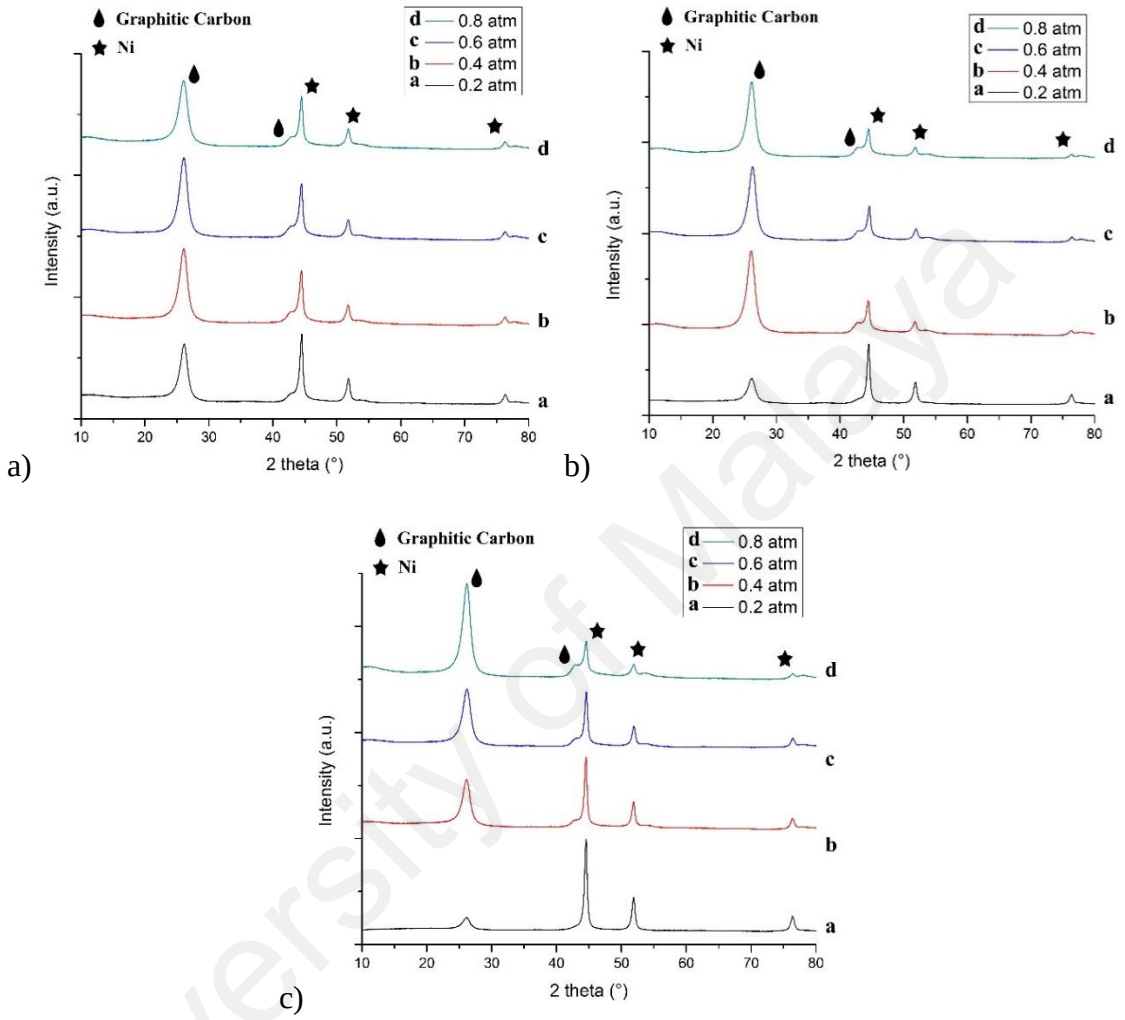

Figure 4.24 XRD patterns of *n*-NiO/SiO_2 catalyst after TCD analysis at a) 550, b) 600, and c) 650 °C.

4.3.3 Methane Decomposition Kinetics over *n*-NiO/SiO_2 Catalyst

According to the methane decomposition balanced equation 1.1 ($CH_4 \rightarrow 2H_2 + C$), the number of accumulated carbon molecules over the catalyst are the half of the number of hydrogen molecules evolved during the process. Hence, the maximal specific molar carbon formation rate (R_{max}) and its variation by time was characterized from the instantaneous hydrogen and methane values recorded in Rosemount Analytical X-STREAM analyzer. R_{max} was calculated by the derivative of the equation of the curve

fitting of mass gain with time and by dividing it with atomic weight of carbon, the final value gives the R_{max} in (mol/g_{cat}.min). The R^2 values were higher than 0.99. In the kinetic point of view, temperature and pressure are the main parameters influencing hydrogen formation rate over time. Figure 4.25 exhibits the relationship between the maximal specific molar carbon formations with temperature for different P_{CH_4}. The results showed that R_{max} values increased with temperature at constant P_{CH_4} values. R_{max} values at 650 °C were increased from 0.0032 (mol/g_{cat}.min) at P_{CH_4} = 0.2 atm to 0.018 (mol/g_{cat}.min) at P_{CH_4} = 0.8 atm. In accordance to the results at 650 °C, R_{max} values were increased at 550 and 600 °C. Similarly, the R_{max} values shift upward as increasing P_{CH_4} at constant temperature, indicates faster rate of carbon deposition at higher temperature and P_{CH_4}, as mentioned before.

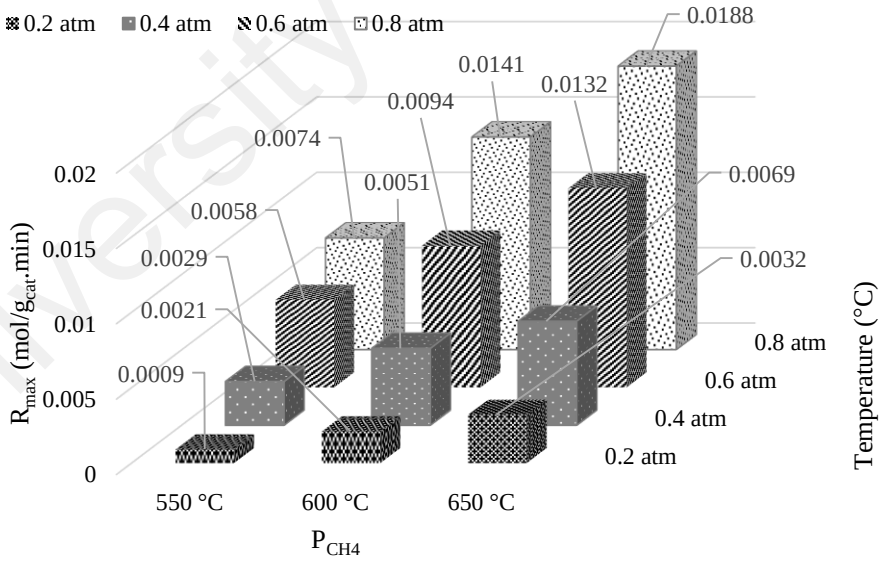

Figure 4.25 Maximal specific molar carbon formation rate vs. temperature for different methane partial pressure.

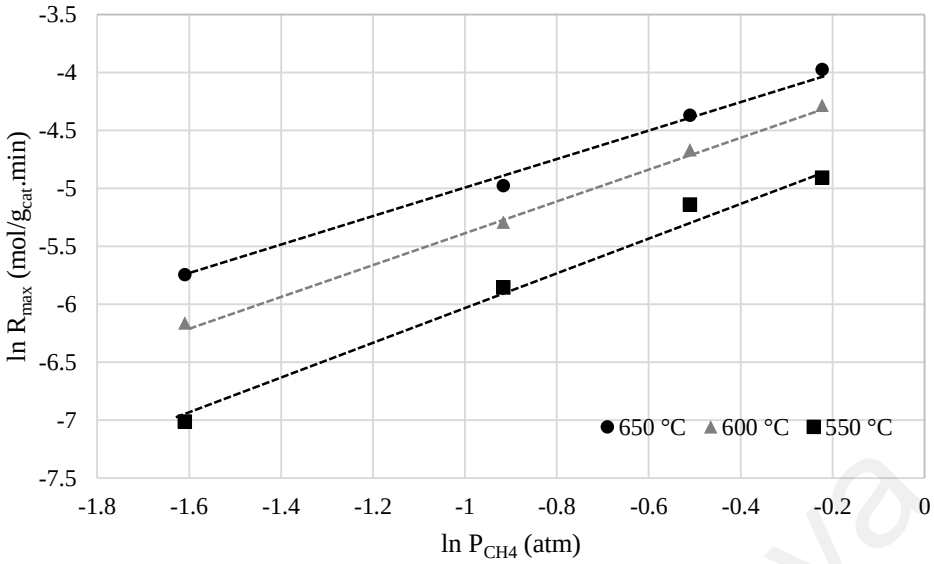

Figure 4.26 Dependence of the ln R_{max} vs. ln P_{CH_4} at different temperatures for TCD reaction over *n*-NiO/SiO_2 catalyst (reaction conditions: catalyst weight = 0.6 g, feed consisting of methane balanced with nitrogen, P_{CH_4} of 0.2–0.8, total flow rate = 0.64 L/min).

Figure 4.26 exhibits the reliance of ln (R_{max}) and ln (P_{CH_4}) calculated at different experimented temperatures. The slopes from Figure 4.26 represents the order of reaction and the values were 1.28, 1.36, and 1.56 at 650, 600, and 550 °C with regression coefficient in the range of 0.99-1. Hence, the average order of methane decomposition over *n*-NiO/SiO_2 catalyst was found to be 1.40. According to the literature survey, the methane reaction order was reported to be 1 for supported metal catalyst (Amin et al., 2011) and 0.5–1 for carbon catalyst (Abbas & Wan Daud, 2010). Hence, the maximal reaction rate can be written as:

$$R_{max} = kpP_{CH4}^{1.4} \quad (4.9)$$

The rate constant kp can be determined from the Arrhenius law:

$$kp = Ae^{-Ea/RT} \quad (4.10)$$

where A is the pre-exponential factor, Ea is the activation energy (kJ mol^{-1}) and R is the gas constant (8.31 JK^{-1} mol^{-1}). Typically, it is expressed as follows:

$$\ln (kp) = \ln (A) - \frac{Ea}{R} . \frac{1}{T} \qquad (4.11)$$

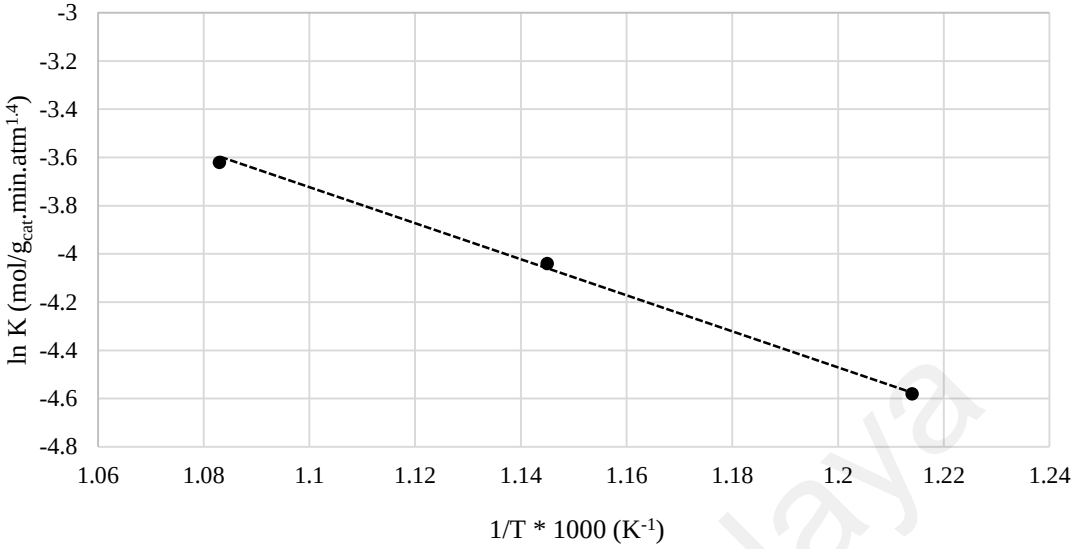

Figure 4.27 Arrhenius plot of lnK versus (1/T) (reaction conditions: 0.6 g catalyst, P_{CH4} of 0.2–0.8, total flow rate = 0.64 L/min).

The slope of logarithm of the rate constant vs. the reciprocal temperature (Kelvin) plot in Figure 4.27 gave the activation energy for the methane decomposition reaction over *n*-NiO/SiO_2 catalyst. The slope of the straight line according to the equation (4.11) is –Ea/R. Hence, the value of Ea was found to be 60.9 kJ mol^{-1} from Figure 4.27. Hence, the maximum rate can then be expressed as:

$$R_{max} = Ae^{-Ea/RT} . P_{CH4}^{1.4} = 4331.7 . e^{-7328.5/T} . P_{CH4}^{1.4} \qquad (4.12)$$

The calculated activation energy value is very close to the pre-reported Ea values for TCD over Ni-based catalysts, such as 60 kJ mol^{-1} (Sharif Zein et al., 2004), 64.6 kJ mol^{-1} (Kvande et al., 2008) and 61.77 kJ mol^{-1} (Nasir Uddin et al., 2014). The reported Ea from some remarkable research contribution in TCD over different Ni-based catalysts are furnished in Table 2.3. H. Y. Wang & Lua (2014) were carried out kinetic studies on methane decomposition over Ni catalyst and found that the average reaction order and activation energy for the methane decomposition over the unsupported nickel was 0.63 and 65.4 kJ mol^{-1}. The reported Ea for the TCD process with nickel based catalysts ranged

in between 50 and 90 kJ mol^{-1}. The wide range of reported activation energies may be due to many factors, including the difficulty of collecting true kinetic data and the highly dynamic characteristics of the process (Kvande et al., 2008).

The observed Ea of 60.9 kJ mol^{-1} for TCD over *n*-NiO/SiO_2 catalyst is very much smaller than the C-H bond energy in CH_4 molecule. CH_4 molecule is highly stable with tetrahedral geometrical structure supported with very strong four C-H bonds with a bond energy of 434 kJ mol^{-1}. Hence, the methane involved reactions are thermodynamically unfavorable as per the Gibbs free energy values (ΔG_r^0 = +50.7 kJ mol^{-1}). Therefore, the gaseous methane decomposition requires a high temperature (> 1200 °C) to activate the C-H bond to twitch a free radical reaction (Havran et al., 2011). Furthermore, studies showed that the initial C-H bond cracking is the rate determining step over the metal catalyst at high temperatures (Abbott & Harrison, 2008). *n*-NiO/SiO_2 catalyst reduced the Ea to 60.9 kJ mol^{-1}, which is very much lower than the C-H bond energy of 434 kJ mol^{-1}. This huge difference in Ea and C-H bond energy results in the absence of induction period or activation stage in TCD reaction and hence the catalyst deactivation starts to deactivate just after the contact with CH_4 molecules. This result is supported with observed gradual decrease in methane decomposition rate in Figure 4.19.

4.3.4 Summary of Major Findings

The calculation based on the specific molar carbon formation rate at different methane partial pressure and temperature showed that the order of methane decomposition reaction is 1.40 and the *n*-NiO/SiO_2 catalyst reduced the Ea to 60.9 kJ/mol.

4.4 PART 4: GOVERNANCE OF POROSITY AND METHANE DECOMPOSITION ACTIVITY SUSTAINABILITY OF *n*-NiO/SiO_2 CATALYST BY CHANGING SYNTHESIS PARAMETERS

Table 3.2 The quantity of each substrates and the solvents used for the production of *n*-NiO/SiO_2. [Table 3.2 copied from page 75 for ease of understanding the compositions]

No.	Catalyst	$Ni(NO_3)_2.6H_2O$ (g)	TEOS (mL)	C18TMS (mL)	Solvent
1	*n*-NiO/SiO_2_(1)	5.81	0.3	0.3	Ethanol
2	*n*-NiO/SiO_2_(2)	11.63	0.6	0.6	Ethanol
3	*n*-NiO/SiO_2_(3)	17.45	1.2	1.2	Ethanol
4	*n*-NiO/SiO_2_(4)	17.45	0.6	0.6	Ethanol
5	*n*-NiO/SiO_2_(5)	17.45	0.3	0.3	Ethanol
6	*n*-NiO/SiO_2_(6)	17.45	1.2	0	Ethanol
7	*n*-NiO/SiO_2_(7)	17.45	0	1.2	Ethanol
8	*n*-NiO/SiO_2_(8)	17.45	0.9	0.3	Ethanol
9	*n*-NiO/SiO_2_(9)	17.45	0.3	0.9	Ethanol
10	*n*-NiO/SiO_2_(10)	17.45	0.6	0.6	Methanol
11	*n*-NiO/SiO_2_(11)	17.45	0.6	0.6	2-Propanol
12	*n*-NiO/SiO_2_(12)	17.45	0.6	0.6	n-Butanol

4.4.1 XRD

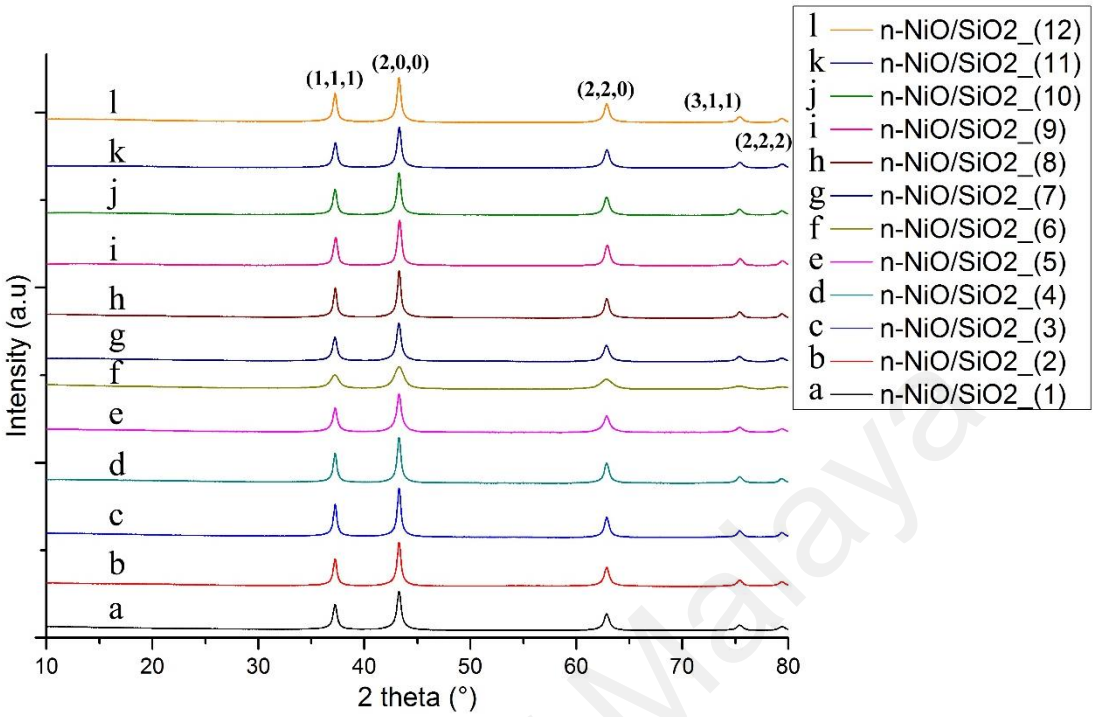

Figure 4.28 XRD patterns of each *n*-NiO/SiO_2 catalysts before reduction treatment with hydrogen. Planes of corresponding peaks are indicated.

Figure 4.28 exhibits the XRD patterns of all freshly prepared *n*-NiO/SiO_2 catalysts before the reduction treatment. The extension of catalytic structural order and apparent size of crystallites are extensively exposed by XRD analysis. Hence, the endurance of catalyst and catalytic activity are verily reliant to those characteristics. Figure 4.28 demonstrates the variance of intensity, broadness, and the position of diffraction patterns according to the variation in precursor quantity and ratios. (h, k, l) miller indices of three major diffraction peaks of *n*-NiO/SiO_2 catalysts are (1, 1, 1), (2, 0, 0), and (2, 2, 0), respectively, which corresponds to the reflections of the NiO solid phases. However, pattern for SiO_2 is absent because of its X-ray amorphous characteristics. Table 4.7 furnishes detailed XRD results. The average crystallite size of *n*-NiO/SiO_2 catalysts calculated using global Scherrer equation (furnished in Table 4.7) were evidently close to the mean particle size obtained from BET analysis (furnished in

Table 4.8). The calcined *n*-NiO/SiO_2 catalysts exhibited cubic NiO phase with typical reflections at 2θ = 37°, 43°, and 62°, respectively. The intensity, width at half maxima and 2θ values slightly varied with precursor ratios. The positions of the diffraction peaks are in good agreement with those given in JCPDS No.: 01-073-1523 for NiO phase. The variation of NiO dispersion in silicate formation media results in the deviation of diffraction peaks as showed in Table 4.7. However, fairly higher content of silicate precursors may reduce the dispersion effect even after ultrasonic treatment (Yao et al., 2011). Among the prepared catalysts, *n*-NiO/SiO_2_(6) prepared with 1.2 mL of TEOS exhibited NiO diffraction peaks with moderately lower intensity approves its lower structural ordering. Accordingly, *n*-NiO/SiO_2_(6) demonstrated poor catalytic stability at 625 °C (Figure 4.32). However, all other catalysts prepared with 1.2 mL of C18TMS and mixture of TEOS and C18TMS shown better crystal order and catalytic performance. Henceforth, porous silicate produced with C18TMS porogen interact with NiO phases more effectively and executed a better catalysis conditions and resulted an improved thermocatalytic methane decomposition. However, examined solvents do not make any significant influence on crystallinity. Catalysts prepared with methanol, ethanol, 2-propanol, and n-butanol exhibited almost similar peak intensity and Scherrer crystal size as shown in Figure 4.28 and Table 4.7.

Table 4.7 2θ angle of major diffraction peaks in degree, crystalline size corresponds to each peak according to Scherrer equation and their average value in nm, interplanar distances in Å and crystal structure of catalysts with different precursor concentration before TCD process from XRD analysis.

Sample	2θ (°)	Ni (111) (nm)	Ni (200) (nm)	Ni (220) (nm)	Avg. crystal size (nm)	Interplanar distances, d (Å)	Structure formed
n-NiO/SiO_2_(1)	37.25, 43.27, 62.81	31.13	26.85	23.77	27.25	2.41373, 2.09085, 1.47935	Cubic
n-NiO/SiO_2_(2)	37.21, 43.26, 62.85	31.13	31.74	31.69	31.52	2.41585, 2.09105, 1.47847	Cubic
n-NiO/SiO_2_(3)	37.22, 43.27, 62.84	34.25	31.44	31.18	32.29	2.41520, 2.09077, 1.47751	Cubic
n-NiO/SiO_2_(4)	37.22, 43.26, 62.81	31.13	31.74	34.57	32.48	2.41546, 2.09133, 1.47944	Cubic
n-NiO/SiO_2_(5)	37.22, 43.26, 62.86	31.13	34.74	34.58	33.48	2.41553, 2.09124, 1.47842	Cubic
n-NiO/SiO_2_(6)	37.21, 43.23, 62.69	38.04	31.80	13.57	27.80	2.41625, 2.09090, 1.48191	Cubic
n-NiO/SiO_2_(7)	37.22, 43.26, 62.84	26.34	24.93	23.77	25.01	2.41532, 2.09121, 1.47876	Cubic
n-NiO/SiO_2_(8)	37.23, 43.27, 62.83	34.25	31.74	38.03	34.67	2.41473, 2.09072, 1.47902	Cubic
n-NiO/SiO_2_(9)	37.30, 43.33, 62.91	24.46	23.28	25.36	24.37	2.41079, 2.08805, 1.47726	Cubic
n-NiO/SiO_2_(10)	37.24, 43.27, 62.82	29.54	30.09	35.57	31.73	2.41392, 2.09080, 1.47926	Cubic
n-NiO/SiO_2_(11)	37.24, 43.31, 62.89	29.54	25.94	39.04	31.51	2.41391, 2.08915, 1.47778	Cubic
n-NiO/SiO_2_(12)	37.22, 43.27, 62.79	32.13	32.74	28.15	31.01	2.41534, 2.09084, 1.47980	Cubic

4.4.2 Nitrogen Adsorption–Desorption Measurements

Table 4.8 Surface characteristics of *n*-NiO/SiO_2 nano-catalyst from N_2 adsorption-desorption analysis.

Catalyst	Single point SA[a] (m^2/g)	BET SA (m^2/g)	Micropore area[b] (%)	Mesopore + external area[c] (%)	Micropore volume[d] (cm^3/g)	Mesoporous volume (cm^3/g)	Total pore volume[e] (cm^3/g)	BET pore size (nm)	Mean particle size (nm)
n-NiO/SiO_2_(1)	91.50	93.18	13.1	86.9	0.0054	0.1747	0.1801	9.987	32.19
n-NiO/SiO_2_(2)	90.62	92.53	13.5	86.5	0.0060	0.1995	0.2055	8.901	32.42
n-NiO/SiO_2_(3)	102.64	104.6	14.9	85.1	0.0041	0.2107	0.2148	8.235	28.65
n-NiO/SiO_2_(4)	81.74	83.26	16.1	83.9	0.0059	0.1444	0.1503	8.182	36.02
n-NiO/SiO_2_(5)	71.60	72.86	10.7	89.3	0.0030	0.1414	0.1444	7.940	41.16
n-NiO/SiO_2_(6)	115.76	117.90	8.1	91.9	0.0051	0.1804	0.1855	7.072	25.44
n-NiO/SiO_2_(7)	70.19	71.84	11.1	88.9	0.0066	0.1747	0.1813	9.273	41.75
n-NiO/SiO_2_(8)	84.76	86.92	13.7	86.3	0.0065	0.1538	0.1603	7.400	34.51
n-NiO/SiO_2_(9)	50.29	51.51	26.8	73.2	0.0079	0.1192	0.1271	6.702	58.92
n-NiO/SiO_2_(10)	77.65	79.43	14.2	85.8	0.0056	0.1809	0.1864	9.525	37.76
n-NiO/SiO_2_(11)	71.91	73.65	16.0	84.0	0.0058	0.1604	0.1663	9.036	40.73
n-NiO/SiO_2_(12)	78.85	80.87	17.6	82.4	0.0071	0.1863	0.1934	9.744	37.09

[a] Represents the values calculated at a relative pressure (P/P_o) of N_2 equal to 0.301.
[b-d] Represents the values calculated from t-plot method.
[e] Represents the total pore volume evaluated from nitrogen uptake at a relative pressure (P/Po) of N_2 equal to 0.98.

The detailed porosity analysis reports of prepared catalysts from BET analysis are exhibited in Table 4.8 and in Appendix B. The BET particle size was calculated from the specific surface area by using the equation 4.1 (B. Akbari et al., 2011; Bowen, 2002), assuming that the particles are in a spherical form. Furthermore, the pore diameter distributions of the samples calculated from desorption division of the isotherm were calculated using Barrett-Joyner-Halenda (BJH) method is shown in Appendix C. As we haven't used any surfactants in our methodology, the accomplishment of free pores by removing any solvent or other organic moieties were easily achieved by calcination at 450 °C. The adsorption–desorption isotherms (Appendix B) indicated that the prepared catalysts exhibit Type IV physisorption showing their mesoporous characteristics (Sing, 1985). Conversely, the initial portion of physisorption isotherms were Type I, indicating the presence of small quantity of micropores with in the materials. The porosity results are exhibited in Table 4.8 confirmed that the addition of C18TMS porogen in to catalyst synthesis mixture increased the microporous area in the material. *n*-NiO/SiO_2 prepared with 0.3 mL of TEOS and 0.9 mL of C18TMS exhibited 26.8% of microporous area. While, catalyst prepared with 1.2 mL of TEOS showed lowest microporous area (8.1%) among the prepared catalysts. Furthermore, considerable shrinkage observed with hysteresis loop of *n*-NiO/SiO_2_(6) prepared with 1.2 mL of TEOS in Appendix B (f), might be attributed to the lower pore size and volume. The lower porosity of *n*-NiO/SiO_2_(6) may be because of the lack of formation of internal pores in silica network by C18TMS polymerization. However, C18TMS alone was also incapable to produce higher quantity of micropores as that formed with mixture of TEOS and C18TMS. The size of nano-particles were comparable at all experimental conditions. However, catalyst prepared with 1.2 mL of C18TMS and mixture of C18TMS and TEOS exhibit slightly higher BET particle size than that of catalyst produced with 1.2 mL of TEOS. In addition to that, *n*-NiO/SiO_2 prepared with methanol solvent exhibit the highest particle size of 58

nm. Particles with larger BET size might be attributed to the existence of particles with more than one crystals with in it, because of asymmetrical polymerization of the silica network by C18TMS (J. Lee et al., 2008). Hence, it is well demonstrated in XRD analysis that the crystal size of all catalysts prepared with mixture of C18TMS and TEOS with various solvents exhibited fairly similar crystal size. BJH pore width distributions of prepared catalysts covered a range from 0 nm to 200 nm (see Appendix C). However, major quantity of pores having width below 30 nm. Furthermore, very limited number of pores can be seen with size above 50 nm. The pores observed in the macroporous region with pore size of above 50 nm could be attributed to the formation of voids due to inter-nanoparticle interaction.

4.4.3 H_2-TPR

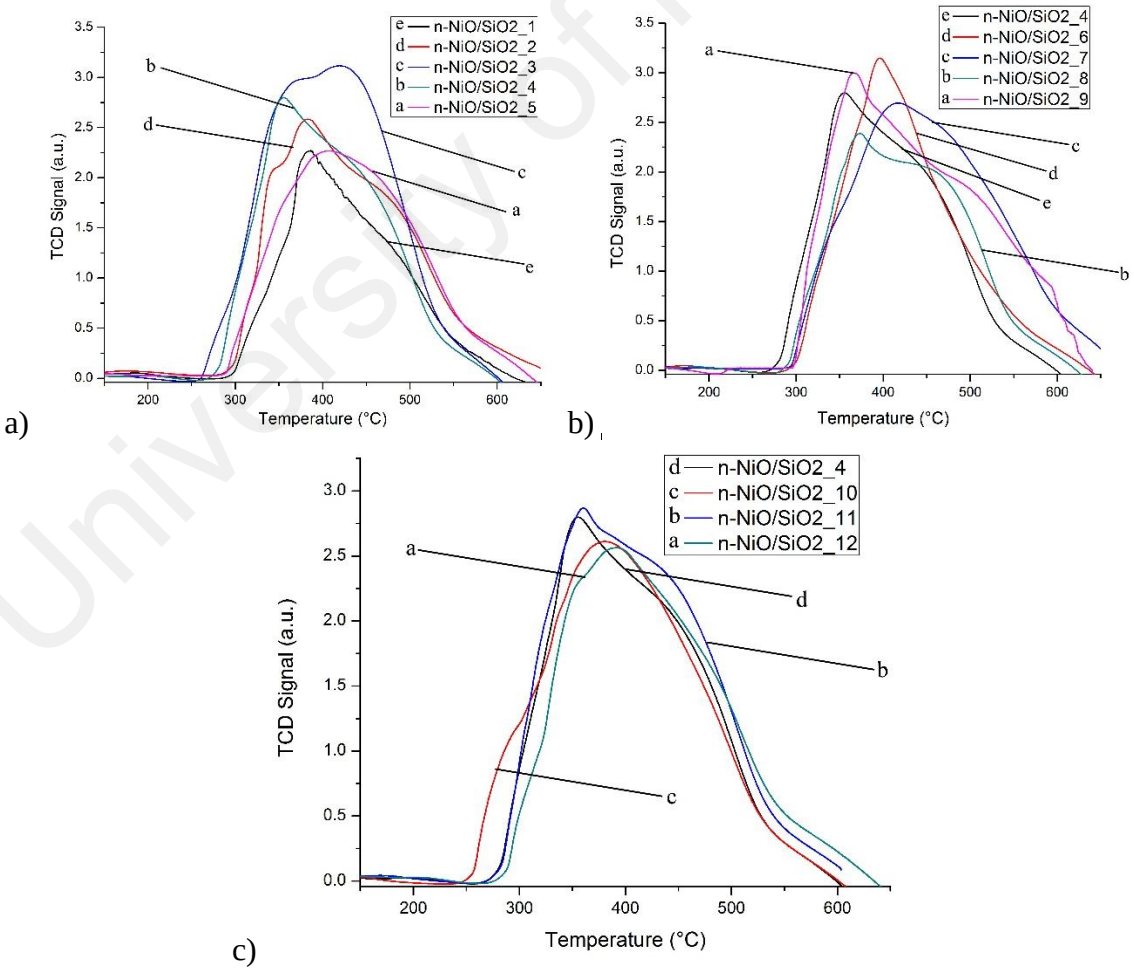

Figure 4.29 Effect of different precursor condition on H_2-TPR profile a) nickel/silicate ratio, b) C18TMS/TEOS ratio, and c) solvent effect.

The influence of nickel/silicate ratio, C18TMS/TEOS ratio and different solvents on the reduction characteristics of produced *n*-NiO/SiO_2 catalysts are exhibited in Figure 4.29 (a-c), respectively. Detailed peak description and the volume of hydrogen consumed by each catalysts are exhibited in Table 4.9. The H_2-TPR profile of *n*-NiO/SiO_2 catalysts prepared with various concentration of precursors and solvents exhibited only one peak in between 250 and 650 °C, could be assigned to the complete reduction of NiO species, supporting previous records (L. Li et al., 2012; L. Li et al., 2012b). The single peak observed with H_2-TPR profiles indicate a homogenous interaction between metal and support. The hydrogen conception quantified from H_2-TPR profile using ChemiSoft TPx V1.02 software indicated that the volume of hydrogen consumed has increased as increasing the quantity of C18TMS in preparation mixture. *n*-NiO/SiO_2_(3) and *n*-NiO/SiO_2_(7) prepared with 1.2 mL of C18TMS consumed 291.349 mL/g_{cat} and 282.038 mL/g_{cat}, respectively, are the highest hydrogen conception recorded among the prepared catalysts. These higher hydrogen conception could be attributed to the difficulty to reduce NiO because of their higher microporous characteristics, supporting BET results in Table 4.8. Hence, the metal support interaction is solidly dependent upon the C18TMS/TEOS ratio. However, solvents such as methanol, ethanol, 2-propanol and n-butanol exhibited negligible variation on the reduction characteristics. In general, *n*-NiO/SiO_2 prepared by co-precipitation cum modified Stöber method exhibited a broader H_2-TPR peak than those prepared by conventional preparation method, indicating the stronger metal-support interaction occurring in modified Stöber method (L. Li et al., 2012; Xie et al., 2011). Hence, a denser silicate support was formed over *n*-NiO and resulted in the difficulty of hydrogen diffusion and hence *n*-NiO reduction. Moreover, the extension of reduction profile of *n*-NiO/SiO_2_(7) to a higher temperature zone compared to other catalysts might be accredited to higher sized NiO particles, as reported in BET results (Table 4.8).

Table 4.9 Hydrogen conception and TPR profile details of each catalyst

Catalyst	Temperature at Maximum (°C)	Volume (mL/g STP)	Peak Height (a.u.)
n-NiO/SiO_2_(1)	386.6	227.327	2.284
n-NiO/SiO_2_(2)	377.0	250.402	2.238
n-NiO/SiO_2_(3)	420.3	291.349	3.230
n-NiO/SiO_2_(4)	355.6	261.602	2.859
n-NiO/SiO_2_(5)	407.1	226.857	2.267
n-NiO/SiO_2_(6)	396.2	243.281	3.172
n-NiO/SiO_2_(7)	383.3	282.038	2.563
n-NiO/SiO_2_(8)	366.6	254.871	2.999
n-NiO/SiO_2_(9)	373.6	271.173	2.419
n-NiO/SiO_2_(10)	379.9	254.357	2.633
n-NiO/SiO_2_(11)	360.4	261.492	2.915
n-NiO/SiO_2_(12)	391.6	255.658	2.573

4.4.4 TEM and EDX

TEM images and comparison chart of average particle sizes are exhibited in Figure 4.30 and 4.31, respectively. The average particle size from TEM clearly supported XRD (Table 4.7), BET (Table 4.8) and H_2-TPR results (Table 4.9). *n*-NiO/SiO_2 particles exhibited almost uniform distribution in the TEM scanned area with a minor standard deviation as shown in Figure 4.31. However, the particles showed different shapes. Furthermore, the TEM images visualize that the catalyst surfaces become rougher as molar ratio of C18TMS increases in the synthesis mixture, because of the sparse and irregular polymerization with in the silica networks as perceived in XRD and BET results (J. Lee et al., 2008). Moreover, the magnetic properties of *n*-NiO resulted in particle agglomeration in some area (Zou et al., 2014).

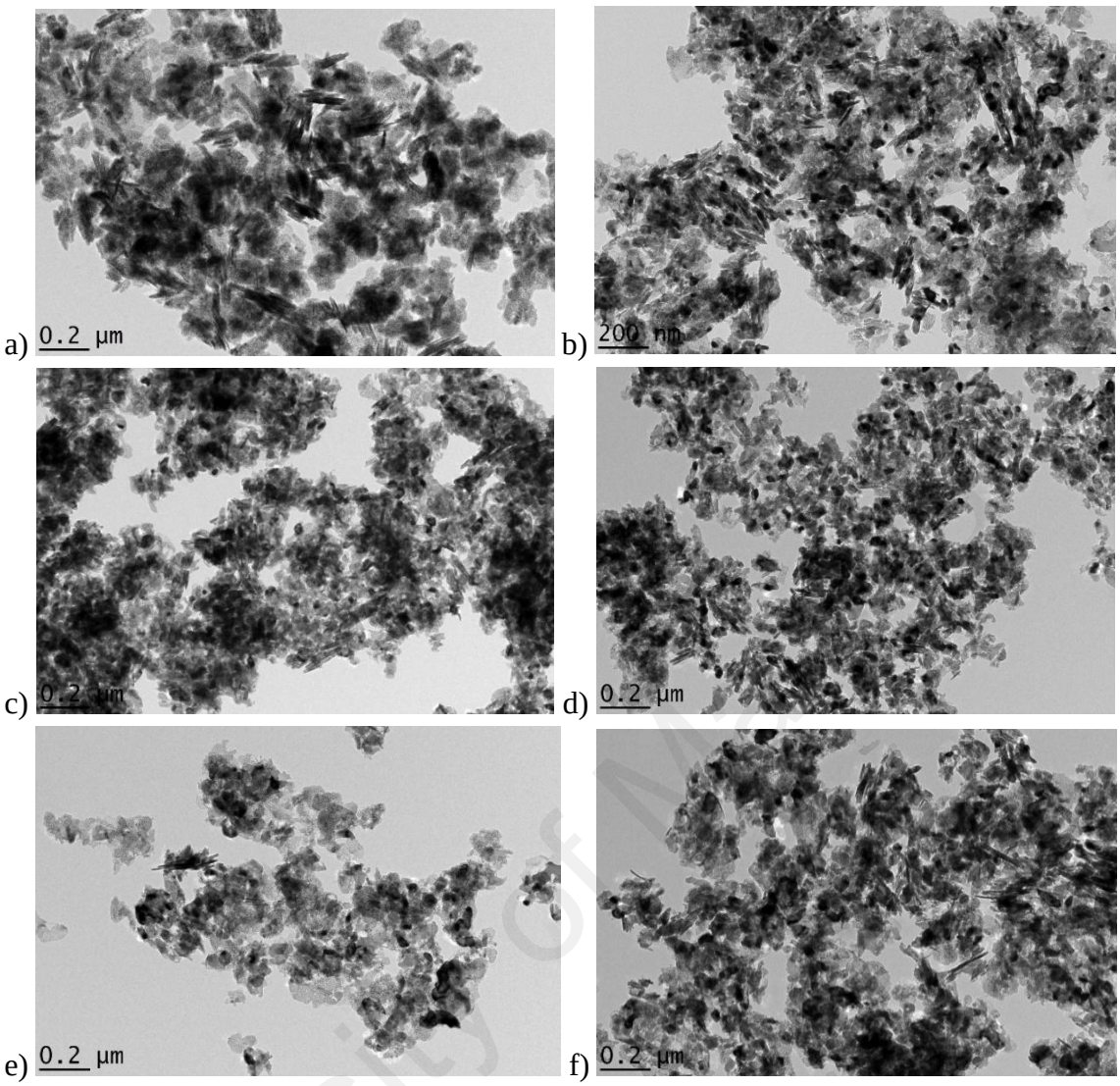

Figure 4.30 TEM images of a) *n*-NiO/SiO_2_(6), b) *n*-NiO/SiO_2_(4), c) *n*-NiO/SiO_2_(7), d) *n*-NiO/SiO_2_(10), e) *n*-NiO/SiO_2_(11), and f) *n*-NiO/SiO_2_(12).

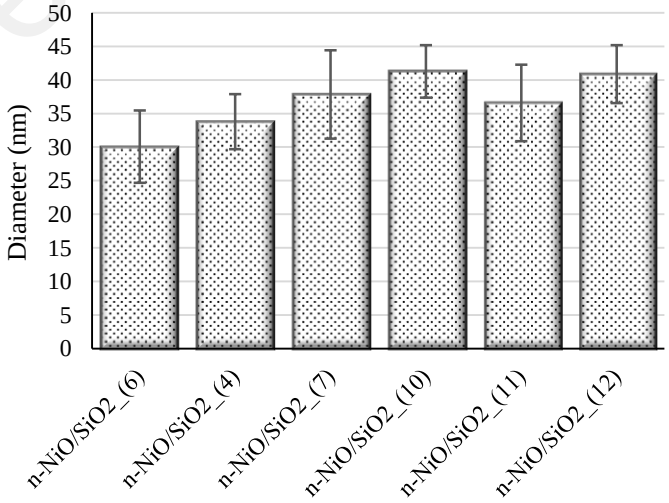

Figure 4.31 Comparison of average particle size calculated from TEM images. 75 nanoparticle were considered to measure average particle size. ImageJ software was used to measure particle size.

The elemental compositions were confirmed by EDX analysis. Weight and atomic percentage of each elements are summarized in Table 4.10 and the elemental mapping are shown in Appendix D. As expected, peaks for Ni, O, and Si elements were observed in the mapped area. The quantity of elements fluctuated in the elemental composition (Table 4.10) according to variation of precursor materials used in synthesis. It can be seen that the quantity of Si increases as increasing the quantity of C18TMS and TEOS in the preparation mixture. However, Ni decreases as increasing C18TMS and TEOS. No other elements were detected in these samples except traces of carbon. The peak observed for carbon could be attributed to the element present in the carbon tap used for EDX analysis and that composition was omitted from elemental percentage composition table.

Table 4.10 Elemental composition of prepared catalysts from EDX reports. EDX mapping is exhibited in Appendix D.

Catalyst	Oxygen			Silicon			Nickel		
	Line type	Weight %	Atomic %	Line type	Weight %	Atomic %	Line type	Weight %	Atomic %
n-NiO/SiO_2_(1)	(K)	20.95	47.67	(K)	3.92	4.38	(K)	75.13	47.95
n-NiO/SiO_2_(2)	(K)	21.26	48.62	(K)	3.38	4.40	(K)	75.36	46.98
n-NiO/SiO_2_(3)	(K)	20.86	47.76	(K)	4.19	5.47	(K)	74.95	46.77
n-NiO/SiO_2_(4)	(K)	18.61	44.48	(K)	3.52	4.80	(K)	77.87	50.72
n-NiO/SiO_2_(5)	(K)	17.87	43.80	(K)	1.88	2.62	(K)	80.25	53.58
n-NiO/SiO_2_(6)	(K)	21.20	48.07	(K)	4.78	6.18	(K)	74.02	45.75
n-NiO/SiO_2_(7)	(K)	19.72	46.67	(K)	2.22	3.00	(K)	78.06	50.34
n-NiO/SiO_2_(8)	(K)	20.11	46.50	(K)	4.63	6.09	(K)	75.26	47.41
n-NiO/SiO_2_(9)	(K)	21.25	48.58	(K)	3.49	4.54	(K)	75.26	46.88
n-NiO/SiO_2_(10)	(K)	19.27	45.31	(K)	4.24	5.68	(K)	76.48	49.00
n-NiO/SiO_2_(11)	(K)	22.01	49.65	(K)	3.56	4.58	(K)	74.43	45.76
n-NiO/SiO_2_(12)	(K)	22.07	49.75	(K)	3.55	4.55	(K)	74.38	45.69

4.4.5 Thermocatalytic Methane Decomposition

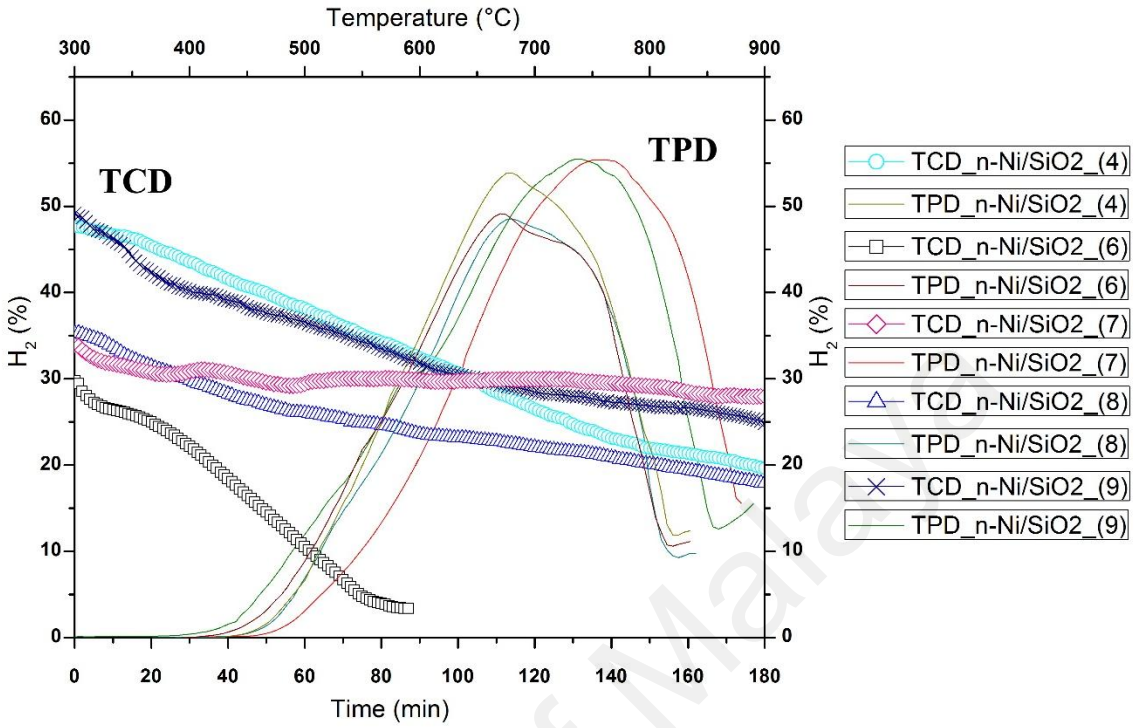

Figure 4.32 Influence of C18TMS/TEOS ratio on the hydrogen formation percentage during temperature programmed methane decomposition (TPMD) and thermocatalytic decomposition of methane (TCD) at 625 °C. Flow rate = 0.6 L/min and catalyst weight = 0.5 g. In figure (b) and (c), bottom x-axis is time (min) and left y-axis is H_2 (%) for TCD. Top x-axis is temperature (°C) and right y-axis is H_2 (%) for TPMD.

Temperature programmed methane decomposition (TPMD) was conducted over 0.5 g of catalyst with 99.995% methane to evaluate catalytically active temperature zone for each catalyst. Influence of C18TMS/TEOS ratio and different solvents on the catalytic active temperature zone of *n*-NiO/SiO_2 catalysts are exhibited in Figure 4.32 and Figure (b) in Appendix E. TPMD results for nickel/silicate ratios are overlapping each other and hence eluded from Figure (a) in Appendix E for clarity. TPMD results evidently demonstrate that the silicate supported nickel catalysts prepared by co-precipitation cum modified Stöber method are truly active from ~450 to ~720 °C. The active zone of *n*-

NiO/SiO_2 catalysts were extended to higher temperature as increasing the quantity of C18TMS in the preparation mixture as shown in Figure 4.32. However, the solvents such as methanol, ethanol, 2-propanol, and *n*-butanol do not make much difference on catalytically active temperature zone [Figure (b) in Appendix E].

Isothermal catalytic methane decomposition was conducted at 625 °C with a flow rate of 0.6 L/min in the fixed catalyst bed reactor for estimating methane decomposition activity sustainability of each catalysts. According to Figure 4.10, *n*-NiO/SiO_2 catalyst prepared by co-precipitation cum modified Stöber method rapidly deactivate above 675 °C because of its high temperature sensitivity. Previous research results also reveal that Ni-based catalysts are not effectively decomposing methane above 700 °C (Takenaka et al., 2003). Similarly, methane conversion was comparatively lower below 575 °C (Takenaka et al., 2003). Hence, we have selected 625 °C for evaluating influence of catalyst preparation parameters on the activity and stability of catalyst. The isothermal methane conversion percentage as well as the activity range undeniably followed the temperature range observed in the TPMD [Figure 4.32 and Figure (b) in Appendix E]. Rosemount Analytical X-STREAM on-line gas analyzer detected only hydrogen and methane according to the methane decomposition equation 1.1 ($CH_4 \rightarrow 2H_2 + C$). *n*-$NiO/SiO_2$_(1), (2), and (3) prepared with 0.02, 0.04, and 0.06 moles of nickel precursor maintaining fairly similar metal/silicate ratio, respectively. Accordingly, *n*-NiO/SiO_2_(1), (2), and (3) maintained similar catalytic performance, irrespective of increasing precursor concentration in catalyst preparation. Correspondingly, catalyst (1), (2), and (3) shown activity loss of 73%, 78%, and 71% after 180 min of methane on stream analysis, as shown in Figure 4.33, respectively. These results clearly demonstrate that the catalytic action of *n*-NiO/SiO_2 prepared by co-precipitation cum modified Stöber method do not vary as increasing the precursor quantity in order to produce catalysts in the gram amount. Furthermore, the carbon yield produced over *n*-NiO/SiO_2_(1), (2), and

(3) are 3108%, 2936%, and 3061%, respectively as shown in Figure 4.34. However, *n*-NiO/SiO_2_(4) prepared with mixture of 0.6 mL of C18TMS and 0.6 mL of TEOS exhibited stable performance with a higher carbon yield compared to catalyst (1), (2), and (3), might be attributed to the more efficient access of methane molecules towards the active nickel metal, because thinner and efficient silicate support. Additionally, further lowering of silicate thickness resulted in the faster activity loss as exhibited by *n*-NiO/SiO_2_(5), which was prepared with mixture of 0.3 mL of C18TMS and 0.3 mL of TEOS. Hence, different C18TMS/TEOS ratio in the catalyst preparation solution undoubtedly influence the catalytic properties as shown in Figure 4.32. One can observe that the *n*-NiO/SiO_2_(7) catalyst prepared with 0 mL of TEOS and 1.2 mL of C18TMS executed lowest activity loss of 17.46% [Figure 4.32 and Figure 4.33). Conversely, *n*-NiO/SiO_2_(6) catalyst prepared with 1.2 mL of TEOS and 0 mL of C18TMS exhibited lowermost catalytic performance and completely deactivated with in the experimented duration. However, the initial hydrogen production of both *n*-NiO/SiO_2_(6) and (7) are comparable. Furthermore, the *n*-NiO/SiO_2 catalysts prepared with mixture of C18TMS and TEOS exhibited higher initial conversion and comparatively lower activity loss by time.

The higher stability of *n*-NiO/SiO_2 catalysts prepared with various quantity of C18TMS might be attributed to the higher amount of microporous area, as indicated in BET results (Table 4.7). 1.2 mL of TEOS and 0 mL of C18TMS produced lower micropores in *n*-NiO/SiO_2_(6), which resulted in its complete deactivation. The addition of C18TMS in to the catalyst preparation mixture enhance the microporosity from 10.7% to 26.8%, which resembles hierarchical porous catalyst (J. Zhang, Jin, Li, Si, et al., 2013). Hence, the synergistic effect between the mesopores and higher quantity of micropores resulted in their higher catalytic activity and stability in TCD. Furthermore, catalyst with higher microporosity resulted in the formation of nanocarbon by tip-growth carbon

formation mechanism (Sinha et al., 2000) with active metal on the tip of carbon and hence conserve the catalytic activity for longer time, as shown in FESEM images of produced carbon (Figure 4.35). These results reveal the significant influence of pore size distribution on the initial activity as well as catalytic activity maintenance during TCD. Irrespective of the influence of C18TMS/TEOS ratio on the methane conversion behavior, analyzed solvents such as methanol, ethanol, 2-propanol, and *n*-butanol do not exhibit significant variation on the catalytic performance with almost similar activity loss of 62±4%, as shown in Figure (b) in Appendix E and Figure 4.33. The higher and conformational stability observed with *n*-NiO/SiO_2 catalysts observed with bulk catalyst may be attributed to the micro-capsular structure with high porosity which provide enough area for methane molecules to collide and decompose to hydrogen and nanocarbon (Joo et al., 2009; Wu et al., 2008; W.-M. Zhang et al., 2008). Furthermore, highly stable silicate support evidently prevented agglomeration of active Ni-phase and maintained the catalyst particle size for carbon nano-filament growth and hence resulted in a superior performance.

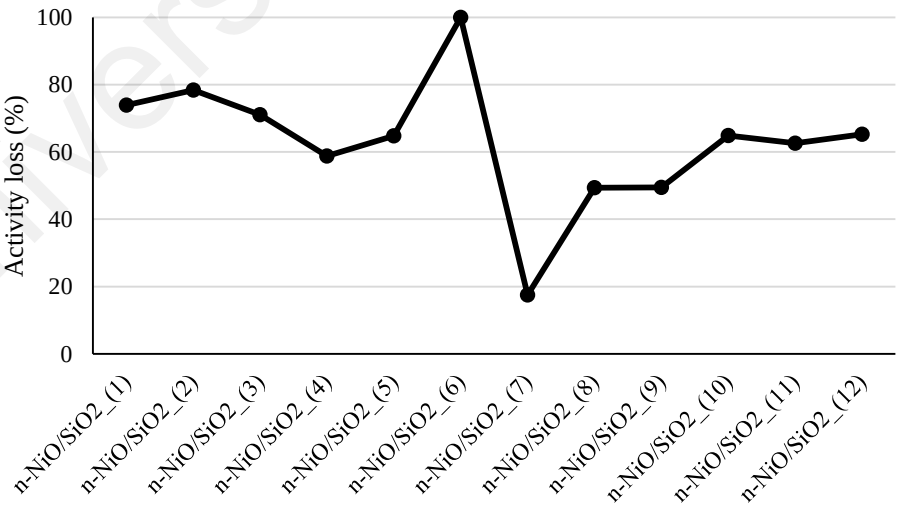

Figure 4.33 Activity loss of each *n*-NiO/SiO_2 catalyst in percentage after 180 min of activity examination.

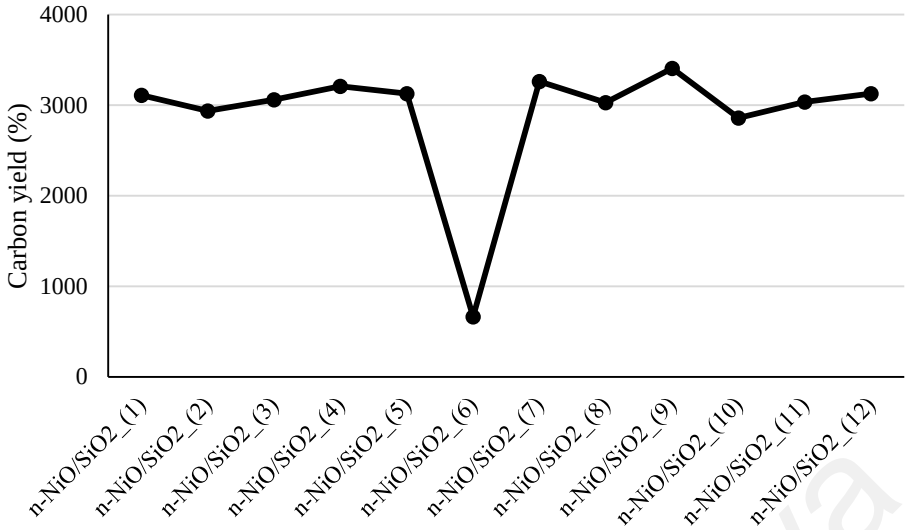

Figure 4.34 Carbon yield calculated over each *n*-NiO/SiO_2 catalysts after 180 min of activity examination.

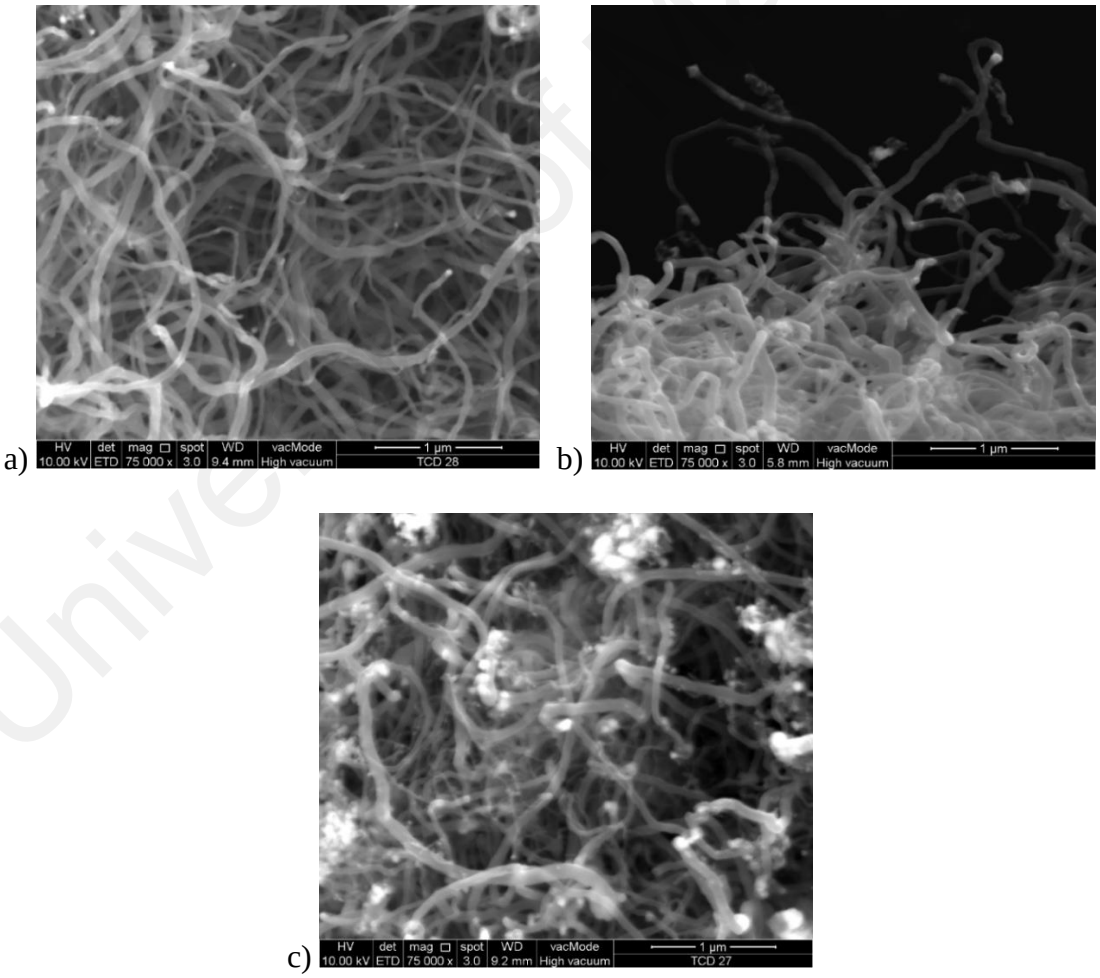

Figure 4.35 FESEM images of produced nanocarbon over a) *n*-NiO/SiO_2_(7), b) *n*-NiO/SiO_2_(4), and c) *n*-NiO/SiO_2_(6) catalysts.

FESEM images of produced nanocarbon over *n*-NiO/SiO_2_(7), *n*-NiO/SiO_2_(4), and *n*-NiO/SiO_2_(6) catalysts are exhibited in Figure 4.35 (a-c), respectively. The presence of nickel particle at the tip of nanocarbons can be identified as bright spots which support the tip-growth mechanism of nanocarbon formation. Furthermore, the average diameter of nanocarbon produced over catalysts are comparable to the Ni crystallite size calculated from XRD patterns after the TCD examination, supporting previous reports (V. R. Choudhary et al., 2001; de Lucas et al., 2005; Takenaka et al., 2001).

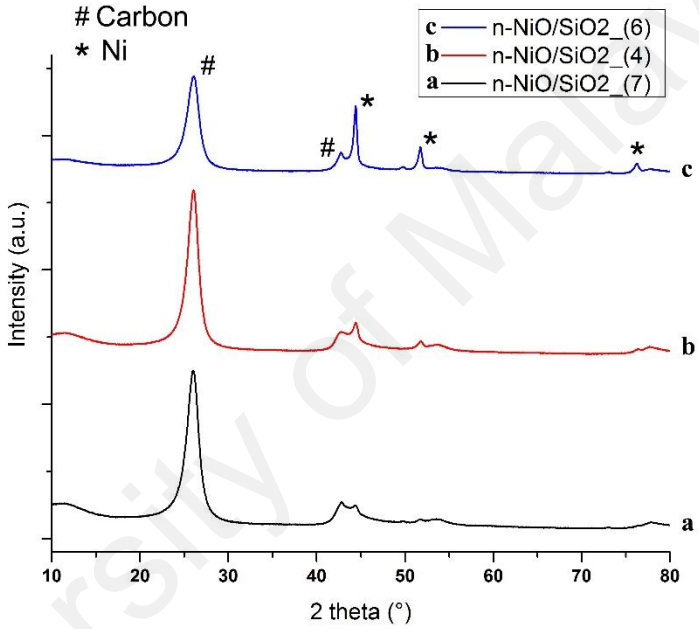

Figure 4.36 XRD patterns of a) *n*-NiO/SiO_2_(7), b) *n*-NiO/SiO_2_(4), and c) *n*-NiO/SiO_2_(6) catalysts after 180 min of TCD.

XRD patterns of catalysts after TCD are exhibited in Figure 4.36. The diffraction peaks at 2θ = 26.2280° and 42.7556° are characteristic to the graphite corresponds to JCPDS No. 98-005-3780. The peaks at 2θ = 44.4252°, 51.7634°, and 76.2959° corresponds to Ni-phases showing good agreement with JCPDS No. 03-065-0380. The crystallite size of *n*-NiO/SiO_2_(7), *n*-NiO/SiO_2_(4), and *n*-NiO/SiO_2_(6) calculated from XRD patterns were 22.86, 26.1, and 33.63 nm, respectively. Similarly, the average diameter of nanocarbon measured with ImagJ software were 24.74±3.1, 27.94±2.8, and

36.84±4.1 nm, respectively. Furthermore, it can be observed that the average diameter of nanocarbon is decreasing as increasing the quantity of C18TMS in the catalyst preparation mixture. These FESEM (Figure 4.35) and XRD (Figure 4.36) results clearly reveals the dependability of C18TMS/TEOS ratio on the stability of nano-nickel catalyst. Additionally, the bright metal particles can be seen highly agglomerated at the tip of nanocarbon produced over *n*-NiO/SiO_2_(6) catalyst (Figure 4.35 (c)). This active phase agglomeration resulted in its faster deactivation. The produced smooth nanocarbons of some micrometer length are closely woven together and hence their actual length cannot be measured.

4.4.6 Summary of Major Findings

Microporous characteristics was increased from 10.7% to 26.8% by increasing the quantity of C18TMS compared to TEOS in preparation mixture. The highest catalytic stability for methane decomposition was observed with catalyst prepared with 1.2 mL of C18TMS and 0 mL of TEOS.

CHAPTER 5: CONCLUSION AND RECOMMENDATION FOR FUTURE STUDIES

5.1 CONCLUSIONS

The followings are the conclusions based on the findings of the study:

5.1.1 Part 1: Stabilization of Ni, Fe, and Co nanoparticles through modified Stöber method to obtain excellent catalytic performance: Preparation, characterization, and catalytic activity for methane decomposition

XRD, BET, H_2-TPR, and TEM investigations demonstrated that the catalytic characteristics of nanometal oxides are enhanced after being supported with silicate. The particle sizes of *n*-NiO, *n*-FeO, and *n*-CoO marginally decreased from 48.02, 85.09, and 207.99 nm to 32.19, 30.26, and 49.92 nm, respectively. Further surface and porous features, crystallite sizes, and reduction characteristics were also enhanced accordingly. Preliminary examination of the catalytic activity revealed that silicate-supported *n*-NiO is superior among other investigated nanoparticles. *n*-NiO/SiO_2 catalysts exhibited an outstanding performance between 450 and 730 °C with a maximum hydrogen production value of 57.28% at 730 °C. However, methane decomposition started above 880 °C only in the absence of any catalyst.

5.1.2 Part 2: Probing the differential methane decomposition behaviors of *n*-NiO/SiO_2, n-FeO/SiO_2, and *n*-CoO/SiO_2 catalysts prepared through co-precipitation cum modified Stöber method

During methane decomposition catalytic activity examination, *n*-NiO/SiO_2 catalyst exhibited an outstanding performance compared to *n*-FeO/SiO_2 and *n*-CoO/SiO_2 catalysts. The poor performance of *n*-FeO/SiO_2 and *n*-CoO/SiO_2

catalysts were attributed to the formation of giant metal particles with unfavorable crystal size for growth of nanocarbon. Furthermore, formation of irregular shaped nanocarbons over Fe and Co-based catalyst because of the metal particle fragmentation also retarding their activity. While, such defects were absent with *n*-NiO/SiO_2 catalyst, which produce fine carbon nano-tubes with active metal at the tip. Maximum hydrogen production over *n*-NiO/SiO_2 was 64.4% at 700 °C, while minimum deactivation after 240 min of examination was found at 500 °C. A variety of nanocarbons were formed over *n*-NiO/SiO_2 catalyst. According to our experimental results, the performance of analyzed catalysts in terms of its stability and activity follow this order *n*-NiO/SiO_2 > *n*-CoO/SiO_2 > *n*-FeO/SiO_2.

5.1.3 Part 3: Methane decomposition kinetics and reaction rate over *n*-NiO/SiO_2 catalyst

Experimental outcomes showed that the accumulation of carbon was increased to a maximal values and, then started to decrease at all experimented temperatures. In fact, the carbon formation remains almost unchanged when changing P_{CH_4} at 550 °C. The highest carbon yield of 1454.08% was observed at 650 °C after the reaction was completed at P_{CH_4} of 0.8 atm. Moreover, TEM analysis confirmed that TCD process produced nanocarbon with "*fish-bone*" or "*bamboo*" morphology in the internal cavity, in addition to open end and closed end carbon nanofibers. The calculation based on the specific molar carbon formation rate at different methane partial pressure and temperature showed that the order of methane decomposition reaction is 1.40 and the *n*-NiO/SiO_2 catalyst reduced the Ea to 60.9 kJ mol^{-1}. The huge difference of Ea value from the C-H bond energy of 434 kJ mol^{-1} eluded the induction period in TCD over *n*-NiO/SiO_2 catalyst.

5.1.4 Part 4: Governance of porosity and methane decomposition activity sustainability of *n*-NiO/SiO_2 catalyst by changing synthesis parameters

Microporous characteristics was increased from 10.7% to 26.8% by increasing the quantity of C18TMS compared to TEOS in preparation mixture. In addition to that, the absence of C18TMS in the preparation mixture resulted in the lower crystal structure order and hence lower catalytic stability. *n*-NiO/SiO_2 catalysts prepared with 0.02, 0.04, and 0.06 mol of nickel precursor established similar catalytic performance elucidating the advantage of co-precipitation cum modified Stöber method for catalyst preparation in gram quantity. Furthermore, maximum catalytic stability for methane decomposition was observed with catalyst prepared with 1.2 mL of C18TMS and 0 mL of TEOS. This higher stability attributed to the superior synergistic effect between higher quantity of micropores and mesopores. Though, the catalyst prepared with 0 mL of C18TMS and 1.2 mL of TEOS exhibited lowest catalytic stability and completely deactivated with in the experimental duration of 180 min. Investigated solvents such as methanol, ethanol, 2-propanol, and *n*-butanol do not make any significant effects on the physicochemical properties of catalysts.

5.2 OVERALL CONCLUSIONS

Co-precipitation cum modified Stöber method was utilized as an efficient methodology to produce nanomaterial with catalytic activity promoting features. The investigations demonstrate that the catalytic characteristics of nanometal oxides were efficiently enhanced after being supported with silicate. The particle sizes of *n*-NiO, *n*-FeO, and *n*-CoO marginally decreased from 48.02, 85.09, and 207.99 nm to 32.19, 30.26, and 49.92 nm, respectively. Further surface and porous features, crystallite sizes, and reduction characteristics were also enhanced accordingly. *n*-NiO/SiO_2 catalyst exhibited an outstanding performance compared to *n*-FeO/SiO_2 and *n*-CoO/SiO_2 catalysts.

According to our experimental results, the performance of analyzed catalysts in terms of their stability and activity follow this order *n*-NiO/SiO_2 > *n*-CoO/SiO_2 > *n*-FeO/SiO_2. The poor performance of *n*-FeO/SiO_2 and *n*-CoO/SiO_2 catalysts were attributed to the formation of giant metal particles with unfavorable crystal size for growth of nanocarbon. Maximum hydrogen production over *n*-NiO/SiO_2 was 64.4% at 700 °C, while minimum deactivation after 240 min of examination was found at 500 °C. A variety of nanocarbons were formed over *n*-NiO/SiO_2 catalyst. The calculations based on the specific molar carbon formation rate at different methane partial pressure and temperature showed that the order of methane decomposition reaction is 1.40 and the *n*-NiO/SiO_2 catalyst reduced the E_a to 60.9 kJ mol^{-1}. The huge difference of E_a value from the C-H bond energy of 434 kJ mol^{-1} eluded the induction period in TCD over *n*-NiO/SiO_2 catalyst. Further investigation on the influence of catalyst preparation parameters on their characteristics revealed that the microporous characteristics increased from 10.7% to 26.8% by increasing the quantity of C18TMS compared to TEOS in preparation mixture. Additionally, the absence of C18TMS in the preparation mixture resulted in the lower crystal structure order and hence lower catalytic stability. Further studies confirmed that the solvents such as methanol, ethanol, 2-propanol, and *n*-butanol do not make any significant effects on the physicochemical properties of catalysts.

5.3 RECOMMENDATIONS FOR FUTURE STUDIES

The following are the recommendation for future studies

- The research using co-precipitation cum modified Stöber method can be extended to multi-metallic catalysts such as *n*-Ni-Fe/SiO_2, *n*-Ni-Co/SiO_2, *n*-Co-Fe/SiO_2, and *n*-Ni-Co-Fe/SiO_2 for producing hydrogen and nanocarbon from methane. Hence, the comprehensive advantages of metal alloy effect can be expounded.
- Optimization of preparation parameters and catalytic activity for thermocatalytic decomposition using response surface methodology.
- Experiment can be conducted to purify as-produced nanocarbon by acid etching and can be used for further application.
- Research can be conducted on application of produced nano-metal particles, purified nanocarbons and nano-metal-carbon alloy as fillers for the production of gas separation membrane as well as for the synthesis of polymer composites for Li-ion battery electrolyte.
- Construction of the membrane (which developed with as-prepared purified carbon nanotubes) integrated methane decomposition reactor to produce high purity hydrogen with improved overall system efficiency by incorporating co-feeds in main stream such as ethane, ethylene, acetylene, and acetaldehyde, as schematized below.

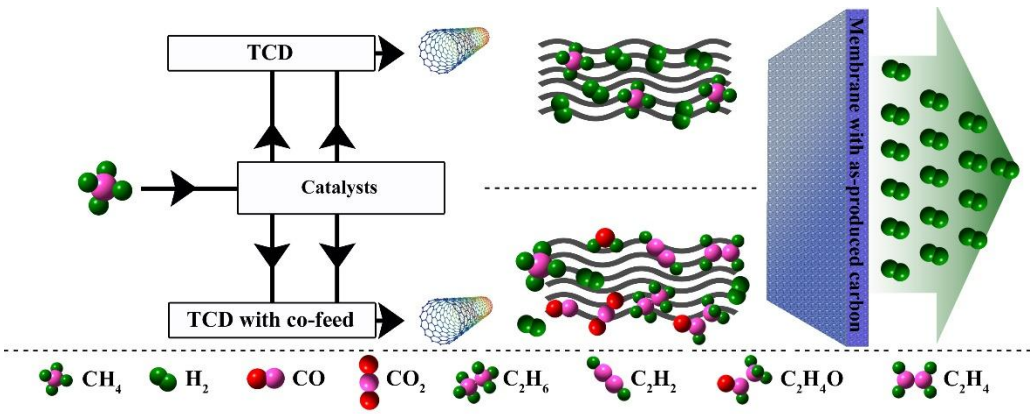

REFERENCES

Abbas, H. F., & Baker, I. F. (2011). Thermocatalytic decomposition of methane using activated carbon: Studying the influence of process parameters using factorial design. *International Journal of Hydrogen Energy, 36*(15), 8985-8993.

Abbas, H. F., & Daud, W. M. A. W. (2009a). Deactivation of palm shell-based activated carbon catalyst used for hydrogen production by thermocatalytic decomposition of methane. *International Journal of Hydrogen Energy, 34*(15), 6231-6241.

Abbas, H. F., & Daud, W. M. A. W. (2009b). Thermocatalytic decomposition of methane for hydrogen production using activated carbon catalyst: Regeneration and characterization studies. *International Journal of Hydrogen Energy, 34*(19), 8034-8045.

Abbas, H. F., & Daud, W. M. A. W. (2010a). Hydrogen production by thermocatalytic decomposition of methane using a fixed bed activated carbon in a pilot scale unit: Apparent kinetic, deactivation and diffusional limitation studies. *International Journal of Hydrogen Energy, 35*(22), 12268-12276.

Abbas, H. F., & Daud, W. M. A. W. (2010b). Influence of reactor material and activated carbon on the thermocatalytic decomposition of methane for hydrogen production. *Applied Catalysis A: General, 388*(1–2), 232-239.

Abbas, H. F., & Wan Daud, W. M. A. (2009). Thermocatalytic decomposition of methane using palm shell based activated carbon: Kinetic and deactivation studies. *Fuel Processing Technology, 90*(9), 1167-1174.

Abbas, H. F., & Wan Daud, W. M. A. (2010). Hydrogen production by methane decomposition: A review. *International Journal of Hydrogen Energy, 35*(3), 1160-1190.

Abbott, H. L., & Harrison, I. (2008). Methane dissociative chemisorption on Ru(0001) and comparison to metal nanocatalysts. *Journal of Catalysis, 254*(1), 27-38.

Aiello, R., Fiscus, J. E., Loye, H.-C. z., & Amiridis, M. D. (2000). Hydrogen production via the direct cracking of methane over Ni/SiO_2: catalyst deactivation and regeneration. *Applied Catalysis A: General, 192*, 227-234.

Al-Hassani, A. A., Abbas, H. F., & Wan Daud, W. M. A. (2014). Hydrogen production via decomposition of methane over activated carbons as catalysts: Full factorial design. *International Journal of Hydrogen Energy, 39*(13), 7004-7014.

Amin, A. M., Croiset, E., Constantinou, C., & Epling, W. (2012). Methane cracking using Ni supported on porous and non-porous alumina catalysts. *International Journal of Hydrogen Energy, 37*(11), 9038-9048.

Amin, A. M., Croiset, E., & Epling, W. (2011). Review of methane catalytic cracking for hydrogen production. *International Journal of Hydrogen Energy, 36*(4), 2904-2935.

Amin, A. M., Croiset, E., Malaibari, Z., & Epling, W. (2012). Hydrogen production by methane cracking using Ni-supported catalysts in a fluidized bed. *International Journal of Hydrogen Energy, 37*(14), 10690-10701.

Anderson, P. E., & Rodríguez, N. M. (2000). Influence of the Support on the Structural Characteristics of Carbon Nanofibers Produced from the Metal-Catalyzed Decomposition of Ethylene. *Chemistry of Materials, 12*(3), 823-830.

Ashok, J., Kumar, S. N., Subrahmanyam, M., & Venugopal, A. (2008). Pure H_2 Production by Decomposition of Methane Over Ni Supported on Hydroxyapatite Catalysts. *Catalysis Letters, 121*(3-4), 283-290.

Ashok, J., Naveen Kumar, S., Subrahmanyam, M., & Venugopal, A. (2007). Production of COX Free Hydrogen by Catalytic Decomposition of Methane Over Ni/HY Catalysts. *Catalysis Letters, 118*(1-2), 139-145.

Ashok, J., Reddy, P. S., Raju, G., Subrahmanyam, M., & Venugopal, A. (2009). Catalytic Decomposition of Methane to Hydrogen and Carbon Nanofibers over Ni−Cu−SiO_2 Catalysts. *Energy & Fuels, 23*(1), 5-13.

Avdeeva, L. B., Goncharova, O. V., Kochubey, D. I., Zaikovskii, V. I., Plyasova, L. M., Novgorodov, B. N., & Shaikhutdinov, S. K. (1996). Coprecipitated Ni-alumina and Ni-Cu-alumina catalysts of methane decomposition and carbon deposition. II. Evolution of the catalysts in reaction. *Applied Catalysis A: General, 141*(1–2), 117-129.

Awadallah, A. E., Aboul-Enein, A. A., & Aboul-Gheit, A. K. (2014). Effect of progressive Co loading on commercial Co–Mo/Al_2O_3 catalyst for natural gas decomposition to COx-free hydrogen production and carbon nanotubes. *Energy Conversion and Management, 77*(0), 143-151.

B. Akbari, M. Pirhadi Tavandashti, & M. Zandrahimi. (2011). Particle size characterization of nanoparticles – A practical approach. *Iranian Journal of Materials Science & Engineering, 8*(2), 48-56.

Bai, Z., Chen, H., Li, B., & Li, W. (2007). Methane decomposition over Ni loaded activated carbon for hydrogen production and the formation of filamentous carbon. *International Journal of Hydrogen Energy, 32*(1), 32-37.

Bai, Z., Li, W., Bai, J., Li, B., & Chen, H. (2012). The effects of textural properties and surface chemistry of activated carbon on its catalytic performance in methane decomposition for hydrogen production. *Energy Sources, Part A: Recovery, Utilization, and Environmental Effects, 34*(12), 1145-1153.

Baird, T., Fryer, J. R., & Grant, B. (1974). Carbon formation on iron and nickel foils by hydrocarbon pyrolysis—reactions at 700°C. *Carbon, 12*(5), 591-602.

Baker, R. T. K., Barber, M. A., Harris, P. S., Feates, F. S., & Waite, R. J. (1972). Nucleation and growth of carbon deposits from the nickel catalyzed decomposition of acetylene. *Journal of Catalysis, 26*(1), 51-62.

Balakrishnan, M., Batra, V. S., Hargreaves, J. S. J., Monaghan, A., Pulford, I. D., Rico, J. L., & Sushil, S. (2009). Hydrogen production from methane in the presence of red mud -making mud magnetic. *Green Chemistry, 11*(1), 42-47.

Balat, M., & Balat, M. (2009). Political, economic and environmental impacts of biomass-based hydrogen. *International Journal of Hydrogen Energy, 34*(9), 3589-3603.

Bartholomew, C. H. (1982). Carbon Deposition in Steam Reforming and Methanation. *Catalysis Reviews, 24*(1), 67-112.

Bartholomew, C. H. (2001). Mechanisms of catalyst deactivation. *Applied Catalysis A: General, 212*(1–2), 17-60.

Borghei, M., Karimzadeh, R., Rashidi, A., & Izadi, N. (2010). Kinetics of methane decomposition to CO_x-free hydrogen and carbon nanofiber over Ni–Cu/MgO catalyst. *International Journal of Hydrogen Energy, 35*(17), 9479-9488.

Botas, J. A., Serrano, D. P., Guil-López, R., Pizarro, P., & Gómez, G. (2010). Methane catalytic decomposition over ordered mesoporous carbons: A promising route for hydrogen production. *International Journal of Hydrogen Energy, 35*(18), 9788-9794.

Bowen, P. (2002). Particle Size Distribution Measurement from Millimeters to Nanometers and from Rods to Platelets. *Journal of Dispersion Science and Technology, 23*(5), 631-662.

Brentner, L. B., Peccia, J., & Zimmerman, J. B. (2010). Challenges in Developing Biohydrogen as a Sustainable Energy Source: Implications for a Research Agenda. *Environmental Science & Technology, 44*(7), 2243-2254.

Chai, S.-P., Seah, C.-M., & Mohamed, A. R. (2011). A parametric study of methane decomposition into carbon nanotubes over 8Co-2Mo/Al2O3 catalyst. *Journal of Natural Gas Chemistry, 20*(1), 84-89.

Chai, S.-P., Zein, S. H. S., & Mohamed, A. R. (2006). Preparation of carbon nanotubes over cobalt-containing catalysts via catalytic decomposition of methane. *Chemical Physics Letters, 426*(4–6), 345-350.

Chai, S.-P., Zein, S. H. S., & Mohamed, A. R. (2007). The effect of reduction temperature on Co-Mo/Al_2O_3 catalysts for carbon nanotubes formation. *Applied Catalysis A: General, 326*(2), 173-179.

Chambers, A., Nemes, T., Rodriguez, N. M., & Baker, R. T. K. (1998). Catalytic Behavior of Graphite Nanofiber Supported Nickel Particles. 1. Comparison with Other Support Media. *The Journal of Physical Chemistry B, 102*(12), 2251-2258.

Chen, D., Christensen, K. O., Ochoa-Fernández, E., Yu, Z., Tøtdal, B., Latorre, N., Monzón, A., & Holmen, A. (2005). Synthesis of carbon nanofibers: effects of Ni crystal size during methane decomposition. *Journal of Catalysis, 229*(1), 82-96.

Chen, J., He, M., Wang, G., Li, Y., & Zhu, Z. J. (2009). Production of hydrogen from methane decomposition using nanosized carbon black as catalyst in a fluidized-bed reactor. *International Journal of Hydrogen Energy, 34*(24), 9730-9736.

Chen, X., Carabineiro, S. A. C., Bastos, S. S. T., Tavares, P. B., Órfão, J. J. M., Pereira, M. F. R., & Figueiredo, J. L. (2013). Exotemplated copper, cobalt, iron, lanthanum and nickel oxides for catalytic oxidation of ethyl acetate. *Journal of Environmental Chemical Engineering, 1*(4), 795-804.

Chesnokov, V. V., & Chichkan, A. S. (2009). Production of hydrogen by methane catalytic decomposition over Ni–Cu–Fe/Al_2O_3 catalyst. *International Journal of Hydrogen Energy, 34*(7), 2979-2985.

Choudhary, T. V., Sivadinarayana, C., Chusuei, C. C., Klinghoffer, A., & Goodman, D. W. (2001). Hydrogen Production via Catalytic Decomposition of Methane. *Journal of Catalysis, 199*(1), 9-18.

Choudhary, V. R., Banerjee, S., & Rajput, A. M. (2001). Continuous Production of H2 at Low Temperature from Methane Decomposition over Ni-Containing Catalyst Followed by Gasification by Steam of the Carbon on the Catalyst in Two Parallel Reactors Operated in Cyclic Manner. *Journal of Catalysis, 198*(1), 136-141.

Cunha, A. F., Órfão, J. J. M., & Figueiredo, J. L. (2008). Catalytic decomposition of methane on Raney-type catalysts. *Applied Catalysis A: General, 348*(1), 103-112.

Cunha, A. F., Órfão, J. J. M., & Figueiredo, J. L. (2009a). Methane decomposition on Fe–Cu Raney-type catalysts. *Fuel Processing Technology, 90*(10), 1234-1240.

Cunha, A. F., Órfão, J. J. M., & Figueiredo, J. L. (2009b). Methane decomposition on Ni–Cu alloyed Raney-type catalysts. *International Journal of Hydrogen Energy, 34*(11), 4763-4772.

de la Casa-Lillo, M. A., Moore, B. C., Cazorla-Amorós, D., & Linares-Solano, A. (2002). Molecular sieve properties obtained by cracking of methane on activated carbon fibers. *Carbon, 40*(13), 2489-2494.

de Lucas, A., Garrido, A., Sánchez, P., Romero, A., & Valverde, J. L. (2005). Growth of Carbon Nanofibers from Ni/Y Zeolite Based Catalysts: Effects of Ni Introduction Method, Reaction Temperature, and Reaction Gas Composition. *Industrial & Engineering Chemistry Research, 44*(22), 8225-8236.

Dell, D. A. J. R. a. R. M. (2008). *Hydrogen Energy: Challenges and Prospects*: RSC Books.

Demirci, U. B., & Miele, P. (2013). Overview of the relative greenness of the main hydrogen production processes. *Journal of Cleaner Production, 52*(0), 1-10.

Derbyshire, F. J., & Trimm, D. L. (1975). Kinetics of the deposition of pyrolytic carbon on nickel. *Carbon, 13*(3), 189-192.

Dou, B., Wang, C., Song, Y., Chen, H., & Xu, Y. (2014). Activity of Ni–Cu–Al based catalyst for renewable hydrogen production from steam reforming of glycerol. *Energy Conversion and Management, 78*(0), 253-259.

Dufour, A., Celzard, A., Fierro, V., Martin, E., Broust, F., & Zoulalian, A. (2008). Catalytic decomposition of methane over a wood char concurrently activated by a pyrolysis gas. *Applied Catalysis A: General, 346*(1–2), 164-173.

Dufour, A., Celzard, A., Ouartassi, B., Broust, F., Fierro, V., & Zoulalian, A. (2009). Effect of micropores diffusion on kinetics of CH_4 decomposition over a wood-derived carbon catalyst. *Applied Catalysis A: General, 360*(2), 120-125.

Dupuis, A.-C. (2005). The catalyst in the CCVD of carbon nanotubes—a review. *Progress in Materials Science, 50*(8), 929-961.

Ermakova, M. A., & Ermakov, D. Y. (2002). Ni/SiO_2 and Fe/SiO_2 catalysts for production of hydrogen and filamentous carbon via methane decomposition. *Catalysis Today, 77*(3), 225-235.

Ermakova, M. A., Ermakov, D. Y., Chuvilin, A. L., & Kuvshinov, G. G. (2001). Decomposition of methane over iron catalysts at the range of moderate temperatures: The influence of structure of the catalytic systems and the reaction conditions on the yield of carbon and morphology of carbon filaments. *Journal of Catalysis, 201*(2), 183-197.

Ermakova, M. A., Ermakov, D. Y., & Kuvshinov, G. G. (2000). Effective catalysts for direct cracking of methane to produce hydrogen and filamentous carbon: Part I. Nickel catalysts. *Applied Catalysis A: General, 201*(1), 61-70.

Figueiredo, J. L. (1982). Carbon Formation and Gasification on Nickel. In J. Figueiredo (Ed.), *Progress in Catalyst Deactivation* (Vol. 54, pp. 45-63): Springer Netherlands.

Figueiredo, J. L., Órfão, J. J. M., & Cunha, A. F. (2010). Hydrogen production via methane decomposition on Raney-type catalysts. *International Journal of Hydrogen Energy, 35*(18), 9795-9800.

Fourth Assessment Report: Climate Change. (2007).

Frusteri, F., Italiano, G., Espro, C., & Arena, F. (2011). CH_4 decomposition on Ni and Co thin layer catalysts to produce H_2 for fuel cell. *Catalysis Today, 171*(1), 60-66.

Fukada, S., Nakamura, N., Monden, J., & Nishikawa, M. (2004). Experimental study of cracking methane by Ni/SiO_2 catalyst. *Journal of Nuclear Materials, 329–333, Part B*(0), 1365-1369.

Gatica, J. M., Gómez, D. M., Harti, S., & Vidal, H. (2013). Monolithic honeycomb design applied to carbon materials for catalytic methane decomposition. *Applied Catalysis A: General, 458*(0), 21-27.

Guevara, J. C., Wang, J. A., Chen, L. F., Valenzuela, M. A., Salas, P., García-Ruiz, A., Toledo, J. A., Cortes-Jácome, M. A., Angeles-Chavez, C., & Novaro, O. (2010). Ni/Ce-MCM-41 mesostructured catalysts for simultaneous production of hydrogen and nanocarbon via methane decomposition. *International Journal of Hydrogen Energy, 35*(8), 3509-3521.

Guil-Lopez, R., Botas, J. A., Fierro, J. L. G., & Serrano, D. P. (2011). Comparison of metal and carbon catalysts for hydrogen production by methane decomposition. *Applied Catalysis A: General, 396*(1–2), 40-51.

Havran, V., Duduković, M. P., & Lo, C. S. (2011). Conversion of Methane and Carbon Dioxide to Higher Value Products. *Industrial & Engineering Chemistry Research, 50*(12), 7089-7100.

Hornés, A., Bera, P., Fernández-García, M., Guerrero-Ruiz, A., & Martínez-Arias, A. (2012). Catalytic and redox properties of bimetallic Cu–Ni systems combined with CeO_2 or Gd-doped CeO_2 for methane oxidation and decomposition. *Applied Catalysis B: Environmental, 111–112*(0), 96-105.

Hussain, S. T., Gul, S., Mazhar, M., Anjum, D. H., & Larachi, F. (2008). Effect of surface structure on the catalytic behavior of Ni:Cu/Al and Ni:Cu:K/Al catalysts for methane decomposition. *Journal of Natural Gas Chemistry, 17*(4), 374-382.

Hussain, S. T., Nadeem, M. A., & Mazhar, M. (2008). Effect of potassium addition on the product selectivity of Ru:Mn/alumina supported catalyst system for Fischer–Tropsch reaction. *Catalysis Communications, 9*(10), 2048-2052.

Hussain, T., & Iqbal, M. (2011). Pyrolysis of methane by catalytic properties exhibited by ceramics. *Journal of Analytical and Applied Pyrolysis, 90*(2), 106-111.

Ishihara, T., Miyashita, Y., Iseda, H., & Takita, Y. (1995). Decomposition of Methane over Ni/SiO_2 Catalysts with Membrane Reactor for the Production of Hydrogen. *Chemistry Letters, 24*(2), 93-94.

Italiano, G., Delia, A., Espro, C., Bonura, G., & Frusteri, F. (2010). Methane decomposition over Co thin layer supported catalysts to produce hydrogen for fuel cell. *International Journal of Hydrogen Energy, 35*(20), 11568-11575.

Jana, P., de la Peña O'Shea, V. A., Coronado, J. M., & Serrano, D. P. (2010). Cobalt based catalysts prepared by Pechini method for CO_2-free hydrogen production by methane decomposition. *International Journal of Hydrogen Energy, 35*(19), 10285-10294.

Jana, P., de la Peña O'Shea, V. A., Coronado, J. M., & Serrano, D. P. (2012). Mild temperature hydrogen production by methane decomposition over cobalt catalysts prepared with different precipitating agents. *International Journal of Hydrogen Energy, 37*(8), 7034-7041.

Jang, H. T., & Cha, W. S. (2007). Hydrogen production by the thermocatalytic decomposition of methane in a fluidized bed reactor. *Korean Journal of Chemical Engineering, 24*(2), 374-377.

Joo, S. H., Park, J. Y., Tsung, C.-K., Yamada, Y., Yang, P., & Somorjai, G. A. (2009). Thermally stable Pt/mesoporous silica core-shell nanocatalysts for high-temperature reactions. *Nature Materials, 8*(2), 126-131.

Jos G.J. Olivier, G. J.-M., Jeroen A.H.W. Peters. (2012). Trends in Global CO_2 Emissions: PBL.

Jung, H., & Thomson, W. J. (1991). Reduction/oxidation of a high loading iron oxide catalyst. *Journal of Catalysis, 128*(1), 218-230.

Jüntgen, H. (1986). Activated carbon as catalyst support: A review of new research results. *Fuel, 65*(10), 1436-1446.

Khaselev, O., & Turner, J. A. (1998). A Monolithic Photovoltaic-Photoelectrochemical Device for Hydrogen Production via Water Splitting. *Science, 280*(5362), 425-427.

Kim, M. H., Lee, E. K., Jun, J. H., Kong, S. J., Han, G. Y., Lee, B. K., Lee, T.-J., & Yoon, K. J. (2004). Hydrogen production by catalytic decomposition of methane over activated carbons: kinetic study. *International Journal of Hydrogen Energy, 29*(2), 187-193.

Kim, M. S., Rodriguez, N. M., & Baker, R. T. K. (1991). The interaction of hydrocarbons with copper-nickel and nickel in the formation of carbon filaments. *Journal of Catalysis, 131*(1), 60-73.

Kodama, T. (2003). High-temperature solar chemistry for converting solar heat to chemical fuels. *Progress in Energy and Combustion Science, 29*(6), 567-597.

Konieczny, A., Mondal, K., Wiltowski, T., & Dydo, P. (2008). Catalyst development for thermocatalytic decomposition of methane to hydrogen. *International Journal of Hydrogen Energy, 33*(1), 264-272.

Krzyżyński, S., & Kozłowski, M. (2008). Activated carbons as catalysts for hydrogen production via methane decomposition. *International Journal of Hydrogen Energy, 33*(21), 6172-6177.

Kuvshinov, G. G., Mogilnykh, Y. I., & Kuvshinov, D. G. (1998). Kinetics of carbon formation from CH_4–H_2 mixtures over a nickel containing catalyst. *Catalysis Today, 42*(3), 357-360.

Kvande, I., Chen, D., Yu, Z., Rønning, M., & Holmen, A. (2008). Optimization and scale-up of CNF production based on intrinsic kinetic data obtained from TEOM. *Journal of Catalysis, 256*(2), 204-214.

Lázaro, M. J., Echegoyen, Y., Alegre, C., Suelves, I., Moliner, R., & Palacios, J. M. (2008). TiO_2 as textural promoter on high loaded Ni catalysts for methane decomposition. *International Journal of Hydrogen Energy, 33*(13), 3320-3329.

Lázaro, M. J., Pinilla, J. L., Suelves, I., & Moliner, R. (2008). Study of the deactivation mechanism of carbon blacks used in methane decomposition. *International Journal of Hydrogen Energy, 33*(15), 4104-4111.

Lázaro, M. J., Pinilla, J. L., Utrilla, R., Suelves, I., Moliner, R., Moreno, F., & Muñoz, M. (2010). H_2−CH_4 Mixtures Produced by Carbon-Catalyzed Methane Decomposition as a Fuel for Internal Combustion Engines†. *Energy & Fuels, 24*(6), 3340-3345.

Lee, E. K., Lee, S. Y., Han, G. Y., Lee, B. K., Lee, T.-J., Jun, J. H., & Yoon, K. J. (2004). Catalytic decomposition of methane over carbon blacks for CO2-free hydrogen production. *Carbon, 42*(12–13), 2641-2648.

Lee, J., Park, J. C., Bang, J. U., & Song, H. (2008). Precise tuning of porosity and surface functionality in Au@SiO_2 nanoreactors for high catalytic efficiency. *Chemistry of Materials, 20*(18), 5839-5844.

Lee, K.-Y., Yeoh, W.-M., Chai, S.-P., Ichikawa, S., & Mohamed, A. R. (2012). Catalytic decomposition of methane to carbon nanotubes and hydrogen: The effect of metal loading on the activity of CoO-MoO/Al_2O_3 catalyst. *Fullerenes, Nanotubes and Carbon Nanostructures, 21*(2), 158-170.

Lee, K. K., Han, G. Y., Yoon, K. J., & Lee, B. K. (2004). Thermocatalytic hydrogen production from the methane in a fluidized bed with activated carbon catalyst. *Catalysis Today, 93–95*(0), 81-86.

Lee, S. Y., Kwak, J. H., Han, G. Y., Lee, T. J., & Yoon, K. J. (2008). Characterization of active sites for methane decomposition on carbon black through acetylene chemisorption. *Carbon, 46*(2), 342-348.

Li, H., Yu, D., Hu, Y., Sun, P., Xia, J., & Huang, H. (2010). Effect of preparation method on the structure and catalytic property of activated carbon supported nickel oxide catalysts. *Carbon, 48*(15), 4547-4555.

Li, L., He, S., Song, Y., Zhao, J., Ji, W., & Au, C.-T. (2012). Fine-tunable Ni@porous silica core–shell nanocatalysts: Synthesis, characterization, and catalytic properties in partial oxidation of methane to syngas. *Journal of Catalysis, 288*(0), 54-64.

Li, L., Lu, P., Yao, Y., & Ji, W. (2012b). Silica-encapsulated bimetallic Co–Ni nanoparticles as novel catalysts for partial oxidation of methane to syngas. *Catalysis Communications, 26*(0), 72-77.

Li, X.-K., Ji, W.-J., Zhao, J., Wang, S.-J., & Au, C.-T. (2005). Ammonia decomposition over Ru and Ni catalysts supported on fumed SiO_2, MCM-41, and SBA-15. *Journal of Catalysis, 236*(2), 181-189.

Li, Y., Chen, J., Qin, Y., & Chang, L. (2000). Simultaneous production of hydrogen and nanocarbon from decomposition of methane on a nickel-based catalyst. *Energy & Fuels, 14*(6), 1188-1194.

Li, Y., Li, D., & Wang, G. (2011). Methane decomposition to CO_x-free hydrogen and nano-carbon material on group 8–10 base metal catalysts: A review. *Catalysis Today, 162*(1), 1-48.

Li, Z., Larsson, J. A., Larsson, P., Ahuja, R., Tobin, J. M., O'Byrne, J., Morris, M. A., Attard, G., & Holmes, J. D. (2008). Copper/molybdenum nanocomposite particles as catalysts for the growth of bamboo-structured carbon nanotubes. *The Journal of Physical Chemistry C, 112*(32), 12201-12206.

Lua, A. C., & Wang, H. Y. (2013). Decomposition of methane over unsupported porous nickel and alloy catalyst. *Applied Catalysis B: Environmental, 132–133*(0), 469-478.

Lund, C. R. F., & Dumesic, J. A. (1981). Strong oxide-oxide interactions in silica-supported Fe_3O_4: III. Water-induced migration of silica on geometrically designed catalysts. *Journal of Catalysis, 72*(1), 21-30.

Malaika, A., & Kozłowski, M. (2009). Influence of ethylene on carbon-catalysed decomposition of methane. *International Journal of Hydrogen Energy, 34*(6), 2600-2605.

Maneerung, T., Hidajat, K., & Kawi, S. (2011). $LaNiO_3$ perovskite catalyst precursor for rapid decomposition of methane: Influence of temperature and presence of H2 in feed stream. *Catalysis Today, 171*(1), 24-35.

Michalkiewicz, B., & Majewska, J. (2014). Diameter-controlled carbon nanotubes and hydrogen production. *International Journal of Hydrogen Energy, 39*(9), 4691-4697.

Moliner, R., Suelves, I., Lázaro, M. J., & Moreno, O. (2005). Thermocatalytic decomposition of methane over activated carbons: influence of textural properties and surface chemistry. *International Journal of Hydrogen Energy, 30*(3), 293-300.

Morales-Torres, S., Silva, A. M. T., Maldonado-Hódar, F. J., Machado, B. F., Pérez-Cadenas, A. F., Faria, J. L., Figueiredo, J. L., & Carrasco-Marín, F. (2011). Pt-

catalysts supported on activated carbons for catalytic wet air oxidation of aniline: Activity and stability. *Applied Catalysis B: Environmental, 105*(1–2), 86-94.

Muradov, N. (2001). Catalysis of methane decomposition over elemental carbon. *Catalysis Communications, 2*(3–4), 89-94.

Muradov, N., Chen, Z., & Smith, F. (2005). Fossil hydrogen with reduced CO_2 emission: Modeling thermocatalytic decomposition of methane in a fluidized bed of carbon particles. *International Journal of Hydrogen Energy, 30*(10), 1149-1158.

Muradov, N., Smith, F., Huang, C., & T-Raissi, A. (2006). Autothermal catalytic pyrolysis of methane as a new route to hydrogen production with reduced CO_2 emissions. *Catalysis Today, 116*(3), 281-288.

Muradov, N., Smith, F., & T-Raissi, A. (2005). Catalytic activity of carbons for methane decomposition reaction. *Catalysis Today, 102–103*(0), 225-233.

Muradov, N. Z. (1998). CO2-Free Production of Hydrogen by Catalytic Pyrolysis of Hydrocarbon Fuel. *Energy & Fuels, 12*(1), 41-48.

Nasir Uddin, M., Daud, W. M. A. W., & Abbas, H. F. (2013). Potential hydrogen and non-condensable gases production from biomass pyrolysis: Insights into the process variables. *Renewable and Sustainable Energy Reviews, 27*(0), 204-224.

Nasir Uddin, M., Wan Daud, W. M. A., & Abbas, H. F. (2014). Kinetics and deactivation mechanisms of the thermal decomposition of methane in hydrogen and carbon nanofiber Co-production over Ni-supported Y zeolite-based catalysts. *Energy Conversion and Management, 87*(0), 796-809.

Nasir Uddin, M., Wan Daud, W. M. A., & Abbas, H. F. (2015). Co-production of hydrogen and carbon nanofibers from methane decomposition over zeolite Y supported Ni catalysts. *Energy Conversion and Management, 90*(0), 218-229.

Navarro, R. M., Sanchez-Sanchez, M. C., Alvarez-Galvan, M. C., Valle, F. d., & Fierro, J. L. G. (2009). Hydrogen production from renewable sources: biomass and photocatalytic opportunities. *Energy & Environmental Science, 2*(1), 35-54.

Ni, M., Leung, M. K. H., Leung, D. Y. C., & Sumathy, K. (2007). A review and recent developments in photocatalytic water-splitting using for hydrogen production. *Renewable and Sustainable Energy Reviews, 11*(3), 401-425.

Nowotny, J., Sorrell, C. C., Sheppard, L. R., & Bak, T. (2005). Solar-hydrogen: Environmentally safe fuel for the future. *International Journal of Hydrogen Energy, 30*(5), 521-544.

Nuernberg, G. D. B., Fajardo, H. V., Foletto, E. L., Hickel-Probst, S. M., Carreño, N. L. V., Probst, L. F. D., & Barrault, J. (2011). Methane conversion to hydrogen and nanotubes on Pt/Ni catalysts supported over spinel $MgAl_2O_4$. *Catalysis Today, 176*(1), 465-469.

Nuernberg, G. D. B., Foletto, E. L., Campos, C. E. M., Fajardo, H. V., Carreño, N. L. V., & Probst, L. F. D. (2012). Direct decomposition of methane over Ni catalyst supported in magnesium aluminate. *Journal of Power Sources, 208*(0), 409-414.

O'Byrne, J. P., Li, Z., Tobin, J. M., Larsson, J. A., Larsson, P., Ahuja, R., & Holmes, J. D. (2010). Growth of Carbon Nanotubes from Heterometallic Palladium and Copper Catalysts. *The Journal of Physical Chemistry C, 114*(18), 8115-8119.

Otsuka, K., Ogihara, H., & Takenaka, S. (2003). Decomposition of methane over Ni catalysts supported on carbon fibers formed from different hydrocarbons. *Carbon, 41*(2), 223-233.

Peharz, G., Dimroth, F., & Wittstadt, U. (2007). Solar hydrogen production by water splitting with a conversion efficiency of 18%. *International Journal of Hydrogen Energy, 32*(15), 3248-3252.

Pinilla, J. L., Suelves, I., Lázaro, M. J., Moliner, R., & Palacios, J. M. (2008). Activity of NiCuAl catalyst in methane decomposition studied using a thermobalance and the structural changes in the Ni and the deposited carbon. *International Journal of Hydrogen Energy, 33*(10), 2515-2524.

Pinilla, J. L., Suelves, I., Lázaro, M. J., Moliner, R., & Palacios, J. M. (2010). Parametric study of the decomposition of methane using a $NiCu/Al_2O_3$ catalyst in a fluidized bed reactor. *International Journal of Hydrogen Energy, 35*(18), 9801-9809.

Pinilla, J. L., Utrilla, R., Karn, R. K., Suelves, I., Lázaro, M. J., Moliner, R., García, A. B., & Rouzaud, J. N. (2011). High temperature iron-based catalysts for hydrogen and nanostructured carbon production by methane decomposition. *International Journal of Hydrogen Energy, 36*(13), 7832-7843.

Pinilla, J. L., Utrilla, R., Lázaro, M. J., Moliner, R., Suelves, I., & García, A. B. (2011). Ni- and Fe-based catalysts for hydrogen and carbon nanofilament production by catalytic decomposition of methane in a rotary bed reactor. *Fuel Processing Technology, 92*(8), 1480-1488.

Prasad, J. S., Dhand, V., Himabindu, V., Anjaneyulu, Y., Jain, P. K., & Padya, B. (2010). Production of hydrogen and carbon nanofibers through the decomposition of methane over activated carbon supported Pd catalysts. *International Journal of Hydrogen Energy, 35*(20), 10977-10983.

Puliyalil, H., Cvelbar, U., Filipic, G., Petric, A. D., Zaplotnik, R., Recek, N., Mozetic, M., & Thomas, S. (2015). Plasma as a tool for enhancing insulation properties of polymer composites. *RSC Advances, 5*(47), 37853-37858.

Punnoose, A., Shah, N., Huffman, G. P., & Seehra, M. S. (2003). X-ray diffraction and electron magnetic resonance studies of M/Fe/Al_2O_3 (M=Ni, Mo and Pd) catalysts for CH4 to H2 conversion. *Fuel Processing Technology, 83*(1–3), 263-273.

Qian, W., Liu, T., Wei, F., Wang, Z., & Li, Y. (2004). Enhanced production of carbon nanotubes: combination of catalyst reduction and methane decomposition. *Applied Catalysis A: General, 258*(1), 121-124.

Rostrup-Nielsen, J.R. (1975). *Steam Reforming Catalysts: An Investigation of Catalysts for Tubular Steam Reforming of Hydrocarbons*. Copenhagen: Teknisk Forlag A/S.

Reilly, P. T. A., & Whitten, W. B. (2006). The role of free radical condensates in the production of carbon nanotubes during the hydrocarbon CVD process. *Carbon, 44*(9), 1653-1660.

Robertson, S. D. (1972). Carbon formation from methane pyrolysis over some transition metal surfaces—II. Manner of carbon and graphite formation. *Carbon, 10*(2), 221-229.

Roine, A. (2002). HSC Chemistry 5.11. *Outokumpu Research Oy, Pori, Finland*.

Rostrup-Nielsen, J. R. (1974). Coking on nickel catalysts for steam reforming of hydrocarbons. *Journal of Catalysis, 33*(2), 184-201.

Ryu, B. H., Lee, S. Y., Lee, D. H., Han, G. Y., Lee, T.-J., & Yoon, K. J. (2007). Catalytic characteristics of various rubber-reinforcing carbon blacks in decomposition of methane for hydrogen production. *Catalysis Today, 123*(1–4), 303-309.

Salmones, J., Wang, J. A., Valenzuela, M. A., Sánchez, E., & Garcia, A. (2009). Pore geometry influence on the deactivation behavior of Ni-based catalysts for simultaneous production of hydrogen and nanocarbon. *Catalysis Today, 148*(1–2), 134-139.

Sarada Prasad, J., Dhand, V., Himabindu, V., & Anjaneyulu, Y. (2011). Production of hydrogen and carbon nanofibers through the decomposition of methane over activated carbon supported Ni catalysts. *International Journal of Hydrogen Energy, 36*(18), 11702-11711.

Saraswat, S. K., & Pant, K. K. (2011). Ni–Cu–Zn/MCM-22 catalysts for simultaneous production of hydrogen and multiwall carbon nanotubes via thermo-catalytic decomposition of methane. *International Journal of Hydrogen Energy, 36*(21), 13352-13360.

Saraswat, S. K., & Pant, K. K. (2013). Synthesis of hydrogen and carbon nanotubes over copper promoted Ni/SiO_2 catalyst by thermocatalytic decomposition of methane. *Journal of Natural Gas Science and Engineering, 13*(0), 52-59.

Serp, P., Corrias, M., & Kalck, P. (2003). Carbon nanotubes and nanofibers in catalysis. *Applied Catalysis A: General, 253*(2), 337-358.

Serrano, D. P., Botas, J. A., Fierro, J. L. G., Guil-López, R., Pizarro, P., & Gómez, G. (2010). Hydrogen production by methane decomposition: Origin of the catalytic activity of carbon materials. *Fuel, 89*(6), 1241-1248.

Serrano, D. P., Botas, J. A., & Guil-Lopez, R. (2009). H2 production from methane pyrolysis over commercial carbon catalysts: Kinetic and deactivation study. *International Journal of Hydrogen Energy, 34*(10), 4488-4494.

Serrano, D. P., Botas, J. Á., Pizarro, P., & Gómez, G. (2013). Kinetic and autocatalytic effects during the hydrogen production by methane decomposition over carbonaceous catalysts. *International Journal of Hydrogen Energy, 38*(14), 5671-5683.

Serrano, D. P., Botas, J. A., Pizarro, P., Guil-Lopez, R., & Gomez, G. (2008). Ordered mesoporous carbons as highly active catalysts for hydrogen production by CH_4 decomposition. *Chemical Communications, 0*(48), 6585-6587.

Serrano, D. P., Coronado, J. M., de la Pena O'Shea, V. A., Pizarro, P., & Botas, J. A. (2013). Advances in the design of ordered mesoporous materials for low-carbon catalytic hydrogen production. *Journal of Materials Chemistry A, 1*(39), 12016-12027.

Shah, N., Panjala, D., & Huffman, G. P. (2001). Hydrogen production by catalytic decomposition of methane. *Energy & Fuels, 15*(6), 1528-1534.

Shah, N., Pattanaik, S., Huggins, F. E., Panjala, D., & Huffman, G. P. (2003). XAFS and Mössbauer spectroscopy characterization of supported binary catalysts for nonoxidative dehydrogenation of methane. *Fuel Processing Technology, 83*(1–3), 163-173.

Shah, N., Wang, Y., Panjala, D., & Huffman, G. P. (2004). Production of hydrogen and carbon nanostructures by non-oxidative catalytic dehydrogenation of ethane and propane. *Energy & Fuels, 18*(3), 727-735.

Shaikjee, A., & Coville, N. J. (2012). The role of the hydrocarbon source on the growth of carbon materials. *Carbon, 50*(10), 3376-3398.

Sharif Zein, S. H., Mohamed, A. R., & Talpa Sai, P. S. (2004). Kinetic studies on catalytic decomposition of methane to hydrogen and carbon over Ni/TiO_2 catalyst. *Industrial & Engineering Chemistry Research, 43*(16), 4864-4870.

Sierra Gallego, G., Barrault, J., Batiot-Dupeyrat, C., & Mondragón, F. (2010). Production of hydrogen and MWCNTs by methane decomposition over catalysts originated from $LaNiO_3$ perovskite. *Catalysis Today, 149*(3–4), 365-371.

Sing, K. S. W. (1985). Reporting physisorption data for gas/solid systems with special reference to the determination of surface area and porosity (Recommendations 1984) *Pure and Applied Chemistry* (Vol. 57, pp. 603).

Sinha, A. K., Hwang, D. W., & Hwang, L.-P. (2000). A novel approach to bulk synthesis of carbon nanotubes filled with metal by a catalytic chemical vapor deposition method. *Chemical Physics Letters, 332*(5–6), 455-460.

Snoeck, J. W., Froment, G. F., & Fowles, M. (1997a). Filamentous carbon formation and gasification: Thermodynamics, driving force, nucleation, and steady-state growth. *Journal of Catalysis, 169*(1), 240-249.

Snoeck, J. W., Froment, G. F., & Fowles, M. (1997b). Kinetic study of the carbon filament formation by methane cracking on a nickel catalyst. *Journal of Catalysis, 169*(1), 250-262.

Statistical Review of World Energy. (2012).

Stephens-Romero, S., Carreras-Sospedra, M., Brouwer, J., Dabdub, D., & Samuelsen, S. (2009). Determining air quality and greenhouse gas impacts of hydrogen infrastructure and fuel cell vehicles. *Environmental Science & Technology, 43*(23), 9022-9029.

Stjerndahl, M., Andersson, M., Hall, H. E., Pajerowski, D. M., Meisel, M. W., & Duran, R. S. (2008). Superparamagnetic Fe_3O_4/SiO_2 nanocomposites: Enabling the tuning of both the iron oxide load and the size of the nanoparticles. *Langmuir, 24*(7), 3532-3536.

Stöber, W., Fink, A., & Bohn, E. (1968). Controlled growth of monodisperse silica spheres in the micron size range. *Journal of Colloid and Interface Science, 26*(1), 62-69.

Suelves, I., Lázaro, M. J., Moliner, R., Echegoyen, Y., & Palacios, J. M. (2006). Characterization of NiAl and NiCuAl catalysts prepared by different methods for hydrogen production by thermo catalytic decomposition of methane. *Catalysis Today, 116*(3), 271-280.

Suelves, I., Lázaro, M. J., Moliner, R., Pinilla, J. L., & Cubero, H. (2007). Hydrogen production by methane decarbonization: Carbonaceous catalysts. *International Journal of Hydrogen Energy, 32*(15), 3320-3326.

Suelves, I., Pinilla, J. L., Lázaro, M. J., & Moliner, R. (2008). Carbonaceous materials as catalysts for decomposition of methane. *Chemical Engineering Journal, 140*(1–3), 432-438.

Suelves, I., Pinilla, J. L., Lázaro, M. J., Moliner, R., & Palacios, J. M. (2009). Effects of reaction conditions on hydrogen production and carbon nanofiber properties generated by methane decomposition in a fixed bed reactor using a NiCuAl catalyst. *Journal of Power Sources, 192*(1), 35-42.

Takenaka, S., Ishida, M., Serizawa, M., Tanabe, E., & Otsuka, K. (2004). Formation of carbon nanofibers and carbon nanotubes through methane decomposition over supported cobalt catalysts. *The Journal of Physical Chemistry B, 108*(31), 11464-11472.

Takenaka, S., Kobayashi, S., Ogihara, H., & Otsuka, K. (2003). Ni/SiO_2 catalyst effective for methane decomposition into hydrogen and carbon nanofiber. *Journal of Catalysis, 217*(1), 79-87.

Takenaka, S., Ogihara, H., Yamanaka, I., & Otsuka, K. (2001). Decomposition of methane over supported-Ni catalysts: effects of the supports on the catalytic lifetime. *Applied Catalysis A: General, 217*(1–2), 101-110.

Takenaka, S., Serizawa, M., & Otsuka, K. (2004). Formation of filamentous carbons over supported Fe catalysts through methane decomposition. *Journal of Catalysis, 222*(2), 520-531.

Tang, L., Yamaguchi, D., Burke, N., Trimm, D., & Chiang, K. (2010). Methane decomposition over ceria modified iron catalysts. *Catalysis Communications, 11*(15), 1215-1219.

Tapia-Parada, K., Valverde-Aguilar, G., Mantilla, A., Valenzuela, M. A., & Hernández, E. (2013). Synthesis and characterization of $Ni/Ce–SiO_2$ and $Co/Ce–TiO_2$ catalysts for methane decomposition. *Fuel, 110*(0), 70-75.

Tesner, P. A., Robinovich, E. Y., Rafalkes, I. S., & Arefieva, E. F. (1970). Formation of carbon fibers from acetylene. *Carbon, 8*(4), 435-442.

Torres, D., de Llobet, S., Pinilla, J. L., Lázaro, M. J., Suelves, I., & Moliner, R. (2012). Hydrogen production by catalytic decomposition of methane using a Fe-based catalyst in a fluidized bed reactor. *Journal of Natural Gas Chemistry, 21*(4), 367-373.

Trimm, D. L. (1977). The formation and removal of coke from nickel catalyst. *Catalysis Reviews, 16*(1), 155-189.

Uddin, M. N., & Daud, W. M. A. W. (2014). Technological diversity and economics: Coupling effects on hydrogen production from biomass. *Energy & Fuels*.

Ueno, Y., Fukui, H., & Goto, M. (2007). Operation of a two-stage fermentation process producing hydrogen and methane from organic waste. *Environmental Science & Technology, 41*(4), 1413-1419.

Venugopal, A., Naveen Kumar, S., Ashok, J., Hari Prasad, D., Durga Kumari, V., Prasad, K. B. S., & Subrahmanyam, M. (2007a). Hydrogen production by catalytic decomposition of methane over. *International Journal of Hydrogen Energy, 32*(12), 1782-1788.

Venugopal, A., Naveen Kumar, S., Ashok, J., Hari Prasad, D., Durga Kumari, V., Prasad, K. B. S., & Subrahmanyam, M. (2007b). Hydrogen production by catalytic decomposition of methane over Ni/SiO_2. *International Journal of Hydrogen Energy, 32*(12), 1782-1788.

Villacampa, J. I., Royo, C., Romeo, E., Montoya, J. A., Del Angel, P., & Monzón, A. (2003). Catalytic decomposition of methane over Ni-Al_2O_3 coprecipitated catalysts: Reaction and regeneration studies. *Applied Catalysis A: General, 252*(2), 363-383.

Wang, G., Jin, Y., Liu, G., & Li, Y. (2013). Production of hydrogen and nanocarbon from catalytic decomposition of methane over a Ni–Fe/Al_2O_3 Catalyst. *Energy & Fuels, 27*(8), 4448-4456.

Wang, H. Y., & Lua, A. C. (2014). Deactivation and kinetic studies of unsupported Ni and Ni–Co–Cu alloy catalysts used for hydrogen production by methane decomposition. *Chemical Engineering Journal, 243*(0), 79-91.

Wang, S. (2008). Application of solid ash based catalysts in heterogeneous catalysis. *Environmental Science & Technology, 42*(19), 7055-7063.

Wang, W., Wang, H., Yang, Y., & Jiang, S. (2012). Ni–SiO_2 and Ni–Fe–SiO_2 catalysts for methane decomposition to prepare hydrogen and carbon filaments. *International Journal of Hydrogen Energy, 37*(11), 9058-9066.

Wei, L., Tan, Y.-s., Han, Y.-z., Zhao, J.-t., Wu, J., & Zhang, D. (2011). Hydrogen production by methane cracking over different coal chars. *Fuel*, *90*(11), 3473-3479.

Westermann, P., Jørgensen, B., Lange, L., Ahring, B. K., & Christensen, C. H. (2007). Maximizing renewable hydrogen production from biomass in a bio/catalytic refinery. *International Journal of Hydrogen Energy*, *32*(17), 4135-4141.

World Energy Outlook. (2012).

Wu, J., Hu, F., Hu, X., Wei, Z., & Shen, P. K. (2008). Improved kinetics of methanol oxidation on Pt/hollow carbon sphere catalysts. *Electrochimica Acta*, *53*(28), 8341-8345.

Xie, R., Li, D., Hou, B., Wang, J., Jia, L., & Sun, Y. (2011). Solvothermally derived Co_3O_4@m-SiO_2 nanocomposites for Fischer–Tropsch synthesis. *Catalysis Communications*, *12*(5), 380-383.

Xiong, J., Dong, X., Dong, Y., Hao, X., & Hampshire, S. (2012). Dual-production of nickel foam supported carbon nanotubes and hydrogen by methane catalytic decomposition. *International Journal of Hydrogen Energy*, *37*(17), 12307-12316.

Yang, J., Sun, Y., Tang, Y., Liu, Y., Wang, H., Tian, L., Wang, H., Zhang, Z., Xiang, H., & Li, Y. (2006). Effect of magnesium promoter on iron-based catalyst for Fischer–Tropsch synthesis. *Journal of Molecular Catalysis A: Chemical*, *245*(1–2), 26-36.

Yao, L., Shi, T., Li, Y., Zhao, J., Ji, W., & Au, C.-T. (2011). Core–shell structured nickel and ruthenium nanoparticles: Very active and stable catalysts for the generation of CO_x-free hydrogen via ammonia decomposition. *Catalysis Today*, *164*(1), 112-118.

Zadeh, J. S. M., & Smith, K. J. (1998). Kinetics of CH_4 decomposition on supported cobalt catalysts. *Journal of Catalysis*, *176*(1), 115-124.

Zapata, B., Valenzuela, M. A., Palacios, J., & Torres-Garcia, E. (2010). Effect of Ca, Ce or K oxide addition on the activity of Ni/SiO_2 catalysts for the methane decomposition reaction. *International Journal of Hydrogen Energy*, *35*(21), 12091-12097.

Zavarukhin, S. G., & Kuvshinov, G. G. (2004). The kinetic model of formation of nanofibrous carbon from CH_4–H_2 mixture over a high-loaded nickel catalyst with consideration for the catalyst deactivation. *Applied Catalysis A: General*, *272*(1–2), 219-227.

Zhang, C.-H., Yang, Y., Teng, B.-T., Li, T.-Z., Zheng, H.-Y., Xiang, H.-W., & Li, Y.-W. (2006). Study of an iron-manganese Fischer–Tropsch synthesis catalyst promoted with copper. *Journal of Catalysis, 237*(2), 405-415.

Zhang, J., Jin, L., He, X., Liu, S., & Hu, H. (2011). Catalytic methane decomposition over activated carbons prepared from direct coal liquefaction residue by KOH activation with addition of SiO_2 or SBA-15. *International Journal of Hydrogen Energy, 36*(15), 8978-8984.

Zhang, J., Jin, L., Hu, H., & Xun, Y. (2012). Effect of composition in coal liquefaction residue on catalytic activity of the resultant carbon for methane decomposition. *Fuel, 96*(0), 462-468.

Zhang, J., Jin, L., Li, Y., & Hu, H. (2013). Ni doped carbons for hydrogen production by catalytic methane decomposition. *International Journal of Hydrogen Energy, 38*(10), 3937-3947.

Zhang, J., Jin, L., Li, Y., Si, H., Qiu, B., & Hu, H. (2013). Hierarchical porous carbon catalyst for simultaneous preparation of hydrogen and fibrous carbon by catalytic methane decomposition. *International Journal of Hydrogen Energy, 38*(21), 8732-8740.

Zhang, J., Jin, L., Liu, S., Xun, Y., & Hu, H. (2012). Mesoporous carbon prepared from direct coal liquefaction residue for methane decomposition. *Carbon, 50*(3), 952-959.

Zhang, T., & Amiridis, M. D. (1998). Hydrogen production via the direct cracking of methane over silica-supported nickel catalysts. *Applied Catalysis A: General, 167*(2), 161-172.

Zhang, W.-M., Hu, J.-S., Guo, Y.-G., Zheng, S.-F., Zhong, L.-S., Song, W.-G., & Wan, L.-J. (2008). Tin-nanoparticles encapsulated in elastic hollow carbon spheres for high-performance anode material in lithium-ion batteries. *Advanced Materials, 20*(6), 1160-1165.

Zhang, W., Ge, Q., & Xu, H. (2009). Influences of Precipitate Rinsing Solvents on Ni Catalyst for Methane Decomposition to CO_x-free Hydrogen†. *The Journal of Physical Chemistry A, 114*(11), 3818-3823.

Zhang, W., Ge, Q., & Xu, H. (2011). Influences of reaction conditions on methane decomposition over non-supported Ni catalyst. *Journal of Natural Gas Chemistry, 20*(4), 339-344.

Zhang, Y., & Smith, K. (2004). Carbon formation thresholds and catalyst deactivation during CH_4 decomposition on supported Co and Ni catalysts. *Catalysis Letters, 95*(1-2), 7-12.

Zhang, Y., & Smith, K. J. (2002). CH_4 decomposition on Co catalysts: effect of temperature, dispersion, and the presence of H_2 or CO in the feed. *Catalysis Today, 77*(3), 257-268.

Zhuang, Q. L., Kyotani, T., & Tomita, A. (1994). DRIFT and TK/TPD Analyses of Surface Oxygen Complexes Formed during Carbon Gasification. *Energy & Fuels, 8*(3), 714-718.

Zou, J., Peng, Y.-G., & Tang, Y.-Y. (2014). A facile bi-phase synthesis of Fe_3O_4@SiO_2 core-shell nanoparticles with tunable film thicknesses. *RSC Advances, 4*(19), 9693-9700.

Züttel, A. (2004). Hydrogen storage methods. *Naturwissenschaften, 91*(4), 157-172.

Appendix A

The pore diameter distributions naked and SiO_2 supported Ni, Fe and Co nanoparticles calculated with Barrett–Joyner–Halenda (BJH) method

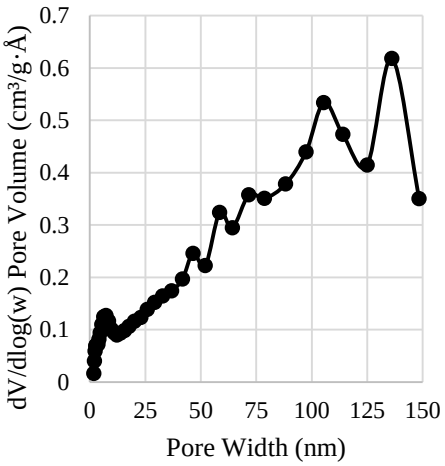

a)

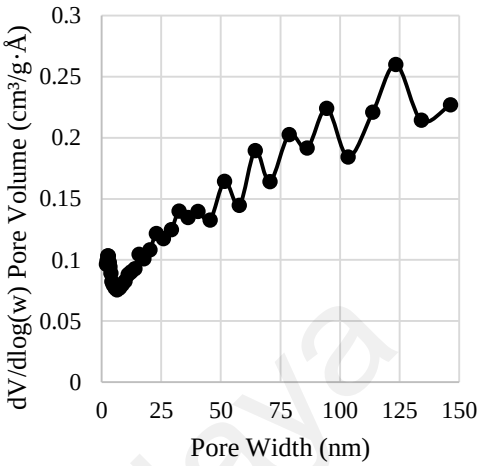

b)

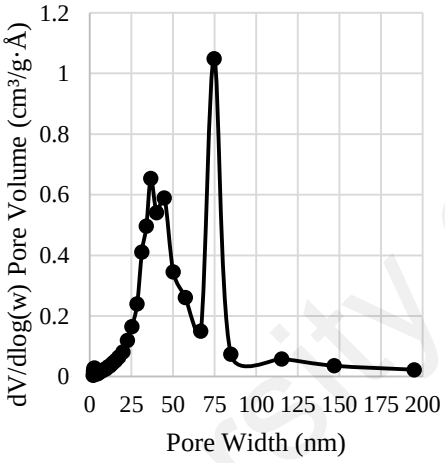

c)

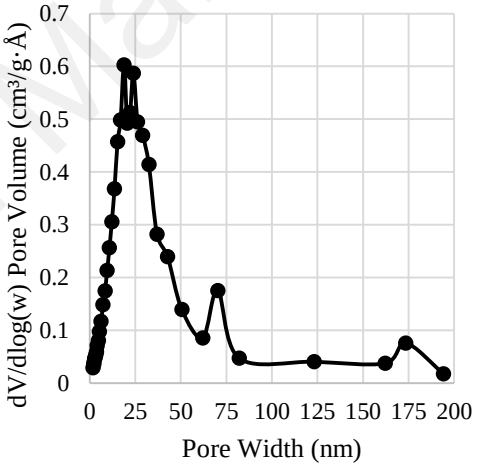

d)

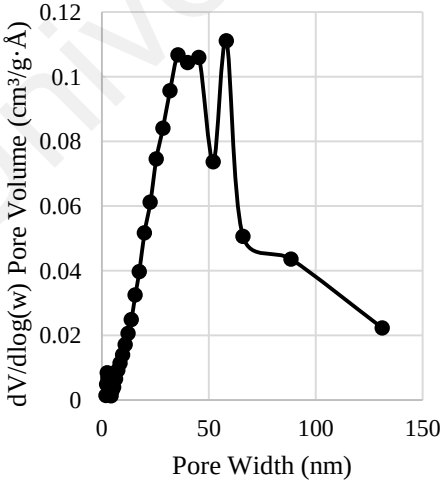

e)

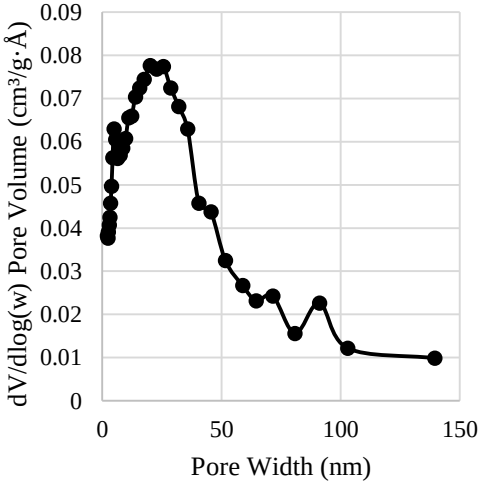

f)

a) *n*-NiO, b) *n*-NiO/SiO_2, c) *n*-FeO, d) *n*-FeO/SiO_2, e) *n*-CoO and f) *n*-CoO/SiO_2.

Appendix B

Loops of N_2-adsorption–desportion isotherms of *n*-NiO/SiO_2 catalyst prepared with different precursor concentration

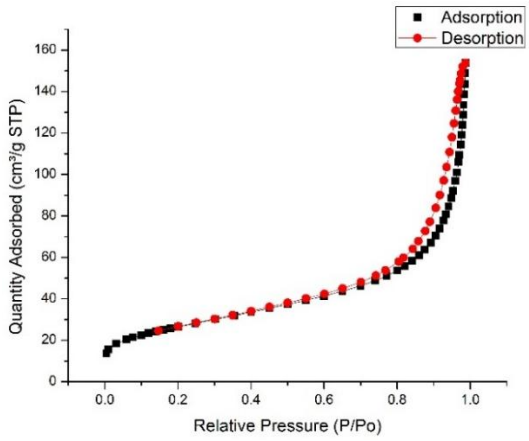

a) *n*-NiO/SiO_2_(1)

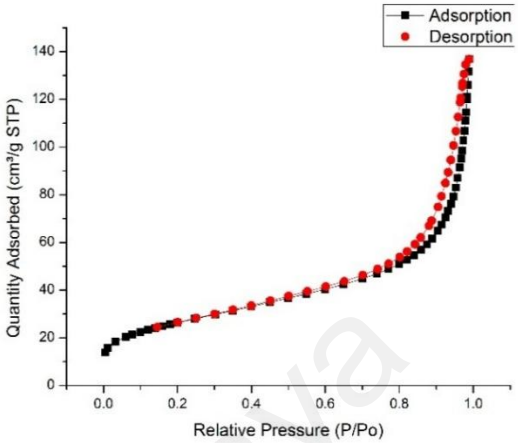

b) *n*-NiO/SiO_2_(2)

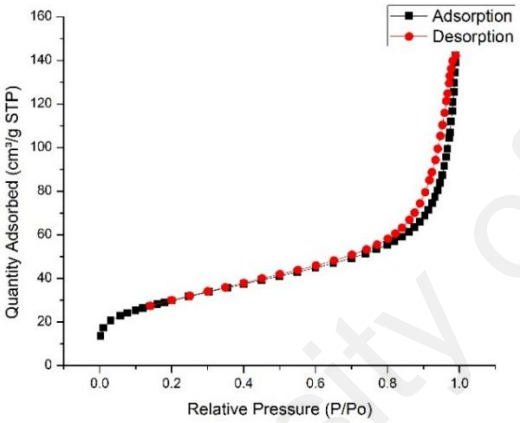

c) *n*-NiO/SiO_2_(3)

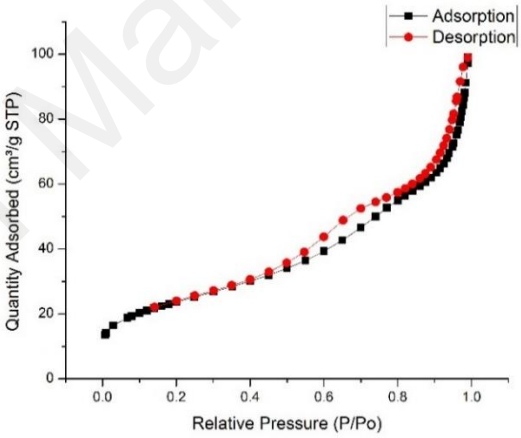

d) *n*-NiO/SiO_2_(4)

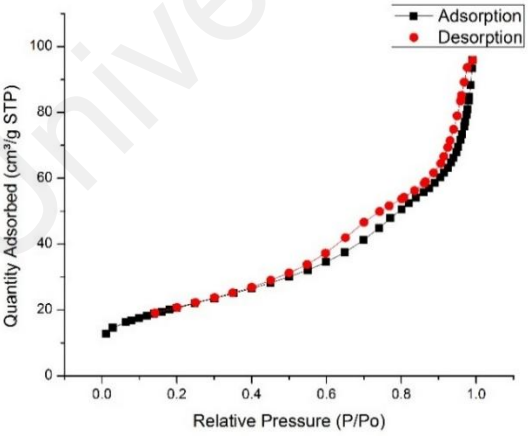

e) *n*-NiO/SiO_2_(5)

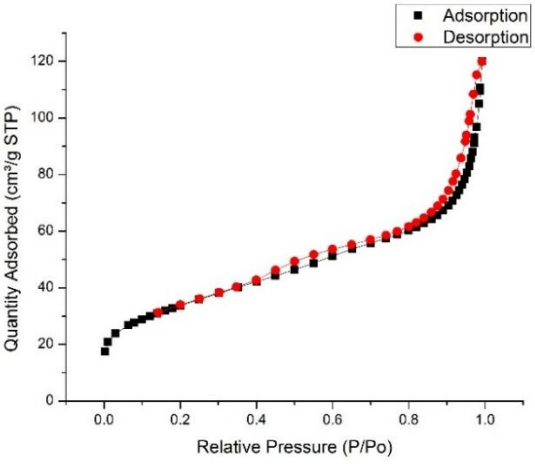

f) *n*-NiO/SiO_2_(6)

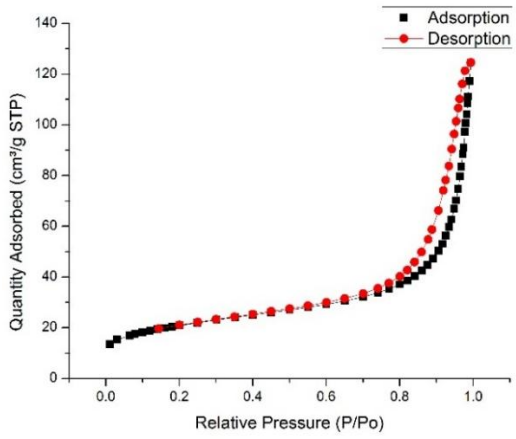

g) *n*-NiO/SiO_2_(7)

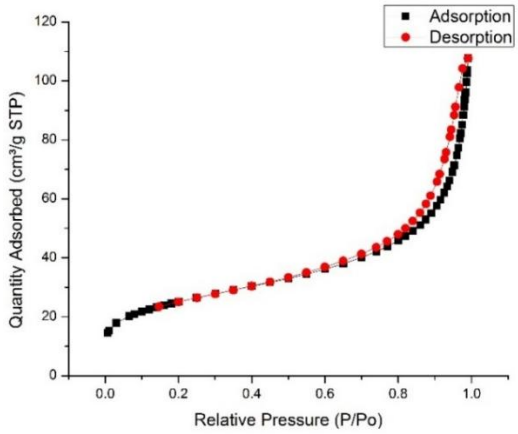

h) *n*-NiO/SiO_2_(8)

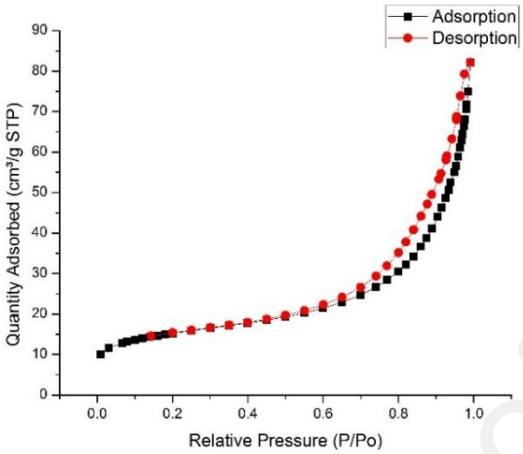

i) *n*-NiO/SiO_2_(9)

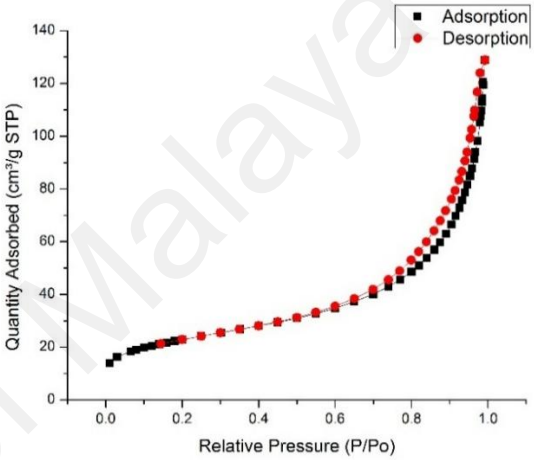

j) *n*-NiO/SiO_2_(10)

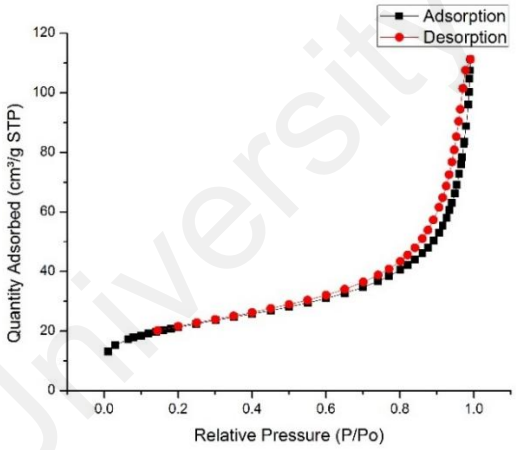

k) *n*-NiO/SiO_2_(11)

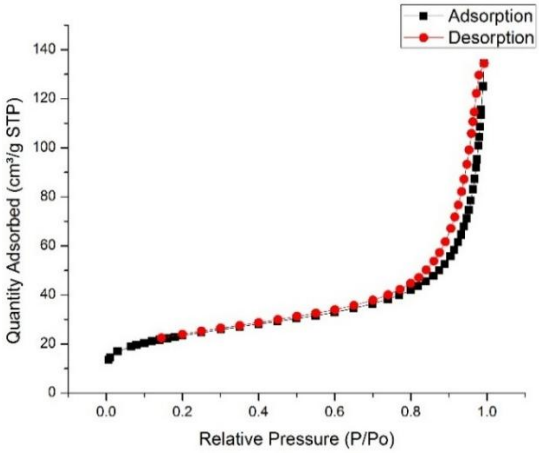

l) *n*-NiO/SiO_2_(11)

Appendix C

The pore diameter distributions of prepared *n*-NiO/SiO$_2$ catalyst calculated with Barrett–Joyner–Halenda (BJH) method

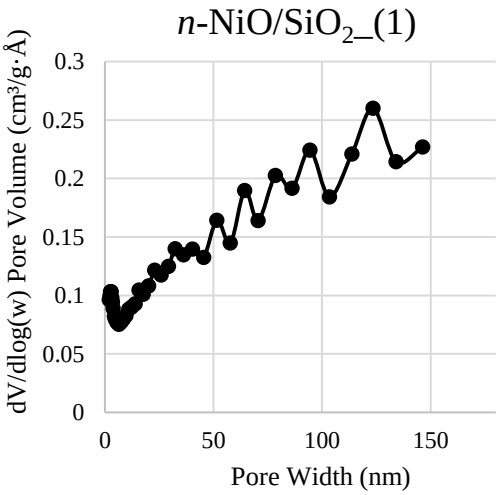

a)

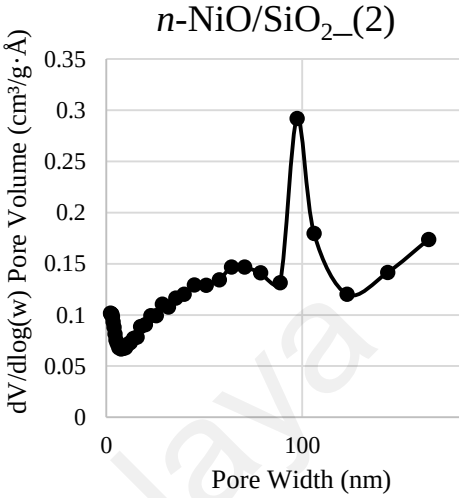

b)

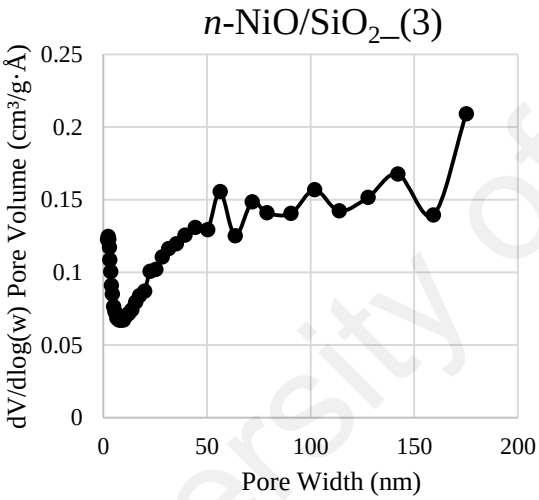

c)

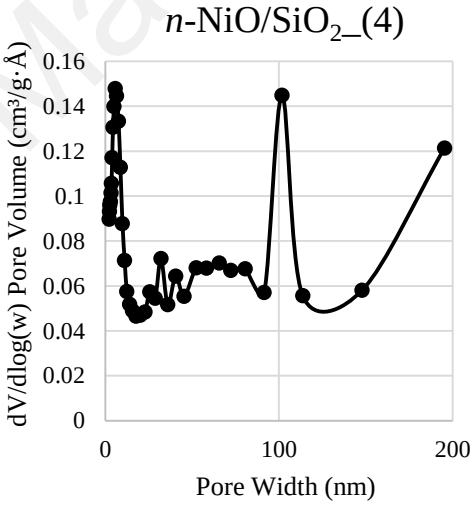

d)

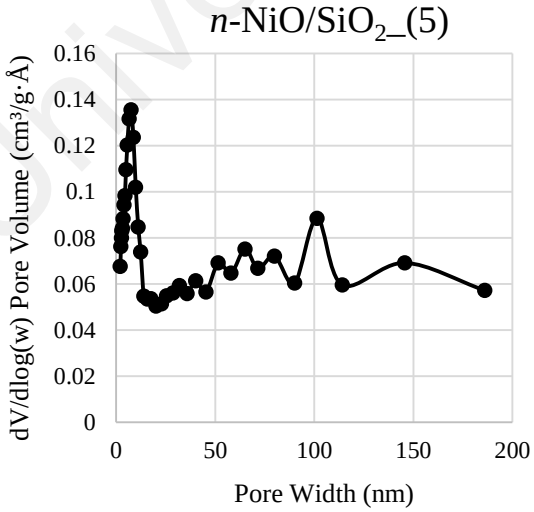

e)

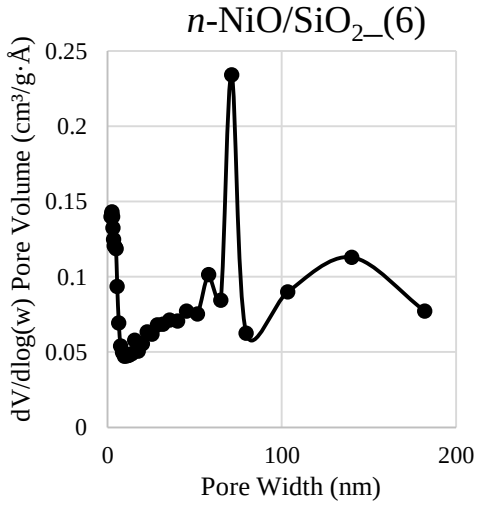

f)

g)

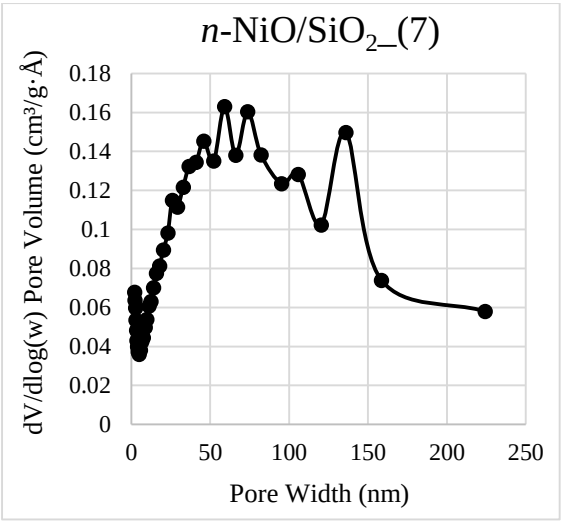

h)

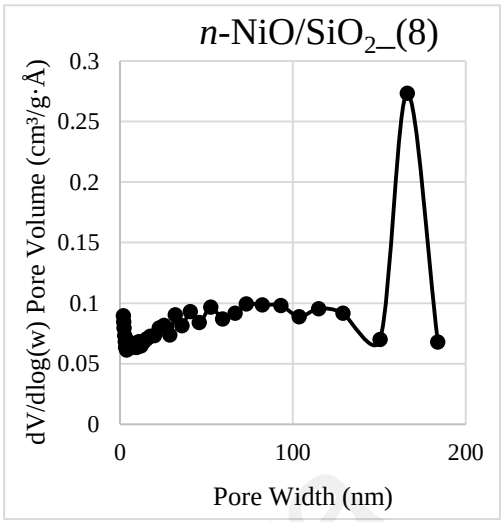

i)

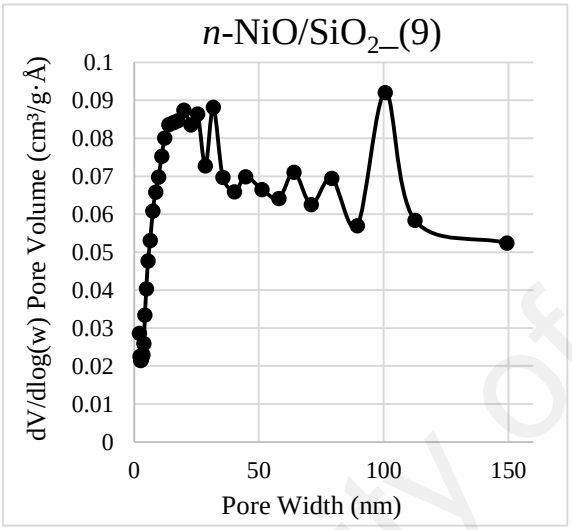

j)

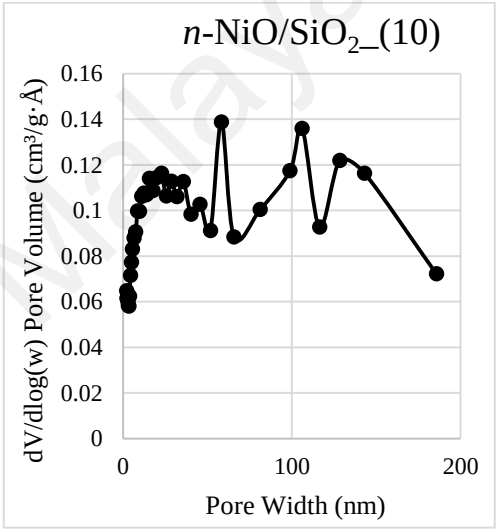

k)

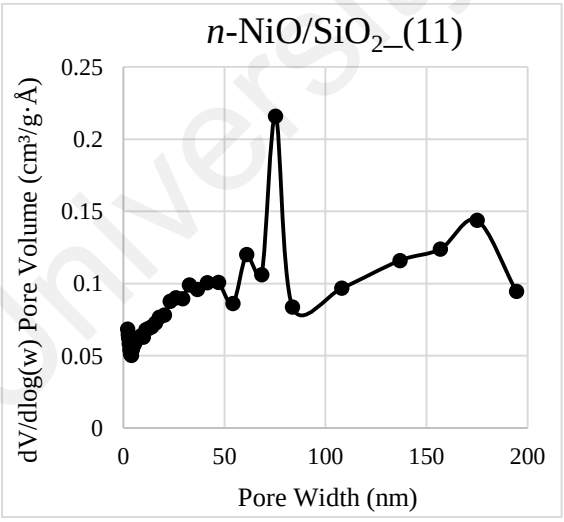

l)

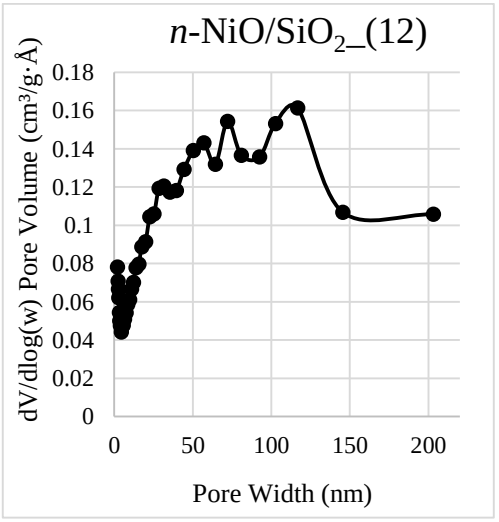

Appendix D

Elemental mapping of prepared *n*-NiO/SiO_2 catalysts prepared with different precursor concentration

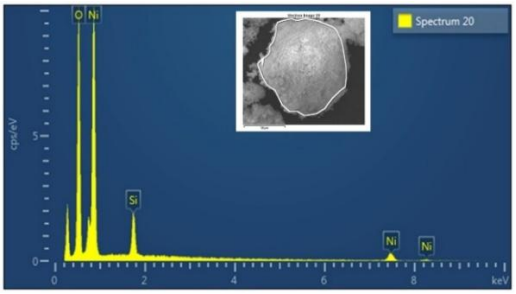

a) *n*-NiO/SiO_2_(1)

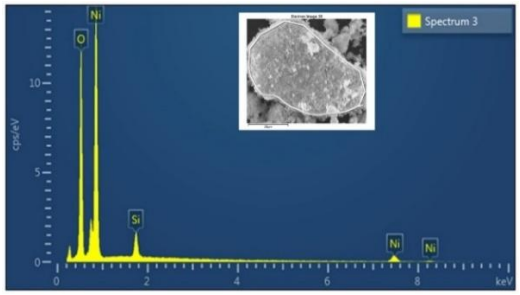

b) *n*-NiO/SiO_2_(2)

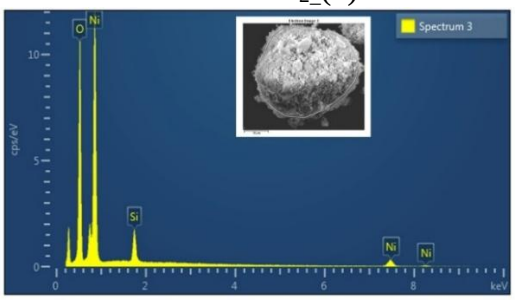

c) *n*-NiO/SiO_2_(3)

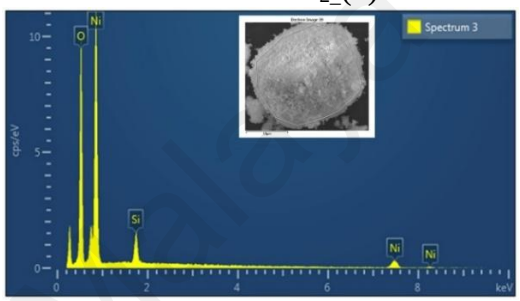

d) *n*-NiO/SiO_2_(4)

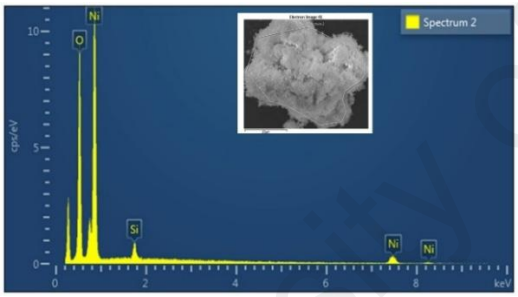

e) *n*-NiO/SiO_2_(5)

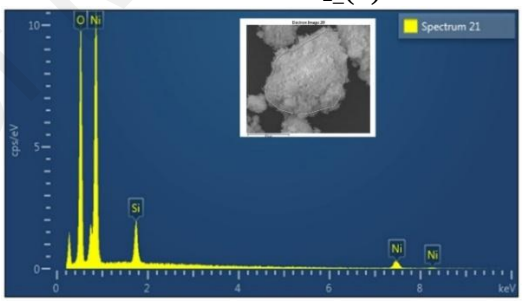

f) *n*-NiO/SiO_2_(6)

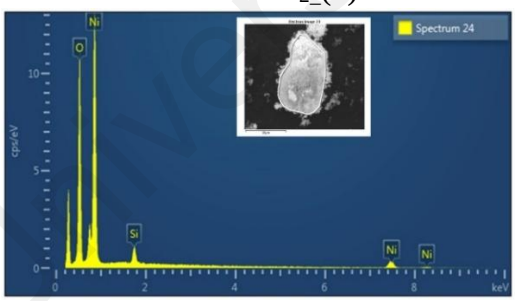

g) *n*-NiO/SiO_2_(7)

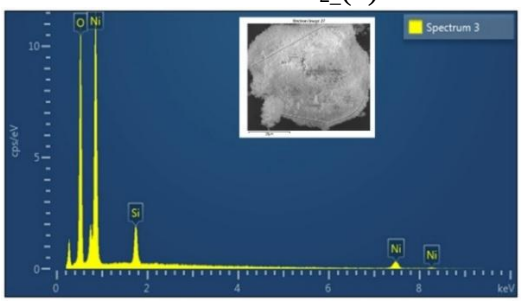

h) *n*-NiO/SiO_2_(8)

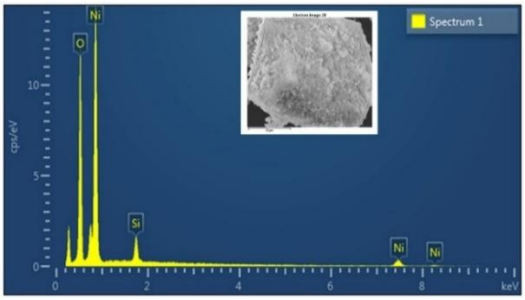

i) *n*-NiO/SiO_2_(9)

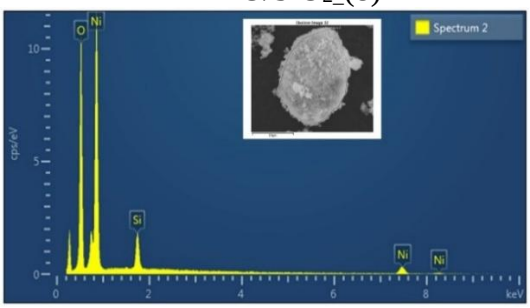

j) *n*-NiO/SiO_2_(10)

k) 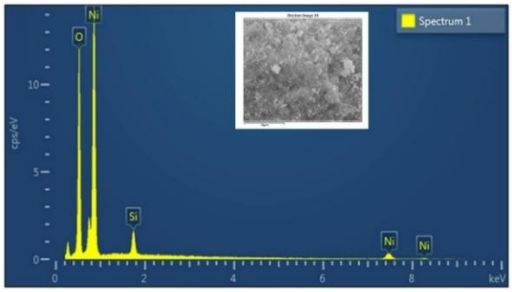

l) 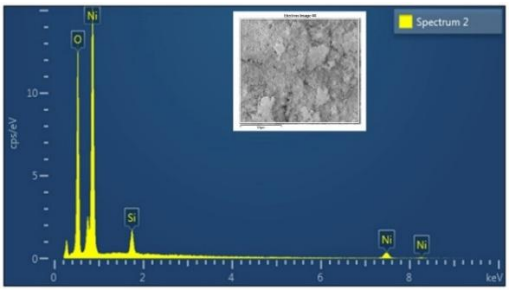

n-NiO/SiO_2_(11)

n-NiO/SiO_2_(12)

Appendix E

Influence of nickel/silicate ratio and influence of different solvents on the activity of *n*-NiO/SiO_2 catalyst

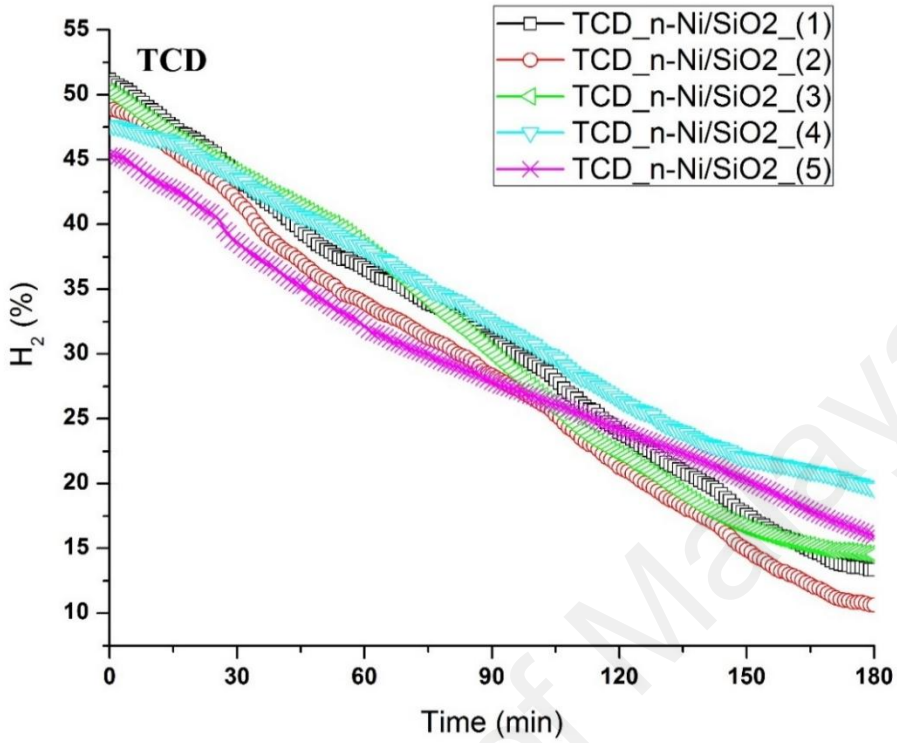

a)

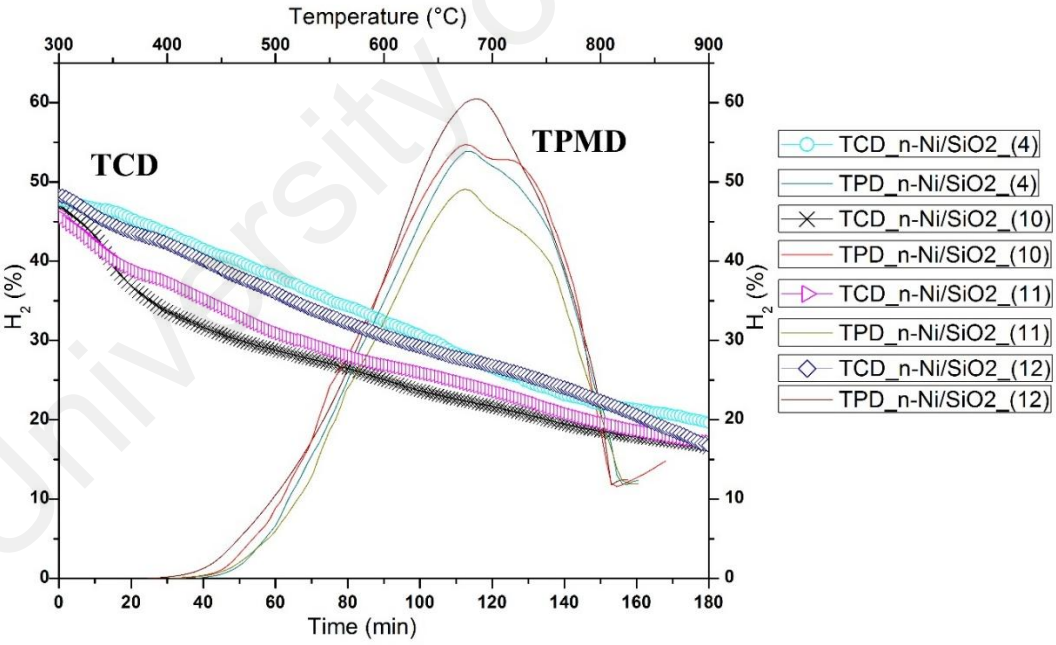

b)

Hydrogen formation percentage during temperature programmed methane decomposition (TPMD) and thermocatalytic decomposition of methane (TCD) at 625 °C, a) Influence of nickel/silicate ratio and b) influence of different solvents. Flow rate = 0.6 L/min and catalyst weight = 0.5 gm. In figure (b), bottom x-axis is time (min) and left y-axis is H_2 (%) for TCD. Top x-axis is temperature (°C) and right y-axis is H_2 (%) for TPMD.

TCD to show the Reproducibility of the process

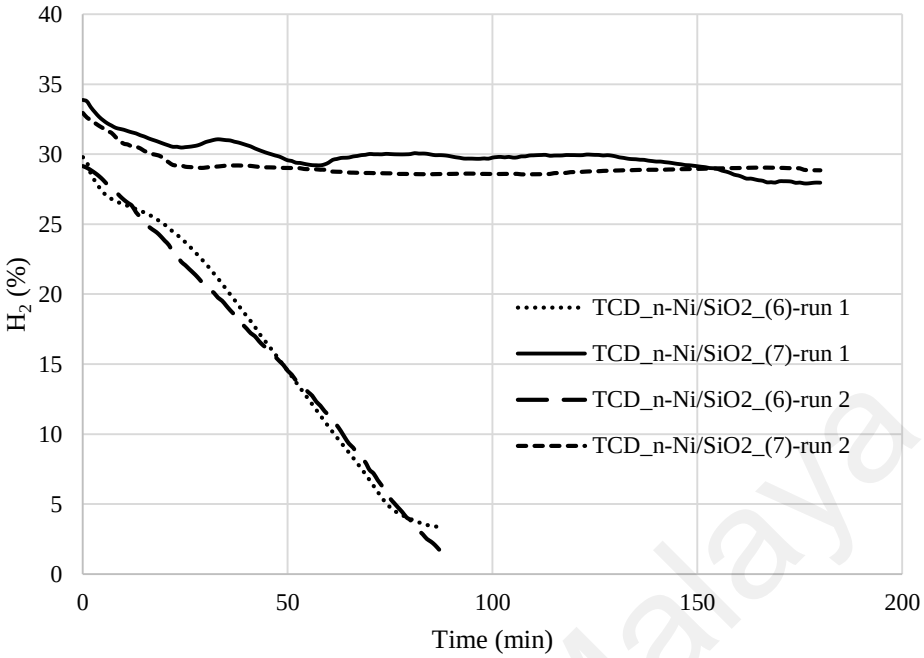

Appendix F:

List of Publications and conference proceedings

The following articles are published in peer reviewed ISI ranked journals as the part of this research.

- Ashik, U. P. M., Wan Daud, W. M. A., & Abbas, H. F. (2015). *Production of greenhouse gas free hydrogen by thermocatalytic decomposition of methane – A review*. Renewable and Sustainable Energy Reviews, **44(0)**, 221-256. DOI: 10.1016/j.rser.2014.12.025

Renewable and Sustainable Energy Reviews 44 (2015) 221–256

Contents lists available at ScienceDirect

Renewable and Sustainable Energy Reviews

journal homepage: www.elsevier.com/locate/rser

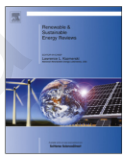

Production of greenhouse gas free hydrogen by thermocatalytic decomposition of methane – A review

U.P.M. Ashik [a], W.M.A. Wan Daud [a,*], Hazzim F. Abbas [b]

[a] Department of Chemical Engineering, University of Malaya, 50603 Kuala Lumpur, Malaysia
[b] Department of Chemical Engineering, University of Nizwa, Al Dakulaya, Oman

ARTICLE INFO

Article history:
Received 10 June 2014
Received in revised form
1 December 2014
Accepted 12 December 2014

Keywords:
Catalytic methane decomposition
Hydrogen production
Metal-carbon catalysts
Methane co-feeding
Hydrogen separation membrane

ABSTRACT

Thermocatalytic decomposition of methane (TCD) is a fully green single step technology for producing hydrogen and nano-carbon. This review studying all development in laboratory-scale research on TCD, especially the recent advances like co-feeding effect and catalyst regeneration for augmenting the productivity of the whole process. Although a great success on the laboratory-scale has been fulfilled, TCD for greenhouse gas (GHG) free hydrogen production is still in its infancy. The need for commercialization of TCD is greater than ever in the present situation of huge GHG emission. TCD usually examined over various kind of catalysts, such as monometallic, bimetallic, trimetallic, combination of metal–metal oxide, carbonaceous and/or metal doped carbon catalysts. Deactivation of catalysts is the prime drawback found in TCD process. Catalyst regeneration and co-feeding of methane with other hydrocarbon are the two solutions put forwarded in accordance to overcome deactivation hurdle. Higher amount of co-feed hydrocarbon in situ produce more amount of highly active carbonaceous deposits which assist further methane decomposition to produce additional hydrogen to a great extent. The methane conversion rate increases with increase in the temperature and decreases with the flow rate in the co-feeding process in a similar manner as observed in normal TCD. The presence of co-components in the post-reaction stream is a key challenge tackled in the co-feeding and regeneration. Hence, this review hypothesizing the integration of hydrogen separation membrane in to methane decomposition reactor for online hydrogen separation.

Contents

Abbreviations: TCD, thermocatalytic decomposition of methane; SRM, steam reforming of methane; POX, partial oxidation; DRM, dry reforming of methane; GHG, greenhouse gas; CNF, carbon nano-fibers; MSI, metal–support interaction; GHSV, gas hourly space velocity; TLC, thin layer catalysts; AC, activated carbon; CB, carbon black; ACPS, activated carbon from palm shell; CNT, carbon nano tube; NCB, nano-sized carbon black; CNF, carbon nano fiber; MWNT, multiwalled nanotube; CLR, coal liquefaction residue; HES, high-energy sites; HPC, hierarchical porous carbon; OSG, oxygen surface group; OCM, oxidative coupling of methane; DFT, density functional theory

* Corresponding author. Tel.: +60 105023818; fax: +60 379675319.
E-mail addresses: upmashik@gmail.com (U.P.M. Ashik), ashri@um.edu.my (W.M.A. Wan Daud), hazzim_f@yahoo.com (H.F. Abbas).

http://dx.doi.org/10.1016/j.rser.2014.12.025
1364-0321/

➢ Ashik, U. P. M., & Daud, W. M. A. W. (2015). *Nano-nickel catalyst reinforced with silicate for methane decomposition to produce hydrogen and nanocarbon: synthesis by co-precipitation cum modified Stober method*. RSC Advances, **5**, 46735-46748. DOI: 10.1039/C5RA07098H

RSC Advances

PAPER

View Article Online
View Journal | View Issue

Cite this: *RSC Adv.*, 2015, **5**, 46735

Nanonickel catalyst reinforced with silicate for methane decomposition to produce hydrogen and nanocarbon: synthesis by co-precipitation cum modified Stöber method†

U. P. M. Ashik and W. M. A. Wan Daud*

Received 20th April 2015
Accepted 1st May 2015

DOI: 10.1039/c5ra07098h

www.rsc.org/advances

Co-precipitation *cum* modified Stöber method is a continuous process avoiding application of higher temperature treatment before supporting nanometal with SiO_2, irrespective of pre-preparation methods. We have conducted the co-precipitation process without undertaking calcination under air in order to avoid even a partial particle agglomeration and hence maintained average particle size ~30 nm after enforcing with SiO_2. This is the first report adopting such an unceasing preparation for preparing metal/silicate nanostructures. Furthermore, n-Ni/SiO_2 nanostructured catalysts were used for thermocatalytic decomposition of methane to produce hydrogen and carbon nanotubes. The catalyst was found to be very stable and the methane transformation activity proceeded for 300 min on methane stream with little deactivation in the temperature range 475–600 °C. We have also successfully extended the catalyst preparation method for Fe and Co metals and conducted preliminary catalyst examinations.

Introduction

Nanostructured materials have recently attracted intensive attention by researchers mainly because of their inbuilt characteristics. Biology, optics, electronics, magnetism, sensing, *etc.* are some fields, chiefly working with nanostructures. Presently, nanostructures produced by applying the Stöber method are scarcely used in catalysis.[1–8] Recent studies have revealed that the enforcement of nanomaterials with inert protective support can enhance the stability of the nanomaterial as well as changing the electron charge, reactivity and functionality of the material.[9–11] Furthermore, nanometal/support composites show dissimilar and advanced properties from those of the individual metal and support materials.[12] Nano-Ni particles have large specific surface area and obviously have large number of active sites which leads to intrinsic surface reactivity, and such nanoparticles tend to aggregate at high temperature, which results in low catalytic stability at higher temperatures. However, shielding of nanoparticles with porous, stable and inert silicates prevents particle agglomeration and gears up the catalyst for higher temperature performance. Silicate supported materials have an advantage of exhibiting a synergetic effect of both metal and support materials. In the case of n-Ni/SiO_2 materials, the Ni phase provides the activity and the porous silica support causes reaction similar to mesoporous silica.

To the best of our knowledge, for the first time we apply n-Ni/SiO_2 catalyst prepared with co-precipitation *cum* modified Stöber method for thermocatalytic decomposition of methane (TCD) for the co-production of hydrogen and nanocarbon. Establishment of clean hydrogen fuel, which does not produce any greenhouse gases (GHG) upon combustion, can profoundly impact on two major contemporary challenges – amelioration of the energy crisis and reduction of environmental pollution from GHGs. The major resources and preparation methods for hydrogen are schematized in Fig. 1. Cell technology, petroleum refining, food, electronics, metallurgical processing industries and many other fields can be fueled by hydrogen and hence its use has attracted tremendous attention by current researchers.[13–16] Global statistics demonstrate that 48% of hydrogen is produced form natural gas, corresponding to 240 billion cubic meters (Bcm) per year. Of the remainder, 30% (150 Bcm per year) comes from petroleum, and 18% (90 Bcm per year) from coal. Regrettably, only 4% (20 Bcm per year) is obtained through water electrolysis without producing any GHG.[17,18] There are different types of methods that have been developed for hydrogen production, such as bio-hydrogen production, reviewed elsewhere,[19] steam reforming of methane (SRM), partial oxidation (POX), coal gasification, water splitting, biomass gasification and thermochemical processes.[20–23] Water splitting is a clean process as it consumes only renewable solar and wind energy, but is not economical because of its very low efficiency and higher processing cost. Furthermore, gasification and reforming of biomass are extensively explored for producing

Department of Chemical Engineering, University of Malaya, 50603, Kuala Lumpur, Malaysia. E-mail: upmashik@gmail.com; ashri@um.edu.my; Fax: +60 379675319; Tel: +60 105023818, +919496844805

† Electronic supplementary information (ESI) available. See DOI: 10.1039/c5ra07098h

➢ Ashik, U. P. M & Daud, W. M. A. W. (2015). *Probing the differential methane decomposition behaviors of n-Ni/SiO₂, n-Fe/SiO₂ and n-Co/SiO₂ catalysts prepared by co-precipitation cum modified Stöber method*, RSC Advances, **5**, 67227-67241. DOI: 10.1039/C5RA10997C

RSC Advances

PAPER

Cite this: *RSC Adv.*, 2015, **5**, 67227

Probing the differential methane decomposition behaviors of *n*-Ni/SiO_2, *n*-Fe/SiO_2 and *n*-Co/SiO_2 catalysts prepared by co-precipitation cum modified Stöber method

U. P. M. Ashik and W. M. A. Wan Daud*

n-Ni/SiO_2, *n*-Fe/SiO_2 and *n*-Co/SiO_2 nano-catalysts were prepared by co-precipitation cum modified Stöber method and applied for thermocatalytic decomposition of methane in order to investigate their thermal stability and activity to produce greenhouse gas free hydrogen and nano-carbon. The mean particles sizes of the produced nano-catalysts obtained from BET analysis are 32.19 nm, 30.26 nm and 49.92 nm, respectively. Temperature programmed methane decomposition were conducted as a preliminary catalytic examination and further isothermal analyses were performed at 700 °C, 600 °C and 500 °C. Production of hydrogen at each experimental temperatures and corresponding carbon yield were measured. Among the three catalysts inspected, *n*-Ni/SiO_2 was found to be the most efficient one for thermocatalytic methane decomposition. Furthermore, significant catalytic stability was observed with *n*-Ni/SiO_2 at 500 °C and 600 °C. While, the rapid deactivation of the *n*-Fe/SiO_2 and *n*-Co/SiO_2 catalysts are attributed to particle agglomeration and the irregular formation of nano-carbon due to metal fragmentation. Physical and chemical characteristics of the produced nano-catalysts were investigated by N_2 adsorption–desorption measurement (BET), X-ray diffraction (XRD), transmission electron microscopy (TEM) and hydrogen-temperature programmed reduction (H_2-TPR). Produced nano-carbon were inspected with TEM, FESEM and XRD.

Received 10th June 2015
Accepted 30th July 2015

DOI: 10.1039/c5ra10997c

www.rsc.org/advances

Introduction

Forthcoming advancements in catalysis are very reliant on the fabrication of catalytic materials with advanced features. Nowadays, investigations on catalyst technology are predominantly focusing on development of smaller materials with efficient properties like activity, selectivity and stability. The novel advancements in nanotechnology have simplified the production of very fine nano-particles with narrow size distributions less than 100 nm.[1] Hence, nano-materials can be defined as those materials having one or more dimension in the nanometer scale (<100 nm) range. These nano-materials have gained predominant consideration because of the immense changes that occur in their physical and chemical properties when micro particles transform to nanoparticles. The catalytic performance of nano-materials is associated with their morphology, size distribution, and electronic properties. It is well known that the preparation methods, stabilizer, as well as supports selected, can individually influence all of these characteristic properties.[2] So far, enormous research efforts have been devoted in order to explore the catalytic application of transition metals with size in the nano-range. Achieving nano-size is quite challenging and hence there are many techniques were developed. Those methods can be broadly classified as (i) condensation from vapor, (ii) synthesis by chemical reaction, and (iii) solid-state processes such as milling. Co-precipitation, a chemical reaction synthesis was adopted in our study to prepare adequate metal oxide nano-particles. The inherent surface characteristics of such nano-particles are highly desirable for catalysis purposes. While, those naked nanoparticles are undergoing easy aggregation at higher temperature results in its faster degradation and hence excluded from higher temperature catalytic applications.[3] We have targeted to safeguard active metal phase with stable, inert and porous material by modified Stöber method.[3] Henceforth, it can effectively prevent higher temperature agglomeration and tolerating its higher temperature utilizations.

The produced porous and high temperature withstanding catalysts were used for thermocatalytic decomposition of methane (TCD) to produce hydrogen and nano-carbon, two cherished products in the field of environmentally benign energy and nanotechnology. Hence, there have been intense research efforts on methane decomposition in recent years as hydrogen is a relevant raw material in chemical and petroleum

Department of Chemical Engineering, University of Malaya, 50603, Kuala Lumpur, Malaysia. E-mail: upmashik@gmail.com; ashri@um.edu.my; Fax: +60 379675319; Tel: +60 105023818; +919496844805

➢ Ashik, U. P. M & Daud, W. M. A. W. (2016). *Stabilization of Ni, Fe, and Co nanoparticles through modified Stöber method to obtain excellent catalytic performance: Preparation, characterization, and catalytic activity for methane decomposition*, Journal of Taiwan Institute of Chemical Engineering, **61**, 247-260. DOI: 10.1016/j.jtice.2015.12.019.

ARTICLE IN PRESS
JID: JTICE [m5G;January 25, 2016;22:11]
Journal of the Taiwan Institute of Chemical Engineers 000 (2016) 1–14
Contents lists available at ScienceDirect
Journal of the Taiwan Institute of Chemical Engineers
journal homepage: www.elsevier.com/locate/jtice

Stabilization of Ni, Fe, and Co nanoparticles through modified Stöber method to obtain excellent catalytic performance: Preparation, characterization, and catalytic activity for methane decomposition

U.P.M. Ashik, W.M.A. Wan Daud*

Department of Chemical Engineering, University of Malaya, 50603, Kuala Lumpur, Malaysia

ARTICLE INFO

Article history:
Received 10 July 2015
Revised 15 November 2015
Accepted 15 December 2015
Available online xxx

Keywords:
Nano-catalysts
Modified Stöber method
Thermocatalytic methane decomposition
Hydrogen
Nano-carbon
Bottom-up method

ABSTRACT

Nanoparticle formation from their respective precursors through bottom-up method is a very fascinating practice in nanotechnology. This research contribution discusses two promising bottom-up methods: (i) controlled precipitation of Ni, Fe, and Co nanoparticles and reinforcement with silicate through modified Stöber method and (ii) chemical vapor deposition of nanocarbon from methane. Experimental results reveal that metal oxide particles were formed as single-crystal nanoparticles after silicate addition and exhibited catalytic activity enhancing features, such as low particle size and high surface area and porosity. The single-point surface area increased from 62.22 m^2/g to 91.50 m^2/g, 35.13 m^2/g to 97.31 m^2/g, and 14.29 m^2/g to 48.96 m^2/g for *n*-NiO, *n*-FeO, and *n*-CoO nanoparticles, respectively, after silicate incorporation. Preliminary catalytic activity was also analyzed in a fixed-bed pilot plant. *n*-NiO/SiO_2 nanoparticles were found to be the most efficient catalyst for thermocatalytic methane decomposition and generated 57.28% hydrogen at 730 °C. Physical and chemical characteristics of the fabricated nanocatalysts were determined using N_2 adsorption–desorption measurement (Brunauer–Emmett–Teller method), X-ray diffraction (XRD), transmission electron microscopy (TEM), hydrogen temperature-programmed reduction (H_2-TPR), and field-emission scanning electron microscopy (FESEM) analyses. Produced nano-carbon was inspected with TEM, FESEM and XRD.

1. Introduction

Nanotechnology exhibits potential applications in almost any scientific field and has exponentially developed over the last couple of decades. The ubiquitous possibilities of using nanotechnology are mainly due to the property enhancement that occurs in nanoparticles at their unique size and shape. Research on nanotechnology primarily focuses on developing novel nanoparticles with small size and refined shapes. As such, preparation of nanoparticles requires thorough understanding of the surface characteristics of these materials. The quality and structure of nanoparticles play a vital role in their potential applications. Nanoparticles can be synthesized using two methods: bottom-up (particle assembling in solution) and top-down (lithographic techniques). The bottom-up approach is a technique in which nanoparticles are built from the bottom through atom-by-atom, molecule-by-molecule, or cluster-by-cluster, as illustrated in Scheme 1. This well-established method ensures the formation of nanoparticles with less defects, homogeneous chemical composition, and improved crystal ordering [1,2]. By contrast, the top–down method is rarely applied to convert giant sized to nanosized particles because the physical stress applies during top–down approach generates surface defects and contaminants [3].

The bottom–up method, in which nanoparticles are formed through precipitation from solution, requires sufficient knowledge on process parameters, which control the size, shape, and other characteristics of nanoparticles. Transition metal nanoparticles with different shapes were synthesized in 1996 and were used to observe variation in catalysis performance [4]. The researchers found that the activity of platinum nanoparticles varies according to their shapes for electron-transfer reaction [5]. Strict control of parameters, such as reactant concentration, pH, and temperature, can produce monodispersed nanoparticles. Scholars succeeded in developing fine Zr- [6], Ti- [7], Cu- [8], Ni- [9], Co- [10] and Cd-based [11] nanoparticles through parameter regulation. The surface-to-volume ratio is generally high with decreasing particle sizes and could increase the specific catalytic activity of metal particles. Therefore, much research effort has been devoted on nanoparticle synthesis with precise size control. Nanoparticles

* Corresponding author. Tel.: +60 105023818/+91 9496844805; fax: +60 379675319.
E-mail addresses: upmashik@gmail.com, ashikumathur@gmail.com (U.P.M. Ashik), ashri@um.edu.my (W.M.A.W. Daud).

http://dx.doi.org/10.1016/j.jtice.2015.12.019
1876-1070/

The results from this research was used to produce following articles, those are submitted to the mentioned ISI ranked journals.

- Ashik, U. P. M & Daud, W. M. A. W. *Governance of methane decomposition activity sustainability of n-NiO/SiO_2 nano-catalysts by changing synthesis parameters: modified Stöber method* (Submitted to Journal of Industrial and Engineering Chemistry).

- Ashik, U. P. M, Daud, W. M. A. W & Abbas, H. F. *Methane decomposition kinetics and reaction rate over n-NiO/SiO_2 catalyst produced through co-precipitation cum modified Stöber method* (Submitted to Renewable Energy)

Conference Proceedings

The following articles are published in conferences proceedings after peer review.

- Ashik, U. P. M & Daud, W. M. A. W. *Production of GHG free hydrogen from methane: significance of porosity of n-NiO/SiO_2 nanocatalysts*. 16th International Conference on Green and Sustainable Technology (GSUS) to be conducted by Global Research & Development Seriveces, May 16-17, 2016, Kuala Lumpur, Malaysia.

- Ashik, U. P. M & Daud, W. M. A. W. *Production of hydrogen and nanocarbon from methane over n-NiO/SiO_2 catalyst prepared by Co-precipitation cum modified Stöber method*. 14th International Conference on Green and Sustainable Technology (GSUS) conducted by Global Research & Development Seriveces, February 20-21, 2016, Dubai.

- Ashik, U. P. M & Daud, W. M. A. W. *Co-production of hydrogen and nano-carbon from methane*. World Sustainable Energy Days – 2016, February 24-26 , 2016. OÖ Energiesparverband, Wels/Austria.

The following article is accepted after peer review to publish in conference proceeding.

- Ashik, U. P. M & Daud, W. M. A. W. *Stability enhancement of nano-NiO catalyst with SiO_2 support to get improved hydrogen yield from methane decomposition*. 4th International Conference on Envirotech, Cleantech and Greentech (ECG) to be conducted by Global Research & Development Seriveces, July 21-22, 2016, University of Malaya, Malaysia.